UNIVERSIDAD DE GRANADA
DEPARTAMENTO DE QUÍMICA INORGÁNICA

POROUS METAL PYRAZOLATES. SELECTIVE ADSORPTION PROPERTIES

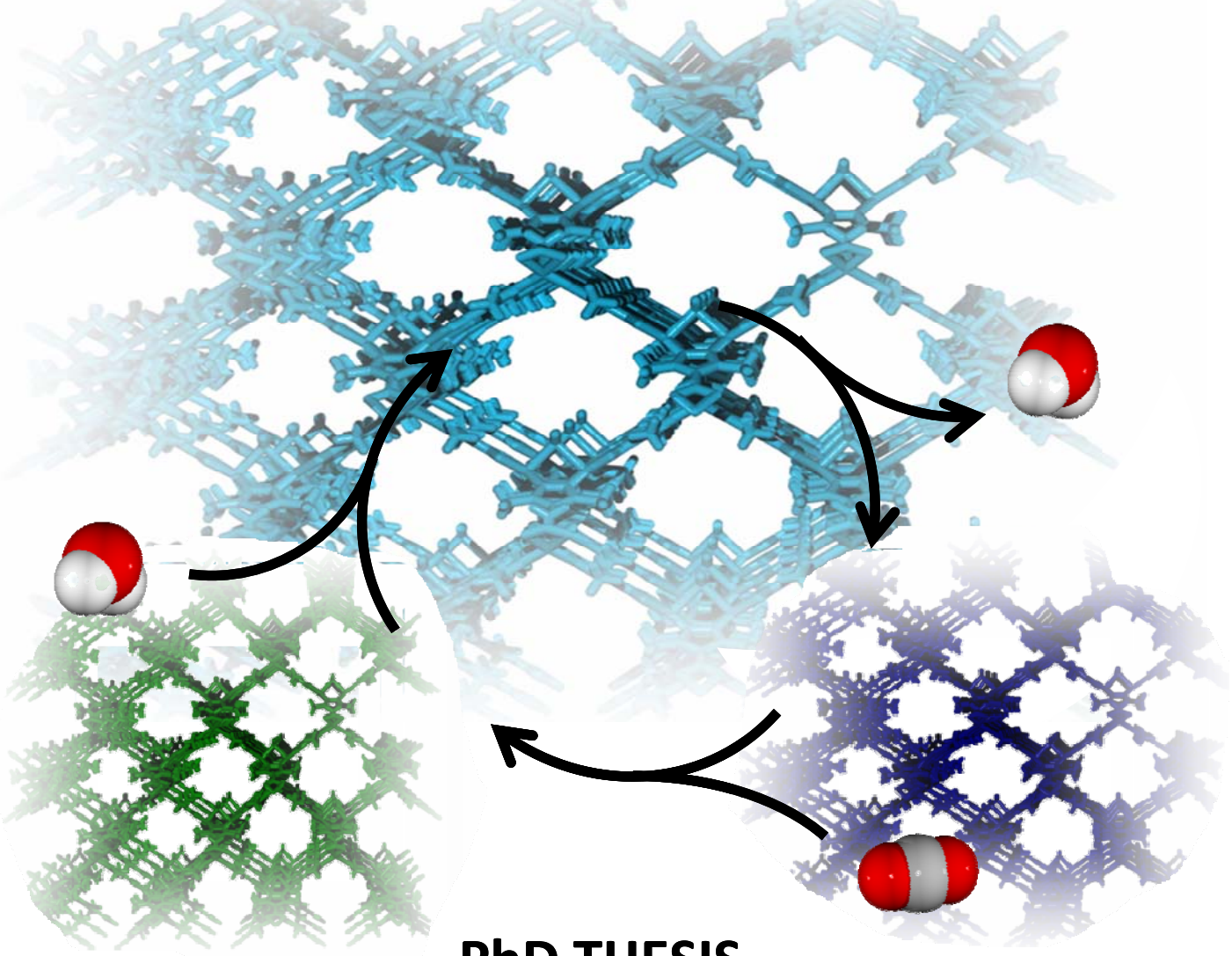

PhD THESIS

ELSA QUARTAPELLE PROCOPIO

Granada, 2012

Editor: Editorial de la Universidad de Granada
Autor: Elsa Quartapelle Procopio
D.L.: GR 1001-2013
ISBN: 978-84-9028-503-9

UNIVERSIDAD DE GRANADA

DEPARTAMENTO DE QUÍMICA INORGÁNICA

POROUS METAL PYRAZOLATES. SELECTIVE ADSORPTION PROPERTIES

Pyrazolatos metálicos porosos. Propiedades adsorbentes selectivas

PhD THESIS

ELSA QUARTAPELLE PROCOPIO

Granada, 2012

La doctoranda Elsa Quartapelle Procopio y los directores de la Tesis Jorge Andrés Rodríguez Navarro y Elisa Barea Martínez, garantizamos, al firmar esta tesis doctoral, que el trabajo ha sido realizado por el doctorando bajo la dirección de los directores de la Tesis y, hasta donde nuestro conocimiento alcanza, en la realización del trabajo, se han respetado los derechos de otros autores, que han sido citados cuando se han utilizado sus resultados o publicaciones.

Granada, 28 de Septiembre 2012

La Doctoranda

Fdo.: Elsa Quartapelle Procopio

Los Directores de la Tesis

Fdo.: Jorge Andrés Rodriguez Navarro
Catedrático de Química Inorgánica de la Universidad de Granada

Fdo.: Elisa Barea Martínez
Profesora Titular de Química Inorgánica de la Universidad de Granada

AGRADECIMIENTOS

Es cierto que lo que he aprendido durante estos años de doctorado no se puede medir de ninguna forma. He aprendido a sintetizar redes moleculares, a estudiar la porosidad de compuestos, a medir cristales… pero no sabría evaluar los efectos que todo esto ha tenido y tendrá en mí. Sin duda he ido "absorbiendo conocimientos en mi porosidad cerebral" que espero que no se desorban nunca!

En primer lugar, quiero agradecer a mis directores de tesis: Elisa Barea, la que tuvo la idea… y Jorge A. R. Navarro, que la apoyó por completo, el que hayan permitido que mi doctorado haya sido tan enriquecedor para mí. Ellos han sido mis maestros (先生), ayudándome en cada momento que me ha hecho falta, dándome consejos cada vez que en mi camino encontraba un cruce, permitiendo que me equivocase para poder buscar yo misma una salida… Pero, sobre todo, me han dejado libertad… La libertad científica que un investigador desea, la libertad de tener opiniones diferentes, la libertad de dar vida a mis pequeñas ideas. Ellos no se han olvidado ni una vez de felicitarme por un trabajo bien hecho y no han dejado nunca que mis dudas se quedasen sin repuestas. Estas dos cosas han sido fundamentales para mí y para el desarrollo de este trabajo. En todo esto (y en mucho más) se basa mi profunda estima para ellos.

El agradecimiento siguiente es para mis compañeras de laboratorio: Fátima Linares, Carmen Montoro, Sara Rojas y Elena López. Con ellas, he compartido tanto momentos de alegría (que siempre han sido parte de cada descubrimiento), como momentos tristes, en los que el camino estaba borroso y los resultados no tenían sentido (si es que había resultados…). Hemos sido un buen equipo, cada una con sus habilidades y sus aportaciones! Gracias a Fátima, con la que compartí mi comienzo y que, por lo tanto, me ha enseñado el inicio de mi camino...

Un agradecimiento especial para el Profesor Enrique Oltra y Natalia Muñoz del Departamento de Química Orgánica de la Universidad de Granada que han llevado a cabo la síntesis de gran parte de los ligandos orgánicos que se han utilizado en esta Tesis. Con regularidad, Natalia me ha estado llenando la mesa de ligandos preciosos: sin ella muy poco de lo que está aquí hubiera sido posible.

Asimismo, sin salir del Departamento de Química Inorgánica de la Universidad de Granada, quiero recordar a todos los profesores y a los demás becarios que forman parte de él. El grupo docente me ha sabido acoger con disponibilidad infinita (no solamente científica) para que yo me sintiera parte del Departamento. Todos los becarios (presentes y pasados….) han sido un apoyo fundamental en muchas ocasiones (uff…el papeleo…!) y una compañía especial en otras. Un especial agradecimiento al grupo del Profesor Javier López con el que hemos colaborado en las medidas de adsorción de gases de algunas de las redes porosas que se presentan en esta Tesis.

Agradezco también al Departamento de Mineralogía de la UGR las facilidades y la disponibilidad para la utilización de su instrumentación.

Inoltre, un ringraziamento speciale va alla mia famiglia. Trattandosi di scienza, devo riconoscere che le critiche, i consigli e i complimenti di mio padre hanno spronato le mie giornate lavorative, motivandomi sempre a capire meglio ogni scoperta. Mia madre invece mi ha sostenuto in ogni cosa...nella scienza e in tutto il resto, quasi come se non fossimo mai state cosí distanti. Mia sorella, credo senza nemmeno saperlo, è stata per me un esempio di dedizione alle proprie passioni...e per questo la voglio ringraziare. Oltre a questo, è importante che ringrazi i miei amici milanesi, per non aver mai lasciato che la distanza ci allontanasse davvero e per credere che io sia piú intelligente di quello che in realtá sono! Tra questi Roberto (che di milanese ha ben poco!) che è sempre stato al mio fianco potendo condividere la mia passione scientifica e molto altro.

También quiero agradecer a todas mis hermanas Fernández: Tati, Carmen, Patri y Ana. Vivir con vosotras ha sido un regalo especial para mí… Me habéis enseñado lo que significa vivir como una española y ahora me siendo más andaluza que nunca… Por el acento, la cocina y miles de cosas más! Aunque no sean Fernández, también Rocío, Paula y Xabi han sido hermanos para mí… Hemos compartido la mayoría de las noches de los primeros dos años y sé que a ninguno nos ha gustado tener que dejarlo… Ahora ya compartimos cosas más serias, como Tesis y trabajo: os agradezco todo lo que habéis hecho al respecto.

Habrá que recordar también a los “hortigueros”, con los que he compartidos vitaminas y agujetas… algo que no se suele compartir con gente cualquiera!

Furthermore, I would like to thank Prof. Susumu Kitagawa, Dr. Horike-san and Fukushima for their kindness during my stage in Kyoto. I learned many things in just three months and this has been possible only because of your scientific willingness and your kind behaviour. Moreover, I want to thank Prof. Rosseinsky for making possible my stage in the University of Liverpool, as well as Dr. Kyriakos for sharing his fumehood with me… no matter if it was so dirty!

A special acknowledgment is reserved to international research groups we had the pleasure to collaborate with: Prof. Norberto Masciocchi, Dr. Simona Galli, Dr. Angelo Maspero and Dr. Valentina Colombo (Università dell'Insubria), Prof. Stefan Kaskel and Dr. Irena Senkowska (Dresden University of Technology). I hope that, in the future, much more could be done together since I realized that any collaboration is a source of scientific richness.

Finalmente, agradezco al Ministerio de Ciencia e Innovación su ayuda económica a través de la beca de Formación de Personal Investigador (BES-2009-011975) y del proyecto CTQ-2008-00037, así como a la Junta de Andalucía por el proyecto P09-FQM-4981 y por aportar fondos al grupo FQM-195.

Un ultimo ringraziamento, un po' inconsueto, lo vorrei rivolgere a mio nonno. Per avermi avvicinato al mondo della chimica, forse sapendo che mi sarebbe piaciuto "essere come lui". Ricordo il consiglio che mi diede, e piú passa il tempo piú sono sicura che sia stato uno dei migliori consigli che io abbia mai ricevuto.

A todos los que me han enseñado algo…

TABLE OF CONTENTS

RESUMEN

Desde hace décadas, los materiales porosos clásicos (como las zeolitas y los carbones activos) son utilizados de forma intensiva en procesos industriales de purificación y separación de gases, intercambio iónico, catálisis heterogénea selectiva, aplicaciones biomédica, etc. Sin duda, las zeolitas son los materiales más utilizados debido a su robustez y excepcional estabilidad térmica así como a su naturaleza cristalina que da lugar a una distribución regular de cavidades y canales de tamaño y forma definidos lo que conlleva interacciones selectivas con átomos, iones y moléculas. Sin embargo, las aplicaciones de las zeolitas se encuentran limitadas por el tamaño máximo del sus cavidades (en general menor de 1 nm) y por la casi total ausencia de flexibilidad y dinámica estructural.

En este contexto, durante los años 90 ha surgido una nueva clase de materiales organometálicos (propuestos por primera vez en 1978) como una posible alternativa versátil a las zeolitas. El primer gran hallazgo en la investigación de estos Polímeros de Coordinación Porosos (PCPs, llamados también MOFs: Redes Metalorgánicas) ha sido la obtención de materiales con porosidad permanente, es decir materiales suficientemente robustos para no colapsar tras la retirada de las moléculas alojadas en sus cavidades. Más tarde, han ido apareciendo una gran cantidad de estructuras, con una amplia gama de posibles aplicaciones.

Aunque los PCPs no pueden competir con las zeolitas y los óxidos porosos inorgánicos en aplicaciones que requieren altas temperaturas debido a su escasa estabilidad térmica, estos materiales presentan algunas ventajas sobre los materiales porosos clásicos: i) se dispone de un número infinito de bloques de construcción orgánicos e inorgánicos que se pueden combinar para dar lugar a una infinidad de estructuras posibles; ii) el tamaño y la forma de los poros pueden ser controlados de manera sistemática, en principio, sin limitaciones; iii) es posible funcionalizar el ligando orgánico o incorporar grupos funcionales directamente en la red, de manera que se obtengan estructuras que contengan grupos químicos capaces de coordinar moléculas huésped y/o catalizar reacciones que involucren a las especies adsorbidas; iv) es posible utilizar los componentes metálicos y/o sus interacciones con las moléculas huésped para diseñar materiales porosos con propiedades físico-químicas inusuales, como por ejemplo actividad redox, propiedades de absorción de luz o momentos magnéticos; v) es

posible utilizar ligandos orgánicos enantiopuros que permitan obtener materiales porosos quirales, útiles en aplicaciones que requieran adsorción o catálisis enantioselectivas.

Sin embargo, la sensibilidad a la humedad y la baja estabilidad térmica de los PCPs son las mayores limitaciones que actualmente presentan en aplicaciones prácticas y, por lo tanto, se requieren muchos esfuerzos para aumentar su robustez.

El trabajo presentado en esta tesis doctoral es parte de un trabajo de investigación mucho más amplio que trata la síntesis y caracterización de polímeros de coordinación porosos útiles en aplicaciones de separación y purificación de gases y vapores de interés industrial y ambiental, con una particular atención en la obtención de sólidos de alta estabilidad térmica y química.

Para conseguir este objetivo, la elección de los grupos funcionales presentes en los espaciadores orgánicos es de gran importancia. Por lo tanto, hemos decidido utilizar una serie de ligandos orgánicos simétricos que contengan el anillo pirazol, en algunos casos combinado con el grupo ácido carboxílico. La razón de esta elección es la naturaleza robusta del enlace de coordinación M-N(pirazolato) mucho más fuerte que el enlace M-O(carboxilato) encontrado con gran frecuencia en la mayoría de la estructuras de PCPs descritos en la literatura.

En este estudio, hemos elegido los iones metálicos de los últimos elementos de la primera serie de transición (Co^{2+}, Ni^{2+}, Cu^{2+} y Zn^{2+}) teniendo en cuenta su naturaleza híbrida de ácidos duros/blandos y química de coordinación versátil, características que los hacen adecuados para la formación de estructuras poliméricas robustas y ordenadas con ligandos N,O dadores de tamaño pequeño o mediano.

Todos los compuestos presentados en este trabajo han sido sintetizados en nuestro laboratorio y caracterizados desde el punto de vista estructural y textural. En la mayoría de los casos, la robustez del enlace de coordinación M-N conlleva la formación de productos policristalinos que han sido caracterizados mediante difracción de rayos X en polvo. Sin embargo, en algunos casos (concretamente con los ligandos mixtos N,O) se han obtenido monocristales de tamaño adecuado para la resolución estructural con la técnica convencional de difracción de rayos X en monocristal.

Tras la caracterización estructural preliminar, se han investigando con detalle las propiedades adsorbentes de los materiales que han presentado porosidad permanente,

prestando especial atención a aplicaciones específicas para cada una de las estructuras prometedoras.

Los compuestos aislados han sido clasificados en cuatro categorías, en función tanto de la estructura local alrededor del átomo metálico como de las propiedades del sólido. Por lo tanto, los materiales han sido divididos en: i) redes zeomiméticas; ii) compuestos de coordinación flexibles; iii) polímeros de coordinación porosos con analogías estructurales al MOF-5; iv) serie isoreticular de PCPs basados en iones Ni^{2+}.

El ensamblaje de moléculas de 4-carboxipirazolato ($L1^{2-}$) con cationes de Cu^{2+} en un medio tamponado NH_3/NH_4^+ da lugar a la formación de una red aniónica de fórmula $[NH_4@Cu_3(\mu_3\text{-}OH)(\mu_3\text{-}L1)_3]_n\cdot solv$ ($NH_4@Cu_3(OH)L1_3$) que se describe en el Capitulo 2. Al contrario de la mayoría de las redes de coordinación zeotípicas (que no suelen dar lugar a procesos de intercambio catiónico debido a su naturaleza neutra o catiónica), la naturaleza aniónica de estos materiales, a semejanza de las zeolitas, puede dar lugar a procesos de intercambio de cationes, abriendo la posibilidad de modular la porosidad del material dependiendo de la carga y tamaño de los cationes intercambiados. Concretamente, hemos demostrado que el proceso de intercambio iónico causa profundos cambios en las propiedades texturales de los materiales porosos $A@Cu_3(OH)L1_3$ (A = catión intercambiable) así como en la adsorción selectiva en diversos procesos de separación de gases y vapores. Por esto, hemos estudiado el efecto del intercambio catiónico en la separación eficiente mediante procesos de adsorción selectiva de mezclas complejas de gases (acetileno, dióxido de carbono, metano, nitrógeno) y de vapores (ciclohexano, benceno).

Inesperadamente, la sustitución del ión Cu^{2+} por Cd^{2+} en el medio de reacción lleva a la formación de un material laminar neutro ($[Cd(H_2O)_2L1]\cdot H_2O$) cuya cristalinidad se pierde tras la activación térmica. De hecho, la eliminación de las moléculas de agua de cristalización de la estructura, da lugar al colapso irreversible de la red. Aunque este material no presenta porosidad permanente, es un ejemplo de un sólido poroso de primera generación puesto que se pierde su porosidad irreversiblemente en cuanto se desorben de la estructura las moléculas huésped de disolvente.

Otra clase de polímeros porosos de interés, comprende aquellos materiales que presentan bi-estabilidad y que son capaces de responder a estímulos externos. Estos materiales flexibles, que han sido clasificados por Kitagawa como polímeros porosos de

tercera generación, poseen inusuales propiedades de separación de gases, como consecuencia de las interacciones de la red porosa con las moléculas huésped. En este aspecto se centra el Capitulo 3, en el que se presentan la síntesis y las propiedades de un nuevo PCP flexible de cobre(II), de formula $([Cu_2(L2)_2(OH_2)]\cdot DMF_{1.5})_n$ ($[Cu_2(H_2O)(L2)_2]$), obtenido en la reacción entre el ligando 3,5-dimetil-4-carboxipirazol (H_2L2) y CuX_2 (X = Cl, Br, NO_3).

Este material poroso presenta interesantes transformaciones estructurales que tienen lugar en respuesta a la eliminación/adsorción de moléculas alojadas en las cavidades. Estas modificaciones estructurales están acompañadas por cambios de color, poniendo de manifiesto que han tenido lugar procesos de reorganización de los ligandos alrededor del los iones Cu^{2+}. Curiosamente, el sistema $[Cu_2(H_2O)(L2)_2]$ posee un puente agua entre los átomos de cobre del bloque de construcción $Cu_2(L2)_2$, cuya eliminación (reversible) da lugar a la formación de centros de coordinación insaturados convergentes así como a bi-estabilidad estructural. En efecto, la fase evacuada meta-estable (γ-$[Cu_2(L2)_2]$) se transforma en un material poroso altamente estable (δ-$[Cu_2(L2)_2]$) al enfriarlo a la temperatura del nitrógeno líquido. A pesar de que δ-$[Cu_2(L2)_2]$ es inerte a la humedad ambiental, recupera instantáneamente el puente acua si se suspende en agua. Las propiedades de adsorción de gases de ambos polímeros con porosidad permanente (γ-$[Cu_2(L2)_2]$ y δ-$[Cu_2(L2)_2]$) se han estudiado mediante isotermas de adsorción de gases monocomponente y cromatografía de gases inversa. De esta manera se han puesto de manifiesto propiedades de adsorción selectivas inusuales en respuesta a comportamientos flexibles causados por la inclusión de moléculas huésped, así como unos coeficientes de selectividad muy grandes para mezclas binarias de gases de interés medioambiental/industrial (por ejemplo CO_2/CO o CO_2/N_2).

Bajo condiciones de reacción parecidas y utilizando los mismos bloques de construcción, se ha aislado otro polímero de coordinación de formula $\{[Cu(HL2)_2]\cdot 4H_2O\cdot 2DMF\}_n$ ($Cu(HL2)_2$). En este material el ligando orgánico está parcialmente desprotonado (solamente en la extremidad del ácido carboxílico, $HL2^-$) y, por lo tanto, genera una red con dimensionalidad reducida que consiste en laminas bidimensionales donde las moléculas de agua se sitúan en el espacio inter-laminar y las moléculas de DMF ocupan los huecos intra-laminares. Desafortunadamente, este material solo se ha podido estudiar desde el punto de vista estructural puesto que no ha sido posible aislarlo con la pureza adecuada.

Teniendo en cuenta la clasificación de polímeros de coordinación porosos propuesta por Kitagawa, el ejemplo más representativo de un PCP rígido con porosidad permanente (material de segunda generación) es el sistema [Zn_4O(benceno-1,4-dicarboxilato)$_3$] conocido como MOF-5. La notoriedad de este compuesto se debe a su elevada porosidad permanente, sin embargo tiene un inconveniente muy importante a la hora de considerar posibles aplicaciones practicas: su baja estabilidad en presencia de humedad ambiental que resulta ser una consecuencia directa de la hidrólisis de los enlaces M-O(carboxilato). Por tanto, a la hora de considerar cualquier aplicación práctica de este material MOF-5, su sensibilidad a la humedad ambiental (que en general no se puede eliminar por completo) se puede considerar como su talón de Aquiles puesto que las moléculas de agua causan la lenta destrucción de la red.

Por lo tanto, el Capitulo 4 se centra en la búsqueda de materiales robustos con estructuras similares a la de MOF-5. En concreto, ha sido posible obtener tres compuestos análogos a MOF-5 de estequiometría [$M_4O(L)_6$] con M = Zn y Co, L = L2 en el caso de [$Zn_4O(L2)_3$] y [$Co_4O(L2)_3$], y M = Co, L = 4,4'-buta-1,3-diine-1,4-diilbis(3,5-dimetil-pirazolato (L6) en el caso de [$Co_4O(L6)_3$]. En estos materiales, los enlaces de coordinación M-O(caboxilato) sensibles a la hidrólisis, han sido remplazados (parcialmente o totalmente) por enlaces más robustos M-N(pirazolato). Además, los grupos metilo que se encuentran en los ligandos L2 y L6, juegan un papel fundamental en la estabilización de estos materiales puesto que protegen los fragmentos M_4O de la hidrólisis. Como consecuencia, estos materiales son altamente hidrofóbicos y presentan una elevada estabilidad térmica y química, características que posibilitan la investigación de las propiedades adsorbentes en presencia de humedad. De esta manera se ha decidido estudiar el comportamiento del MOF [$Zn_4O(L2)_3$] tanto en la captura selectiva de gases perjudiciales (COVs, es decir, modelos de gases de guerra química como el gas Sarin y el gas Mostaza), como en la separación de mezclas benceno/ciclohexano. La extraordinaria selectividad para los COVs frente al agua demostrada por [$Zn_4O(L2)_3$] es la clave para una posible aplicación de este material en condiciones reales: el material [$Zn_4O(L2)_3$] policristalino podría ser incorporado en mascarillas o en tejidos protectores.

Por ultimo, el Capitulo 5 se centra sobre una serie de MOFs isoreticulares basados en clusters octanucleares $Ni_8(OH)_4(H_2O)_2$, conectados entre si por ligandos lineales bis-

pirazolato o carboxi-pirazolato. Estos materiales, de formulación general $[Ni_8(OH)_4(OH_2)_2(L)_6]_n$ ($Ni_8(L)_6$), poseen porosidad permanente que se incrementa con el tamaño del ligando espaciador, dando lugar a valores de área superficial de BET extremadamente elevados. Es interesante resaltar que el empaquetamiento cúbico compacto de los clusters $Ni_8(OH)_4(H_2O)_2$ encontrado en este tipo de sistemas genera *n* huecos octaédricos y 2*n* huecos tetraédricos por fórmula unidad. Estas cavidades resultan ser altamente hidrofóbicas, especialmente en el caso de los ligandos bis-pirazolato y, por lo tanto, sus propiedades de captura de dietilsulfuro (modelo del gas Mostaza) han sido evaluadas tanto en condiciones secas como en presencia de humedad. Los resultados obtenidos son comparables a los que presentan los dos carbones activos de mayor hidrofobicidad y capacidad de adsorción del mercado.

Además, el compuesto $Ni_8(L5)_6$ que contiene el ligando 4,4'-buta-1,3-diine-1,4-diilbis(pirazolato) (L5) presenta una alta estabilidad en Fluido Corporal Simulado (FCS) por lo que ha sido usado para la incorporación y liberación controlada del metalofármaco no convencional [Ru(*p*-cimeno)Cl_2(pta)] (RAPTA-C). Los resultados muestran que el sistema $Ni_8(L5)_6$ es un ejemplo interesante del posible uso de MOFs como vehículos para la liberación controlada de metalofármacos.

En resumen, tras la combinación (bajo las condiciones químicas adecuadas) de ligandos orgánicos específicos con iones metálicos del primer periodo de transición, ha sido posible obtener una serie de compuestos de coordinación, tanto rígidos como flexibles, que poseen elevada estabilidad térmica, mecánica y química. Además, las propiedades adsorbentes que presentan hacen posible su aplicación en campos diversos, tales como la separación de mezclas complejas de gases o la liberación controlada de metalodrogas no convencionales, las cuales han sido evaluadas. Los resultados presentados son de gran interés para el futuro diseño de nuevos MOFs con diferentes aplicaciones de gran impacto social.

SUMMARY

Since many decades, classical inorganic porous materials (i.e. zeolites and activated carbons) are widely used in industrial processes such as gas purification and separation, ion exchange, selective heterogeneous catalysis, biomedical applications, etc. Zeolites are by far the most employed materials not only because of their robustness and exceptional thermal stability but also for the regular distribution of its pores' size and shape that allow the interaction with atoms, ions and molecules throughout the bulk of the material. Nevertheless, the application of zeolites is limited by the pore size restriction (typically smaller than 10 nm) and by the lack of flexibility and transformability.

In this context, a new class of hybrid organic-inorganic materials, firstly approached in 1978, gained renewed interest in the 1990*s* as a much more versatile alternative to zeolitic materials. The first big challenge of the research dealing with these Porous Coordination Polymers (PCPs, also called MOFs: Metal Organic Frameworks) was the achievement of materials with permanent porosity (i.e. materials robust enough not to collapse upon activation of the porous structure). Soon after, a huge number of structures have been synthesized envisaging an incredible range of applications.

In general, PCPs are unlikely to compete with zeolites and other oxide-based porous materials in high-temperature applications owing to their limited long-term stability. In spite of that, these materials presents many advantages that must be pointed out: i) an unlimited number of combination of organic and inorganic bricks can be explored giving rise to a virtually infinite number of possible structures; ii) pores' size and shape can be systematically tuned with, in principle, no limits; iii) it is possible to functionalize the organic linker, or incorporate functional organic groups directly into the framework, so that porous solids, containing chemical groups capable of binding guests and/or catalysing reactions involving adsorbed guests, may be obtained; iv) it is possible to exploit the metal component and/or its interactions with guest molecules to design porous materials with unusual physicochemical properties, such as redox activity, light absorption properties or magnetic effects; v) it is possible to use enantiopure organic ligands to obtain chiral porous materials for applications requiring enantioselective adsorption and catalysis.

Anyway, so far, the low thermal and chemical stability as well as high sensitivity to moisture are the major limitations of PCPs materials for practical applications and consequently many efforts still must be done to improve their robustness.

The work presented in this doctoral thesis is part of a much wider investigation concerning the synthesis and characterization of porous coordination polymers for the adsorption/desorption and separation of gases and small molecules of industrial, environmental or biomedical interest. A special focus is addressed to the achievement of thermally and chemically stable solids.

To achieve this goal, a careful choice of the organic linkers' chemical nature is of paramount importance. Therefore, we decided to employ a set of symmetric organic ligands containing the pyrazole ring, eventually combined with the carboxylic acid functional group. The reason of this choice is the much more robust nature of the M-N(pyrazolate) coordinative bond compared to the quite labile M-O(carboxylate) bond, generally found in the vast majority of published PCPs structures.

In this study we have chosen the late first row transition metal ions (Co^{2+}, Ni^{2+}, Cu^{2+} and Zn^{2+}) taking into account their borderline soft/hard acidic nature, their coordination versatility and labile nature, features that are adequate for the formation of robust and ordered polymeric structures with small or middle size N,O ligands.

All the compounds presented in this work have been synthesized in our laboratories and characterized from the structural and textural points of view. In most cases, the robust nature of the M-N coordination bonds leads to the formation of polycrystalline products that have been characterized by means of X-ray powder diffraction. In few cases, the achievement of single crystal of suitable size (particularly in the case of mixed N,O-ligands) for X-ray diffraction measurements has been possible, allowing to solve the structure in a conventional way.

After the preliminary structural characterization, the adsorptive properties of those solids exhibiting permanent porosity have been investigated in detail, with a further insight into some specific applications envisaged for each promising structure.

The isolated compounds have been classified in four categories, focusing either on the local structure around the metal centre or on the properties of the bulk material. Therefore, the materials have been categorized as i) zeomimetic frameworks; ii) soft

porous coordination compounds; iii) porous coordination polymers with structural analogies to MOF-5 material and iv) a series of isoreticular nickel based PCPs.

The assembly of 4-carboxypyrazolate ligand molecules ($L1^{2-}$) with Cu^{2+} cations in NH_3/NH_4^+ buffer gives rise to the anionic network of formulation $[NH_4@Cu_3(\mu_3\text{-}OH)(\mu_3\text{-}L1)_3]_n\cdot solv$ ($NH_4@Cu_3(OH)L1_3$) which is presented in Chapter 2. Unlike most zeotypic coordination networks (that do not usually permit cation-exchange processes since they have neutral or cationic nets) the anionic nature of this material, much alike zeolites, can give rise to exchange of the extraframework cations with the possibility to modulate the porosity of the network depending on the charge and size of the exchanged cations. Indeed, we have demonstrated that the ion-exchange processes lead to profound changes in the textural properties of $A@Cu_3(OH)L1_3$ (A = extraframework cation) porous surface and in the adsorption selectivity for different separation processes of gases and vapours. Therefore, we studied the effect of extraframework cation exchange on the efficiency of the separation process by adsorption of complex mixtures of gases (acetylene, carbon dioxide, methane, dinitrogen) and vapours (benzene, cyclohexane).

Unpredictably, the substitution of Cu^{2+} by Cd^{2+} cations in the reaction medium affords a neutral layered material ($[Cd(H_2O)_2L1]\cdot H_2O$) that does not maintain its crystallinity upon thermal activation. As a matter of fact, the removal of crystallization water molecules from the structure causes the irreversible collapse of the framework. Despite its leak of permanent porosity, this material is a nice example of first generation porous framework since its porosity is irreversibly lost upon removal of the solvent guest molecules.

Another class of porous polymers of interest comprises those materials which are bi-stable and are able to respond to external stimuli. These flexible porous materials, classified by Kitagawa as third-generation materials, exhibit unusual gas separation properties as a consequence of guest responsive behaviour. In this regard, the research presented in Chapter 3 is devoted to the synthesis and properties of a novel flexible-PCP of formulation ($[Cu_2(L2)_2(OH_2)]\cdot DMF_{1.5})_n$ ($[Cu_2(H_2O)(L2)_2]$), obtained in the reaction of the 3,5-dimethyl-4-carboxypyrazole ligand (H_2L2) with CuX_2 (X = Cl, Br, NO_3).

This porous material shows intriguing structural transformations taking place upon guest removal/uptake. These structural transformations are accompanied by evident colour changes, proving that a spatial rearrangement of the ligands around Cu^{2+} metal

centres takes place. Interestingly, $[Cu_2(H_2O)(L2)_2]$ system has an unprecedented acua bridge between the two copper atoms in the dimeric building unit, the (reversible) removal of which gives rise to unusual coordinatively unsaturated convergent adsorption active sites as well as to structural bi-stability. Indeed, the metastable evacuated phase (γ-$[Cu_2(L2)_2]$) transforms into an extremely stable porous material (δ-$[Cu_2(L2)_2]$) after freezing at liquid nitrogen temperature. Although δ-$[Cu_2(L2)_2]$ is inert to ambient moisture, it recovers the acua bridge upon soaking in water. The gas adsorption properties of both permanent porous materials (γ-$[Cu_2(L2)_2]$ and δ-$[Cu_2(L2)_2]$) have been studied by single component gas adsorption isotherms and variable temperature pulse gas chromatography. The results reveal intriguing gas adsorption properties with guest triggered breathing phenomena as well as very high selectivity coefficients for binary gas mixtures of industrial/environmental interest (e.g. CO_2/CO or CO_2/N_2).

Under similar reaction conditions and with the same building units, another coordination polymer of formulation $\{[Cu(HL2)_2]\cdot 4H_2O\cdot 2DMF\}_n$ ($Cu(HL2)_2$) has been obtained. In this material the organic ligand is partially deprotonated (just at the carboxylic acid moiety, $HL2^-$) therefore, the resulting net has reduced dimensionality and consists of 2D sheets where water guest molecules lye in the space between two adjacent layers while DMF molecules are located in the same plane of the sheets. This material has been studied just by the structural point of view, as a consequence of the unavailability of phase pure bulk solid.

Going back to Kitagawa's classification of coordination polymers, the milestone of rigid-PCPs with permanent porosity (second generation material) is the $[Zn_4O$(1,4-benzene-dicrboxylate$)_3]$ system, also known as MOF-5. This material exhibits very high permanent porosity. Despite its tremendous notoriety, MOF-5 has a considerable drawback for possible practical applications: its low stability to air moisture, a direct consequence of the M-O(carboxylate) bond hydrolysis. So, when MOF-5 material is envisaged for any practical application, this feature becomes its Achilles' heel since ambient moisture (that can not be generally completely removed) relentlessly destroy the framework.

Consequently, Chapter 4 is devoted to the search of robust MOF-5 type materials. Thus, three novel materials with the $[M_4O(L)_6]$ stoichiometry analogous to MOF-5,

where M = Zn and Co, L = L2 for $[Zn_4O(L2)_3]$ and $[Co_4O(L2)_3]$; M = Co, L = 4,4'-buta-1,3-diyne-1,4-diylbis(3,5-dimethyl-pyrazolate) (L6) for $[Co_4O(L6)_3]$, are presented in which the hydrolysis sensitive M-O(carboxylate) coordination bonds are replaced (partially or completely) by the robust M-N(pyrazolate) coordination bonds. Another important contribution to the stability of these frameworks is provided by the methyl groups on L2 and L6 ligands that stabilize and protect the M_4O moieties from hydrolisis. The resulting materials are highly hydrophobic and show enhanced thermal and chemical stabilities that open the way to the investigation of adsorptive properties in the presence of moisture. Therefore, the behaviour of $[Zn_4O(L2)_3]$ MOF for the selective capture of harmful VOCs (i.e. models of chemical warfare agents such as Sarin nerve gas and Mustard vesicant gas) as well as for the separation of benzene/cyclohexane mixtures has been investigated. The extraordinary selectivity for VOCs compared to water shown by $[Zn_4O(L2)_3]$ material would be the key feature to open the way to a possible use under real conditions: eventually $[Zn_4O(L2)_3]$ powders could be incorporated into air filters and protective textiles.

Finally, Chapter 5 is dedicated to a series of isoreticular MOFs based on $Ni_8(OH)_4(H_2O)_2$ octanuclear clusters connected by both bis-pyrazolate and carboxy-pyrazolate linear ligands. These materials, of general formulation $[Ni_8(OH)_4(OH_2)_2(L)_6]_n$ ($Ni_8(L)_6$), show permanent porosity that increases with the ligand length, with very high values of BET specific surface areas for the materials with the longest organic linkers. The cubic close packing of the $Ni_8(OH)_4(H_2O)_2$ clusters give rise to *n* octahedral and 2*n* tetrahedral cavities per MOF formula unit. These cavities result to be highly hydrophobic especially for those materials containing bis-pyrazolate ligands and, therefore, their performances in the capture of diethylsulfide (Mustard gas, chemical warfare agent model) have been evaluated under dry and humid conditions. The results have been compared to those exhibited by two selected activated carbons exhibiting the highest capacity and highest hydrophobicity available in the market.

Moreover, $Ni_8(L5)_6$ compound containing 4,4'-buta-1,3-diyne-1,4-diylbis(pyrazolate) ligand (L5) has been proved to be highly stable in Simulated Body Fluid (SBF) and therefore it has been used as a scaffold system for the incorporation and release of the non-conventional metallodrug [Ru(*p*-cymene)Cl_2(pta)] (RAPTA-C). This system results to be a proof of concept of the suitability of MOF materials for drug delivery purposes.

SUMMARY

Summarizing, a wide range of rigid as well as flexible porous coordination networks exhibiting high chemical, mechanical and thermal stabilities have been synthesized by the combination of metal ions and ligands under the appropriate conditions. Moreover, their adsorptive properties have been evaluated towards relevant applications such as the separation of complex mixtures of gases and vapours as well as the release of non-conventional metallodrugs. All these results are of interest for the future design of MOF materials suitable for applications of high social impact.

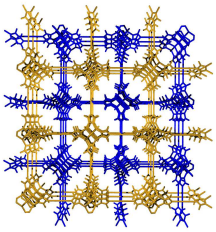

1. POROUS COORDINATION POLYMERS

1.1. Introduction

In olden times, the third century BC, Aristotele stated: “Nature abhors vacuum”. Actually, porous materials such as zeolites and active carbons had been already found in nature although their porosity used to be disguised as long as their cavities are commonly filled with water small size molecules or charged atoms. In our times, in the last decades, inspired by the great amount of applications involving natural porous materials, scientists devoted a manifold extent of efforts to the synthesis of artificial porous materials.[1] They realized the potential advantages of synthetic compounds compared to natural ones, since the control of reaction conditions opens the way to products with desired properties. In this respect, two big steps in the field of synthetic porous coordination frameworks have been made in earlier 1936, when the structure of the three-dimensional coordination framework of Prussian Blue was solved[2] and in 1995, when permanent porosity have been measured in three-dimensional frameworks by the groups of Yaghi[3] and Moore.[4]

The term Metal-Organic-Frameworks (MOFs) appeared in literature for the first time in 1995[3] and, together with the expression Porous-Coordination-Polymers (PCPs), is currently used for synthetic porous materials based on coordination networks.

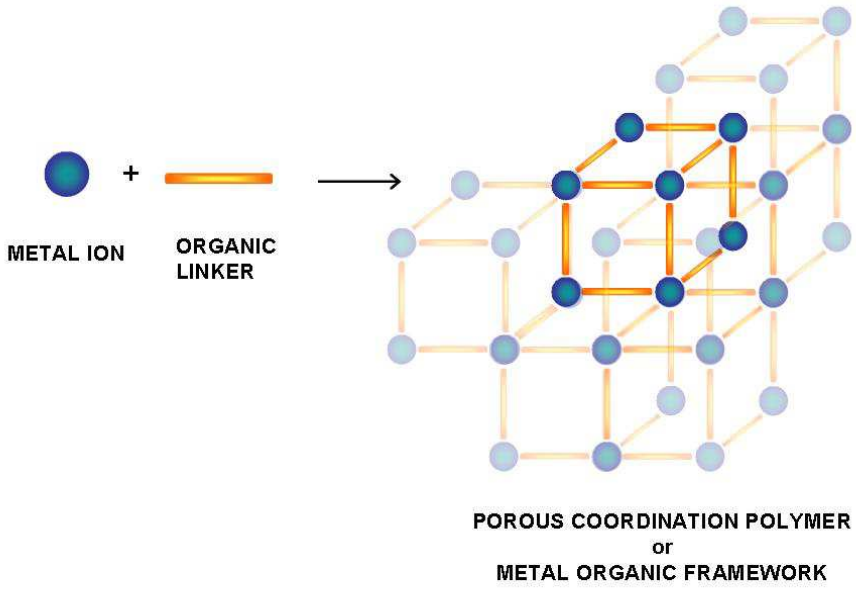

Figure 1.1. Schematic representation of the construction of Porous Coordination Polymers (PCPs).

To define extensively PCPs (or MOFs), we can say that they are a class of synthetic porous crystalline materials based on metal ions connected through spacing ligands (Figure 1.1) giving rise to the formation of an open network accessible to guest molecules.

At first, the interest for this kind of porous solids focused on structural and textural characterisation. Then it moved from the stage of zeolite mimicry towards the search for advanced materials with applications in different fields,[5] such as, for instance, in processes of separation and purification of gases,[6] heterogeneous catalysis,[7] biomedical applications[8] and nanomaterials.[9] As a matter of fact, these materials present some features that improve the classical porous materials (zeolites and activated carbons). Indeed, they can be well ordered porous structures showing dynamic and flexible behaviour in response to external stimuli,[10] they can have functionalisable pore surface incorporating selective catalytic properties[11] or they can have a structural skeleton responsible for magnetic, electrical and optical properties.[12]

It is evident that PCPs outclass by far the molecular sieving properties of classical porous materials and the infinite possible assembling of metal ions and organic molecules would permit to design a large number of structures exhibiting unique and desired properties.

1.2. The design of PCPs

1.2.1. Building blocks

The building blocks of porous frameworks are metal ions and organic linkers which must be chosen carefully according to the desired properties of the final material. In addition, there are some auxiliary components, such as blocking ligands, counter ions, non-bonding guest or template molecules that can take part in the reaction and influence the spatial arrangement of the main components.

The most important characteristics of connectors and linkers are their coordination numbers and the coordination geometries of their binding sites (see Figure 1.2).

Metal fragments. Transition-metal ions are often utilized as versatile connectors in the construction of coordination polymers. Depending on the metal and its oxidation state, coordination numbers can range from 2 to 6, giving rise to various

geometries, which can be linear, T- or Y-shaped, tetrahedral, square-planar, square-pyramidal, trigonal-bipyramidal, octahedral, trigonal-prismatic, pentagonal-bipyramidal, and the corresponding distorted forms. Larger coordination numbers, namely from 7 to 10, can be achieved with lanthanide ions and would lead to new or unusual network topologies. Most of the metal ions have various coordination numbers and geometries which can be expressed by changing reaction conditions.

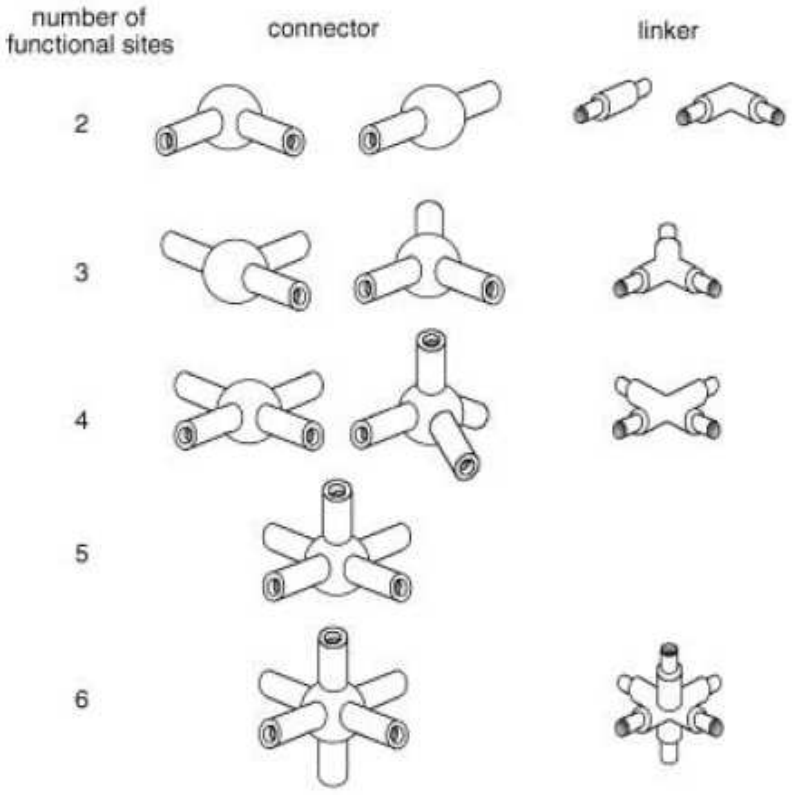

Figure 1.2. Components of coordination polymers.

Ligands. There is a huge number of linking ligands used for the construction of coordination polymers (see Figure 1.3). The simplest ones comprise halide, CN^- and SCN^- anions, while middle or large sized organic-type molecules include carboxylates, diazines and mixed donors. Similarly to the metal nodes, the organic spacers used in PCP synthesis have their own geometry constrictions thereby leading to a defined spatial arrangement. Thus, for simple linear ligands such as 4,4'-bipy or terephthalic acid, the structure's network topology is directly governed by the coordination environment and geometry of the metal ion, while for three-, four-, or six-connected linkers, the resulting topologies are a combination of metals' and ligands' three-dimensional arrangements.

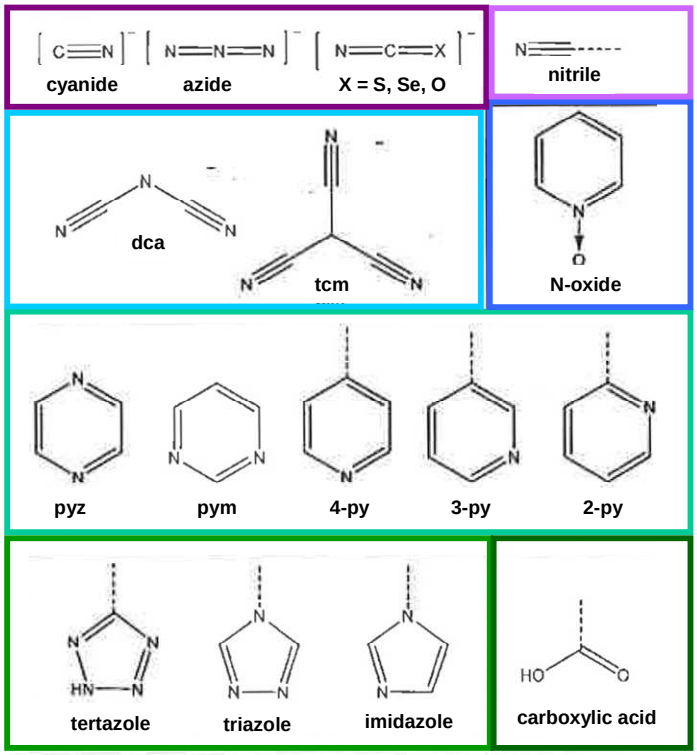

Figure 1.3. Example of ligand functional groups which are used in coordination polymers with transition metals.

The possibility to tune the size of the organic ligands keeping constant their functionalities should be pointed out. For example, benzene-1,4-dicarboxylic acid could be replaced by the longer biphenyl-4,4'-dicarboxylic acid linker, in order to get larger pore size in the resulting framework.

The appropriate combination of metal ions and organic spacers allows to give rise to a periodic network built on covalent bonds, coordination bonds, hydrogen bonds and van der Waals interactions. It is well known that the strength of the coordinative bond lyes between the strong covalent bonds and the weak hydrogen bonds or van der Waals interactions, thus the stability of the coordination network will mainly depend on the strength of the chemical bonds between metal ions and linkers.

1.2.2. Synthetic conditions

During the synthesis of a new MOF structure, there is a huge number of experimental parameters that need to be controlled and optimised (Scheme 1.1). In general, the modification of a certain parameter will strongly influence the final architecture to be achieved.

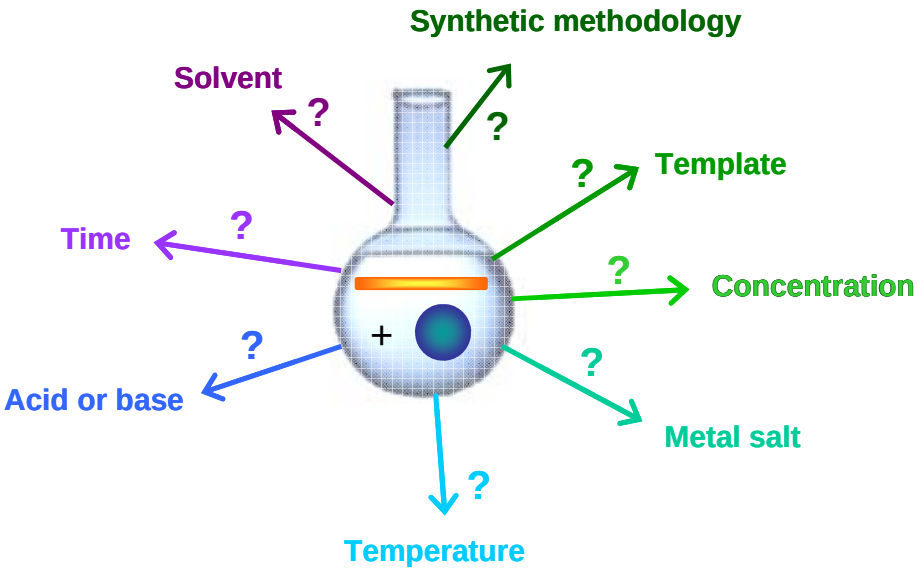

Scheme 1.1. Experimental variables that will determine the obtention of the desired coordination network.

The experimental conditions that should be taken into account while devising a new reaction are summarized in Scheme 1.1 and detailed below:

-*Synthetic methodology*. Methodologies range from classical synthesis in a flask or in a test tube to hydro- or solvo-thermal reactions in Teflon liners, freeze-drying method, microwave synthesis or electrochemical and mecanochemical syntheses.

-*Metal salt.* A wide range of metal salts can be chosen: chloride, bromide, nitrate, perchlorate, acetate, sulphate, oxide, etc. Less coordinative anions are preferred since their use will facilitate the achievement of crystalline products.

-*Solvent*. Water and common organic solvents (such as ethanol, methanol, acetonitrile and dimethylformamide) are widely used in the synthesis of MOF materials. The use of high boiling point solvents (i.e. DMF, DEF or DMSO) is quite common, since high temperature is often required to form and break coordination bonds during the nucleation phase. Mixtures of solvents are also widely used.

-*Acid or base.* The control of the reaction pH is of outmost importance to permit the partial o complete deprotonation of the ligands, to allow the formation of hydroxide complexes and to influence the rate of the nucleation process. Therefore, strong/weak acids or bases can be added in the reaction in order to modulate its kinetics.

-*Temperature.* Reaction temperatures range from liquid nitrogen temperature (for freeze-drying method) to around 250 ºC, the upper limit being settled by the ligand's decomposition temperature. The possibility to make the reaction in liners or

autoclaves permits one to reach temperatures well above the boiling point of the used solvents.

-*Time*. Reaction times can be very short (few seconds) or very long (some days or even weeks).

-*Concentration of reagents*. Both the ratio between metal and ligand, and the dilution of the reaction mixture must be carefully controlled. In some cases different frameworks can be obtained keeping constant all the experimental variables and just changing the amount of solvent used.

-*Templates*. The use of molecules that do not take part in the reaction but influence the growth of the microcrystals is quite common in PCPs synthesis. Examples of this kind of templates are benzene, cyclohexane, dimethylformamide and dimethylsulfoxide.

1.2.3. Classification of porosity

The correct combination of building blocks and reaction conditions can give rise to ordered materials whose pores have a uniform size and shape distribution. Therefore PCPs can be divided into three classes based on their pore size.[13]

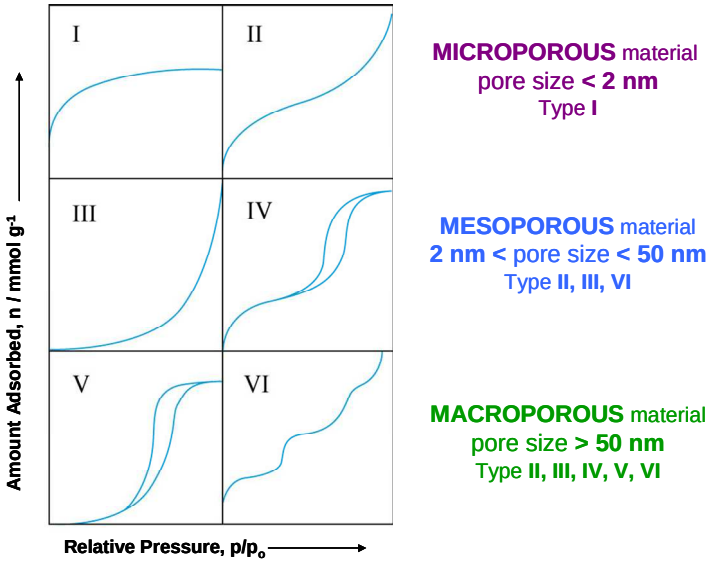

Figure 1.4. (Left) General shape of isotherm for different classification type I-VI; (right) porosity classification depending on pore size.

Indeed, materials with pore size smaller than 2 nm are defined as *microporous*, materials with pore size between 2 and 50 nm are *mesoporous* while those with pore size larger than 50 nm are termed *macroporous* (see Figure 1.4-right). The majority of PCPs falls into the microporous and mesoporous range since the presence of

cavities in the macropore range would probably lead to the collapse of the metal organic framework.

Information on the topology, pore size and guest molecule-surface interactions are usually provided by static gas adsorption studies. Characteristic gas sorption isotherm shapes are shown in Figure 1.4-left. They can also give information on the interactions taking place between the host molecule and the guest framework. There are six general isotherm types (types I-VI). Crystalline microporous materials generally show type I behaviour, characterized by a sharp increase in the adsorbed amount of probe molecules at low relative pressures; mesoporous materials show type II, III and VI isotherms while macroporous material can show type II, III, IV, V or VI isotherms, depending on the kind of interactions taking place between host and guest.

1.2.4. Classification of networks

In coordination chemistry, a network is a polymeric collection of interlinked nodes. Therefore, each link (organic molecule) connects two nodes (metal ions) and each node is linked to three or more other nodes so that a node becomes a link if it connects to two nodes only and, similarly, a link become a node if it connects more than two nodes. Moreover, the network must have a repeating pattern and thus a finite number of definite nodes and links. Needless to say, the networks are classified according to their dimensionality as 1D, 2D and 3D nets.

1D nets. This is the simplest class of nets and it gives rise to linear (possibly helical) geometries. In Figure 1.5 are represented some examples of 1D nets. We can see that ladder-like nets follow into this category as well as distortion from the ideal ladder net can give rise to tubular geometry.

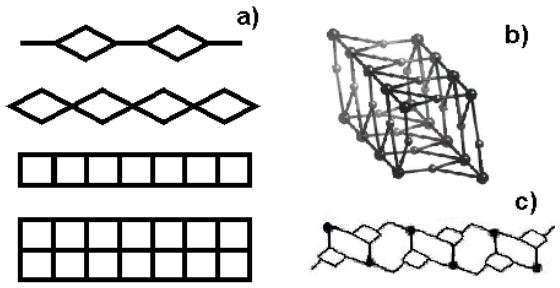

Figure 1.5. a) A selection of 1D nets; b) schematic representation of the 1D tubes in $M(dca)_2(apym)$;[14] c) a 1D tube network constructed from AgI and 1,3,5-triaminocyclohexane, side on view.[15]

2D nets. This class of nets comprises a great number of planar structures and some of them are shown in Figure 1.6. Simple examples of 2D nets are the square grid and the hexagonal grid in which the nodes are 4-connecting and 3-connecting respectively.

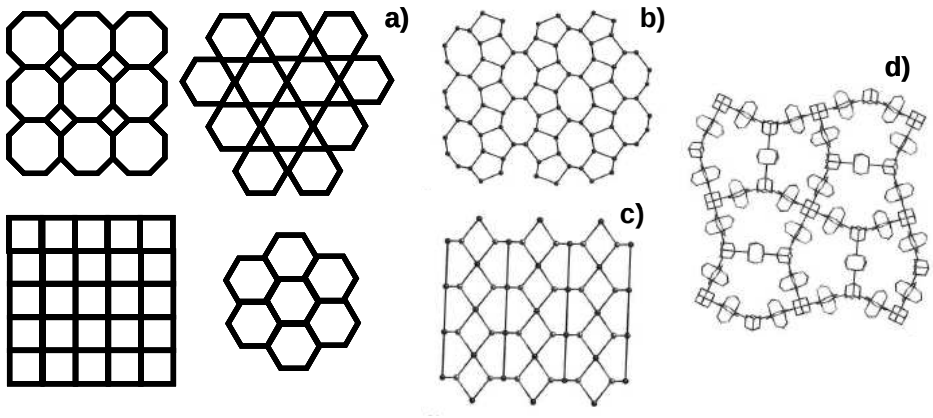

Figure 1.6. a) A selection of 2D nets; b) schematic representation of the sheet structure in [Cu(4,4'-bipyridine)$_{1.5}$(PPh_3)]$BF_4 \cdot 1.33THF \cdot 0.33CHCl_3$;[16] c) schematic representation of the 3,4-connected sheet structure in M(dca)$_2$(H_2O)·phenazine;[17] d) the 2D sheet formed in [$Cu_2(O_2CEt)_4$]$_5$(HMTA)$_3$.[18]

Although the majority of 2D nets have a sheet structure, some of them can have a 3D aspect in the sense that, although their polymeric architectures is only two-dimensional, they can have a certain "thickness". In general, these nets are better described in terms of interconnected layers and many of them are interpenetrated.

3D nets. In principle, there are thousands of possible 3D nets, but a small number of them are sufficient to describe a significant fraction of coordination polymers. Same examples of 3D net are shown in Figure 1.7a. The best way to classify 3D nets is from the point of view of node connectivity, therefore it is common to have 3-, 4-, 5-, 6-connected nets while connectivities higher than 6 are quite unusual, mainly due to the difficulty for transition metals to fit so many donor atoms in their coordination sphere.

A very important issue for 3D nets is interpenetration. In general, porous frameworks do generate spacious voids, cavities and channels, which may account for a high fraction of the crystal volume, up to 50 % or even more.[19, 20] These large spaces are usually occupied by highly disordered solvent molecules. In other cases, remarkable interpenetrating structures are formed in which the voids associated with

one framework are occupied by one or more independent frameworks. Hence, such entangled structures can be disentangled only by breaking internal connections.

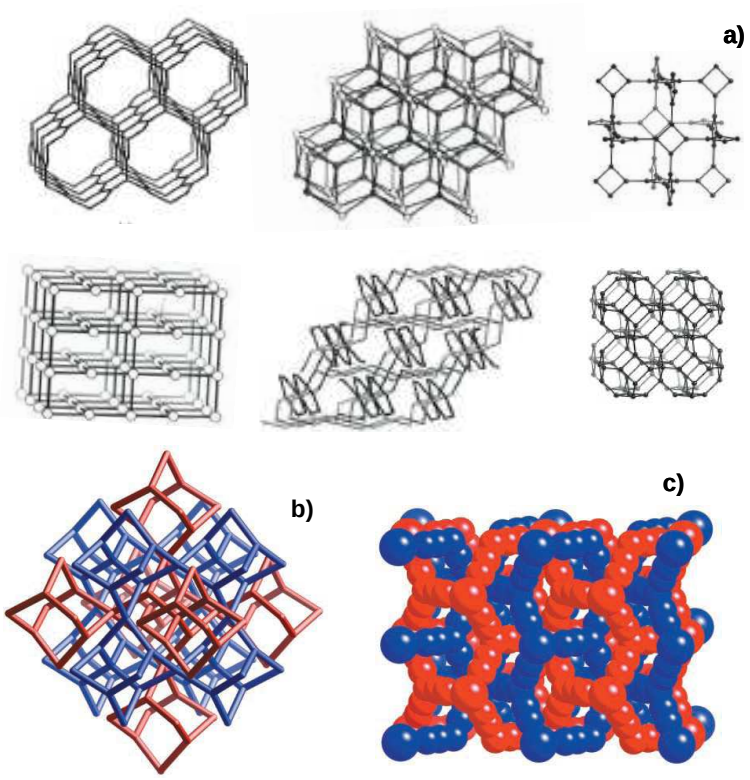

Figure 1.7. a) A selection of 3D nets; b) two independent interpenetrating 3D networks in the structure of $Cu^{I}(tpt)_{4/3}(ClO_4)$;[21] c) two interpenetrating 3D nets with the rutile topology in the structure of $M[C(CN)_3]_2$ (M = Cr, Mn, Fe, Co, Ni, Cu, Zn, Cd or Hg).[22]

The individual 3D nets involved in interpenetration, as far as it is presently known, belong to a restricted number of topological classes with only a few exceptions. The diamondoid net is by far the most common type currently known to participate in interpenetration.

It is evident that interpenetration has a deep influence in the adsorption properties of porous materials, mainly giving rise to a strong reduction of their void volume. Anyhow, it often plays a very important role in framework stabilization since it can prevent the collapse of the network once solvent molecules are removed from the pores.

1.2.5. Flexibility and stability of porous coordination networks

In 1998 Kitagawa proposed a classification for porous coordination compounds into three categories: first, second and third generation materials (see Figure 1.8).[23] The

first generation compounds, which show a wide variety of porous structures, loose their crystal order upon removal of the molecules included in the cavities. Hence, the frameworks collapse irreversibly and the materials are unable to exhibit permanent porosity.

The second generation compounds possess stable and robust frameworks which reversibly lose and readsorb guest species without undergoing any change in phase or morphology. These materials can be used as adsorbents and are generally considered as analogous to zeolites. The third generation compounds exhibit dynamic structures, which change their own frameworks responding to external stimuli, not only chemical but also physical. These solids have a potential application in areas such as molecular sensing. Indeed, with the weak linkages, guest molecules readily change the bond orientation, distance and cleavage. So, even a weak interaction between guest and pore-wall molecules can induce a structural change because of a cooperative effect based on a large ensemble over an infinite framework.

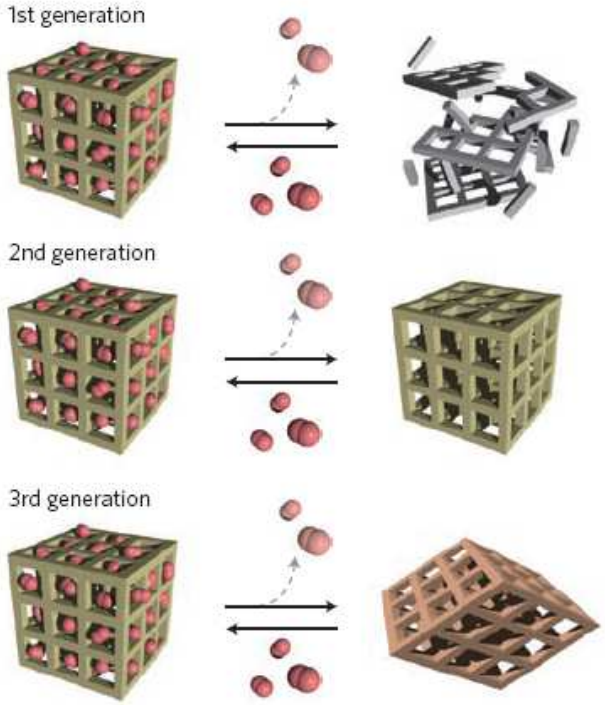

Figure 1.8. Schematic view of first, second and third generation microporous coordination polymers.[24]

Third generation compounds, also called Soft Porous Crystals, have emerged in the last years thanks to the recent discoveries that enable scientists to perform on-demand syntheses of functional pores by tuning their size, shape and chemical properties. Soft porous crystals are defined as porous solids that possess both a

highly ordered network and structural stability. They are bi- or multi-stable crystalline materials with long range structural ordering, reversible transformability between states and permanent porosity.[24] For soft porous crystals, extensive cooperativity would be expected between the molecules throughout the crystal, such that rearrangements can occur in a well-concerted fashion, in order to maintain its macroscopic integrity.

The most common way to achieve soft porous materials is by the loose assembly of coordination networks. Coordination polymers with stiff linkers and rigid metal fragments use to lead to second generation frameworks, while the third generation ones requires an intrinsic flexibility of the building units. The softness is often induced by interpenetration or interdigitation of independent, identical networks.

1.3. Examples of relevant Metal Organic Frameworks

The number of published papers concerning MOFs synthesis, characterisation and applications is growing very fast (Figure 1.9) and, in 2011, 540 publications containing the "Metal Organic Framework" entry can be found.

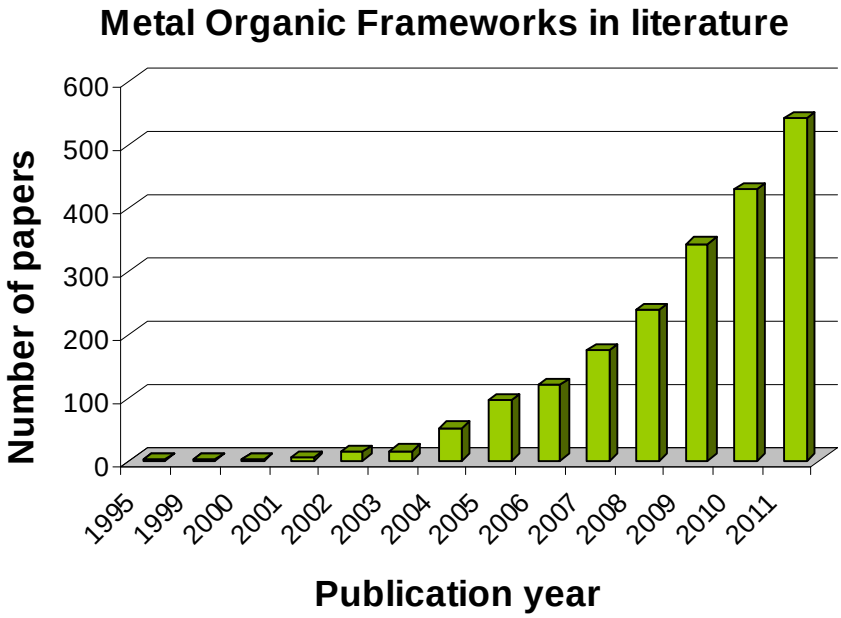

Figure 1.9. Graphical summary of the number of publications containing the concept "MOF" over the last 16 years.

A relevant number of these papers contain the synthesis and structural characterization of new porous materials, therefore in the following paragraphs only a very limited number of well-known structures will be presented, focusing on their

peculiarities and/or applications. Figure 1.10 presents a historical overview of the milestone coordination polymers presented in this section.

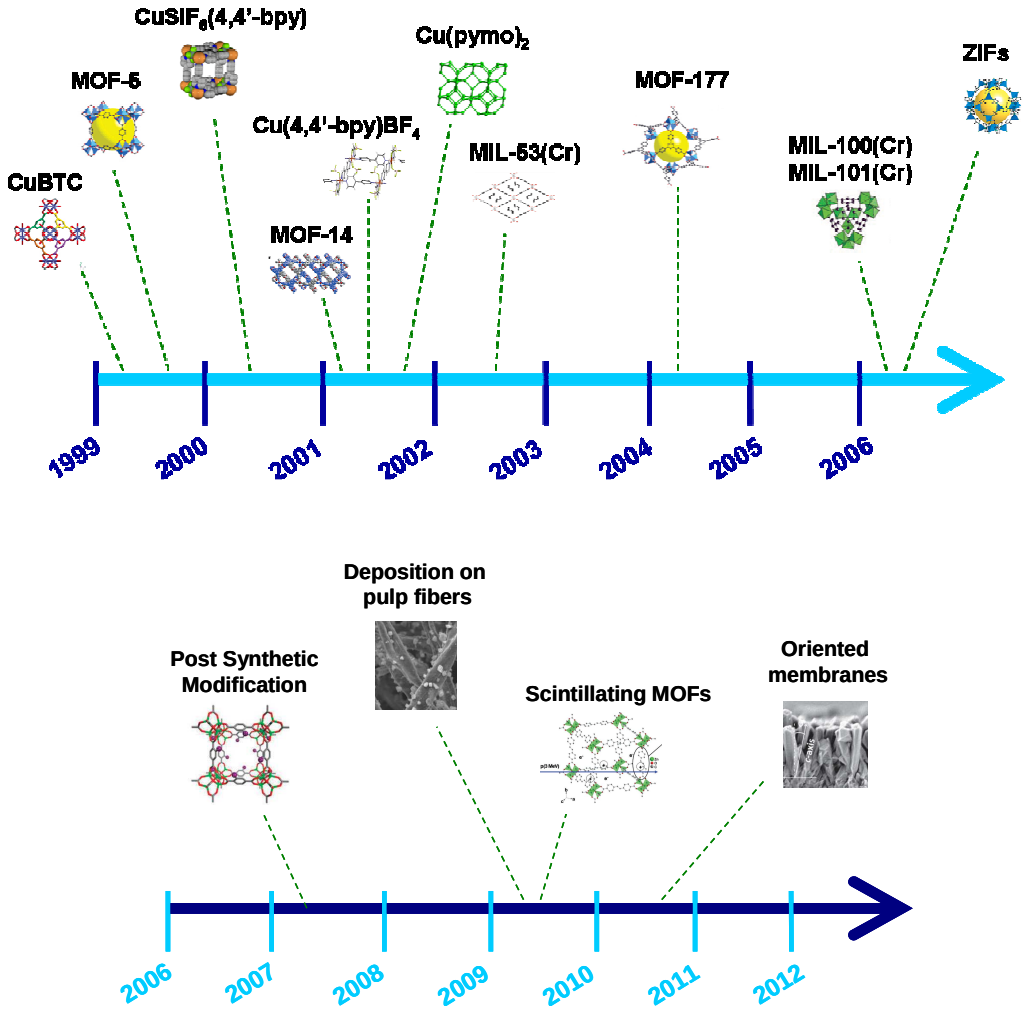

Figure 1.10. Graphical, historical summary of (above) the milestone coordination polymer structures (1999–2006) and (below) selected applications of MOF materials (2006–2012) presented in this section.

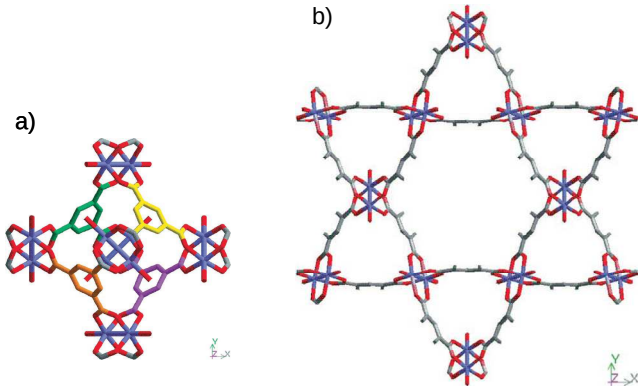

Figure 1.11. a) Secondary building unit for $[Cu_3(BTC)_2(H_2O)_3]_n$ viewed along the [100] direction; b) $[Cu_3(BTC)_2(H_2O)_3]_n$ viewed along the cell body diagonal [111], showing an hexagonal shaped 18 Å window at the intersection of the nanopores.

In 1999, we find the report on a key microporous three-dimensional framework, of formulation $[Cu_3(BTC)_2(H_2O)_3]$, also known as CuBTC or HKUST-1 (see Figure 1.11).[25] This MOF has interconnected $[Cu_2(O_2CR)_4]$ units (R = aromatic ring) with the paddle-wheel structure of copper acetate, which creates a three-dimensional system of channels with pore windows of 8.6 x 8.6 $Å^2$ with accessible porosity of about 40 % in the solid, giving rise to a Langmuir surface area higher than 900 $m^2\ g^{-1}$. The most characteristic feature of this structure is the bound aqua ligands to the axial sites on the paddle-wheel cluster. These H_2O molecules are directed from the Cu atoms to the interior of the nanopores and can be removed upon thermal activation, affording open metal sites that could be functionalized with other suitable small molecules. When activated CuBTC material is exposed to air moisture, it quickly recovers the coordinated water molecules, in a perfectly reversible adsorption process.

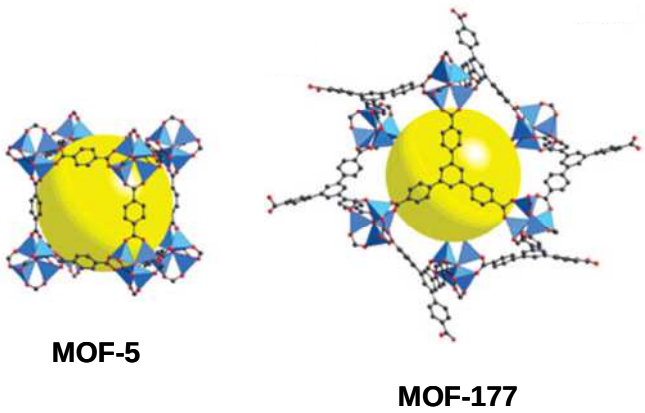

Figure 1.12. Single crystal X-ray structures of MOF-5 and MOF-177. **Zn** (polyhedra), **O** (spheres), **C** (spheres).

At the end of 1999, the same year CuBTC structure has been published, Yaghi and co-workers published on the scientific journal *Nature* the synthesis and characterization of a new three-dimensional framework, that has now become the prototypical MOF with an open simple cubic packing network topology (see Figure 1.12). This compound is the well-known MOF-5, based on regular Zn_4O tetrahedrons, where a single μ_4-oxide ion binds four Zn atoms, the edges of which are capped by carboxylate groups to form a $Zn_4(O)(CO_2)_6$ SBU. The relevance of this solid dealt both on its unprecedented structural stability (compared to the porous framework synthesized to the time) and on its adsorptive properties outperforming zeolite

materials: high apparent Langmuir surface area of around 2900 $cm^3\ g^{-1}$ (calculated from N_2 isotherm, 77 K) and pore volume of 0.61⁻0.54 $cm^3\ cm^{-3}$ (calculated using Dubinin-Raduskhvich equation).

Later on, in 2004, Yaghi reported in *Nature* the structure of another 3D porous framework based on the same Zn_4O tetrahedral clusters connected by the tripodic 1,3,5-benzenetribenzoate (BTB) ligand. This solid, known as MOF-177 (see Figure 1.12) had the highest observed surface area (4500 $m^2\ g^{-1}$ using the Langmuir model) of any porous material at the time and combined this exceptional level of surface area with an ordered structure that has extra-large pores capable of binding polycyclic organic guest molecules, attributes not previously combined in one material.

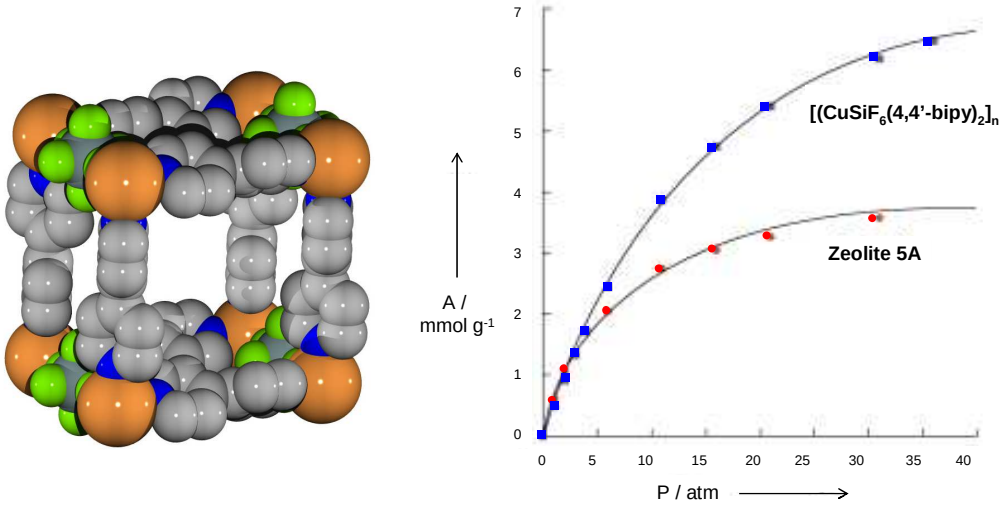

Figure 1.13. (Left) Crystal structure of the polymer $\{[CuSiF_6(4,4'\text{-bipyridine})_2]\cdot 8H_2O\}_n$; **Cu**, **Si**, **F**, **N**, **C**; (right) methane adsorption isotherms (298 K, pressure range 0–36 atm) for $\{[CuSiF_6(4,4'\text{-bipyridine})_2]\cdot 8H_2O\}_n$ and zeolite 5A.

Soon after the publication of MOF-5 structure, Kitagawa and co-workers [26] reported the 3D open framework $\{[CuSiF_6(4,4'\text{-bipyridine})_2]\cdot 8H_2O\}_n$, on the year 2000, which exhibited a high adsorption capacity at room temperature and safe pressures for the energetic gas CH_4 outperforming zeolite 5A (see Figure 1.13). This milestone material opened up a new dimension for the study of adsorbent materials based on coordination polymers for their possible utility for the storage of supercritical environmentally friendly energetic gases such as CH_4 or H_2 for mobile applications.[27]

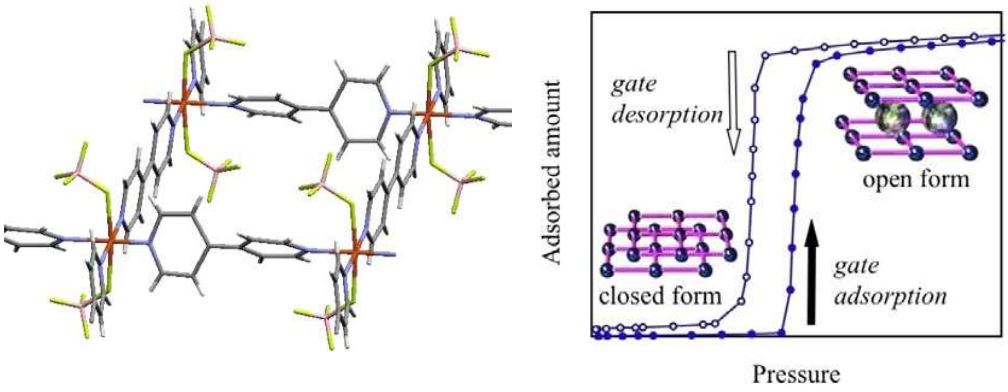

Figure 1.14. (Left) Local structure of layered [Cu(4,4'-bipyridine)$_2$(BF_4)$_2$] system; **Cu**, **C**, **N**, **B**, **F**, **H** (white). (Right) Schematic representation of the gate adsorption and transformation between the close and the open forms.

One year later, the first examples of flexible porous networks (third generation PCPs) were simultaneously reported by Kaneko[28] and Navarro.[29] The former one is a layered coordination polymer of formulation [Cu(4,4'-bipirydine)$_2$(BF_4)$_2$] which exhibits gate pressure adsorption towards different gases related to interlayer swelling in order to accommodate guest molecules (Figure 1.14). The latter is the sodalite type network [Cu(pymo)$_2$] (pymo = pyrimidin-2-onate) that shows wide hysteresis loops in the solid-liquid adsorption isotherms of $AClO_4$ ion pairs (A = NH_4, Li, Na, K, Rb) to yield [Cu(pymo)$_2$]·1/3$AClO_4$ systems concomitant with a crystal phase transition (Figure 1.15).

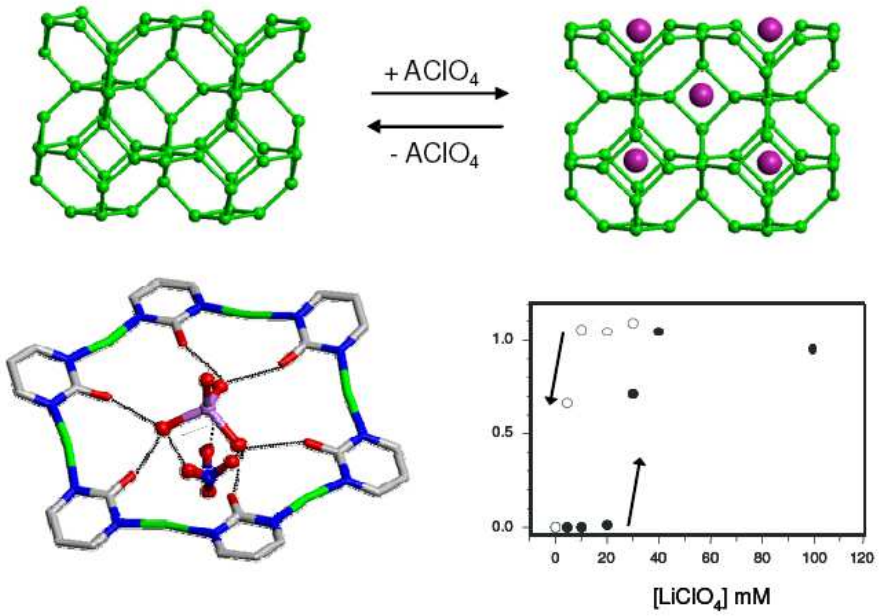

Figure 1.15. (Top) Schematic representation of the ion pair $AClO_4$ (A = NH_4, Li, Na, K, Rb) solid-liquid adsorption process by the sodalite type framework of [Cu(pymo)$_2$] with concomitant trigonal to

cubic phase transition; (bottom) H-bonding molecular recognition of hydrated ion pairs by exocyclic pyrimidine oxygen atoms of hexagonal windows and solid-liquid adsorption isotherm of $LiClO_4$ exhibiting hysteresis concomitant to crystal to crystal phase transition.

Anyway, the most popular third generation PCPs are those named MIL-53 (MIL = Materials of Institut Lavoisier) series, formed on the reaction of 1,4-benzene dicarboxylate (H_2BDC) and trivalent metal salts of Cr,[30] Al,[31] and Fe.[32] The crystal structures of these materials are built up from chains of M(III) octahedra linked through terephthalate dianions. This creates a three-dimensional structure with an array of one-dimensional large pore channels filled with free disordered terephthalic acid molecules (MIL-53as) or water molecules (MIL-53lt); when the hosted molecules are removed, this leads to a nanoporous solid (MIL-53ht) with a Langmuir surface area over 1500 $m^2\ g^{-1}$. The transition between the hydrated form (MIL-53lt) and the anhydrous solid (MIL-53ht) is fully reversible and is followed by a very high breathing effect (more than 5 Å), the pores being clipped in the presence of water molecules (MIL-53lt) and reopened when the channels are empty (MIL-53ht) (Figure 1.16).

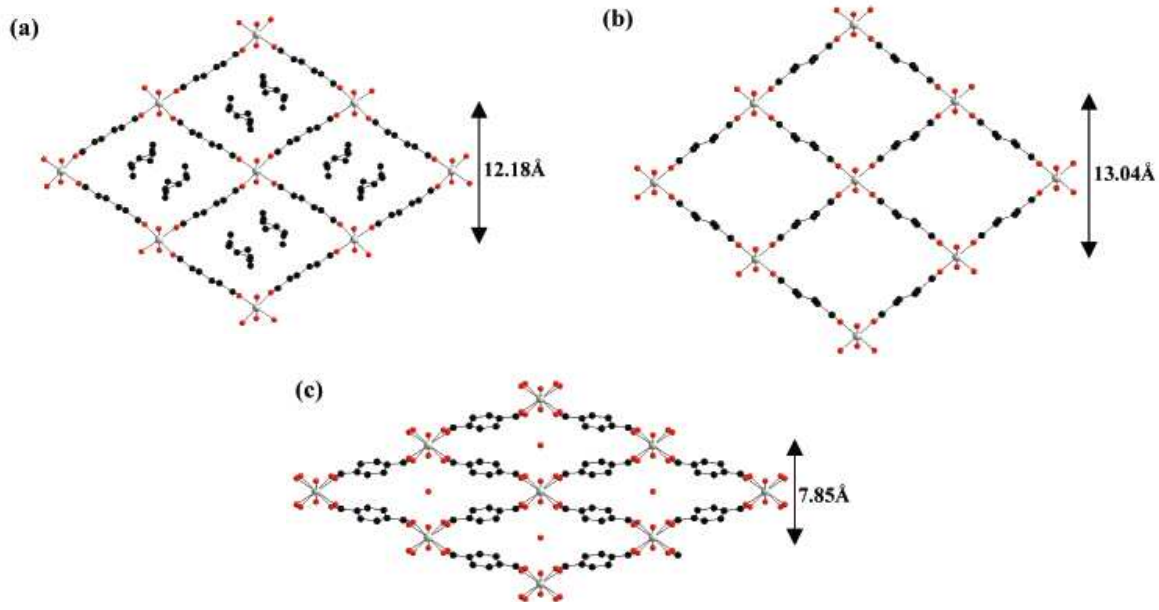

Figure 1.16. View of the pore systems of (a) MIL-53(Cr)as, (b) MIL-53(Cr)ht, and (c) MIL-53(Cr)lt.

Few years later the publication of the structure of MIL-53(Cr), two new cubic zeotypic metal carboxylates, denoted MIL-100 and MIL-101 built up from trimers of cromium octahedra and di- or tricarboxylic acids were reported by the same research

group.[33] The formula of these compound are: $Cr_3OX(H_2O)_2L_n$, where X = F, OH and L = 1,3,5-benzenetricarboxylic acid (BTC) and n = 2 for MIL-100 or L = 1,4-benzenedicarboxylic acid (BDC) and n = 3 for MIL-101 (Figure 1.17). Initially they are hydrated and exhibit giant pores (diameter = 25–34 Å) and unprecedented surface areas (3100–5900 m^2 g^{-1}) without any loss of crystallinity. The rigidity and robustness of these structures suggested a possible biological application as materials for the delivery of small drug molecules.

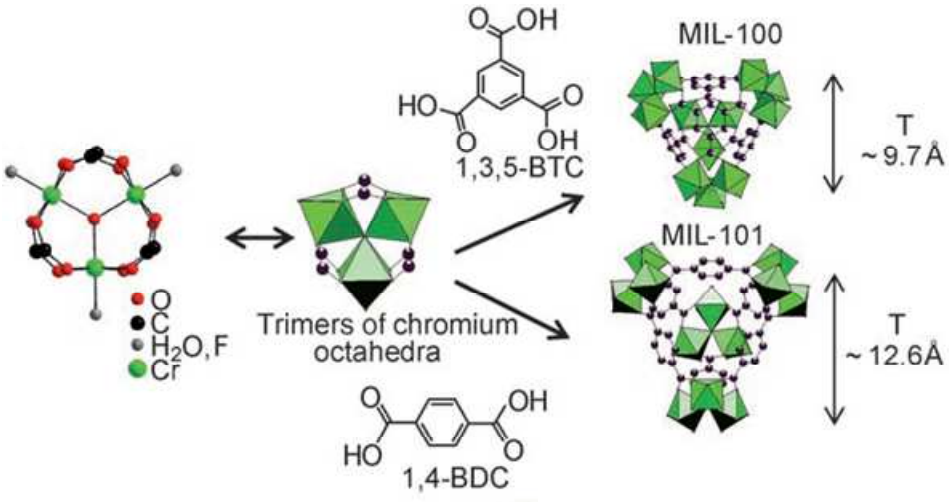

Figure 1.17. Schematic 3D representation of the tetrahedra (T) built up from trimers of chromium octahedra and BDC moieties or BTC groups in MIL-101 and MIL-100, respectively.

Furthermore, the possibility to post-functionalize MIL100(Cr) and MIL101(Cr) with alcohol molecules [34] or with organic multifunctional amines [35] suggested a potential application of these materials as catalysts and indeed they were found to be active for the Knoevenagel condensation reaction.

Another important class of compounds comprises a wide variety of zeolitic-imidazolate frameworks. The synthesis of a Fe(II) based azolate framework had been published in 1999[36] and afterwards new structures of Co(II),[37] Cu(II)[38] and Zn(II)[39] based on zeolite-like tetrahedral nets appeared. Anyway, the most important work dealing with this class of compounds was published in 2006 by Yaghi and co-workers which reported on an extense library of Zn(II) based imidazolate compounds, named ZIFs (Figure 1.18).[40] The ZIFs crystal structures are based on the nets of seven distinct aluminosilicate zeolites where the tetrahedral Si(Al) and the bridging O are replaced by Zn ion and imidazolate link, respectively. ZIF-8 (Zn(2-methylimidazolate)$_2$) sodalite type framework is still the most studied among these

compounds, because of its high chemical as well as thermal stability (up to 420 ºC in air) and permanent porosity. Indeed it contains a porous structure composed of cavities of 11.4 Å diameter and small apertures of 3.2 Å, and its pore surface is highly hydrophobic due to the presence of methyl groups pointing to the inner of the pores.

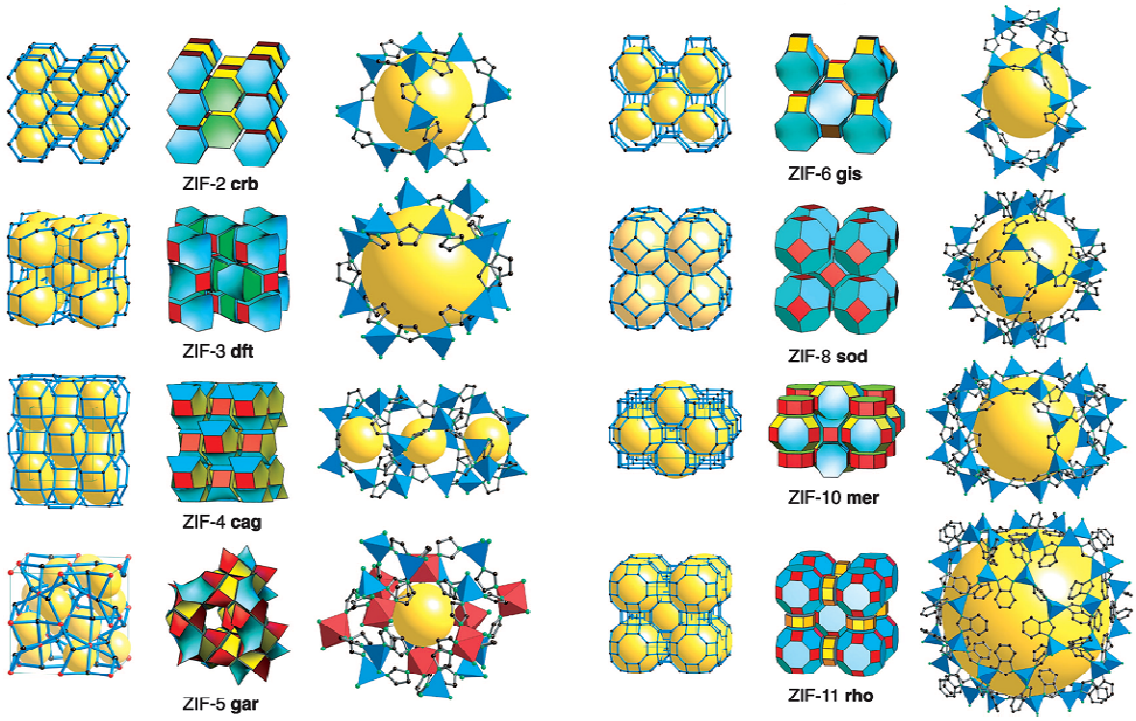

Figure 1.18. Single crystal X-ray structures of ZIFs. Net shown as a stick diagram (left) and as a tiling (centre); (right) largest cage in each ZIF. **ZnN_4 tetrahedra**, **InN_6 octahedra** (for ZIF-5). H atoms have been omitted for clarity.

Finally, it is worth presenting another important structure obtained, once again by Yaghi and co-workers, [41] based on Cu(II) cations linked by 1,3,5-benzene tricarboxylic acid (BTB). This framework, of exact formulation $[Cu_3(BTB)_2(H_2O)_3]\cdot(DMF)_9(H_2O)_2$ (MOF-14) is a representative example of interpenetrated network whose stability is enhanced by interpenetration (Figure 1.19). Indeed MOF-14 structure reveals a pair of interwoven metal-organic frameworks that are mutually reinforced. Each BTB is linked to three paddle-wheel clusters and each cluster to four BTB units, resulting in a (3,4)-connected net with the Pt_3O_4 topology. Despite interpenetration, this material has a very high Langmuir surface area (1502 $m^2\ g^{-1}$) with cavities size substantially larger than that of the highly prorous MOF-5 material.

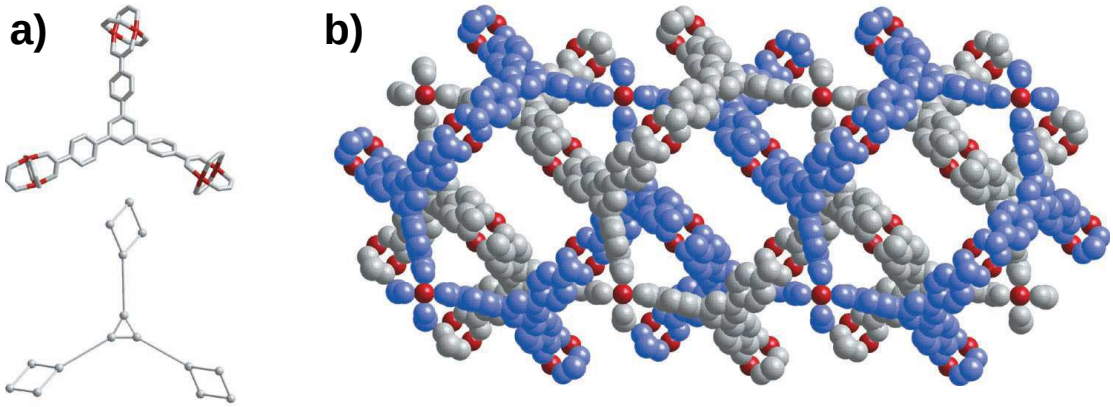

Figure 1.19. Single-crystal structure of MOF-14 composed of: a) square paddle-wheel and triangular BTB SBUs; b) pair of interwoven three-dimensional porous frameworks. **Cu**, C (or **C**).

1.4. Advanced materials based on Metal Organic Frameworks

At this point, it is necessary to note that the initial interest for searching outperforming MOF systems has been overcome by the necessity of finding materials useful for practical applications. In this regard, much effort has recently been focused on the formation of advanced materials: e.g. functionalised systems and membranes for gas separation, formation of films for gas sensing purposes, inclusion of nanoparticles for advanced catalysis, shaping the MOFs materials, etc. Few, selected examples of advanced applications of MOF materials are presented below.

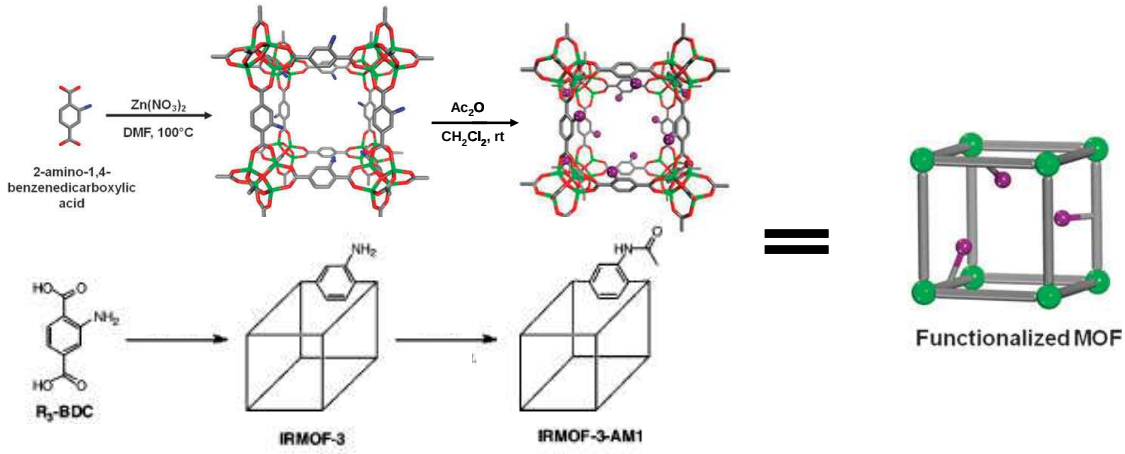

Figure 1.20. Scheme for the preparation of the functionalized IRMOF-3 (IRMOF-3-AM) by postsynthetic acetylation reaction.

The research of Cohen and col. has been of outmost importance in the field of modification of MOF structures (Figure 1.20). Indeed, in 2007,[42] he used for the first time the term “postsynthetic modifications” referring to metal organic frameworks.

In the same paper he theorized and demonstrated the possibility to transform the starting MOF material into a new MOF with altered functional groups and thereby showing different physical and chemical properties. The presence of organic ligands as constituents of the inorganic-organic hybrid MOF structures makes these materials attractive targets for their manipulation by means of organic reactions, a feature that is not so feasible for classical inorganic materials (e.g. zeolites). Therefore, by targeting the organic linking components of the MOF, a vast array of organic reactions can be exploited generating MOFs with unprecedented structures and functions.

As a proof of the concept of this new strategy, the postsynthetic modification of the IRMOF-3 material[43] was presented. IRMOF-3 is prepared from $Zn(NO_3)_2$ and 2-amino-1,4-benzene dicarboxylic acid (R_3-BDC). The 2-amino group of the R_3-BDC ligand does not participate in the coordination to the tetranuclear Zn_4O nodes so that it is potentially available for undergoing the desired organic transformations. The reaction of this MOF with acetic anhydride has been explored (see Figure 1.20) and the percent conversion after 5 days results to be > 80 %.

In this way, Cohen and Wang proved that postsynthetic modification can efficiently take place in a MOF and they realized that this is an important method for modifying the cavities of a porous structure, resulting in the modulation of solubility and stability of the MOF particles.

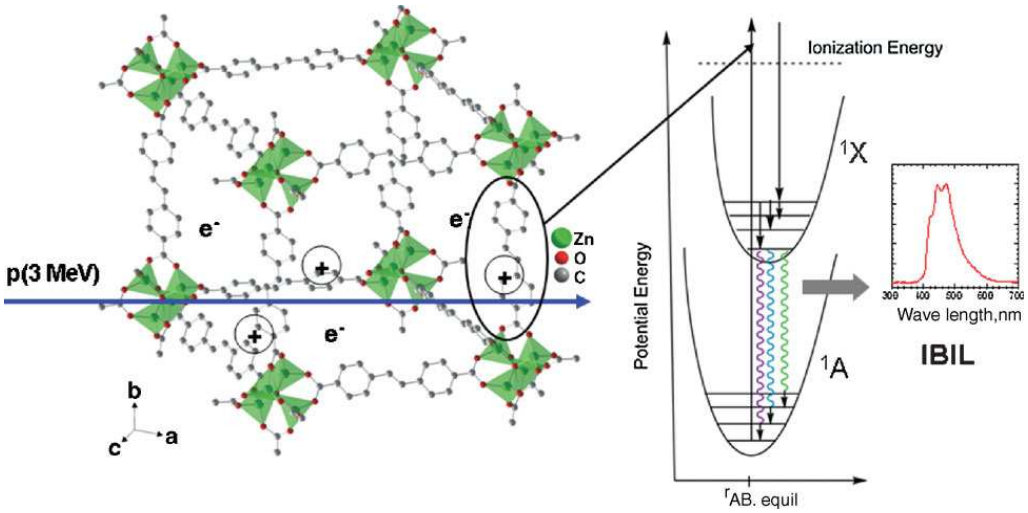

Figure 1.21. Schematic representation of the ion-beam-induced luminescence (IBIL) process on MOF-S1 structure showing (left) the interaction of a high-energy proton that ionizes the material; (middle) the resulting excitation decays and produces the IBIL luminescence with vibronic structure(right).

The extraordinary versatility of MOF materials is also exemplified in the research leaded by Allendorf whose interest focus on the photoluminescent properties of these metal organic materials. In the pioneering paper "Scintillating Metal-Organic Frameworks: A New Class of Radiation Detection Materials"[44] the authors studied the scintillation properties of two MOFs reported by Allendorf's group two years earlier.[45] These structures (MOF-S1 and MOF-S2) are based on Zn^{2+} ions connected by stilbene dicarboxylate linker (SDC). The d^{10} configuration of Zn(II) metal ion reduces the fluorescence and emission spectra associated to transitions originating with the linker and it results in the absence of optical transitions in the near UV-vis region of the spectrum. Nevertheless, SDC ligand's orientation is constrained within the MOF lattice so that the non-radiative *cis–trans* isomerization pathway would be inhibited. As a consequence, MOF-S1 and MOF-S2 respond to ionizing radiation by emitting light (Figure 1.21). Interestingly, this is the first completely new class of scintillation materials with quantum yields comparable to commercial organic scintillators, and that are also exceptionally resistant to radiation damage. This opens a new route to the development of high-performance scintillators with properties tailored to the detection of specific particle types and new applications.

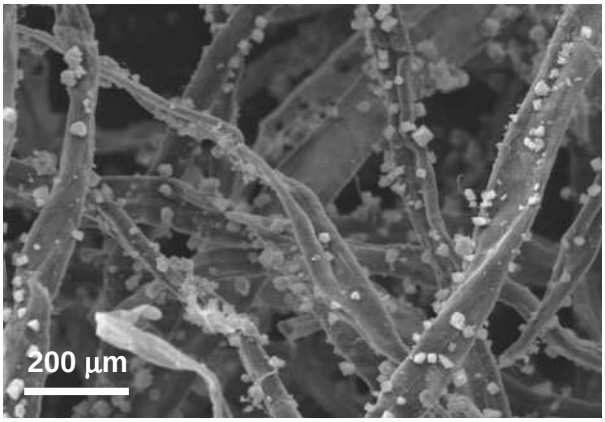

Figure 1.22. Scanning electron micrograph of CuBTC crystals on pulp fibers.

Furthermore, in the very last years new strategies for MOF deposition on surfaces have emerged. The need to immobilize MOFs on flat surfaces is often connected to a specific application so that mass transport, capacity and accessibility could be optimized.

In this field the scientific research of Kaskel has been of very high relevance. Besides other previous works (often resulted in patents),[46] we would like to highlight

a study on the deposition of CuBTC microcrystals on pulp fibers.[47] This type of material is a very appropriate carrier in filter technology as it provides a high degree of flexibility and can easily be molded to sheets or papers featuring a well-known and inexpensive technology. For this purpose, two different ways to incorporate CuBTC MOF into paper hand-sheets have been explored. Firstly CuBTC powder was added to the pulp slurry in a Rapid–Köthen sheet mold,[48] but the resulting sheets showed an inhomogenous distribution of powder. As alternative, the in situ direct synthesis of CuBTC in the presence of pulp fibers provides much better results giving rise to regularly distributed crystals on the fiber surface appropriate for filter applications (see Figure 1.22).

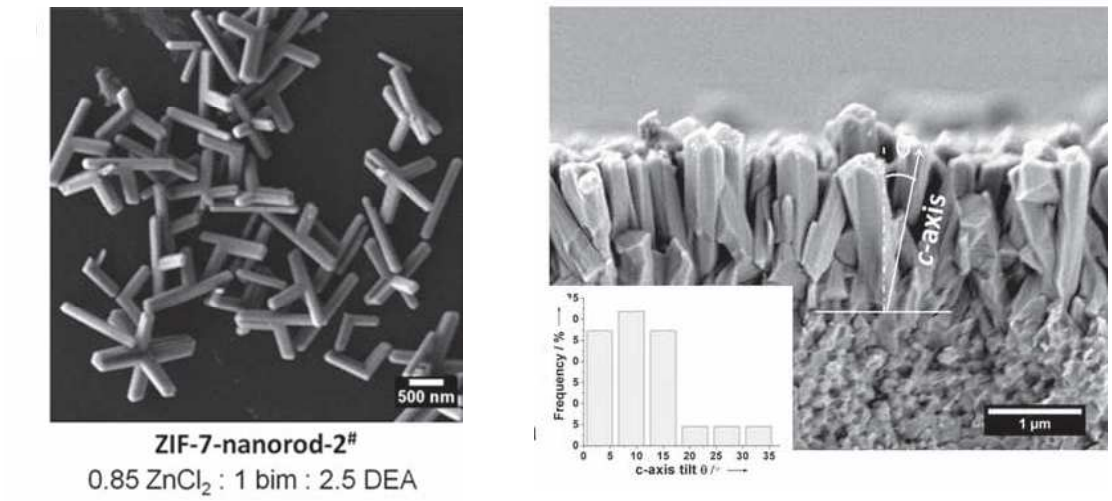

Figure 1.23. (Left) SEM images of the ZIF-7 nanorods and (right) SEM cross section of the ZIF-7 membrane obtained after different 225 min of microwave assisted secondary growth.

Another new and interesting application of these frameworks rewards the growth of MOF crystals on surfaces that can produce membranes, where size and shape of the built crystals can be finely controlled. In this context, the work of Caro and collaborators should be highlighted and, in particular, a recent report on the synthesis of ZIF-7 oriented membranes (Figure 1.23) that have been evaluated in H_2/CO_2 mixture gas separation.[49]

In this work, a general and effective solvothermal route is introduced to tailor the crystal size and morphology of MOF materials and to manipulate the orientation of MOF films through a van der Drift–type growth originating from randomly oriented seed layers. This discovery could have a big impact in MOF thin films field since the

ability to manipulate channel orientation and grain morphology is of great significance when targeting applications in catalytic coatings, chemical sensors and related advanced nanodevices.

1.5. Our Investigation

1.5.1. The advantages of N-donor ligands

Most of the MOF structures published up to date have the inconvenience of low thermal, chemical and mechanical stabilities, significantly lower than that of classical porous materials (zeolites and activated carbons). This is a serious drawback if these materials are aimed for practical applications.

The main cause of the fragile structure of PCPs is the weakness of the M-O(carboxylate) coordination bond, very often encountered in metal organic frameworks. The labile nature of this type of coordination bond is advantageous in order to assure a three-dimensional ordered array of metal ions and organic linkers in the final crystal structure since it can be dynamically formed and cleaved during the reaction period. In this way, building blocks can assume the correct spatial arrangement that permits the formation of a crystalline framework, in some cases in the form of single crystal of suitable size for X-ray diffraction measurement. However, the weakness of this approach is the low robustness of the resulting material.

Therefore, the need for robust structures to be used in practical applications opens the way to the search of new organic ligands with increased basicity that could form a stronger M-L bond, to provide the required structural stability.

In this context, five-membered ring nitrogen donor (N-donor) ligands can give rise to M-N coordination bond of the adequate strength depending on the basicity of the N-donor groups.[50] This group of azoles includes imidazole, triazole, tetrazole and pyrazole ligands (see Scheme 1.2).

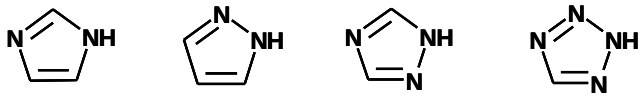

	imidazole	pyrazole	triazole	tetrazole
pK_a	14.5	14.0	10.3	4.9

Scheme 1.2. Azole heterocycles ring and the correspinding values of pK_a.

Although azoles are mostly known as bases, they can also be deprotonated by using a base such as triethylamine or sodium hydroxide, to form the corresponding azolate anion. In the case of azolates, all the N atoms of the aromatic ring can coordinate with metal ions in many different coordination modes and, moreover, the possibility to generate azolate anions further increases the basicity of these donor sites. In this regard, a direct consequence is the extremely high thermal and chemical stability of the coordination compounds formed with azolate derivatives. This high stability is of outmost importance for practical applications involving coordination polymers since the resulting materials can be used under severe conditions like boiling solvents or high (or low) pH. Anyhow, this kind of ligands have not been widely used in MOF field until the last decade, probably because of their reduced size that entails short bridging length and because of the extreme difficult of growing single crystals upon increasing the robustness of the coordination bond, as a consequence of the high basicity of this type of azolate ligands. Indeed, most of the PCPs formed with pyrazolate linkers are recovered as polycrystalline powders and consequently no crystals of suitable size for single crystal X-ray diffraction can be obtained.

In addition to purely azolate-based ligands, organic chemistry provides a wide range of hetero-functional azolate-based ligands, such as pyridine-tetrazolates,[51] carboxylate-tetrazolates[52] or imidazole-tetrazolates.[53] The use of these ligands afforded, in some cases, crystalline coordination polymers and, at present, these mixed ligands can be found much more frequently in the new reported structures.[54] The advantage is that the properties of more than one ligand type can be combined in the same molecule then affording more versatile materials. In particular, the combination of azolate functional groups with carboxylates, can lead to organic ligands that can form robust structures with a high degree of crystallinity since the labile M-O coordination bond can be dynamically formed/broken to give rise to a well ordered material.

For PCPs synthesis, the dinitrogen moiety is desirable because it is capable of bis-monodentate coordination to metal ions ($M_2(N_2\text{-azR})$) in a similar fashion to carboxylates. Indeed, as in the case of carboxylates, azolates can coordinate multiple metals to form clusters which can become potential secondary building units in the construction of MOFs. In general, when bridging ligands containing two five-membered azolates are used in the formation of coordination polymers, they may

occupy all the coordination sites around the metal ions or the structure can contain terminal coordinated solvent or anions to fulfil the metal coordination sphere, thereby forming 2D or 3D networks.

Among the dinitrogen ligands, pyrazoles have been widely used for the synthesis of PCPs and, typically, they are bound to metal ions in a variety of coordination modes as pyrazolates moieties (i.e. deprotonated at the N(1)-H position). Three different coordination modes can be found for deprotonated pyrazolate ligands: the mono-dentate, the exo-bidentate (η^1-η^1) and the endo-bidentate (η^2) modes (see Figure 1.24.a). Therefore, a wide variety of secondary building units can be obtained and some examples are shown in Figure 1.24.b.

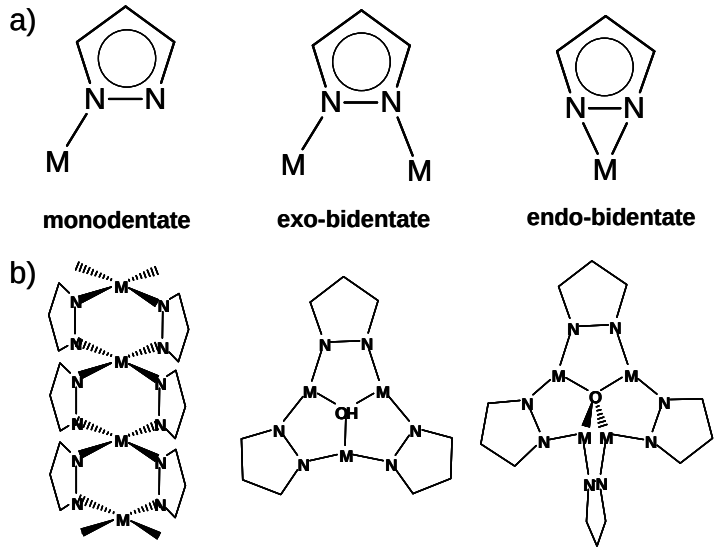

Figure 1.24. a) Common coordination modes for the pyrazolate anion; b) common structural motives found in coordination polymers with pyrazolate ligands.

1.5.2. Our ligands

We focused our investigation on anionic linear pyrazolate based linkers. We can divide them into two main groups, namely bis-pyrazolate ligands (where two azolate rings are linked together by the desired organic spacer) and carboxy-pyrazolate mixed ligands (where a five member pyrazolate ring and the carboxylate functional group are the two edges of the linear linker). The reasons for the choice of these linkers can be summarized in the following points:

- ligands' high symmetry may favour the auto-assembly process and lead to well ordered polymeric systems;

- the anionic nature of bridging linkers will compensate the charge of metal ions so that there will be no need of counterions (that would reside in the cavities reducing

the overall porosity) and at the same time the final network will be highly robust as a consequence of the resulting electrostatic interactions with the metal ions;

- their length is supposed to give rise to an adjustable pore size so that guest molecules of different size and shape can be accommodated in the structures;
- the variety of possible structural motives (see Figure 1.24.b) will determine the final assembly of the framework;
- the high connectivity of the proposed ligands will favour the formation of networks with high dimensionality;
- the presence of benzene rings and alkyne functional groups should also open the way to the post-synthetic functionalisation of the isolated MOFs.

In Figure 1.25 the structures of the organic molecules used to prepare PCPs presented in this doctoral thesis are depicted. Besides these seven molecules, many other linkers have been considered and the investigation is still ongoing due to the wide variety of frameworks that can be obtained. Finally, it should be noted that the increasing length of the ligand is limited since very long linkers may eventually lead to interpenetration or unstable and disordered structures.

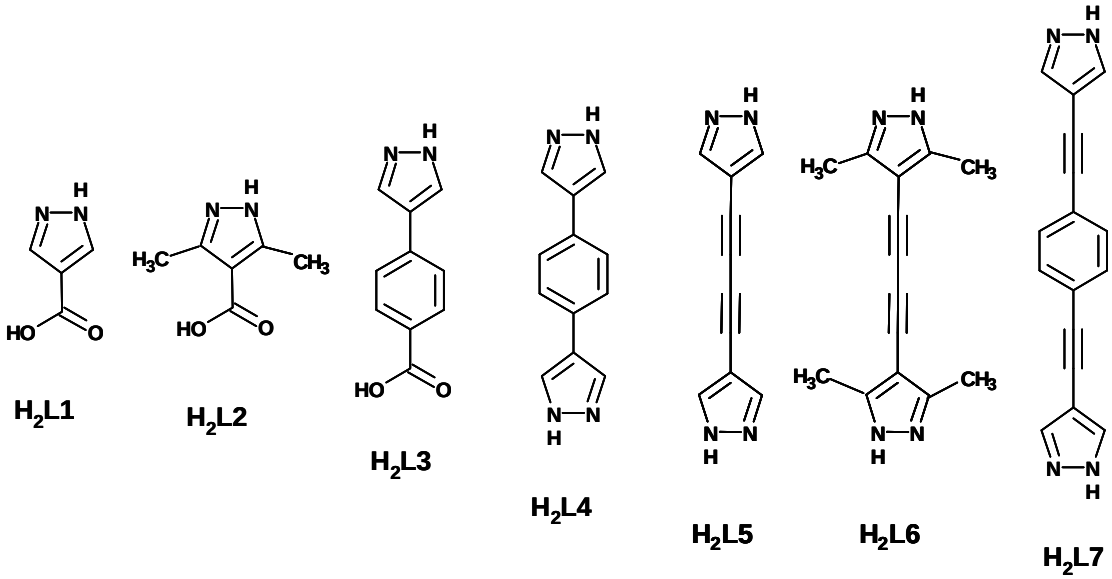

Figure 1.25. Pyrazole based ligands used in the synthesis of PCPs presented in this thesis.

Another important feature is that these molecules, thanks to the presence of benzene rings, methyl groups and C-C triple bonds, are expected to give rise to highly hydrophobic porous structures that could be employed under open air (and even under more severe humid conditions, including water itself) without any damage of the framework.

Since none of the used ligands is commercially available (except for H_2L2), it has been necessary to develop efficient synthetic strategies to yield them in relatively high amount and high purity prior to the inorganic synthesis of PCPs. In this regard, it should be highlighted that the presence of impurities dramatically reduces the degree of crystallinity of the final product and this will make it very difficult (or even impossible) to establish the relation between the properties of the bulk solid and its crystal structure. The optimization of the reaction conditions for the syntheses of H_2L5, H_2L6 and H_2L7 bis-pyrazolate ligands has been carried by Mrs. Natalia Muñoz, PhD student in the Department of Organic Chemistry under the supervision of Professor Enrique Oltra.

1.5.3. Synthetic strategies for the organic synthesis of ligands

H_2L1: oxidation of 4-methyl-1H-pyrazole

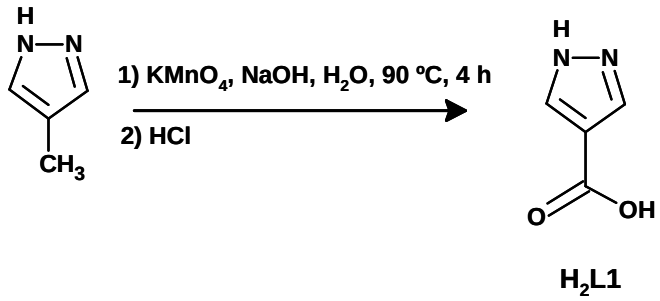

Scheme 1.3. Oxidation reaction of 4-methyl-1*H*-pyrazole to give H_2L1.

The synthesis of H_2L1 consists in the oxidation of the methyl group in the 4-position of the pyrazole substituted ring, by the use of $KMnO_4$ in basic aqueous medium (see Scheme 1.3). A large excess of potassium permanganate should be used to push the oxidation reaction to completeness, therefore yielding the corresponding carboxylic acid. The final product is recovered in moderate yield as a white precipitate after the addition of concentrated hydrochloric acid to the filtered reaction mixture.

H_2L2: hydrazinolysis of ethyldiacetoacetate

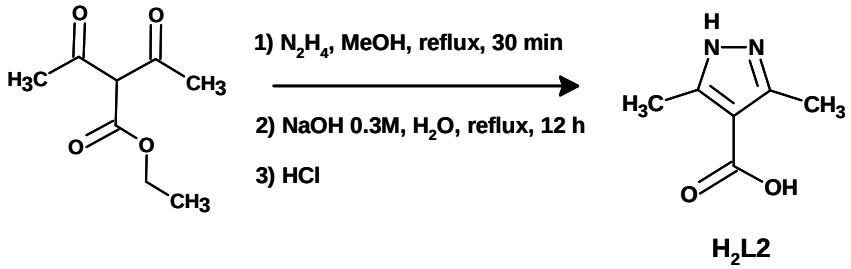

Scheme 1.4. Hydrazinolysis reaction of ethyl diacetoacetate followed by hydrolysis to give H_2L2.

Although 3,5-dimethyl-1*H*-pyrazole is commercially available from Maybridge supplier, we used to synthesize this ligand in our laboratories for economical reasons. Indeed, the cost of the final product can be halved if the synthetic procedure summarized in Scheme 1.4 is followed. The addition of hydrazine to a methanolic acid solution containing ethyl diacetoacetate, results in the concerted [3+2] cycloaddition reaction, yielding the ethyl-ester of the desired H_2L2 product that is obtained as a pure white powder after hydrolysis in basic medium at reflux temperature and further acidification with concentrated hydrochloric acid.

H_2L3: Suzuki reaction on protected 4-I-pyrazole

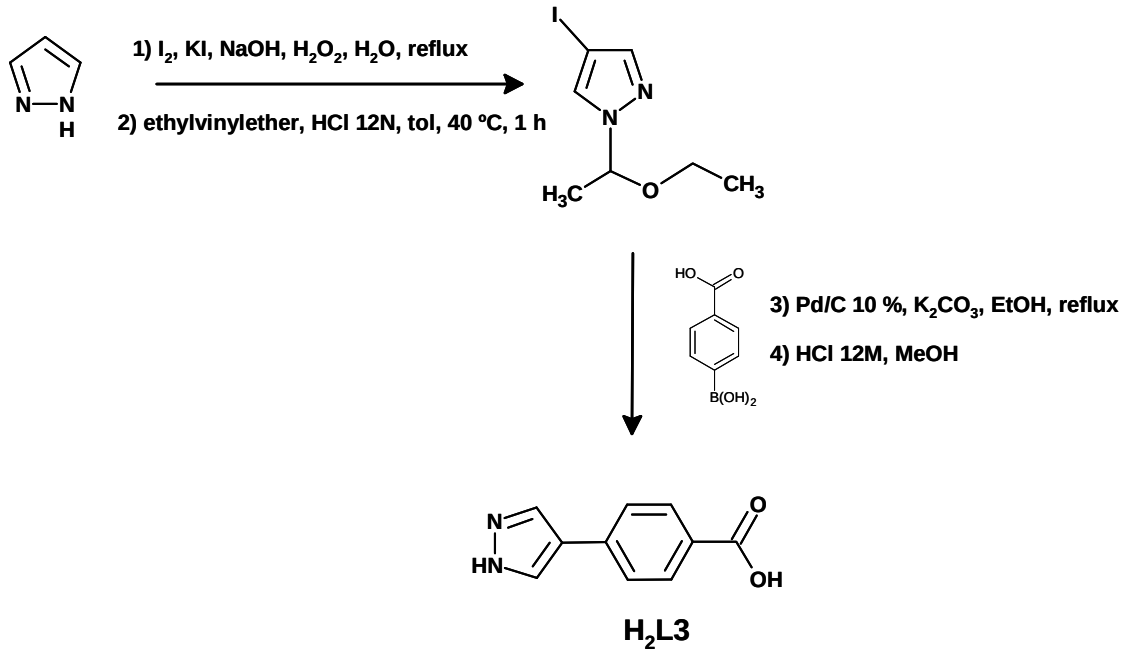

Scheme 1.5. Suzuki reaction for the synthesis of the H_2L3 ligand.

The main step in the synthesis of H_2L3 ligand is the Suzuki coupling reaction between 1-(1-ethoxyethyl)-4-I-1*H*-pyrazole and 4-carboxyphenilboronic acid, as can be seen in Scheme 1.5, step 3. Previously, the pyrazole molecule was iodated in the position 4 of the aromatic ring and protected on the N(1) by the use of ethylvinylether, while, after the Suzuki reaction, the protecting group will be cleaved in strong acidic medium to afford pure H_2L3 ligand.

H_2L4: Vilsmeier-Haack-Arnold (VHA) formylation reaction on p-phenylenediacetic acid and hydrazinolysis

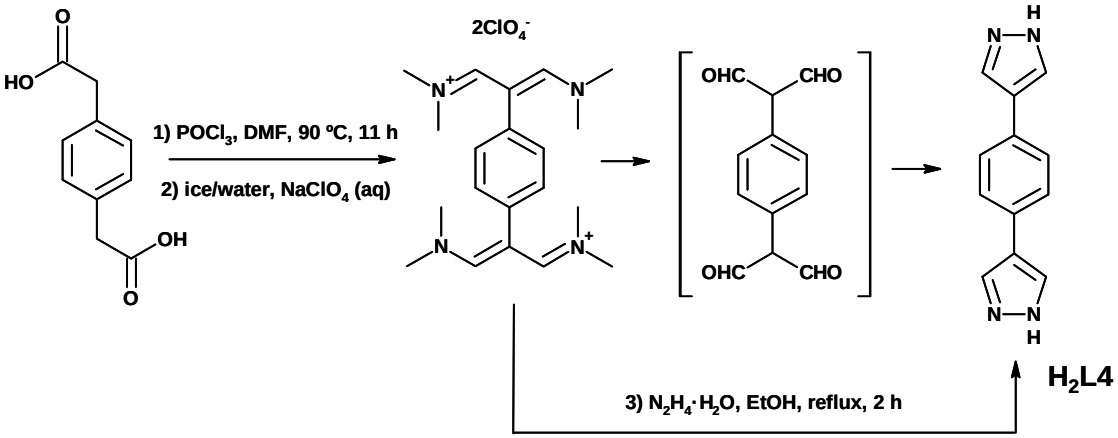

Scheme 1.6. VHA formylation of *p*-phenylenediacetic acid followed by hydrolysis to give H_2L4 ligand.

The synthesis of 1,4-bis(pyrazol-4-yl)benzene ligand (H_2L4) has been previously published in 2008 by Maspero and co-workers.[55] It consists in the heterocyclization of *p*-phenylenebis(malondialdehyde)[56] (or its synthetic equivalents) with hydrazine.

Thus, H_2L4 was best prepared from commercially available *p*-phenylenediacetic acid (Scheme 1.6) by a sequence of reactions starting with the Vilsmeier-Haack-Arnold (VHA) formylation reaction followed by quenching in water and metathesis with $NaClO_4$, overcoming the necessity of isolating the rather unstable tetraldehyde, as done by other research groups,[57] the resulting bis(perchlorate) vinamidinium salt was directly reacted with hydrazine monohydrate to provide the required ligand in good yields.

$(Boc)_2$L5, $(Boc)_2$L6 and $(Boc)_2$L7: protection of 4-I-pyrazole with –Boc and Sonogashira coupling

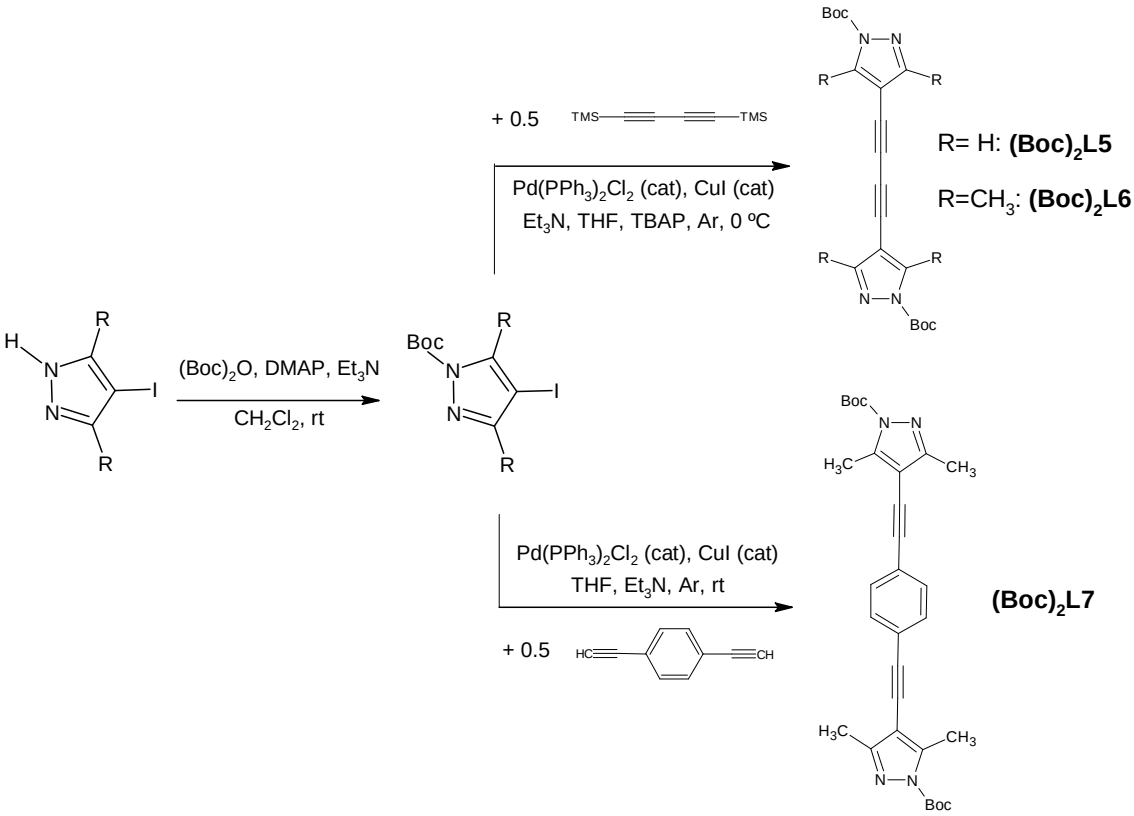

Scheme 1.7. Summary of the syntheses of $(Boc)_2$L5, $(Boc)_2$L6 and $(Boc)_2$L7 ligands.

The first step in the syntheses of $(Boc)_2$L5, $(Boc)_2$L6 and $(Boc)_2$L7 ligands consists in the quantitative protection of the commercial 4-I-1*H*-pyrazole (or of the previously iodinated[58] 3,5-dimethyl-4-I-1*H*-pyrazole) with di-*tert*-butyl-dicarbonate (Boc_2O) in the presence of 4-dimethylaminopyridine (DMAP) and triethylamine, to yield the 1-Boc-4-I-pyrazole (or 1-Boc-3,5-dimethyl-4-I-pyrazole) intermediate.

Next, 1-Boc-4-I-pyrazole (or 1-Boc-3,5-dimethyl-4-I-pyrazole) is used in the Sonogashira reaction [59] together with 1,4-bis(trimethylsilyl)butadiynetrimethyl[4-(trimethylsilyl)-1,3-butadiynyl]silane (for the synthesis of $(Boc)_2$L5 and $(Boc)_2$L6) or 1,4-diethynilbenzene (for the synthesis of $(Boc)_2$L7). In general, the Sonogashira coupling gives rise to the formation of a carbon–carbon bond between a terminal alkyne and a vinyl halide (or an aryl) using $Pd(PPh_3)_2Cl_2$ and CuI as catalysts in THF/Et_3N medium. Therefore, as can be seen in Scheme 1.7, $(Boc)_2$L5, $(Boc)_2$L6 and $(Boc)_2$L7 ligands are directly recovered after a double Sonogashira coupling, although in the case of $(Boc)_2$L5 and $(Boc)_2$L6, the coupling follow the *in situ*

cleavage of TMS groups of the 1,3-butadiynyl reagent, by reaction with tetra-*n*-butylammonium fluoride. In all cases the final product is obtained in good yield.

Even if the purity of the ligands recovered in the above described syntheses is quite good, we proceed to a further purification by solid-liquid chromatography on silica gel (*n*-hexane/ethylacetate 8:2). It is worth noticing that purification by solid-liquid chromatography on silica gel could not be used for the rest of the ligands. Indeed, they bear 1*H*-pyrazole ring and carboxylic acid functional groups which anchor the molecules on the silica bed precluding their recover.

1.6. Objectives

The objectives we would like to accomplish with the present PhD thesis are summarized in the following points:

1. Design and synthesis of new linear organic ligands, based on the pyrazolate heterocycle or a combination of carboxylate and pyrazolate functional groups. In this way, we pretend to finely tune the size and the stereochemistry of the linkers, resulting in different and interesting physical properties that are the hallmarks of our investigation.
2. Synthesis and full characterization of novel Porous Coordination Polymers based on these linear ligands. The reaction between organic ligands and metal salts under the appropriate conditions can afford 3D structures whose stability should be enhanced by the presence of the M-N coordination bond. For mixed pyrazolate-carboxylate ligands, the combination in the network of feeble M-O bonds with much stronger M-N bonds will give rise to network robustness without precluding the structural order typically found in carboxylate-based PCPs.
3. Study of the zeomimetic behaviour of $NH_4[Cu_3(\mu_3\text{-}OH)(\mu_3\text{-}4\text{-carboxypyrazolato})_3]$ anionic coordination network and, particularly, the possible modulation of its porosity by means of ion exchange processes of extraframework cations.
4. Study of the structural flexibility in a Cu(II) based PCP. The dynamic behaviour of some porous coordination polymers is a consequence of the plasticity of the metal atom and its local structure. Therefore we aim to understand correlations between the crystal structures and the macroscopic properties (with a particular

focus on gas adsorption and separation), as well as to rationalize the processes taking place during the structural transformations.

5. Study of the structural stability and gas adsorption properties of frameworks containing the same M_4O building unit found in MOF-5 and analogous nets. A deep insight in chemical, physical and mechanical stability of these structures will be the base for understanding their gas adsorption properties.
6. Thanks to the extraordinary stability of M-N bonds, we demonstrate the possibility to modulate the size of 3D porous structures yielding a series of isoreticular materials based on Ni^{2+} octanuclear clusters with exceptional, periodic properties. The scalability of the pores' size would permit to tune the adsorptive behaviour with special focus on the outstanding robustness and uncommon hydrophobicity of these materials.
7. Study of the possible practical application of porous coordination networks as releasing systems for non-conventional metallodrugs. Taking advantage of the high chemical stability and hydrophobicity of $Ni_8(L5)_6$ framework this system have been investigated in the possible use for the adsorption/desorption of a Ru-based metallodrug.

1.7. Bibliography

[1] P. A. Wright, *Microporous Framework Solids*, RSC Publishing, Cambridge, **2008**.

[2] J. F. Keggin, F. D. Miles, *Nature*, **1936**, *137*, 577.

[3] O. M. Yaghi, G. Li, H. Li, *Nature*, **1995**, *378*, 703.

[4] D. Venkataraman, G. B. Gardner, S. Lee, J. S. Moore, *J. Am. Chem. Soc*. **1995**, *117*, 11600.

[5] O. M. Yaghi, J. R. Long, *Chem. Soc. Rev*. **2009**, *38*, 1203.

[6] a) E. Barea, F. Turra, J. A. R. Navarro in *Metal-Organic Frameworks: Applications from Catalysis to Gas Storage*, Gas separation and purification by MOFs, (Ed. D. Farruseng) Wiley-VCH, Weinheim, **2011**, pp. 69-97; b) J.-R. Li, R. J. Kuppler, H. -C. Zhou, *Chem. Soc. Rev*. **2009**, *38*, 1477.

[7] a) A. Corma, H. García, F. X. Llabrés i Xamena, *Chem. Rev*. **2010**, *110*, 4606; b) L. Ma, C. Abney, W. Lin, *Chem. Soc. Rev*. **2009**, *38*, 1248; c) S. M. Cohen, *Chemical Science*, **2010**, *1*, 32.

[8] a) B. Xiao, P. S. Wheatley, X. Zhao, A. J. Fletcher, S. Fox, A. G. Rossi, I. L. Megson, S. Bordiga, L. Regli, K. M. Thomas, R. E. Morris, *J. Am. Chem. Soc*. **2007**, *129*, 1203; b) A. C. McKinlay, R. E. Morris, P. Horcajada, G. Ferey, R. Gref, P. Couvreur, C. Serre, *Angew. Chem. Int. Ed*. **2010**, *49*, 6260.

[9] a) B. Bonhommeau, G. Molnàar, A. Galet, A. Zwick, J. A. Real, J. J. Mcgargey, A. Bousseksou, *Angew. Chem. Int. Ed*. **2005**, *44*, 4069; b) P. Naumov, K. Sakurai, A. Nukui, M. Tanaka, *Chem. Commun*. **2007**, 347; c) D. Zacher, O. Shekhah, C. Wöll, R. A. Fischer, *Chem. Soc. Rev*. **2009**, *38*, 1418.

[10] T. Fukushima, S. Horike, Y. Inubushi, K. Nakagawa, Y. Kubota, M. Takata, S. Kitagawa, *Angew. Chem. Int. Ed*. **2010**, *49*, 4820.

[11] a) W. J. Rieter, K. M. Pott, K. M. L. Taylor, W. Lin, *J. Am. Chem. Soc*. **2008**, *130*, 11584; b) M. Dan-Hardi, C. Serre, T. Frot, L. Rozes, G. Maurin, C. Sanchez, G. Ferey, *J. Am. Chem. Soc*. **2009**, *131*, 10857.

[12] a) N. Roques, V. Mugnaini, J. Veciana, *Topics in Current Chemistry*, **2010**, *293*, 207; b) M. D. Allendorf, C. A. Bauer, R. K. Bhakta, R. J. T. Houk, *Chem. Soc*. **2009**, *38*, 1330.

[13] S. Takamizawa, in *Making Crystals by Design: Nanoporosity, Gas Storage, Gas Sensing* (Eds D. Braga, F. Grepioni), Wiley-VCH, Weinheim, **2007**.

[14] G. Saito, H. Yamochi, T. Nakamura, T. Komatsu, N. Matsukawa, T. Inoue, H. Ito, T. Ishiguro, M. Kusunoki, K. Sakaguchi, T. Mori, *Synth. Met*. **1993**, *56*, 2883.

[15] B. F. Abrahams, S. R. Batten, B. F. Hoskins, R. Robson, *Inorg. Chem*. **2003**, *42*, 2654.

[16] D. B. Leznoff, B.-Y. Xue, R. J. Batchelor, F. W. B. Einstein, B. O. Patrick, *Inorg Chem*. **2001**, *40*, 6026.

[17] M. L. Tong, X.-M. Chen, B.-H. Ye, L.-N. Ji, *Angew. Chem. Int. Ed*. **1999**, *38*, 2237.

[18] J. M. Knaust, S. Lopez, S. W. Keller, *Inorg. Chim. Acta*, **2001**, *324*, 81.

[19] B. F. Hoskins, R. Robson, *J. Am. Chem. Soc*. **1990**, *112*, 1546.

[20] D. Venkataraman, G. B. Gardner, S. Lee, J. S. Moore, *J. Am. Chem. Soc*. **1995**, *117*, 11600.

[21] B. F. Abrahams, S. R. Batten, H. Hamit, B. F. Hoskins, R. Robson, *Angew. Chem., Int. Ed. Engl*. **1996**, *35*, 1690.

[22] S. R. Batten, B. F. Hoskins, R. Robson, *J. Chem. Soc., Chem. Commun.*, **1991**, 445; *J. Chem. Soc., Dalton Trans.* **1999**, 2977.

[23] S. Kitagawa, M. Kondo, *Bull. Chem. Soc. Jpn.* **1998**, *71*, 1739.

[24] S. Horike, S. Shimomura, S. Kitagawa, *Nat. Chem.* **2009**, *1*, 695.

[25] S. S.-Y. Chui, S. M.-F. Lo, J. P. H. Charmant, A. G. Orpen, I. D. Williams, *Science*, **1999**, *2837*, 1148.

[26] S. Noro, S. Kitagawa, M. Kondo, K. Seki, *Angew. Chem. Int. Ed*. **2000**, *39*, 2082.

[27] N. L. Rosi, J. Eckert, M. Eddaoudi, D. T. Vodak, J. Kim, M. O'Keeffe, O. M. Yaghi, *Science*, **2003**, *300*, 1127.

[28] D. Li, K. Kaneko, *Chem Pys. Lett.* **2001**, *335*, 50.

[29] L. Tabares, J. A. R. Navarro, J. M. Salas, *J. Am. Chem. Soc*. **2001**, *123*, 383.

[30] C. Serre, F. Millange, C. Thouvenot, M. Noguès, G. Marsolier, D. Louër, G. Férey, *J. Am. Chem. Soc.* **2002**, *124*, 13519.

[31] T. Loiseau, C. Serre, C. Huguenard, G. Fink, F. Taulelle, M. Henry, T. Bataille, G. Férey, *Chem. Eur. J*. **2004**, *10*, 1373.

[32] R. T. Whitfield, X. Wang, L. Liu, A. J. Jacobson, *Solid State Sciences*, **2005**, *7*, 1096.

[33] P. Horcajada, C. Serre, M. Vallet-Regí, M. Sebban, F. Taulelle, G. Férey, *Angew. Chem. Int. Ed.* **2006**, *45*, 5974.

[34] A. Vimont, J. M. Goupil, J. C. Lavalley, M. Daturi, S. Surblé, C. Serre, F. Millange, N. Audnerand, *J. Am. Chem. Soc.* **2006**, *128*, 3218.

[35] Y. K. Hwang, D. Y. Hong, J. S. Chang, S. H. Jhung, Y. K. Seo, J. Kim, A. Vimont, M. Daturi, C. Serre, G. Férey, *Angew. Chem. Int. Ed*. **2008**, *47*, 4144.

[36] S. J. Rettig, A. Storr, D. A. Summers, R. C. Thompson, J. Trotter, *Can. J. Chem.* **1999**, *77*, 425.

[37] Y.-Q. Tian, C.-X. Cai, J. Ji, X.-Z. You, S.-M. Peng, G.-H. Lee, *Angew. Chem. Int. Ed.* ***2002***, *41*, 1384.

[38] N. Masciocchi, S. Bruni, E. Cariati, F. Cariati, S. Galli, A. Sironi, *Inorg. Chem.* **2001**, *40*, 5897.

[39] X.-C. Huang, J.-P. Zhang, X.-M. Chen, *Chin. Sci. Bull.* **2003**, *48*, 1531.

[40] K. S. Park, Z. Ni, A. P. Côté, J. Y. Choi, R. Huang, F. J. Uribe-Romo, H. K. Chae, M. O'Keeffe, O. M. Yaghi, *Proc. Natl. Acad. Sci. USA*, **2006**, *103*, 10186.

[41] B. Chen, M. Eddaoudi, S. T. Hyde, M. O'Keeffe, O. M. Yaghi, *Science*, **2001**, *291*, 1021.

[42] Z. Wang, S. M. Cohen, *J. Am. Chem. Soc.* **2007**, *129*, 12368.

[43] M. Eddaoudi, J. Kim, N. Rosi, D. Vodak, J. Wachter, M. O'Keffe, O. M. Yaghi, *Science*, **2002**, *295*, 469.

[44] F. P. Doty, C. A. Bauer, A. J. Skulan, P. G. Grant, M. D. Allendorf, *Adv. Mater*. **2009**, *21*, 95.

[45] C. A. Bauer, T. V. Timofeeva, T. B. Settersten, B. D. Patterson, V. H. Liu, B. A. Simmons, M. D. Allendorf, *J. Am. Chem. Soc*. **2007**, *129*, 7136.

[46] a) S. Kaskel, *Sorptionfiltersmaterial und seine Verwendung* DE-Patent DE10200 8005218 A1 Blücher GmbH, Erkrath Anmeldetag:18.01.2008; b) S. Kaskel, *Sorption filter material and use thereof*, WIPO Patent Application, **2008**, WO/2009/056184.

[47] P. Küsgens, S. Siegle, S. Kaskel, *Adv. Eng. Mat*. **2009**, 11, 93.

[48] O. Töppel, in *Prüfung von Papier, Pappe, Zellstoff und Holzstoff*, Vol. 3 (Ed: W. Franke), Springer Verlag, Heidelberg, **1993**, 43.

[49] Y.-S. Li , H. Bux, A. Feldhoff, G.-L. Li, W.-S. Yang , J. Caro, *Adv. Mater*. **2010**, *22*, 3322.

[50] J.-P. Zhang, Y.-B. Zhang, J.-B. Lin, X.-M. Chen, *Chem Rev*. **2012**, *112*, 1001.

[51] C. Jang, Z. Yu, S. Wang, C. Jiao, J. Lim, Z. Wang, Y. Cui, *Eur. J. Inorg. Chem.* **2004**, 3662.

[52] a) J. Li, J. Tao, R. Huanga, L. Zhang, *Acta Crystallogr*. **2005**, *E61*, m984; b) Z.-R. Qu, H. Zhao, X.-S. Whang, Y.-H. Li, Y.-M. Song, Y.-J. Liu, Q. Ye, R.-G. Xiong, B. F. Abrahams, Z.-L. Xue, X.-Z. You, *Inorg. Chem.* **2003**, *42*, 7710.

[53] H. Zhao, Q. Ye, Q. Wu, Y. Song, Y. Liu, R. Xiong, *Z. Anorg. Allg. Chem*. **2004**, *630*, 1367.

[54] a) C. Montoro, F. Linares, E. Quartapelle Procopio, I. Senkovska, S. Kaskel, S. Galli, N. Masciocchi, E. Barea, J. A. R. Navarro, *J. Am. Chem. Soc.* **2011**, *133*, 11888; b) S. Barman, H. Furukawa, O. Blacque, K. Venkatesan, O. M. Yaghi, G.-X. Jin, H. Berke, *Chem. Commun*. **2011**, *47*, 11882.

[55] A. Maspero, S. Galli, N. Masciocchi, G. Palmisano, *Chem. Letters*, **2008**, *37*, 956.

[56] Z. Arnold, *Coll. Czech. Chem. Commun*. **1985**, *30*, 2783.

[57] V. Lozan, P. Y. Solntsev, G. Leibeling, K. V. Domasevitch, B. Kersting, *Eur. J. Inorg. Chem.* **2007**, 3217.

[58] M. I. Rodríguez-Franco, I. Dorronsoro, A. I. Hernández-Higueras, G. Antequera, *Tetrahedron Lett.* **2001**, *42*, 863.

[59] K. Sonogashira, Y. Tohda, N. Hagihara, *Tetrahedron Lett.* **1975**, *16*, 4467.

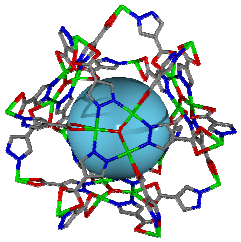

2. ZEOMIMETIC FRAMEWORKS

2.1. Introduction

Among porous materials, zeolites have a privileged role due to their physical and chemical properties that are responsible for their use for different applications in fields of paramount social impact.

The word “zeolite” derives form the Greek ζέω (*zéō*), meaning "to boil", and λίθος (*líthos*), meaning "stone" and underlines the property of these materials to release water steam when rapidly heated.[1] Indeed, the term was coined at the half of XVIII century by the Swedish mineralogist Axel Fredrik Cronstedt for a mineral that, when heated, released a large amount of water vapour previously adsorbed into its pores. Therefore zeolites can be defined as crystalline, hydrated aluminosilicates having an infinite, open and anionic, three-dimensional structure which host exchangable extraframework cations and that can reversibly lose and gain water without change of the crystal structure.

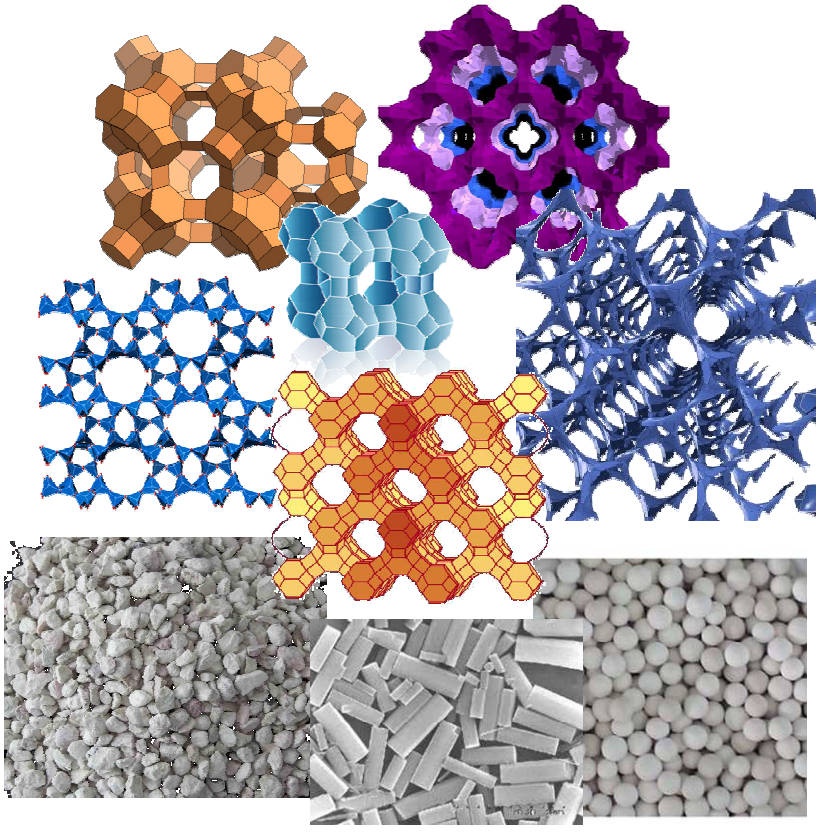

Figure 2.1. Some examples of zeolite materials: local structures and solids eventually used for practical applications.

This class of microporous minerals comprises 194 different structures of both natural and synthetic nature, few of which are widely used in industries as catalysts or molecular sieves.[2]

The main characteristic of zeolite materials is their local crystal order that lends unusual homogeneity in their porous structures and favours the diffusion of fixed size molecules within the pores. Therefore, the selective incorporation process of guest molecules in zeolite materials is a consequence of the polarity, shape and size of their pores.

These pure inorganic frameworks are probably the most prominent and utilized group of porous functional materials and their applications spread from petroleum refinement [3] to molecular adsorption, [4] from catalysis [5] to water softening and purification.[6] Nevertheless, zeolite applications have generally been limited to small size molecules due to their restricted pore and cavity sizes (typically $\leq$ 1 nm), in addition to their limited functionalities, [7] intrinsic rigidness and poor atomic composition.[8]

Since the discovery of these materials and their unusual properties, the search for other systems with similar molecular sieving features, have attracted more and more the attention of material scientists. However, no systematic approach to the construction of this class of solid-state materials had been introduced until the end of XX century, namely in 1989, when Hoskins and Robson proposed the design of open metal-organic-materials[9] based on a node-and-spacer approach. In this interesting paper they show how tetrahedral nodes can be linked by linear molecular spacers to construct an open structure based on the extension of cubic diamond. But it was just in 1990, when the first synthetic zeomimetic materials of Cu, Cd, and Zn, capable of anion exchange, were published by the same authors[10] and that the node-and-spacer concept theorized the year before had been realized (see Figure 2.2). In the same paper, Robson and Hoskins allude to the tunability of these frameworks, suggesting the ability to target functional open materials by variations in nodes and spacers required to construct the structures.

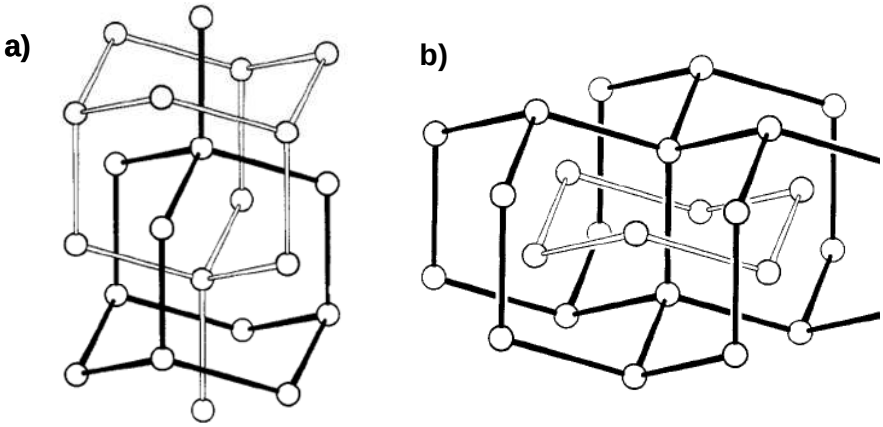

Figure 2.2. a) View of interpenetrating adamantane units in $Zn(CN)_2$, and $Cd(CN)_2$; b) view of $Zn(CN)_2$, and $Cd(CN)_2$, structures revealing multiple catenane associations.

Afterwards, a great scientific effort has been devoted to the design and synthesis of frameworks with network topologies and properties mimicking those of zeolites. These materials are basically constructed by the assembly of Tetrahedral Building Units (TBUs) that share all corners giving rise to 3D non-interpenetrated structures. Therefore, by replacing the single-metal (Al or Si) tetrahedral vertices with larger tetrahedral clusters or by expanding the edges with the incorporation of longer linkers, it will be possible to expand the zeolite-like nets. Using this strategy, widely applied by many research groups as for example by Yaghi,[11] Férey,[12] Eddaoudi,[13] and Navarro[14] a relevant number of zeolite-like metal organic frameworks have been published in the last years.

It should be noted, however, that most of these zeolite like systems possess neutral frameworks and consequently are unable to give rise to prototypical cationic exchange processes of zeolites. Nevertheless, some of the reported structures are ionic and show very interesting properties as a consequence of the incorporation of ions (of different charges and sizes) into the pores. A nice example concerns the *rho*-ZMOF and *sod*-ZMOF frameworks (see Figure 2.3) that have been synthesized by metal-ligand-directed assembly of rigid and directional tetrahedral building units: InN_4 and doubly deprotonated bis(bidentate) imidazoledicarboxylic acid ligands.[15] These frameworks are anionic and the organic cations in the cavities can be fully exchanged by Na^+, Li^+ or Mg^{2+} inorganic ions. Moreover, the effect of extraframework cations on H_2 binding has been investigated by the same research group three years later,[16] evidencing the possibility to tune ZMOF properties by cation exchange process.

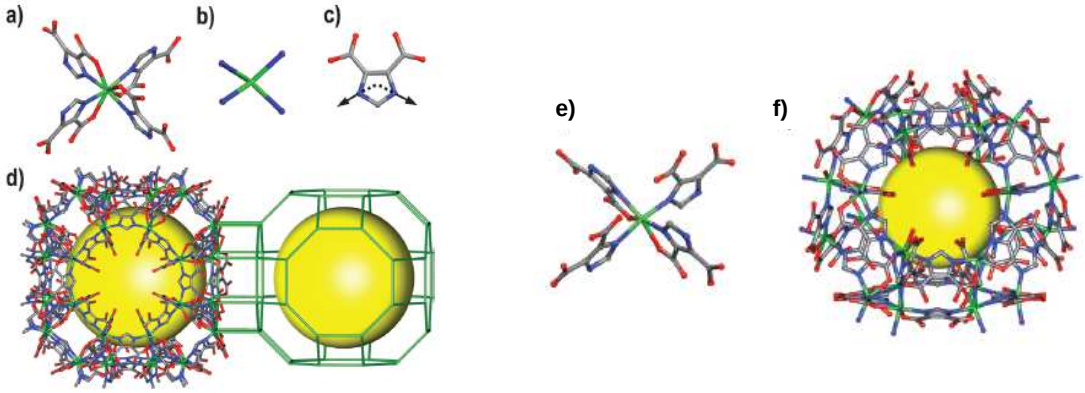

Figure 2.3. (Left) Single-crystal structure of *rho*-ZMOF composed of (a) eight-coordinated molecular building blocks which can be viewed as (b) 4-connected TBUs; (c) angle in the 4,5-imidazoledicarboxylic acid ligand; (d) fragment of the *rho*-ZMOF. (Right) Single-crystal structure of *sod*-ZMOF composed of (e) six-coordinated molecular building blocks which can be regarded as TBUs, InN_4, and (f) fragment of the *sod*-ZMOF. The yellow spheres represent the largest sphere that would fit in the cavities. **In**, **O**, **N**, **C**.

Some charged MOF structures that do not show a true zeolite-like topology but that behave in a similar way to zeolitic materials have been recently reported. Interestingly, they can undergo ion exchange or display some properties typical of pure inorganic zeolite networks. Among them, it is worth mentioning an intriguing Zn-based metal-organic framework that is built of interpenetrating cationic and anionic nets able to give rise to cation exchange processes in addition to adsorption and luminescent properties (Figure 2.4).[17]

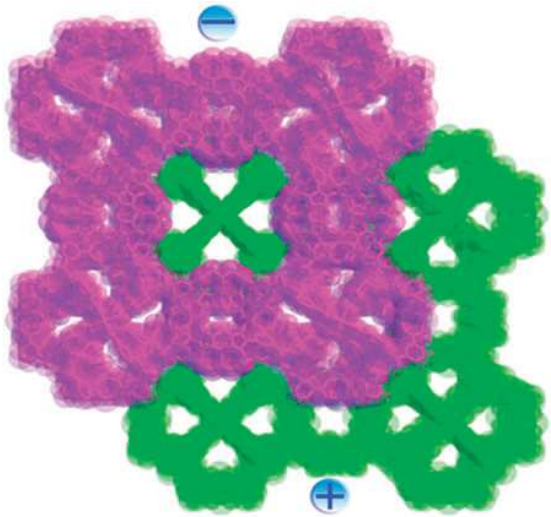

Figure 2.4. Representation, along the *a* direction, of two-fold interpenetrated Zn-based framework (green for cationic MOF and purple for anionic MOF).

A series of coordination polymers with anionic (M = Co, Mn, Cd) and cationic (M = Y, Dy, In) metal-carboxylate frameworks, synthesized by using a flexible tetrapodal ligand which can undergo ion exchange processes, is also remarkable.[18]

Finally, it should be highlighted an anionic MOF material built of In(III) centres and tetracarboxylic acid ligands named NOTT-200 containing piperazinium cations which can be exchanged by lithium ions thereby giving rise to kinetics trapping behaviour of hydrogen (Figure 2.5).[19]

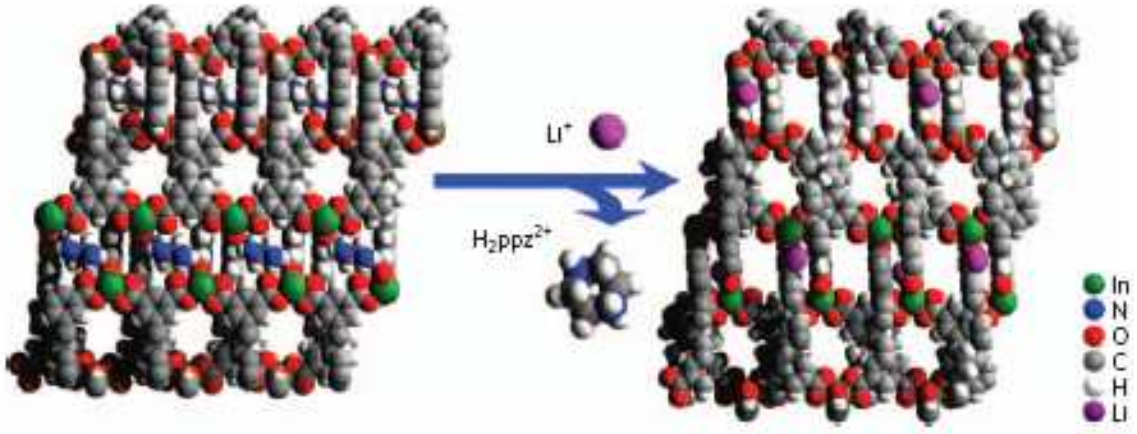

Figure 2.5. Space-filling view of framework structures of NOTT-200 (left) and NOTT-201 (right) along the crystallographic *b* axis. The piperazinium dications in the channels of NOTT-200 can be completely exchanged with Li^+ ions in the channels of NOTT-201.

In this context, we have been able to synthesize an anionic Cu-metal organic framework of formulation $NH_4[Cu_3(\mu_3\text{-}OH)(\mu_3\text{-}L1)_3]$ ($NH_4@Cu_3(OH)L1_3$), based on the 1*H*-pyrazole-4-carboxylic acid ligand (H_2L1) that, much alike zeolites, has been shown to experience exchange of the extra-framework cations, resulting in the modulation of its adsorption properties. As a matter of fact, the replacement of Cu^{2+} metal centres with Cd^{2+} in the reaction mixture, does not lead to an isoreticular framework, but to a crystalline, neutral, layered compound of formulation $[Cd(\mu_3\text{-}L1)(H_2O)_2]\cdot(H_2O)$ (CdL1). This is a remarkable example of the complexity of MOF syntheses and to the hurdles that can put up if dealing with poorly predictable reaction products.

2.2. Results and discussion

The reaction of $M(NO_3)_2\cdot nH_2O$ (M = Cd, Cu), with 1*H*-pyrazole-4-carboxylic acid (H_2L1) in H_2O/NH_3 15:1 at room temperature, gives rise to single crystal products of

formulation $NH_4[Cu_3(\mu_3\text{-}OH)(\mu_3\text{-}L1)_3]\cdot nH_2O$ ($NH_4@Cu_3(OH)L1_3$) and $[Cd(\mu_3\text{-}L1)(H_2O)_2]\cdot(H_2O)$ (CdL1). The profound structural difference between these two coordination polymers reflects the complexity of framework formation processes since the favoured geometric configuration of the central atom is of key importance in the assembly of the building units.

2.2.1. $NH_4@Cu_3(OH)L1_3$ compound

Crystal structure

When H_2L1 ligand is reacted with $Cu(NO_3)_2\cdot 3(H_2O)$ in H_2O/NH_3 15:1 solution, the dark blue mixture affords in three days at room temperature, dark blue crystals of $NH_4@Cu_3(OH)L1_3$ formulation suitable for single crystal X-ray diffraction (Figure 2.6). The presence of ammonia is unavoidable for a series of reasons: it favours the deprotonation of H_2L1 giving rise to a NH_4^+/NH_3 buffer media, as well as it coordinates Cu^{2+} ion to form the labile $[Cu(NH_3)_4]^{2+}$ complex. This species is the one actually involved in the reaction with $L1^{2-}$ anion leading to the slow ligand exchange processes with the pyrazolate or carboxylate functional groups of $L1^{2-}$ thereby favouring the ordered arrangement of the building blocks in the crystal structure of $NH_4@Cu_3(OH)L1_3$.

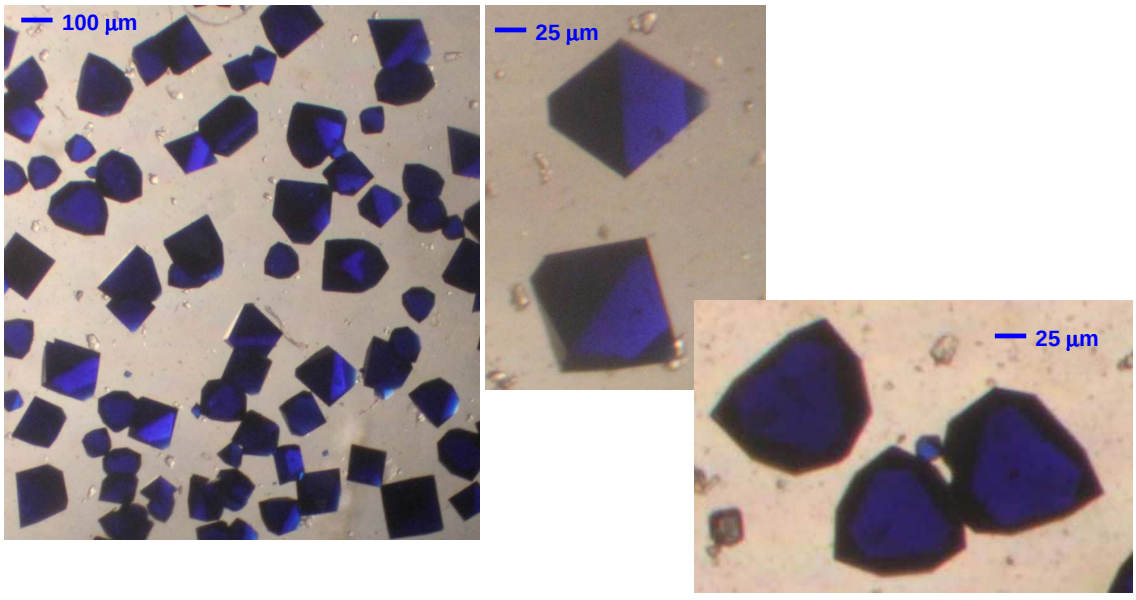

Figure 2.6. Single crystals of $NH_4@Cu_3(OH)L1_3$ material. The cubic symmetry can be deduced from the octahedral shape of many of these crystals.

$NH_4@Cu_3(OH)L1_3$ crystallizes in the cubic space group *Fd-3c* with cell parameter *a* = 30.1955(9) Å, cell volume *V* = 27531(1) $Å^3$ and calculated density of 1.351 g cm^{-3}. Its

crystal structure is based on an anionic 3D porous framework built up of trinuclear $Cu_3(\mu_3\text{-OH})$ clusters connected to another six ones through μ_3-4-carboxypyrazolato bridges (Figure 2.7). In this way, tetrahedral cages with an inner diameter of *ca*. 13 Å are generated, which host two extraframework NH_4^+ cations and crystallisation water molecules. Calculations with Platon,[20] after removal of the hosted water molecules, give rise to a high potentially accessible empty volume, accounting to *ca*. 49 % of the crystal cell. The tetrahedral voids are 3D connected through 4.5 Å and 8 Å wide windows along the [100] and [111] crystallographic directions, respectively (Figure 2.8).

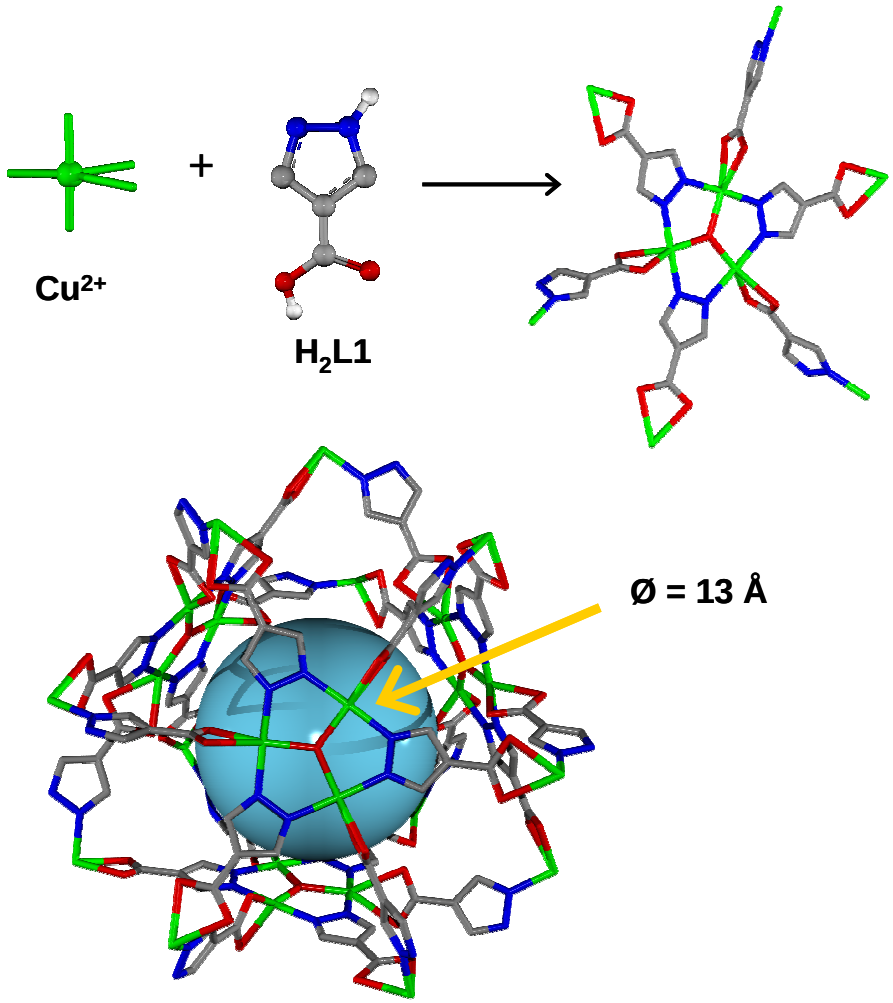

Figure 2.7. (Above) Cu^{2+} and H_2L1 building blocks in the trinuclear $Cu_3(\mu_3\text{-OH})$ cluster of formula $[Cu_3(\mu_3\text{-OH})(\mu_3\text{-L1})_3]$; (below) view of the tetrahedral cages found in $NH_4@Cu_3(OH)L1_3$ crystal structure. The blue sphere indicates the size of the inner voids. **Cu**, **N**, **O**, **C**. H atoms have been omitted for clarity.

Overall, the $NH_4@Cu_3(OH)L1_3$ framework is reminiscent to the one found in the $[Cu_3(\mu_3\text{-OH})(4\text{-pyridyltetrazolato})_3(OH)_2(DMF)_4]$ system reported by Zubieta and co-workers,[21] however, in our case the framework is anionic whereas in the latter it is

neutral. Taking the $Cu_3(\mu_3\text{-}OH)$ structural motifs as nodes of the framework, the structure can be described as hxg-type topology with the $\{4^6.6^9\}$ point symbol and the $[4.4.4.4.4.4.6_4.6_4.6_4.6_6.6_6.6_6.6_6.6_6.6_6]$ vertex symbol.[22]

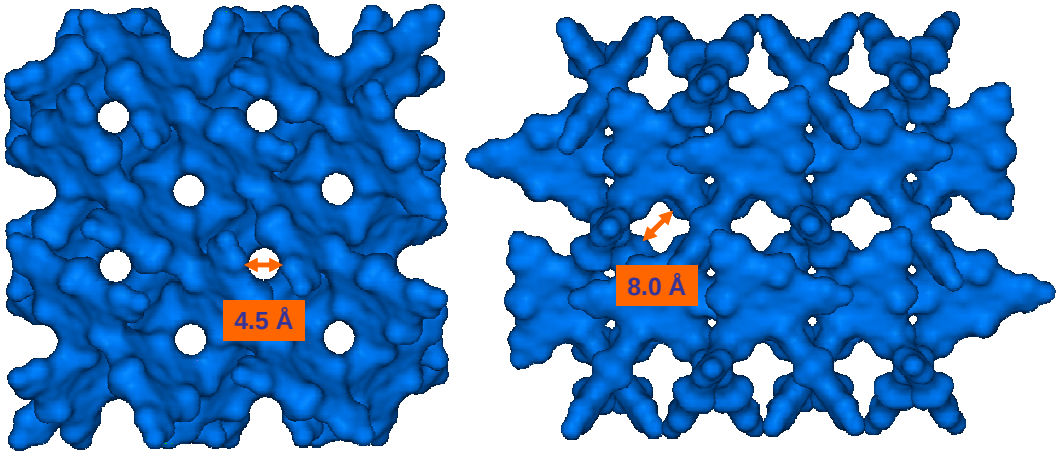

Figure 2.8. Solvent accessible surface view along the crystallographic [100] and [111] directions for the $NH_4@Cu_3(OH)L1_3$ framework.

Stability tests

Keeping in mind the extraordinary thermal and chemical stability of zeolite materials and the relevance of these properties for any practical application, we performed a series of chemical, mechanical and thermal essays in order to establish the robustness of $NH_4@Cu_3(OH)L1_3$ material. We have already mentioned (and will prove along this thesis), that the robustness of the metal-nitrogen(heterocycle) coordinative bond originates MOF materials with enhanced chemical and thermal stabilities. Therefore, in order to test the chemical stability of $NH_4@Cu_3(OH)L1_3$ material, 100 mg of this species were soaked in the applicable test solution then removed, filtered, dried at room temperature and checked by X-ray powder diffraction analysis. As it can be appreciated in Figure 2.9, this system remains unaltered in boiling organic solvents (methanol, benzene, cyclohexane), in aqueous solution (up to 80 ºC, for 4 h) and at room temperature in dilute acidic (0.001 M HNO_3, for 4 h) or basic (0.001 M NaOH, for 4 h) aqueous solutions.

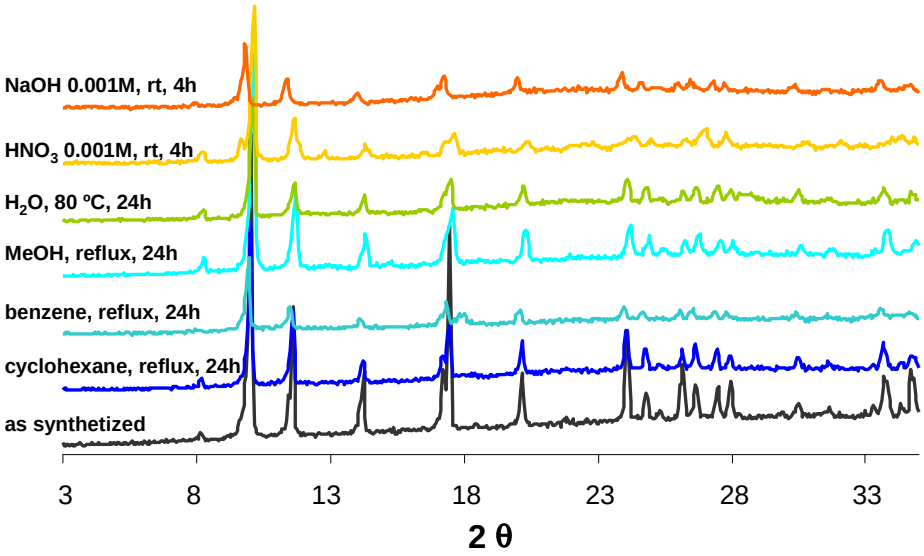

Figure 2.9. XRPD for $NH_4@Cu_3(OH)L1_3$ after different chemical stability tests.

Moreover, the thermal analysis of $NH_4@Cu_3(OH)L1_3$ material (TGA, DSC and TXRPD) is indicative of its sequential dehydration in the 40-135 ºC range (-8 H_2O) and 150-180 ºC (-1 H_2O) with the framework remaining stable, in air, up to 280 ºC (see Figure 2.10).

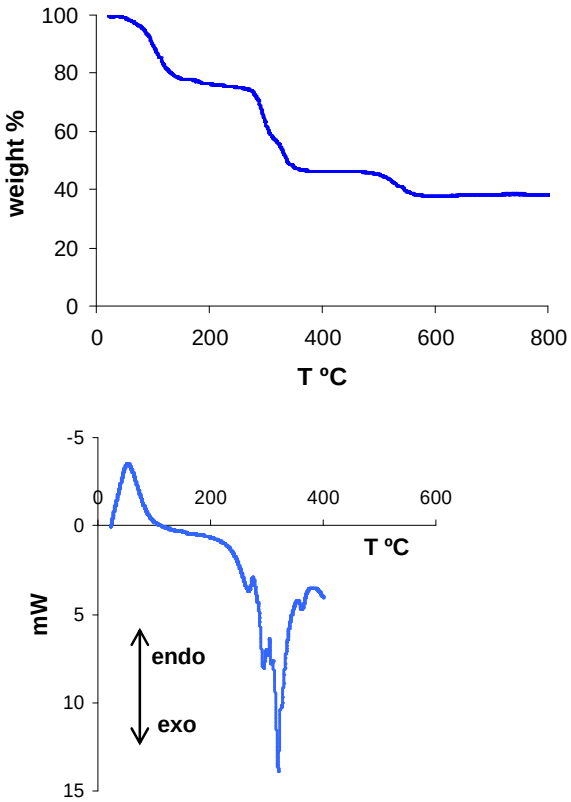

Figure 2.10. TG (above) and DSC (below) traces for $NH_4@Cu_3(OH)L1_3$ material.

The variable temperature XRPD studies (Figure 2.11) show that the framework does not undergo significant stress during heating with a $\delta \ln V/\delta T$ value of -4.8 10^{-5} K^{-1}, which suggests just a slight cell contraction concomitant to the dehydration process. Noteworthy, the dehydration process is also accompanied by the occurrence of new reflexions, above 90 ºC, indicative of a new born phase (probably a superlattice). This process is not swiftly reversed upon lowering the temperature during the experiment period, but the original hydrated material is recovered in few hours, after exposition of the solid to open air, at room temperature.

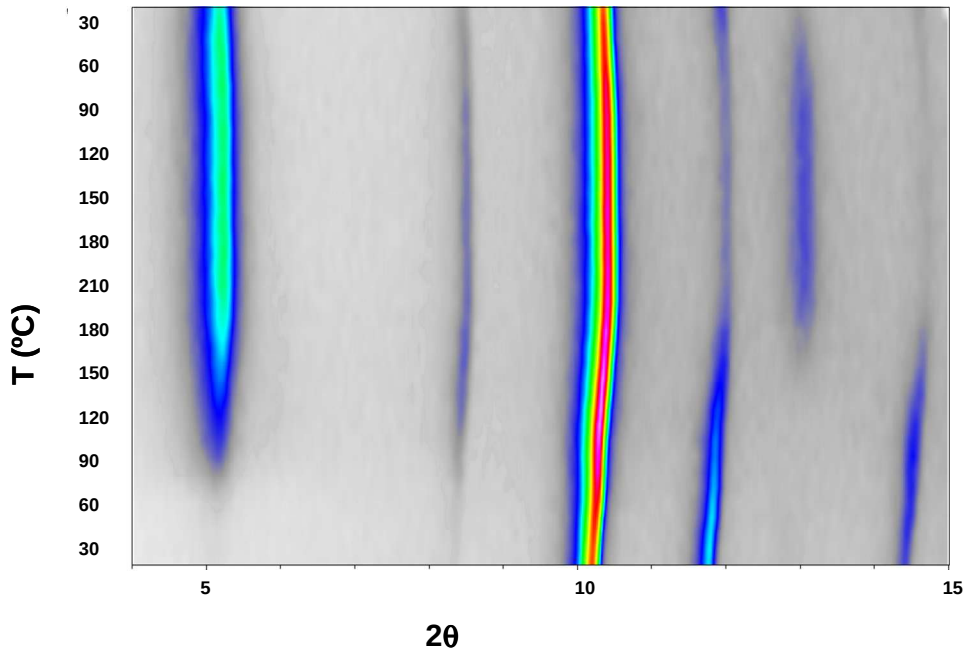

Figure 2.11. Thermal X-ray powder diffractogram for $NH_4@Cu_3(OH)L1_3$ in the 2θ range: 4-15 º.

Finally, mechanical stress tests have been performed on $NH_4@Cu_3(OH)L1_3$ material, by applying pressure of 4 tonns. As can bee seen in Figure 2.12, despite the maintenance of the sample's cristallinty, the adsorption properties are markedly affected when the material is compressed up to such high pressures, since the N_2 adsorption capacity of the original material is havened. Tanking into account these results, it is evident that, for chromatographic experiments, $NH_4@Cu_3(OH)L1_3$ compound cannot be compressed at high pressures (> 1 ton) and therefore it will be treated at pressures lower than 1 ton to give a reasonable particle size, necessary to prevent any pressure drop in the column.

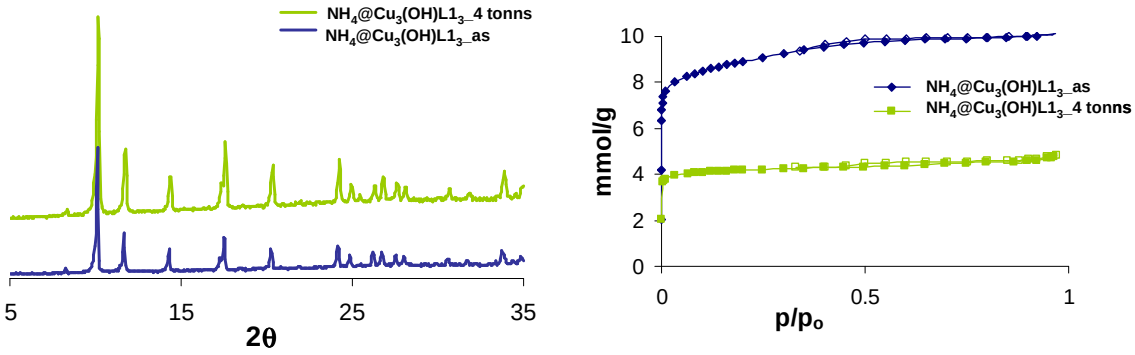

Figure 2.12. (Left) XRPD data and (right) N_2 adsorption isotherms for $NH_4@Cu_3(OH)L1_3$ before and after mechanical stress tests. Empty symbols denote desorption.

Magnetic properties

The thermal dependence of magnetic susceptibility for $NH_4@Cu_3(OH)L1_3$ is shown in Figure 2.13. Taking into account the connectivity of $NH_4@Cu_3(OH)L1_3$ network, its magnetic behaviour is expected to be dominated by the $Cu_3(OH)L1_3$ trinuclear core with an additional weak contribution by the connecting carboxilate bridges. Indeed, experimental results show that the magnetic behaviour is in agreement with the one previously reported for other compounds with similar $[Cu^{II}(OH)(\mu\text{-pz})]_3$ cores,[23] with the magnetic susceptibility (χ_M) increasing and the $\chi_M T$ values decreasing upon cooling in the high temperature region.

It can also be appreciated that upon temperature lowering, that the effective magnetic moment per formula unit slightly decreases until 70 K and lies around μ_{eff} = 1.80 BM which is very close to the spin only value of a single Cu^{II} metal centre. This is an indication of the strong antiferromagnetic exchange taking place inside the trinuclear core in which two of the three spins are cancelled. On further cooling, a local maximum on the μ_{eff} vs T curve is identified at 50 K, while below 30 K a pronounced drop of the effective magnetic moment takes place. This drop below the value expected for one unpaired electron suggests that additional weaker antiferromagnetic interactions are operative. On the basis of the three-dimensional structure of this material, we can suppose that inter-trimer interactions are involved in this low temperature magnetic ordering. Unlike the isolated Cu_3 clusters reported in reference 23, we deal here with an extended 3D network where each Cu_3 trimer is linked to six others by means of L1

ligands. Hence L1 linkers could be considered as carriers of the magnetic interaction within the material at extremely low temperatures.

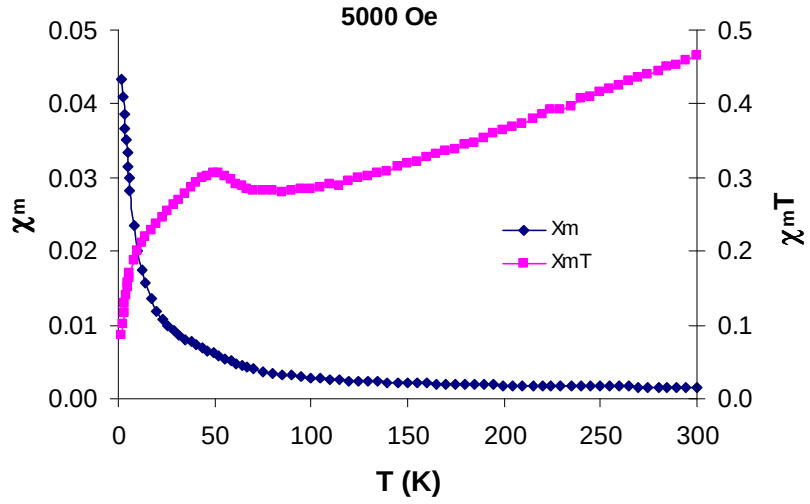

Figure 2.13. Plots of χ_m and χ_mT *vs* T for $NH_4@Cu_3(OH)L1_3$ in the range 2–300 K at 5 kOe.

On the other hand, the local maximum in the magnetic susceptibility of $NH_4@Cu_3(OH)L1_3$, at about 50 K, is probably caused by some minor structural change of the complex, such as twisting of the $[Cu^{II}(OH)(\mu\text{-pz})]_3$ metallacycle, or freezing of the dynamic Jahn-Teller distortion. It should be recognized that the 3D arrangement of the Cu_3 trimers really complicates the magnetic behaviour of the material, especially at low temperatures. Therefore, a complete understanding of the magnetic properties in $NH_4@Cu_3(OH)L1_3$ proves to be much more difficult than it would be for isolated Cu_3 clusters.

Cation exchange

Inspired by the anion exchange processes taking place in zeolite materials (widely studied over the time [24, 25]), we have examined the exchangeable nature of the extraframework NH_4^+ cations in $NH_4@Cu_3(OH)L1_3$, as a way to modulate the porous structure of this material. Indeed, the suspension of $NH_4@Cu_3(OH)L1_3$ in 0.1-0.5 M aqueous solutions of ANO_3 salts ($A = Li^+$, Na^+, K^+, $Ca^{2+}/2$, $La^{3+}/3$) or 0.5 M methanolic solutions of organic amines (Me_3N, Et_3N) gives rise to the exchanged $A_x(NH_4)_{1-x}[Cu_3(\mu_3\text{-}OH)(\mu_3\text{-}L1)_3]$ ($A@Cu_3(OH)L1_3$) systems, which show unaltered XRPD patterns according to the maintenance of the original topology (see Figure 2.15).

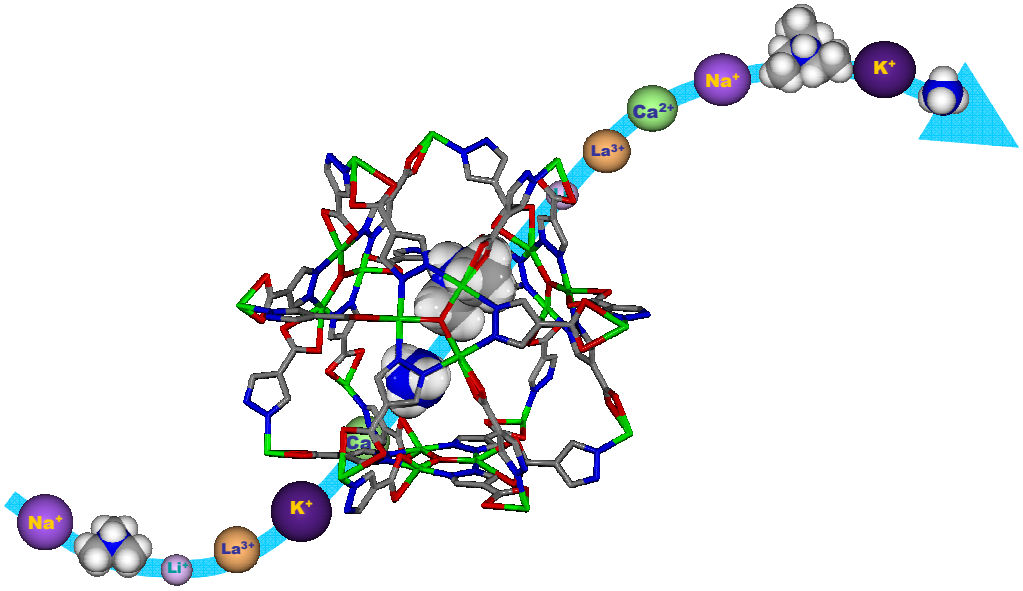

Figure 2.14. Graphical summary of the cation exchange processes taking place in $NH_4@Cu_3(OH)L1_3$ material.

Moreover, the effectiveness of ion exchange on $A@Cu_3(OH)L1_3$ with triethyl ammonium cations, was examined by IR spectroscopy (Figure 2.16). Unfortunately, the signals of the organic amine are just visible as weak bands in the exchanged framework due to the presence of large amount of solvent molecules that overshadow the high energy region of the spectra.

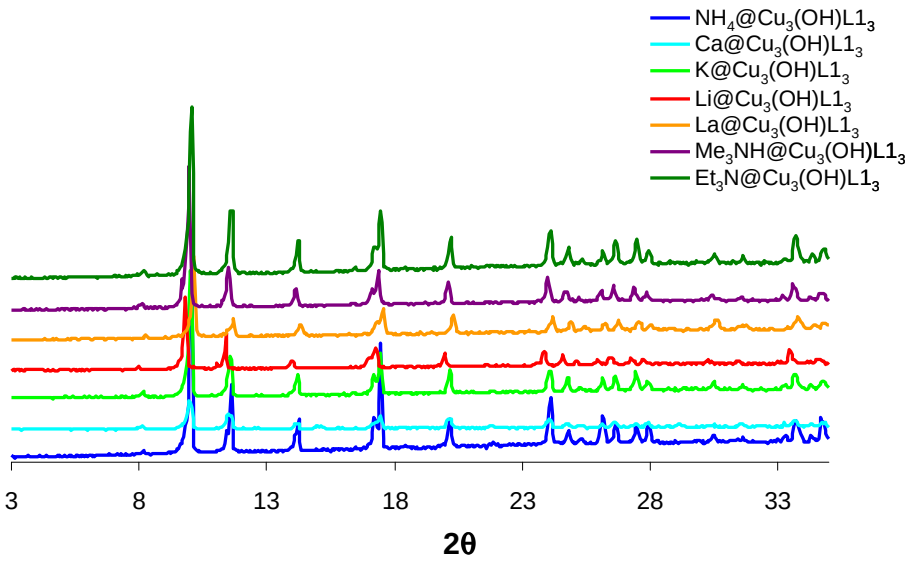

Figure 2.15. XRPD for the exchanged $A@Cu_3(OH)L1_3$ materials.

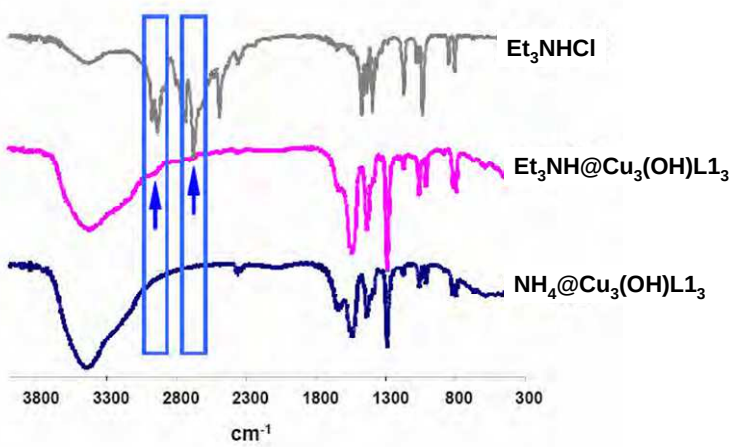

Figure 2.16. Comparison of IR spectra of as-synthesized $NH_4@Cu_3(OH)L1_3$, $Et_3NH@Cu_3(OH)L1_3$ and Et_3NHCl. The broad band around 3000 cm^{-1} is attributed to the water molecules into framework's pores.

The exact values of *x*, indicating the extent of cation exchange, have been determined by atomic absorption measurements (for A = Li^+, K^+, Na^+, $Ca^{2+}/2$) or by elemental analysis (for A = Et_3NH^+, Me_3NH^+). The results provide values $x \geq 0.5$ values, indicating that monovalent cations give rise to exchange of 50 % NH_4^+ cations only, affording materials of $A_{0.5}(NH_4)_{0.5}[Cu_3(OH)(L1)_3]$ (A = Et_3NH^+, Me_3NH^+, Li^+, Na^+, K^+) formulation, which means that only one of the two NH_4^+ ions per cavity is exchanged.

Noteworthy, in the case of ions with higher charge (i.e. Ca^{2+}), complete ion exchange takes place. It should be noted that in the case of $Me_3NH@Cu_3(OH)L1_3$ and $Et_3NH@Cu_3(OH)L1_3$ materials a slight contamination with $Cu(OH)_2$ is detected in the elemental analysis but not in the XRPD. These results are in agreement with the zeolite ion exchange behaviour.[26]

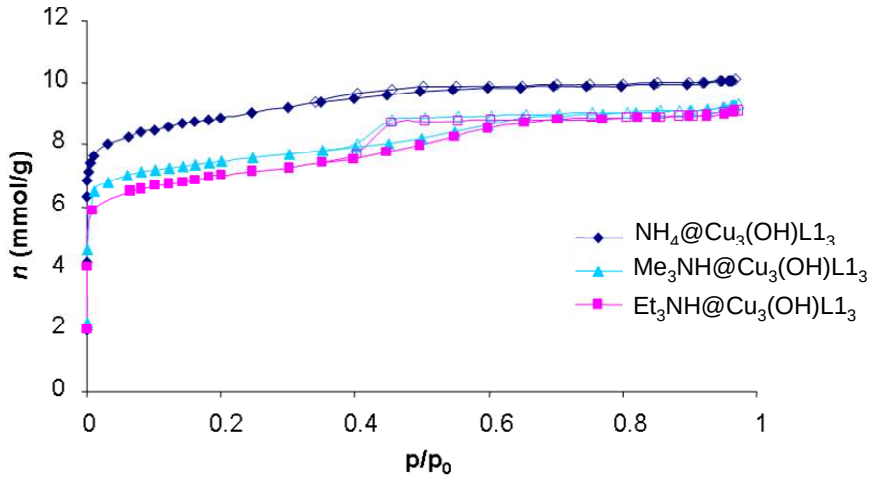

Figure 2.17. Cation exchange modulation of the porous network in $A@Cu_3(OH)L1_3$ systems (A = NH_4^+, Me_3NH^+, Et_3NH^+) as shown by N_2 adsorption isotherms at 77 K. $NH_4@Cu_3(OH)L1_3$ (blue diamonds),

$Me_3NH@Cu_3(OH)L1_3$ (light blue triangles), $Et_3NH@Cu_3(OH)L1_3$ (pink squares). Open symbols denote desorption.

After these preliminary results on the ion exchange equilibria, we decided to focus on the original material (A = NH_4^+) and on the amine (A = Me_3NH^+ and Et_3NH^+) exchanged ones, with the aim of having an insight on the modulation of the framework properties upon variation of the guests' size. N_2 adsorption measurements performed on the exchanged systems show profound changes in the adsorption isotherms which are indicative of the actual modulation of the porosity of $R_3NH@Cu_3(OH)L1_3$ framework (Figure 2.17). Indeed, on passing from NH_4^+ to Et_3NH^+ a lowering of the adsorption capacity and pore surface is appreciated (BET surface of 680 $m^2\ g^{-1}$ for $NH_4@Cu_3(OH)L1_3$ diminishes to 505 and 510 $m^2\ g^{-1}$ for $Me_3NH@Cu_3(OH)L1_3$ and $Et_3NH@Cu_3(OH)L1_3$, respectively). This result agrees with a reduction of the accessible pore volume as a consequence of the bulkier nature of R_3NH^+ cations (R = Me, Et) compared to NH_4^+.

Gas and vapours separation experiments

We have also examined the effect of ion exchange processes on the separation selectivity by adsorption of gases of environmental and industrial interest (N_2, CH_4, CO_2, C_2H_2) and harmful vapours (benzene, cyclohexane). The interest in finding alternative methods for the efficient separation of CO_2/C_2H_2 as well as benzene/cyclohexane mixtures lies in the similarity of their physical properties (such as size, polarity or boiling point).[27]

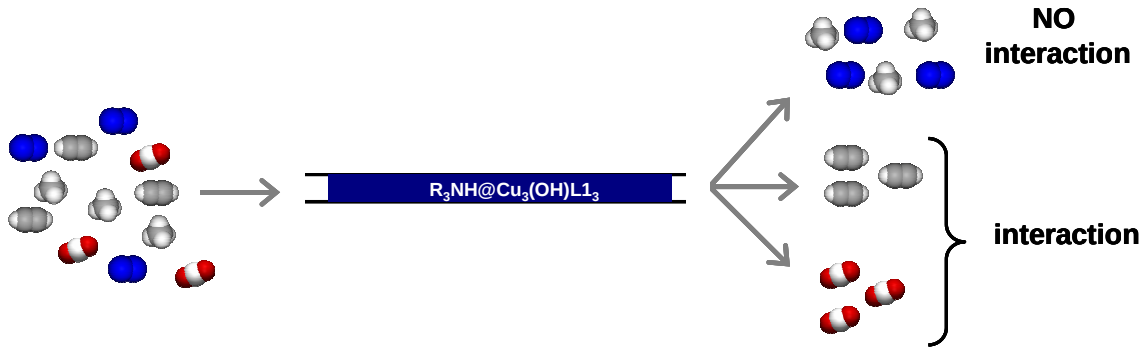

Figure 2.18. Graphical summary of the pulse gas chromatography experiments.

Variable temperature pulse gas chromatography experiments (graphically summarized in Figure 2.18) have been carried out in the 273-363 K temperature range

with a complex gas mixture (N_2, CH_4, CO_2, C_2H_2) in order to examine the possible utility of these systems for gas separation purposes. Actually, there is a growing interest in the development of adsorbents capable to store and purify acetylene, due to the explosive character of this gas and its wide use/production in industrial processes. Its singular hazard is associated with its intrinsic instability, especially when it is pressurized, so MOF materials have been demonstrated to be good candidates for its storage under relatively safe conditions.[28] Nevertheless, very few metal organic frameworks have demonstrated selectivity for the adsorption of this gas over carbon dioxide, although there is a great industrial interest in their separation.[29]

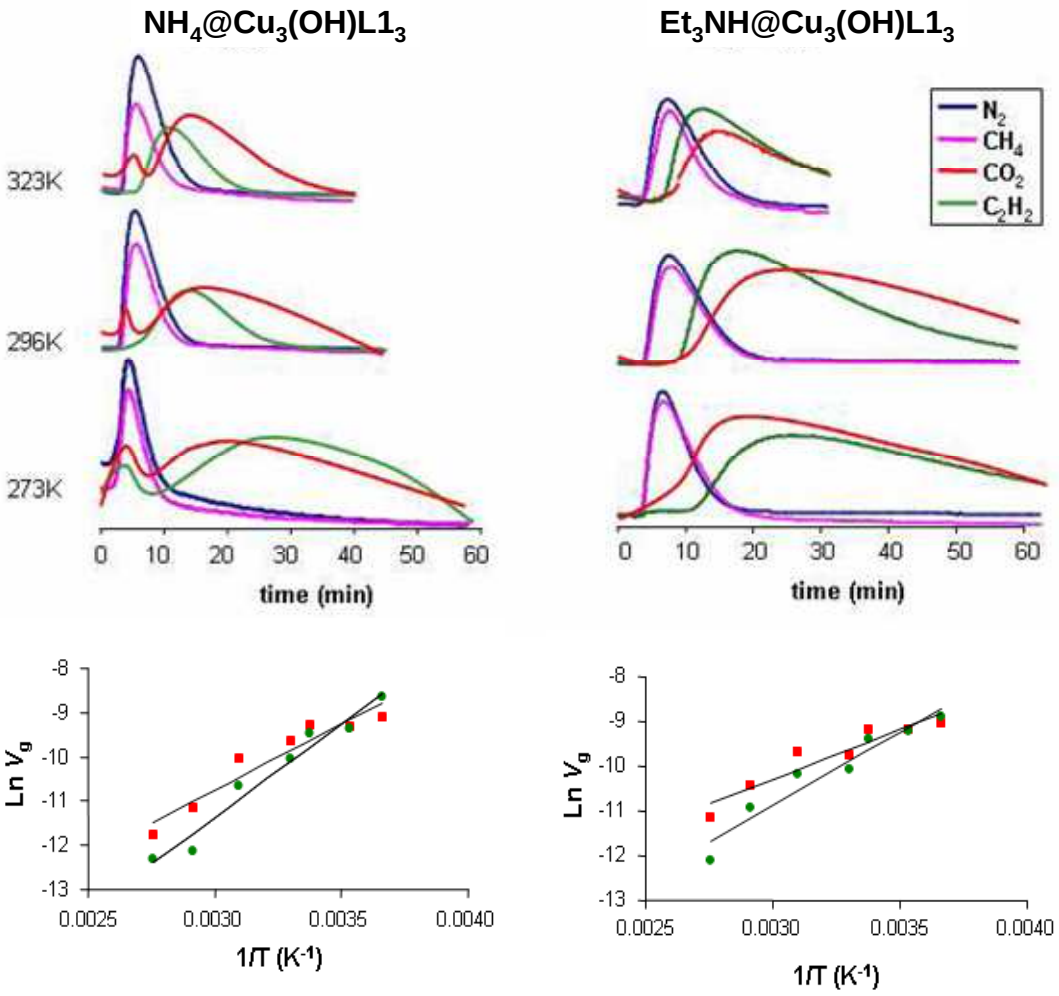

Figure 2.19. (Above) Variable temperature pulse gas chromatography experiments of an equimolecular N_2, CH_4, CO_2, C_2H_2 gas mixture passed through a chromatographic column packed with $NH_4@Cu_3(OH)L1_3$ (left) and $Et_3NH@Cu_3(OH)L1_3$ (right) using a He flow of 10 mL min^{-1}. (Below) Variation of CO_2 (red squares) and C_2H_2 (green circles) retention volumes V_g (m^3 g^{-1}) for $NH_4@Cu_3(OH)L1_3$ (left) and $Et_3NH@Cu_3(OH)L1_3$ (right) as a function of adsorption temperature (273-363 K).

To prove the suitability of this material for gas separation purposes we have employed an equimolecular gas mixture of C_2H_2, N_2, CH_4, CO_2 gases which has been injected at 1 bar on a home made chromatographic column (previously activated at 110 ºC under high vacuum) at different temperatures (273-363 K) and the separation performance has been examined by means of a mass spectrometer gas analysis system. The results (Figure 2.19) show that $A@Cu_3(OH)L1_3$ ($A = NH_4^+$, Et_3NH^+) frameworks allow for significant interactions with acetylene and carbon dioxide, whereas the interactions with dinitrogen and methane are negligible. Noteworthy, at low temperatures ($T < 286$ K), acetylene is more tightly retained by $A@Cu_3(OH)L1_3$ frameworks than carbon dioxide while at higher temperatures ($T > 286$ K) the reverse situation is found, with C_2H_2 being eluted before than CO_2. This kind of behaviour is unique in MOF materials, but is a simple consequence of the different temperature dependence for the interaction with the framework of CO_2 and C_2H_2 gases: acetylene retention is much more affected by temperature changes than the retention of carbon dioxide is.

This temperature dependent behaviour can be easily visualized in ln*V*g (m^3 g^{-1}, retention volume) vs 1/T graphs showing the intersection of the CO_2 and C_2H_2 tendency lines about 286 K, a temperature at which CO_2/C_2H_2 separation become ineffective. The zero coverage adsorption heats (ΔH_{ads}) for CO_2 and C_2H_2 have been calculated from the slope of the plots of lnV_g vs 1/T (Figure 2.19) according to $\Delta H_{ads} = -R\delta(\ln V_g)/\delta(1/T)$[30] and the results are summarised in Table 2.1. These ΔH_{ads} values are similar to the ones reported by Kitagawa and others on MOFs with narrow basic pores, obtained from monocomponent adsorption isotherms, applying the Clausius-Clapeyron equation.[31] In this regard, these authors indicated the possible utility of this type of microporous networks for the separation of C_2H_2/CO_2 mixtures but no experiments with a bicomponent mixture were performed to demonstrate it. Consequently, to the best of our knowledge, we have assessed experimentally for the first time the utility of MOFs for this difficult separation process, highlighting the importance of the adsorption temperature on the efficiency of the separation (see above).

As a matter of fact, the discrimination of $R_3NH@Cu_3(OH)L1_3$ systems towards $C_2H_2/CO_2/CH_4$ mixture might be of interest for acetylene purification obtained from partial burning of methane and oxygen. The efficiency of the separation is probably a consequence of a good balance of polarity gradients of the ionic structure, basic sites

(carboxylates), coordination unsaturated metal ions, H-bonding and size of the cavities.[27] In this regard, the separation coefficients (*K*r) calculated for a binary mixture according to ln*K*r = ($\Delta Hads_1 - \Delta Hads_2$)/(*R*T)[32] are large enough to ensure the separation of C_2H_2/CO_2 (Table 2.1). Moreover, in the case of C_2H_2/CH_4 or CO_2/CH_4 mixtures, the separation coefficients are expected to be nearly infinite, because methane is not retained by the framework.

Table 2.1. Calculated adsorption heats ΔH_{ads}, Henry constants K_H and partition coefficients K_r for CO_2 and C_2H_2 from variable temperature zero coverage gas chromatography experiments on $NH_4@Cu_3(OH)L1_3$ and $Et_3NH@Cu_3(OH)L1_3$ materials.

	$NH_4@Cu_3(OH)L1_3$	**$Et_3NH@Cu_3(OH)L1_3$**
$-\Delta H_{ads}$ C_2H_2 (kJ mol^{-1})	34.9	27.3
$-\Delta H_{ads}$ CO_2 (kJ mol^{-1})	24.7	18.4
K_H C_2H_2 (cm^3 m^{-2}) [a]	0.358	0.325
K_H CO_2 (cm^3 m^{-2})[a]	0.225	0.280
lnK_r [a]	4.51	3.92

[a] calculated values at 273K.

We are also aware of the great importance of the separation of CO_2 and CH_4 mixtures since the natural gas stream contains 5 % carbon dioxide impurity averagely[33] and this impurity strongly reduce the efficiency of the burning process. So, a system that shows high selectivity for CO_2 over CH_4, would allow the purification of natural gas: methane will not be retained while carbon dioxide will be and thereby the outgoing stream will contain only pure methane.

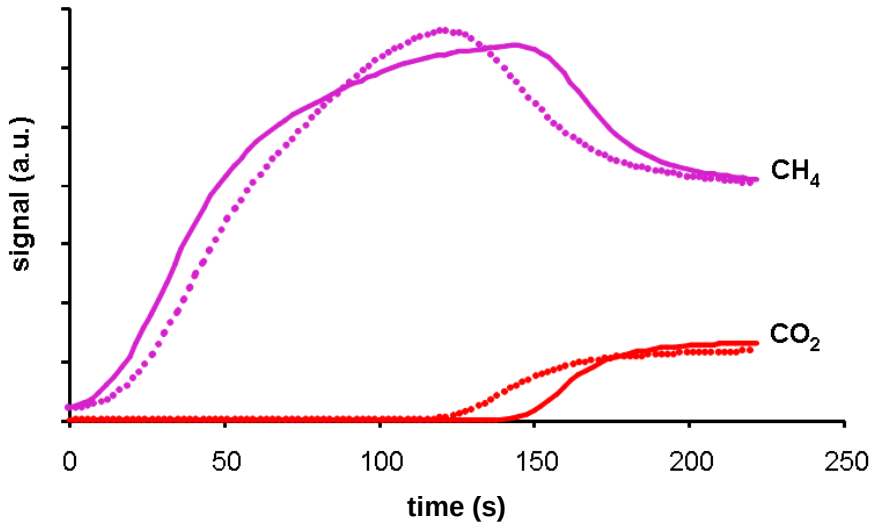

Figure 2.20. Breakthrough curves for the separation of a 0.27:0.67 (v/v) 10 mL min^{-1} flow of CO_2/CH_4 mixture at 273 K by $NH_4@Cu_3(OH)L1_3$ (solid lines) and $Et_3NH@Cu_3(OH)L1_3$ (dotted lines).

Therefore, we measured breakthrough curves of a 0.27:0.73 (v/v) mixture of CO_2/CH_4 flowing through chromatographic columns packed with $NH_4@Cu_3(OH)L1_3$ and $Et_3NH@Cu_3(OH)L1_3$ at 273 K. As wished for a material suitable for the purification of methane gas, we reveal the passage of CH_4 through this material and the selective retention of CO_2 (Figure 2.20). The breakthrough takes place *ca.* 150 s after dosing the gas mixture, which represents 0.42 mmol of CO_2 being retained per gram of $NH_4@Cu_3(OH)L1_3$ under these dynamic conditions. This kind of behavior was expected in view of the differentiated interactions of these two gases with the $NH_4@Cu_3(OH)L1_3$ framework, as we pointed out with pulse gas chromatography experiments. When we performed a similar measurement with $Et_3NH@Cu_3(OH)L1_3$ we observed a related behavior with the breakthrough taking place after *ca.* 125 s and the CO_2 removal capacity being diminished down to 0.30 mmol g^{-1}, in agreement with the lower surface area of this material compared to $NH_4@Cu_3(OH)L1_3$ one.

Another challenging mixture to be separated is benzene/cyclohexane, since the similarity in their boiling points (80.1 ºC for benzene and 80.7 ºC for cyclohexane) makes their separation by distillation inefficient. Therefore, an attractive option would be their separation by shape/size selective adsorption since the molecular geometry (benzene, 3.3 x 6.6 x 7.3 $Å^3$; cyclohexane, 5.0 x 6.6 x 7.2 $Å^3$)[34] permits to differentiate them. Indeed, exposition of $A@Cu_3(OH)L1_3$ materials to a saturated atmosphere of a 1:1 benzene/cyclohexane mixture in a Schlenk tube during 24 h at 25 ºC shows a significant enrichment of the adsorbate phase in the benzene component. The exact amount of the adsorbed vapours has been quantified by both careful measurement of the increase in weight and by ^1H NMR measurement of the adsorbed phase composition (Figure 2.21).

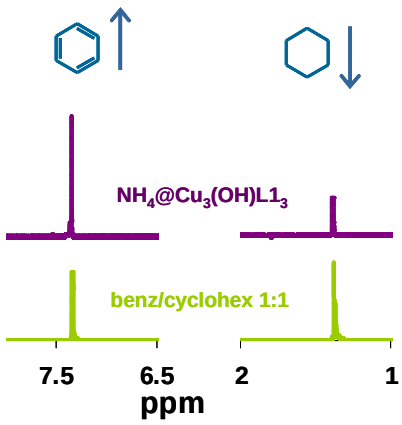

Figura 2.21. ^{1}H NMR of the original benzene/cyclohexane 1:1 mixture and after adsorption by $NH_4@Cu_3(OH)L1_3$ material.

In the case of the original $NH_4@Cu_3(OH)L1_3$ material, the composition of the adsorbed benzene:cyclohexane phase reaches 5:1 ratio actually showing a stronger interaction of the framework with benzene compared to its saturated form. This is further substantiated in the case of $Me_3NH@Cu_3(OH)L1_3$ and $Li@Cu_3(OH)L1_3$ materials with benzene:cyclohexane ratios reaching 10:1 and 12:1 values, respectively (see Table 2.2).

Table 2.2. Adsorption selectivity of $A@Cu_3(OH)L1_3$ towards a 1:1 benzene:cyclohexane mixture at 25 ºC.

	benzene/cyclohexane
$Li@Cu_3(OH)L1_3$	11.8
$Et_3NH@Cu_3(OH)L1_3$	9.5
$Me_3NH@Cu_3(OH)L1_3$	10.5
$Ca@Cu_3(OH)L1_3$	7.4
$K@Cu_3(OH)L1_3$	6.1
$La@Cu_3(OH)L1_3$	7.4
$NH_4@Cu_3(OH)L1_3$	4.9

Catalytic experiments

As already mentioned in the introduction of this chapter, zeolites are widely used in industries as catalysts, so we considered $NH_4@Cu_3(OH)L1_3$ material which is built of redox active Cu(II) metal ions as a possible heterogeneous catalyst in the oxidation of simple organic molecules. Indeed, industrial oxidation or oxygenation reactions typically require very high turn-over numbers and frequencies, which have not been achieved to date by current MOF catalysts.

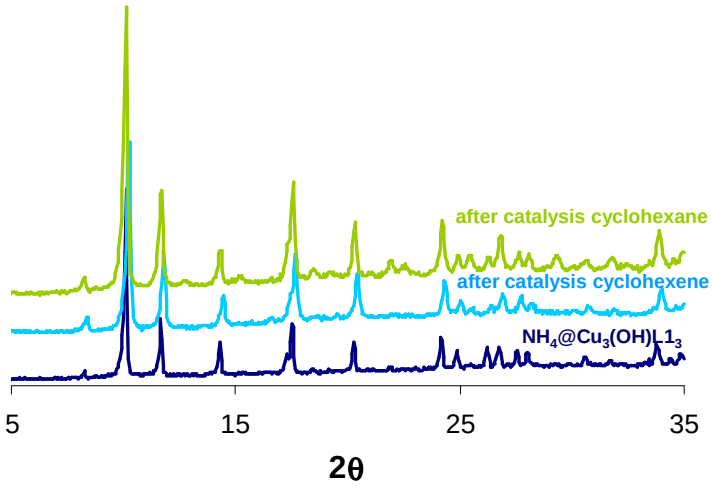

Figure 2.22 XRPD spectra of $NH_4@Cu_3(OH)L1_3$ before and after catalytic oxidation of cyclohexene (light blue line) and cyclohexane (green line).

Hence, considering the ability of this framework to incorporate cyclohexane vapours, we choose this molecule as well as cyclohexene as substrates for the evaluation of catalytic activity of $NH_4@Cu_3(OH)L1_3$.[35] The evolution of the reactions has been followed by ^1H NMR on fixed aliquots of the reaction mixture.

The results show that $NH_4@Cu_3(OH)L1_3$ is catalytically active in both reactions and that the catalyst can be recovered intact from the reaction vessel after the catalytic run as can be seen in XRPD spectra of the material before and after catalytic reactions (Figure 2.22). Atomic adsorption analyses of the filtrates after the catalytic tests are also indicative of no copper leaching from $NH_4@Cu_3(OH)L1_3$ with Cu^{2+} concentration being below 6×10^{-2} % of the initial amount of catalyst. The reaction of cyclohexane (16 mmol) with *t*-BuOOH (8 mmol) at 70 ºC in the presence of $NH_4@Cu_3(OH)L1_3$ gives rise to cyclohexanone as a single product with a yield of 4 % (based on the initial amount of cyclohexane) after 24 h (see Figure 2.23). Moreover, no significant diminution of activity occurs after a second run. It should also be noted that removal of the catalyst after 2 hours leads to a significant decrease of the catalytic activity similar to the behaviour of the blank reaction.

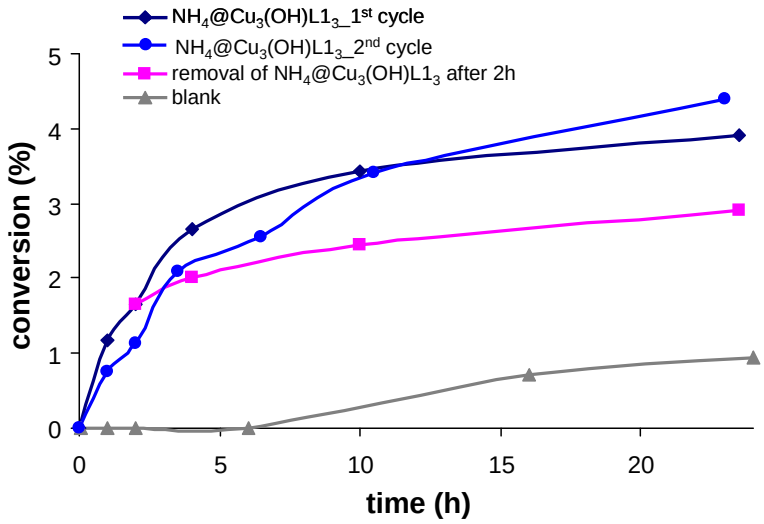

Figure 2.23. Evolution of oxidation reaction of cyclohexane to cyclohexanone catalysed by $NH_4@Cu_3(OH)L1_3$ and effect of catalyst removal after 2 hours. 1st oxidation cycle (dark blue diamonds), 2nd oxidation cycle (blue circles), removal of $NH_4@Cu_3(OH)L1_3$ after 2 h (pink squares) and blank (grey triangles).

In the case of cyclohexene oxydation under similar conditions, the results show the formation of different products, namely *tert*-butyl-2-cyclohexenyl-1-peroxide, followed by 2-cyclohexen-1-one and cyclohexene oxide and, again, no relevant diminution of the activity is detected in the second run (see Figure 2.24.a). The maximum substrate conversion achieved after 15 h was *ca.* 20 % (based on the initial amount of cyclohexene). However, it should be noted that in contrast to the previous case and to the results reported by Volkmer and co-workers,[35] we also appreciate a significant progress of the reaction in the absence of the catalyst, namely *ca.* 8 % conversion after 4 h *vs* 18 % conversion in the presence of catalyst (Figure 2.24.b).

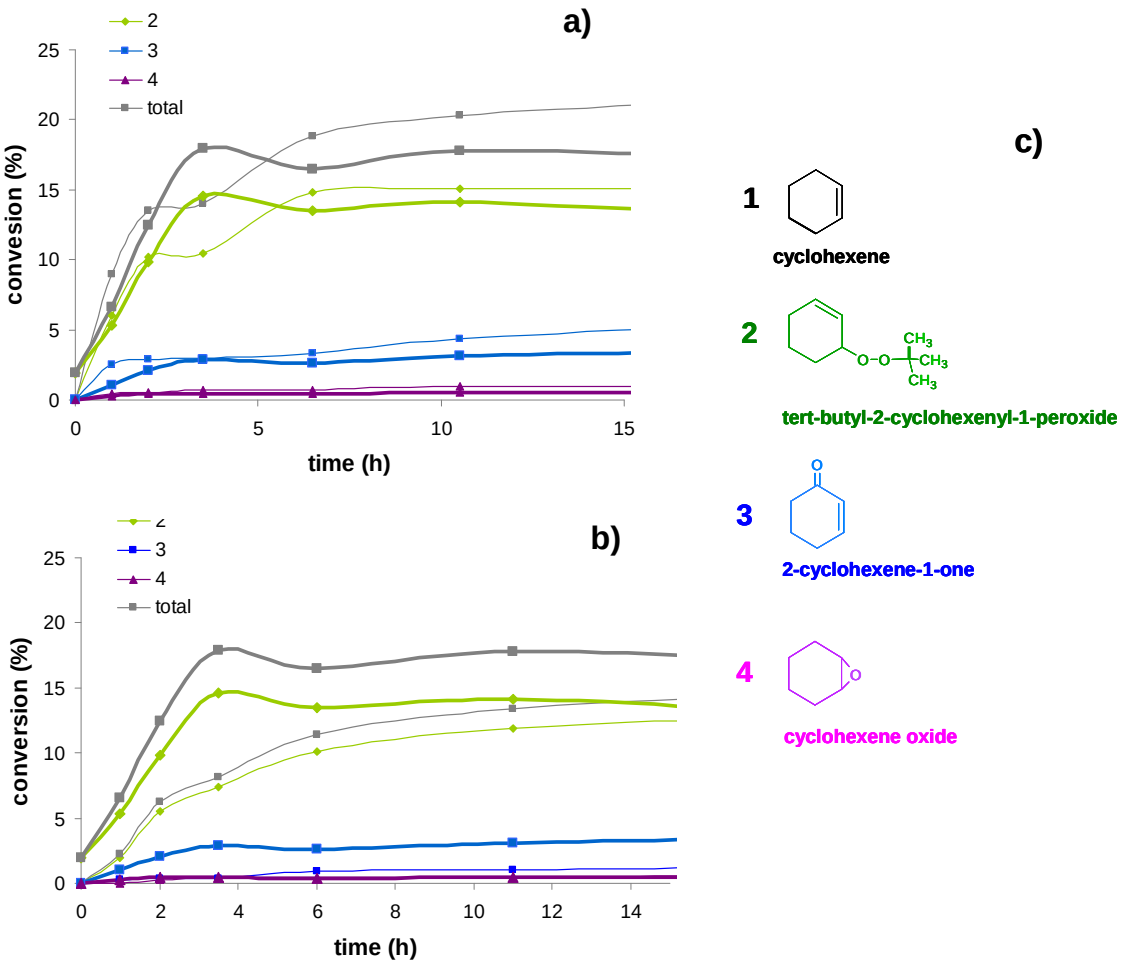

Figure 2.24. a) Progress of the oxidation reaction between cyclohexene and terbutoxyhydroxyperoxyde catalysed by $NH_4@Cu_3(OH)L1_3$ within two cycles. 1st catalytic cycle (thick lines), 2nd catalytic cycle (thin lines); b) progress of the oxidation reaction with (thick lines) and without (thin lines) $NH_4@Cu_3(OH)L1_3$; c) scheme of the different oxidation products.

2.2.2. CdL1 compound

Crystal structure

As mentioned above, the slow evaporation of both the base (NH_3) and the solvent (H_2O) in the reaction of equimolar amount of $Cd(NO)_3 \cdot (H_2O)_4$ and H_2L1 ligand, leads to the recover of colourless block crystals of formulation $[Cd(H_2O)_2L1] \cdot H_2O$ (CdL1) whose size is suitable for Single Crystal X-ray diffraction measurement (Figure 2.25).

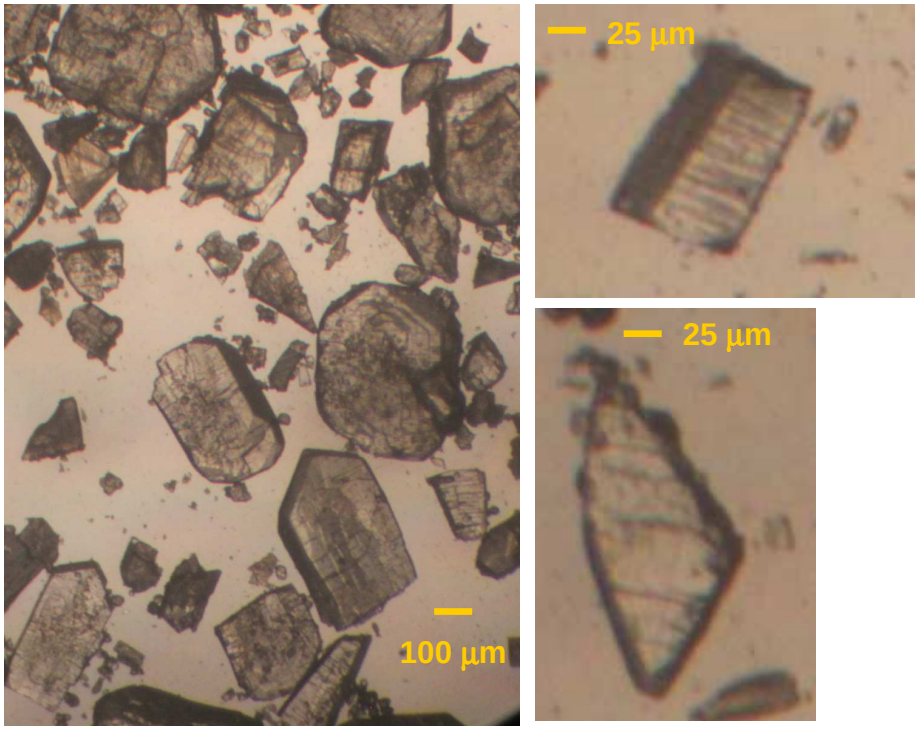

Figure 2.25. Single crystals of CdL1 material.

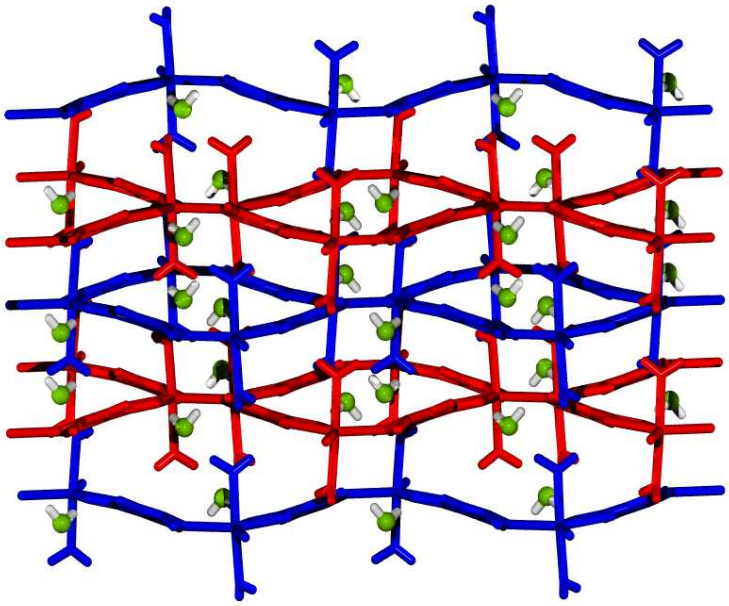

Figure 2.26. View of the layered structure in CdL1 material with included water molecules (green).

CdL1 crystallizes in the $P2_1/c$ space group with cell parameters a = 7.9120(16) Å, b = 14.055(3) Å, c = 8.1020(16) Å, $\alpha = \gamma = 90^{o}$ and β = 114.08(3)^{o}, resulting in a cell volume V = 822.544 Å^3. It is a two-dimensional (2D) layered structure with free water molecules mainly located in the space between the planes. The distance between two consecutives planes is 4.05 Å and the same arrangement is repeated every other plane (Figure 2.26). Each layer is independent and no coordinative bonds can be found between the planes as can be seen in Figure 2.27.

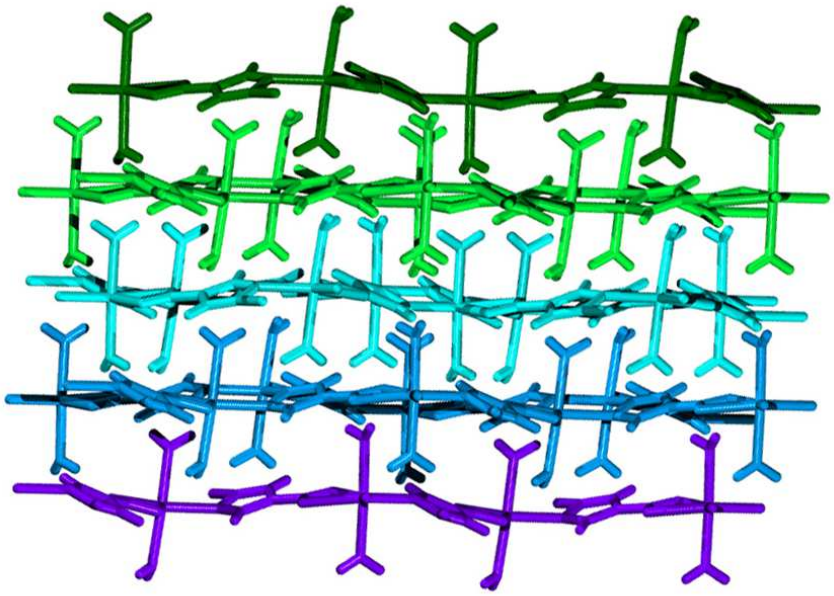

Figure 2.27. View of the 2D layered structure in CdL1 material. Each plane is represented in different colour to evidence the absence of coordinative bonds between consecutive planes.

The planes lye parallel to each other and every layer is formed by a square grid whose nodes are occupied by a cadmium dimeric unit (see Figure 2.28-left). Each pair of nodes is connected by one L1 ligand. The CdN_2O_4 coordination polyhedron exhibits a distorted octahedral geometry. The axial positions are occupied by two N donor atoms from two different pyrazolate moieties (hence doubly bridging the Cd_2 dimeric unit) (Cd-N = 2.252-2.244 Å), and two O donor atoms form a carboxylate group acting in a bidentate coordination mode (Cd-O = 2.382-2.415 Å). The two apical positions are occupied by two water molecules, directly coordinated to the cadmium atoms (Cd-O = 2.335-2.306 Å) (see Figure 2.28-right). Each ligand thus coordinates three Cd atoms in a O,O'endo-bidentate, N,N'exo-bidentate coordination mode.

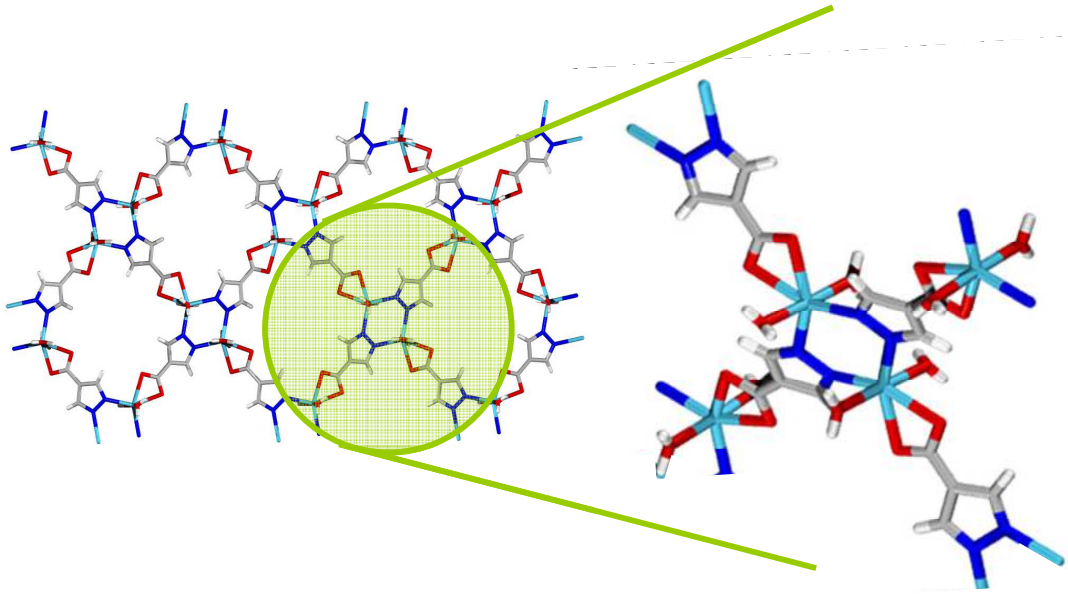

Figure 2.28. (Left) View of the layer structure in CdL1 material and (right) expansion of the Cd_2 dimeric building unit.

Interestingly, one of the two Cd atoms in the dimeric unit lies 0.752 Å above the plane formed by one coordinated pyrazolate ring and the other Cd atom of the dimer, as shown in Figure 2.29, forming a zig-zag arrangement of the pyrazole rings along the plane of each layer.

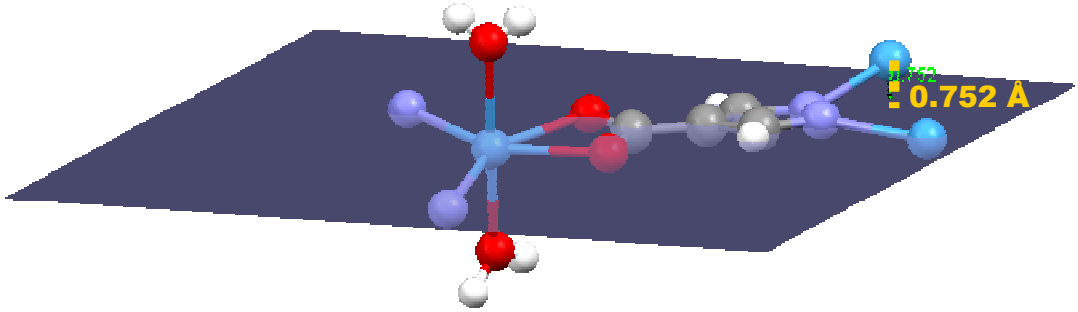

Figure 2.29. View of the distance between the plane formed by the pyrazole ring and one Cd atom, and the second Cd atom in the dimeric building unit.

The three-dimensional structure is maintained thanks to the presence of a complicate net of H-bonds between the free water molecules and either the coordinated water molecules (2.879 Å) and the O atoms of the carboxylate groups (2.651 Å), as well as between the coordinated water molecules and the carboxylate groups (2.936 Å), as shown in Figure 2.30.

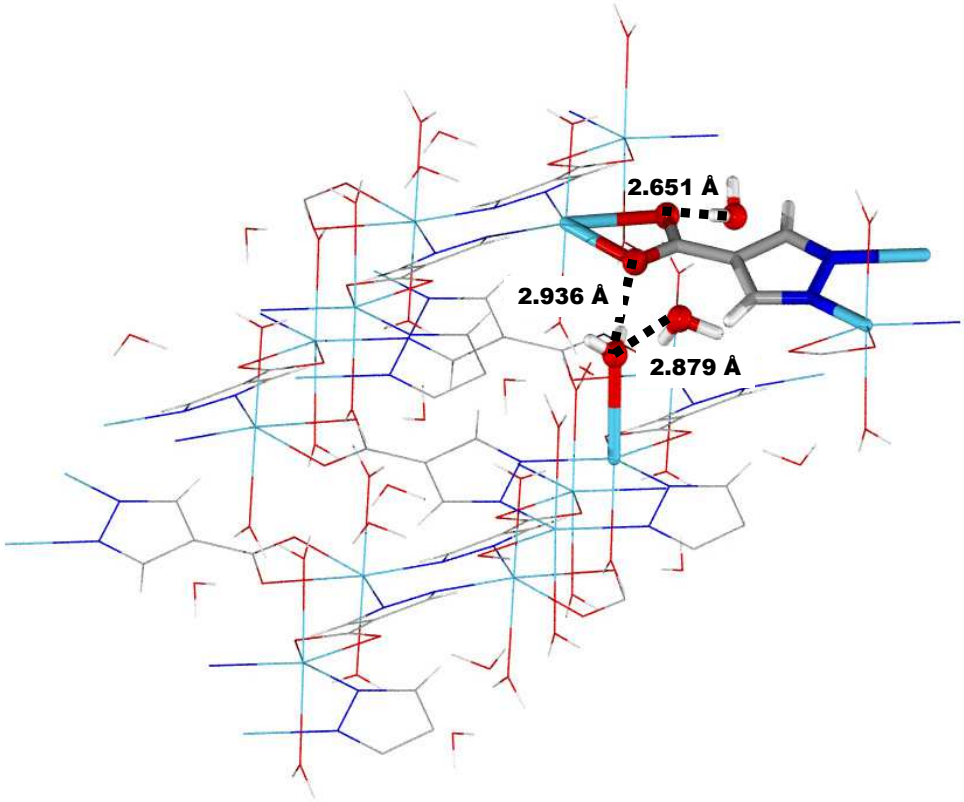

Figure 2.30. View of the H-bonds found in CdL1 structure.

Lastly we proved that the bulk solid obtained in a typical reaction has the same composition and structure found for the single crystal. As can be see in Figure 2.31,

there is a good matching between the X-ray powder diffraction patterns of the as-synthesized material (experimental) and the one calculated from single crystal diffraction data (simulated). This permits us to use the bulk solid to evaluate the thermal stability of CdL1 material.

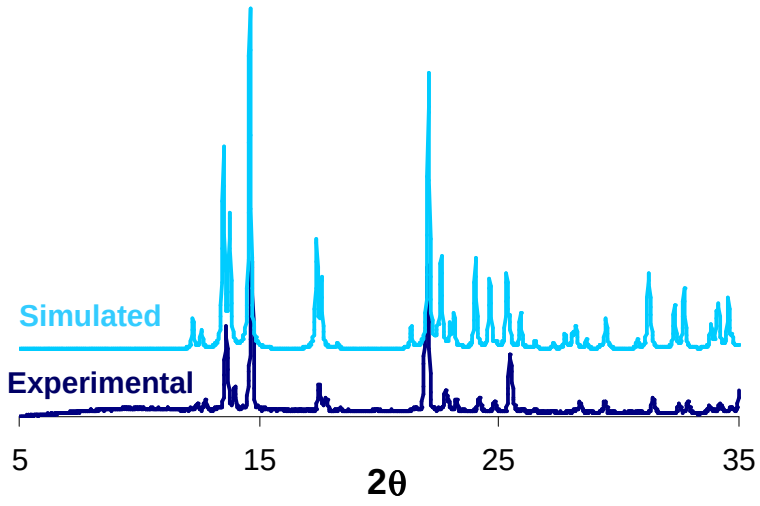

Figure 2.31. Comparison between simulated (from single crystal data) and experimental XRPD for CdL1 material.

Thermal stability

The thermal stability of CdL1 material has been evaluated by means of TG analysis (Figure 2.32). According to the crystal structure data, the weight sample undergoes two different weigth loss events at temperatures of 100 ºC and 210 ºC. The former step corresponds to the loss of 1 guest water molecule per CdL1 unit (calc: -6.5 %, exp: -8.7 %) while the latter concerns the removal of the 2 water molecules apically coordinated to each cadmium atom (calc: -13.0 %, exp: -17.4 %). The considerable difference between theory and experiment is possibly caused by a partial sublimation of the sample. The final decomposition of the material takes place at temperatures higher than 330 ºC.

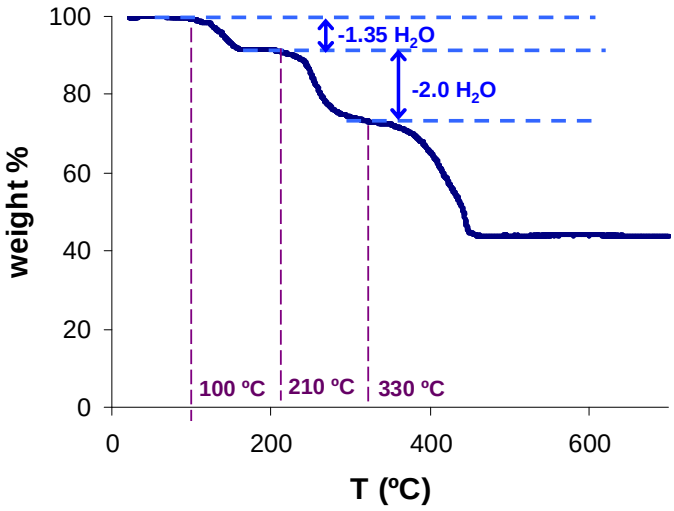

Figure 2.32. TGA trace for CdL1 material.

Unfortunately, the removal from the structure of uncoordinated guest water molecules, leads to the 3D arrangement collapse (Figure 2.33). This has been proved by checking material's cristallinty after heating CdL1 sample under N_2 atmosphere at increasing temperatures. The results show that the crystallinity of CdL1 material is no longer maintained when it is heated at 65 ºC for two hours. Indeed a clear change in the powder diffraction pattern can be seen in the step between 50 º and 65 ºC, while the almost complete lost of crystallinity takes place at temperatures above 150 ºC when (as confirmed by TGA measurements) the uncoordinated water molecules progressively leave the structure (Figure 2.34). The CdL1 original structure is not recovered by soaking the material in distilled water, after the phase transition taking place above 65 ºC. So the phase transition is irreversible and leads to a dense material.

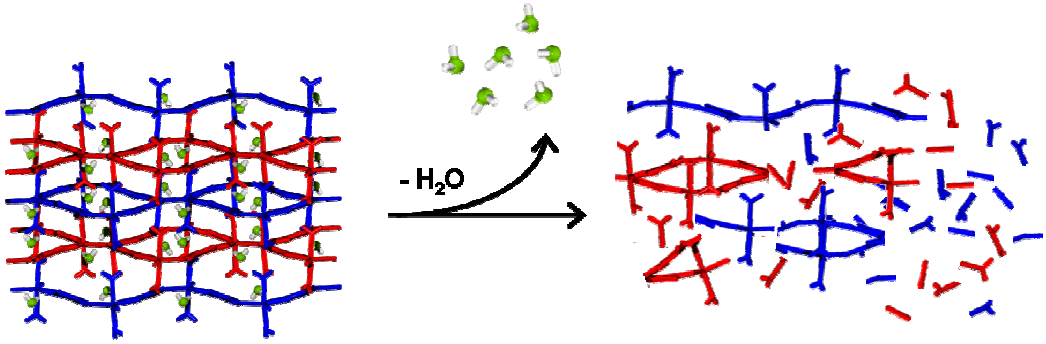

Figure 2.33. Graphical representation of the CdL1 framework collapse upon removal of uncoordinated guest water molecules.

Indeed, as a consequence of phase transition and subsequent framework degradation, the solids activated both by thermal treatment (150 ºC) under dynamic vacuum or by lyophilisation process, show no porosity towards N_2 at 77 K.

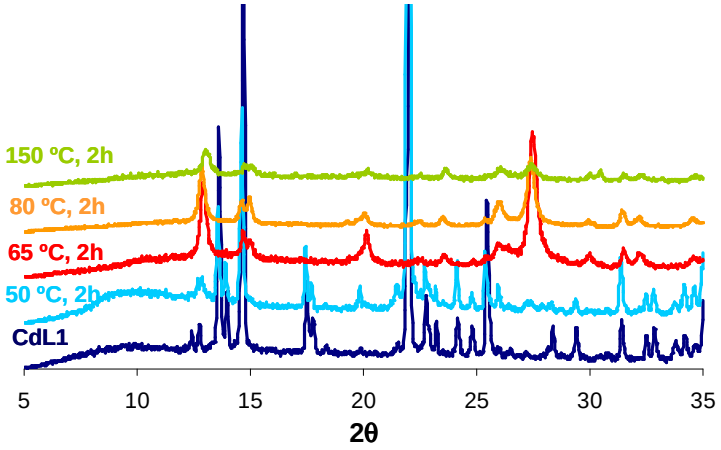

Figure 2.34. XRPD patterns of the thermal activation of CdL1 material.

Although the low thermal stability displayed by the CdL1 solid does not permit to consider any possible application as adsorbent material, it is a nice example of first generation framework since its porosity is irreversibly lost upon removal of the solvent guest molecules. It has been proved indeed that soaking CdL1 in water for 24 h after thermal treatment at 80 ºC, does not permit to recover the original crystal structure indicating that the activation process irreversibly affect the crystalline ordering.

2.3. Conclusions

In this chapter we presented the crystal structure and, as far as possible, chemical and physical characterization of two coordination polymers obtained with M(II) salts (M = Cu, Cd) and 4-carboxypyrazole linker (H_2L1) as single crystals.

The cadmium solid (CdL1) is a non-charged 2D polymer formed by layered sheets giving rise to a 3D structure with water molecules being trapped between the planes. Unfortunately, no strong chemical bonds connect the layered planes, although a complicate net of weak hydrogen bonds (also involving crystallization water molecules) gives rise to the final structure. Thus, when water molecules are removed from the crystal structure, it unavoidably collapses and no permanent porosity can be found in CdL1. Although this material is hardly useful for practical applications, it is a nice example of first generation coordination polymer.

On the other hand the Cu derivative ($NH_4@Cu_3(OH)L1_3$), that has been obtained under the same reaction conditions, is a 3D porous anionic framework which maintains its crystallinity also after the removal of guest water molecules. The negative charge of the ionic framework is compensated by the inclusion of two NH_4^+ ions *per* cavity.

This framework shows reasonably high thermal, mechanical and chemical stabilities that withstand the typical conditions found in practical applications. As a matter of fact, we proved that, much alike zeolites, cation exchange processes of extraframework NH_4^+ cations leads to $A@Cu_3(OH)L1_3$ materials thereby permitting to modulate the porosity of the network. The results show that the increasing bulk of the exchanged cations still permits the access of molecules to their porous structure with a concomitant increased size exclusion selectivity. In this regard, the discrimination properties of $A@Cu_3(OH)L1_3$ framework towards complex mixtures i.e. $CO_2/C_2H_2/CH_4$ and C_6H_6/C_6H_{12} should be highlighted. We also pointed out a rare temperature dependence for CO_2/C_2H_2 separation since, for $NH_4@Cu_3(OH)L1_3$ framework, carbon dioxide is eluted before acetylene at temperatures below 286 K while the opposite trend is found at higher temperatures.

Finally, we have found that these systems behave as efficient heterogeneous oxidation catalysts which might be related to the redox active nature of Cu centres and their coordination unsaturated nature.

2.4. Bibliography

[1] Dictionary of Chemistry, III. X 8.

[2] F. A. Mumpton, *Proc. Nat. Ac. Sci USA*, **1999**, *96*, 3463.

[3] I. E. Maxwell, W. H. J. Stork, *Stud. Surf. Sci. Catal.* **2001**, *137*, 747.

[4] D. W. Breck, in *Zeolite Molecular Sieves: Structure, Chemisty and Use*, Wiley-Interscience, New York, **1974**.

[5] a) R. Glaeser, J. Weitkamp, *Springer Ser. Chem. Phys*. **2004**, *75*, 161; b) G. Hourdin, A. Germain, C. Moreau, F. Fajula, *Cat. Lett*. **2000**, *69*, 241.

[6] R. Le Van Mao, N. T. Vu, S. Xiao, A. Ramsaran, *J. Mater. Chem.* **1994**, *4*, 1143.

[7] C. W. Jones, T. Katsuyuki, M. E. Davis, *Nature*, **1998**, *393*, 52.

[8] A. K. Cheetham, G. Férey, T. Loiseau, *Angew. Chem. Int. Ed*. **1999**, *38*, 3268.

[9] B. F. Hoskins, R. Robson, *J. Am. Chem. Soc.* **1989**, *111*, 5962.

[10] B. F. Hoskins, R. Robson, *J. Am. Chem. Soc*. **1990**, *112*, 1546.

[11] a) H. Li, A. Laine, M. O'Keeffe, O. M. Yaghi, *Science*, **1999**, *283*, 1145; b) A. Phan, C. J. Doonan, F. J. Uribe-Romo, C. B. Knobler, M. O'Keeffe, O. M. Yaghi, *Acc. Chem. Res.* **2010**, *43*, 58; c) M. Eddaoudi, J. Kim, N. Rosi, D. Vodak, J. Wachter, M. O'Keeffe, O.M. Yaghi, *Science*, **2002**, *295*, 469.

[12] G. Férey, C. Mellot-Draznieks, C. Serre, F. Millange, J. Dutour, S. Surblé, I. Margiolaki, *Science*, **2005**, *309*, 2040.

[13] a) M. H. Alkordi, J. A. Brant, L. Wojtas, V. C. Kravtsov, A. J. Cairns, M. Eddaoudi, *J. Am. Chem. Soc*. **2009**, *131*, 17753; b) Y. Liu, V. Kravtsov, R. D. Walsh, P. Poddar, H. Srikanth, M. Eddaoudi, *Chem. Commun*. **2004**, 2806; c) Y. Liu, V. C. Kravtsov, D. A. Beauchamp, J. F. Eubank, M. Eddaoudi, *J. Am. Chem. Soc*. **2005**, *127*, 7266.

[14] J. A. R. Navarro, E. Barea, A. Rodríguez-Diéguez, J. M. Salas, C. O. Ania, J. B. Parra, N. Masciocchi, S. Galli, A. Sironi, *J. Am. Chem. Soc.* **2008**, *130*, 3978.

[15] Y. Liu, V. C. Kravtsov, R. Larsen, M. Eddaoudi, *Chem. Commun*. **2006**, 1488.

[16] F. Nouar, J. Eckert, J. F. Eubank, P. Forster, M. Eddaoudi, *J. Am. Chem. Soc*. **2009**, *131*, 2864.

[17] Z.-J. Zhang, W. Shi, Z. Niu, H.-H. Li, B. Zhao, P. Cheng, D.-Z. Liao, S.-P. Yan, *Chem. Commun.* **2011**, *47*, 6425.

[18] T.-F. Liu, J. Lü, C. Tian, M. Cao, Z. Lin, R. Cao, *Inorg. Chem*. **2011**, *50*, 2264.

[19] S. Yang, X. Lin, A. J. Blake, G. S. Walker, P. Hubberstey, N. R. Champness, M. Schröder, *Nat. Chem.* **2009**, *1*, 287.

[20] A. L. Spek, *J. Appl. Crystallogr.* **2003**, *36*, 7.

[21] W. Ouellette, H. Liu, C. J. O'Connor, J. Zubieta, *Inorg. Chem.* **2009**, *48*, 4655.

[22] V. A. Blatov, M. O'Keeffe, D. M. Proserpio, *Cryst. Eng. Commun*. **2010**, *12*, 44.

[23] a) P. A. Angaridis, P. Baran, R. Boča, F. Cervantes-Lee, W. Haase, G. Mezei, R. G. Raptis, R. Werner, *Inorg. Chem*. **2002**, *41*, 2219; b) M. Angaroni, G. A. Ardizzoia, T. Beringhelli, G. La Monica, D. Gatteschi, N. Masciocchi, M. Moret, *J. Chem. Soc. Dalton Trans*. **1990**, 3305.

[24] a) R. M. Barrer, *J. Chem. Soc*. **1948**, 2158; b), R. M. Barrer, *J. Chem. Soc*. **1950**, 2342.

[25] E. N. Coker, in *From Zeolites to Pororus MOF materials*, (Eds: R. Xu, Z. Gao, J. Chen, W. Yan), **2007**, pp. 110-120.

[26] L. E. Smart, E. A. Moore, in *Solid State Chemistry An Introduction*, Taylor & Francis, CRC, Boca Raton, **2005**.

[27] J.-R. Li, R. J. Kuppler, H.-C. Zhou, *Chem. Soc. Rev*. **2009**, *38*, 1477.

[28] a) S. C. Xiang, W. Zhou, Z. J. Zhang, M. A. Green, Y. Liu, B. L. Chen, *Angew. Chem. Int. Ed.* **2010**, *49*, 4615; b) J. P. Zhang, X. M. Chen, *J. Am. Chem. Soc*. **2009**, *131*, 5516; c) Y. X. Hu, S. C. Xiang, W. W. Zhang, Z. X. Zhang, L. Wang, J. F. Bai, B. L. Chen, *Chem. Commun*. **2009**, 7551.

[29] a) R. Matsuda, R. Kitaura, S. Kitagawa, Y. Kubota, R. V. Belosludov, T. C. Kobayashi, H. Sakamoto, T. Chiba, M. Takata, Y. Kawazoe, Y. Mita, *Nature*, **2005**, *436*, 238; b) D. Tanaka, M. Higuchi, S. Horike, R. Matsuda, Y. Kinoshita, N. Yanai, S. Kitagawa, *Chem. Asian J.* **2008**, *3*, 1343; c) D. G. Samsonenko, H. Kim, Y. Y. Sun, G. H. Kim, H. S. Lee, K. Kim, *Chem. Asian J.* **2007**, *2*, 484.

[30] E. Diaz, S. Ordoñez, A. Vega. *J. Colloid Interf. Sci*. **2007**, *305*, 7.

[31] a) R. Matsuda, R. Kitaura, S. Kitagawa, Y. Kubota, R. V. Belosludov, T. C. Kobayashi, H. Sakamoto, T. Chiba, M. Takata, Y. Kawazoe, Y. Mita, *Nature*, **2005**, *436*, 238; b) J. P. Zhang, X. M. Chen, *J. Am. Chem. Soc.* **2009**, *131*, 5516; c) S. Xiang, W. Zhou, J. M. Gallegos, Y. Liu, B. Chen, *J. Am. Chem. Soc.* **2009**, *131*, 12415.

[32] N. V. Keltsev, *The Essential Principles of Adsorption Engineering*, Moscow, **1984**.

[33] Y.-S. Bae, K.-L. Mulfort, H. Frost, P. Ryan, S. Punnathanam, L. J. Broadbelt, J. T. Hupp, R. Q. Snurr, *Langmuir*, **2008**, *24*, 8592.

[34] C. E. Webster, R. S. Drago, M. C. Zerner, *J. Am. Chem. Soc*. **1998**, *120*, 5509.

[35] M. Tonigold, Y. Lu, B. Bredenkötter, B. Rieger, S. Bahnmüller, J. Hitzbleck, G. Langstein, D. Volkmer, *Angew. Chem. Int. Ed*. **2009**, *48*, 7456.

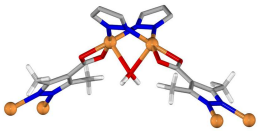

3. SOFT COORDINATION POLYMERS

3.1. Introduction

In the fundamental review "Soft Porous Crystals" published on *Nature Chemistry* in 2009, Kitagawa and co-workers give an exhausting definition of soft porous crystals: they "are defined as porous solids that possess both a highly ordered network and structural transformability".[1] The authors provide an original description of this class of materials by stating that Soft-PCPs possess integrated attributes of both crystallinity and flexibility typical of zeolite materials and enzymes respectively. According to the review, this new type of frameworks have to combine pore regularity and rigid properties typical of zeolite porous materials, with transformability and specificity usually found in enzymes (Figure 3.1). In this way intelligent host materials, responsive to external stimuli, can be produced: they exhibit reversible transformability between states (two or even more) with long range structural ordering and permanent porosity.

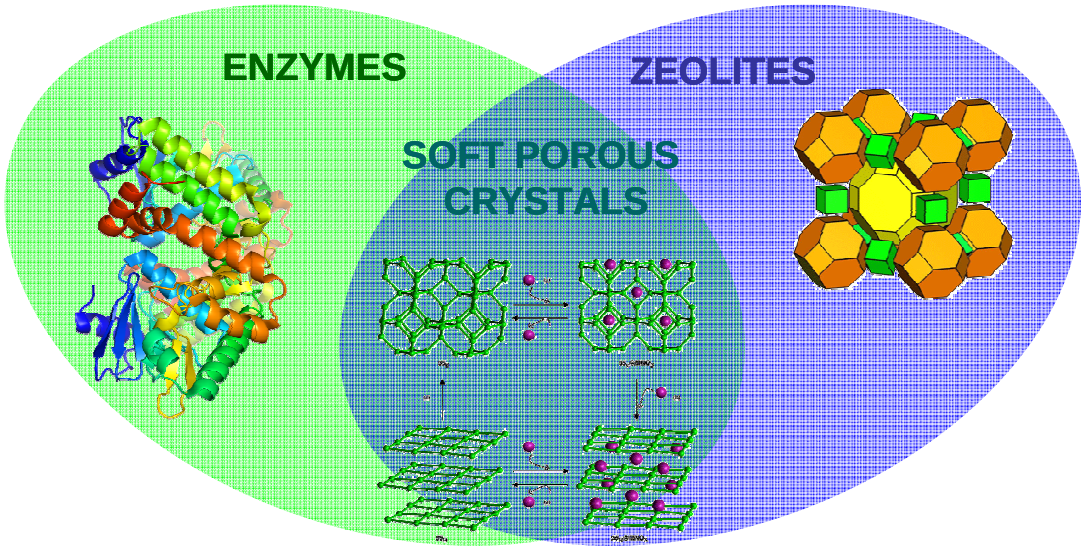

Figure 3.1. Pictorial summary of the combination of typical properties of enzymes and zeolites in Soft Porous Crystal materials.

3.1.1. Sources of flexibility in Soft Porous Coordination Polymers

To better understand the dynamic behaviour of PCPs, we should consider the sources of flexibility in their structural organization.

Bond elongation and shortening. A change in the length of a coordination bond between metal and organic spacer inevitably leads to a modification of the framework's structure. This is, in general, associated to the enhanced plasticity of coordination

polyhedron or to a change in the electronic structure of the central atom. Distortions from a regular geometry of the central metal atom could be the consequence of Jahn-Teller effect, since the break of molecular orbitals degeneracy leads to the anisotropic elongation of coordination bonds (a typical example are octahedral Cu(II) complexes).[2] Otherwise, another source of polyhedron plasticity can be the low spin (LS)-high spin (HS) reversible transition known as spin-crossover phenomenon.[3] For example, in $\{Fe(3\text{-}CNpyridine)_2[Ag(CN)_2]_2\}\cdot 2/3H_2O$ 3D interpenetrated framework (Figure 3.2) the Ag-Ag distance decreases by 0.0967 Å (Δ = 3.1 %) on passing from the HS to the LS form.

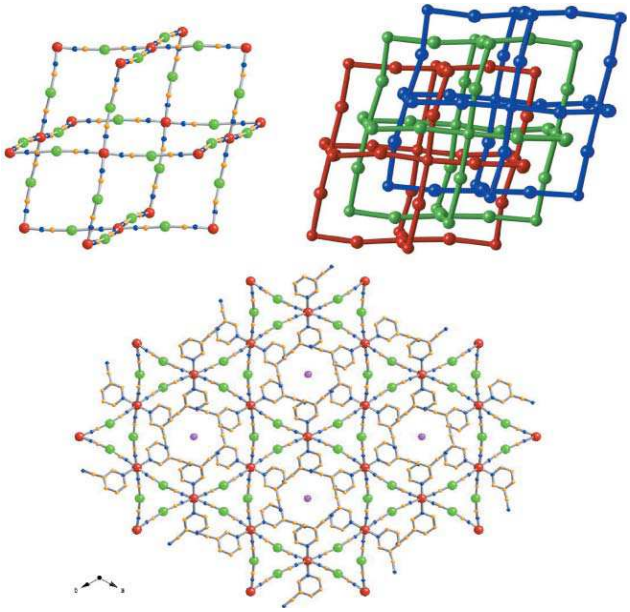

Figure 3.2. Structure of $\{Fe(3\text{-}CNpyridine)_2[Ag(CN)_2]_2\}\cdot 2/3H_2O$. (Above) Fragment of the NbO net and interpenetration of three networks; (below) perspective view along the *c* axis of the framework. **Ag**, **Fe**, **N**, **C**, **H_2O**. H atoms have been omitted for clarity.

Bond cleavage and reformation. Dealing with extended structures, a particular class of weak bonds can break in a reversible way without entailing framework collapse. Thus the framework rearranges adopting a much more favourable configuration, but the original one can be restored under particular conditions. The lability of coordination bonds is an advantage if the system is used for sensing, electronic and biomedical applications. In addition, the possibility for a metal centre to give oxidative additions or reductive elimination of ligands, is at the basis of catalytic activity of PCPs, particularly in those containing square planar d^8 metal ions.[4]

A nice system undergoing this kind of structure transformation is $[Cu(2\text{-pymo})_2]_n$ material, already presented in Chapter 1. The incorporation/release of guest nitrate salts leads to a new phase where the connectivity of the Cu centres has changed as a result of cleavage and reformation of M-L bonds (Figure 3.3).

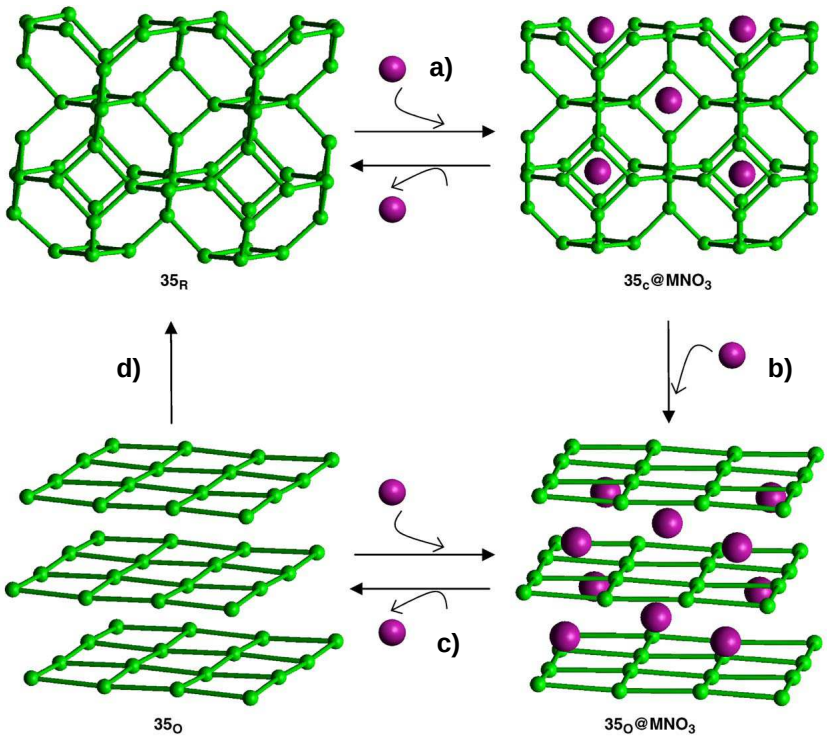

Figure 3.3. Guest induced crystal to crystal phase transitions taking place on $[Cu(2\text{-pymo})_2]_n$ (35_R) upon MNO_3 ion pair incorporation/release from water/methanol solutions. a) Inclusion of *n/3* MNO_3; b) additional inclusion of *n/6* MNO_3; c) removal of *n/2* MNO_3 guests by treatment with 18-crown-6-ether; d) exposition of 35_O to water. Green balls, green rods and purple balls represent copper centres, 2-pymo bridges and MNO_3 ion pair guests, respectively.

M-L Bond rotation. The rotation about metal-to-ligand bond permits a high degree of conformational flexibility giving rise to a much wider choice of polygons and polyhedra assemblies eventually found in porous coordination polymers. Thus, the combination of the bonding vectors of central metal atoms with those of ligands provides a wide variety of possible geometries. The dynamic transformation between different geometries in the framework allows a high degree of flexibility that can be triggered by external stimuli and does not affect the intrinsic stability of the net. A representative example of this source of flexibility in coordination polymers are the well known MIL-53 materials. In this case, there is huge guest induced response of the

framework that is sustainable thanks to the adaptability of the metal centred polyhedron (see Figure 3.4).[5]

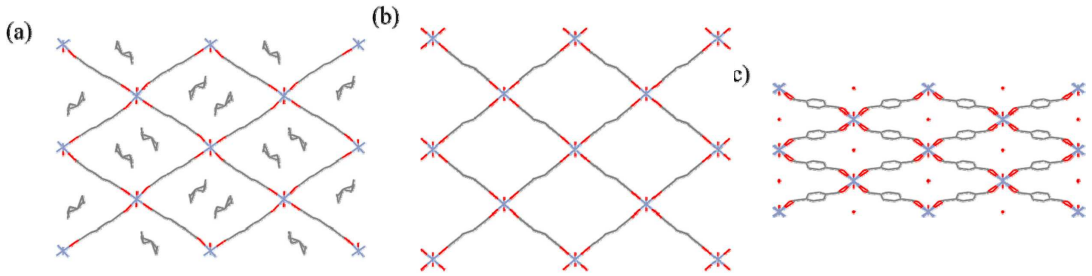

Figure 3.4. View of the pore systems of (a) MIL-53as (1,4-BDC accommodated phase); (b) MIL-53ht (degassed phase) and c) MIL-53lt (water-accommodated phase).

Bond rotation within the ligand. The ligand itself can undergo a partial motion such as rotation. For example, if two carbons of two phenyl rings are connected by a single C-C bond, the planes of the two rings can be parallel or form an angle between 0º and 90º. Any transformation taking place once the framework is already formed is a source of net flexibility. For instance, the study by ^{2}H solid state NMR of the ligand rotation in the diamagnetic compound $[Zn_2(1,4\text{-ndc})_2(dabco)]_n$ (1,4-ndc = 1,4-naphthalene-dicarboxylate, dabco = 1,4-diazabicyclo[2,2,2]octane) reveals that under guest-free condition, naphthalene rings can rotate around their C1–C4 axes whereas under benzene guest-inclusion condition, the rotation of the ligand is inhibited (see Figure 3.5).[6]

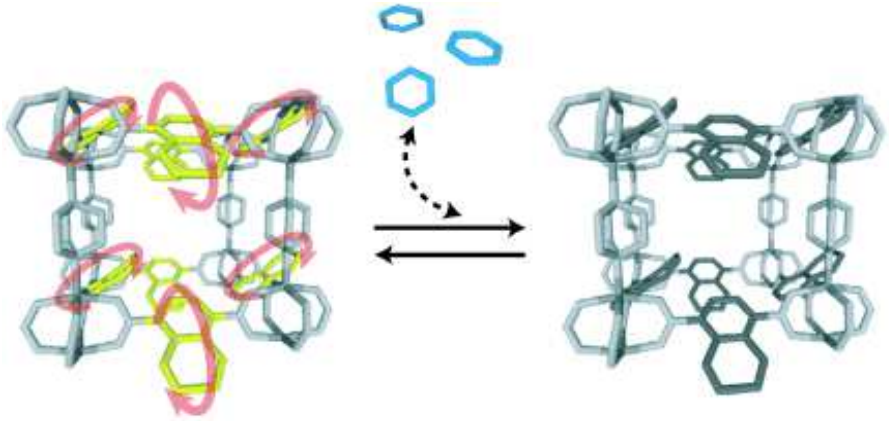

Figure 3.5. View of guest-induced reversible rotation in $[Zn_2(1,4\text{-ndc})_2(dabco)]_n$. Benzene guests are blue; rotationally free naphthalene rings are yellow.

Ligand flexibility. The use of flexible ligands for the construction of flexible frameworks is a challenging topic since the flexibility of the linker makes much more difficult the achievement of an ordered porous structure. Anyway there are compounds that substitute rigid ligands by flexible ones with the same size and connectivity as, for

example some coordination polymers where 4,4'-bipyridine ligands are replaced by flexible *trans*-bispyridylethylene in the construction of extended networks containing Cu(II),[7] Co(II),[8] and Cu(I).[9] In these cases a *cis-trans* switching could be triggered by photochemical reactions[10] as well as by spin conversion.[11]

An example is the $[Zn_2(BDC)_2(dabco)]_n$ (BDC = 1,4-benzene dicarboxylate, dabco = diazabicyclo[2.2.2]octane) material, functionalized with alkyl ether groups of the type $-O-(CH_2)_n-O-CH_3$ (n = 2–4) tethered to the BDC ligand.[12] Unlike the corresponding non-functionalized framework, this porous material shows structural flexibility, as well as high sorption selectivity towards CO_2 over N_2 and CH_4 (Figure 3.6). The structural transformations respond to the presence/absence of guest molecules and are undoubtedly related to the presence of the alkyl ether flexible chains on the linker.

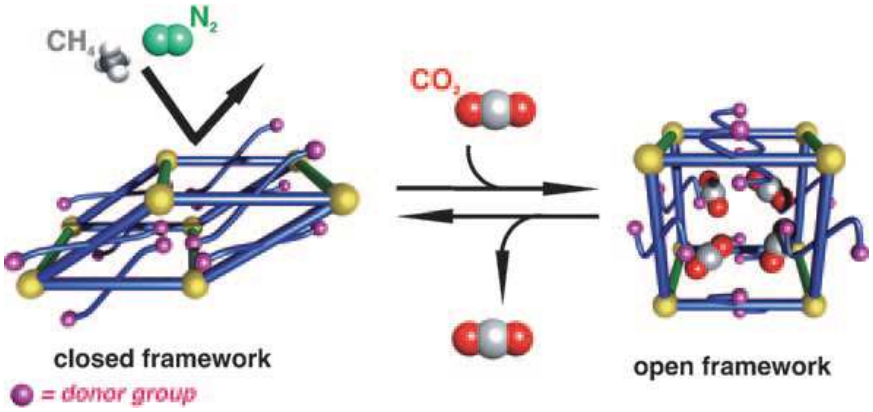

Figure 3.6. Sketch of the selective sorption in $[Zn_2(BDC)_2(dabco)]_n$. CH_4 and N_2 cannot enter the pores in the closed state and will not be adsorbed in the functionalised MOF, whereas CO_2 is able to penetrate in the pores and transforms the structure to the open state.

Weak interactions. The presence of weak interactions (such as H-bonding, van der Waals or electrostatic interactions, π–π stacking, etc.) is quite common in the assembly of coordination polymers. In some cases, thermal activation of these materials will lead to the irreversible collapse of the structure, while in other cases the lability of this kind of interactions confers them dynamic properties. Indeed, small perturbations can give rise to modulation of the structure and properties of the investigated system.

A nice example is $\{[Co(L)_2(H_2O)_2](NO_3)_2 \cdot 1.5H_2O\}_n$ (L = 2,2'-{[3,6-di(pyridin-4-yl)benzene-1,2-diyl]bis(oxy)}diethanol) material published by Fujita and co-workers[13] which reversibly loses the guest H-bonded water molecules if heated at 423 K. Noteworthy, the dehydrated material $[Co(L)_2(NO_3)_2]_n$ maintains the same crystal system

and space group but shows considerable distortion of the bridging ligand resulting in framework flexibility (Figure 3.7).

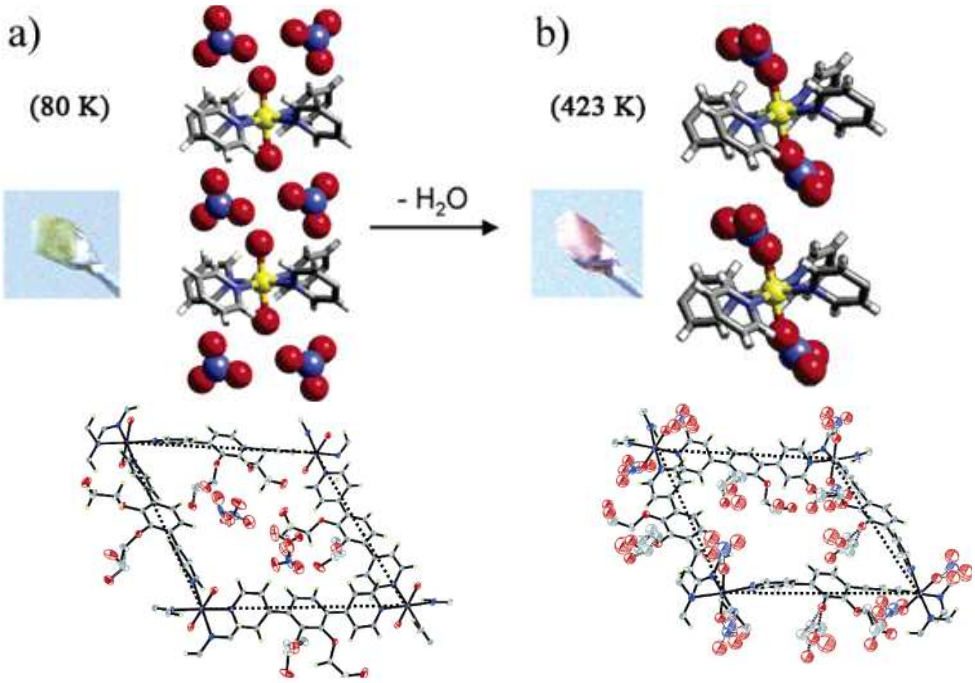

Figure 3.7. Photographs of crystals, local structures and ORTEP drawing (30 % probability level) of a square-grid unit around the cobalt ion of a) the original crystal $\{[Co(L)_2(H_2O)_2](NO_3)_2 \cdot 1.5H_2O\}_n$ and b) the crystal after heating at 423 K for 24 h $[Co(L)_2(NO_3)_2]_n$

3.1.2. Influence of flexibility on the properties of the frameworks

The flexible nature of a coordination polymer's structure has usually a significant influence on the bulk properties of the material. Selective adsorption, catalytic or conductive (ionic or electrical) properties are typically affected by the breathing phenomena taking place within the net.

Considering the adsorption properties, we know that in conventional porous (rigid) materials a multistep adsorption profile comes from the distribution of various porous structures (i.e. pores of different size, shape and nature) in a robust static framework (type VI isotherm).[14] By contrast, soft porous crystals show another type of multistep adsorption based on structural transformations that occur in response to guest concentration. For instance, the adsorption isotherm of N_2 (77 K) in the [Co(1,4-benzenedipyrazolate)]$_n$ material,[15] presents five distinct steps pointing out that various structural phase transitions occur under different adsorbate pressures (Figure 3.8).

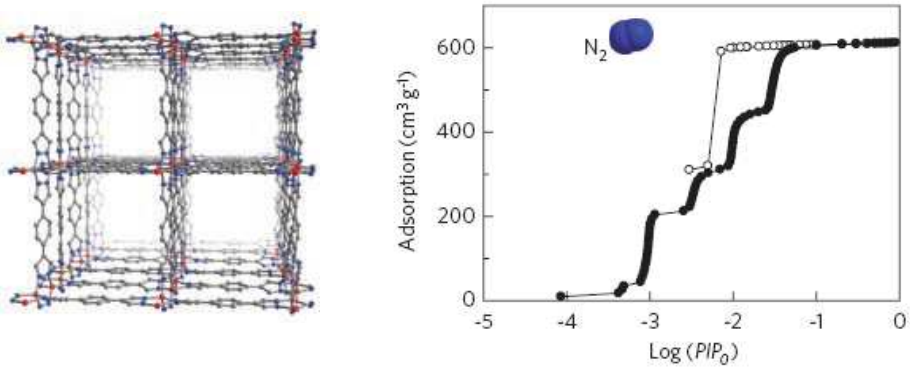

Figure 3.8. (Left) 3D porous crystal structure of $[Co(1,4\text{-benzenedipyrazolate})]_n$ and (right) its N_2 adsorption isotherm (77 K).

Moreover, shrinking or contracting behaviour can be observed selectively for specific guests that suitably fit to the shape of micropores. For example, in the copper pillared-layer-type compound, $[Cu_2(pzdc)_2(bpy)]_n$ (pzdc = pyrazine-2,3-dicarboxylate, bpy = 4,4'-bipyridine) which has 1D channels, shrinking behaviour is observed for benzene guest.[16] This species is strongly bound inside the pores and the initial square pyramidal coordination geometry of Cu^{2+} converts into square planar with a large reduction in pore volume (Figure 3.9). In other words, this is a shape-responsive fitting mediated by the cleavage/formation of a weak bond.

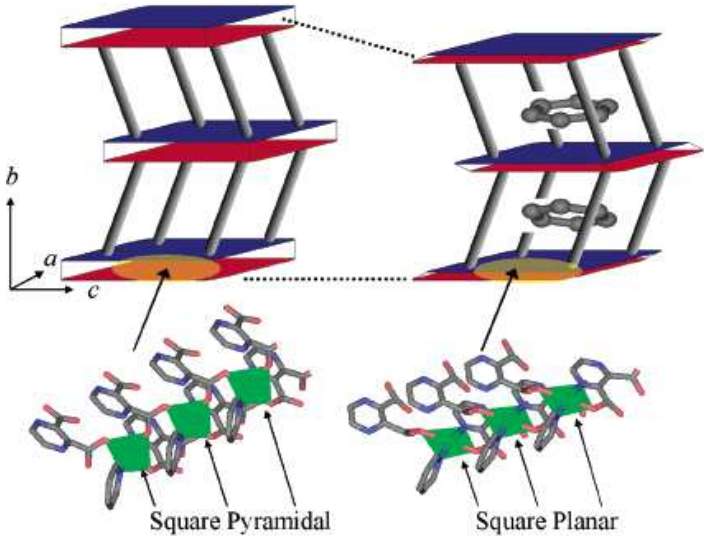

Figure 3.9. Schematic representation of the structural transformation in $[Cu_2(pzdc)_2(bpy)]_n$ triggered by benzene adsorption. The mutual slide of the 2D sheets and the pore shrinking is observed, accompanied by the change of Cu coordination geometry. Two-dimensional sheets of $[Cu(pzcd)]_n$ and the pillar of bpy are represented by blue and red boards, and by gray sticks, respectively.

Besides the influence of framework flexibility on gas adsorption properties, we should also mention its effect on catalytic reactions eventually taking place inside the network. In fact, the dynamic nature of soft PCPs is a highly advantageous feature since it will facilitate the incorporation of reactives and the adaptable nature of pores should also facilitate the formation of products with a specific shape as well as favour their release. The dynamic nanospace of soft PCPs has sometimes a strong effect on the properties of the guest. In this regard, polymerization of guest molecules in $[Zn_2(1,4\text{-}BDC)_2(dabco)]_n$ is an intriguing example.[17] Unlike its rigid isostructural material $[Cu_2(1,4\text{-}BDC)_2(dabco)]_n$, the Zn derivative can dynamically arrange molecules of *p*-divinylbenzene as a consequence of its flexibility. The responsive crystalline framework arranges the guest molecules uniformly in the channels and this causes their crystallization (see Figure 3.10). This effect brings the monomers regioselectively closer and therefore topotactic selective polymerization can be achieved (any ramification being precluded by channel's constrictions).

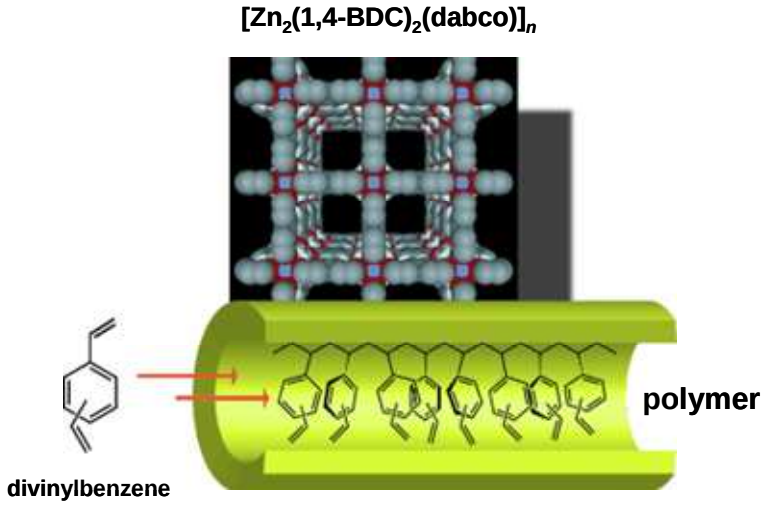

Figure 3.10. Structure of $[Zn_2(1,4\text{-}BDC)_2(dabco)]_n$ and schematic encapsulation and polymerization of divinylbenzene in its nanochannels.

A further interesting feature of soft PCPs can be the magnetic responsive behaviour upon incorporation of guest molecules. As a matter of fact, magnetic properties are defined and dominated by the arrangement of the atoms, on which structural transformation has a profound effect. In other words, manifold magnetic properties can take place when a reversible crystalline transition occurs within a framework. The 3D $\{Fe(pyz)[Pt(CN)_4]\}_n$ (pyz = pyrazine) breathing framework can be taken as a model.

This material normally shows expansion with guest accommodation and the resulting enlargement of cell volume stabilizes the high spin (HS) states. However, as it can be appreciated in Figure 3.11, in the case of inclusion of guests with high affinity for the pore surface, the framework shrinks to accommodate guest molecules which results in a reduction of the cell volume, for which the low spin state (LS) is stabilized.

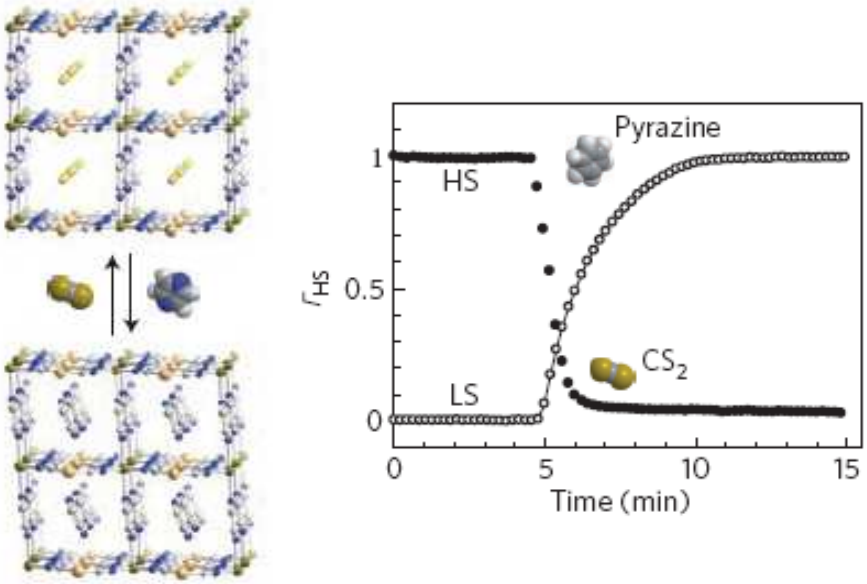

Figure 3.11. (Left) Alteration of the porous structure of $\{Fe(pyz)[Pt(CN)_4]\}_n$ by exchange of guest molecules of CS_2 and pyrazine; (right) the high-spin (HS)/low-spin (LS) states conversion by accomodation of CS_2 at 298 K.

The combination of structural flexibility with the presence of open-metal sites in soft PCPs is not rare although not interrelated. Therefore, in some cases, the removal of molecules directly coordinated to the metal centre (as for water molecules in HKUST-1)[18] does not affect at all the three dimensional structure, while in other cases, a deep variation can be detected with the framework modifying its conformation as a response to the change. This is the case of $\{[Cd_2(pzdc)_2L(H_2O)_2] \cdot 3(H_2O) \cdot (CH_3CH_2OH)\}_n$ (H_2pzdc = 2,3-pyrazinedicarboxylic acid; L = 2,5-bis(2-hydroxyethoxy)-1,4-bis(4-pyridyl)benzene) PCP wherein the removal of guest molecules as well as of coordinated water molecules affords $[Cd_2(pzdc)_2L]_n$ material with the concomitant rearrangement of the coordination polyhedra around Cd atoms (see Figure 3.12).[19]

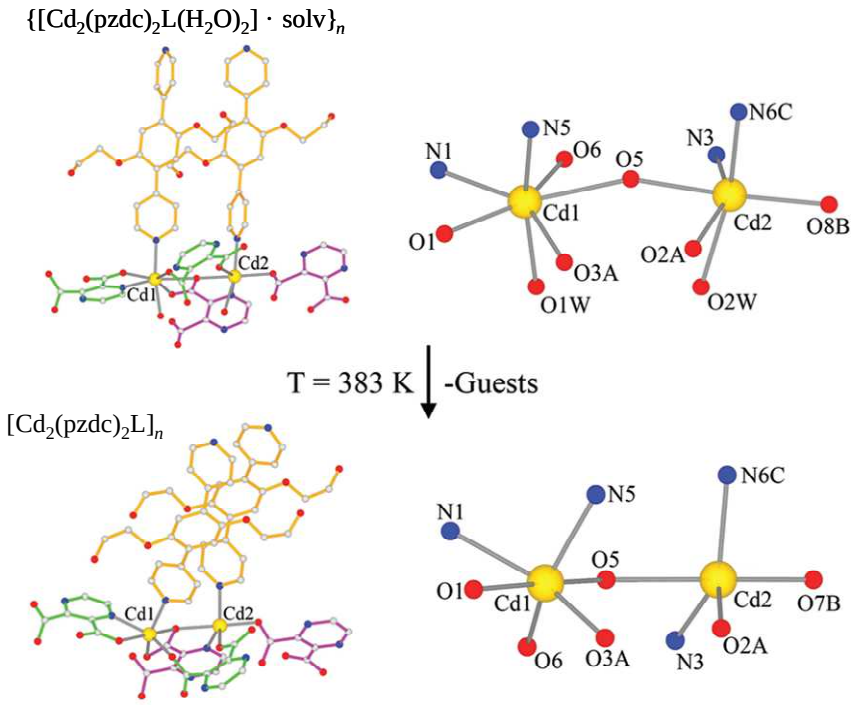

Figure 3.12. (Left) View of the ligand coordination modes and (right) coordination geometries of the two crystallographically independent Cd^{2+} centers of $\{[Cd_2(pzdc)_2L(H_2O)_2] \cdot 3(H_2O) \cdot (CH_3CH_2OH)\}_n$ and $[Cd_2(pzdc)_2L]_n$ materials. **Cd**, **O**, **N**, **C**. Non coordinated solvent molecules, disordered atoms and hydrogen atoms have been omitted for clarity.

In this introduction we outlined the versatility of Soft-PCPs and we pointed out that these materials can find applications in many and very different fields. However, it should be noted that the flexible behaviour is very difficult (if not impossible) to be predicted and that only a deep investigation of the properties of a crystalline material is needed to reveal its structural flexibility.

3.2. Results and discussion

With this background, we succeed to synthesizing a flexible 3D porous coordination polymer of formulation $\{[Cu_2(H_2O)L2_2]solv\}_n$, where the plastic coordination polyhedron of Cu^{2+} cation is combined with the small 3,5-dimethyl-4-carboxypyrazole (H_2L2) ligand. In this case, the soft behaviour arises from the concerted removal of coordinated water molecules combined with the adaptation to such a profound structural change by copper ions' coordination geometry. Interestingly, under similar reaction conditions we obtain another coordination framework of $\{[Cu(HL2)_2] \cdot solv\}_n$ formulation, with a completely different structure, connectivity and stability, thus pointing out the importance of a thoughtful control of reaction conditions.

3.2.1. $[Cu_2(H_2O)(L2)_2]$ compound

Crystal structure

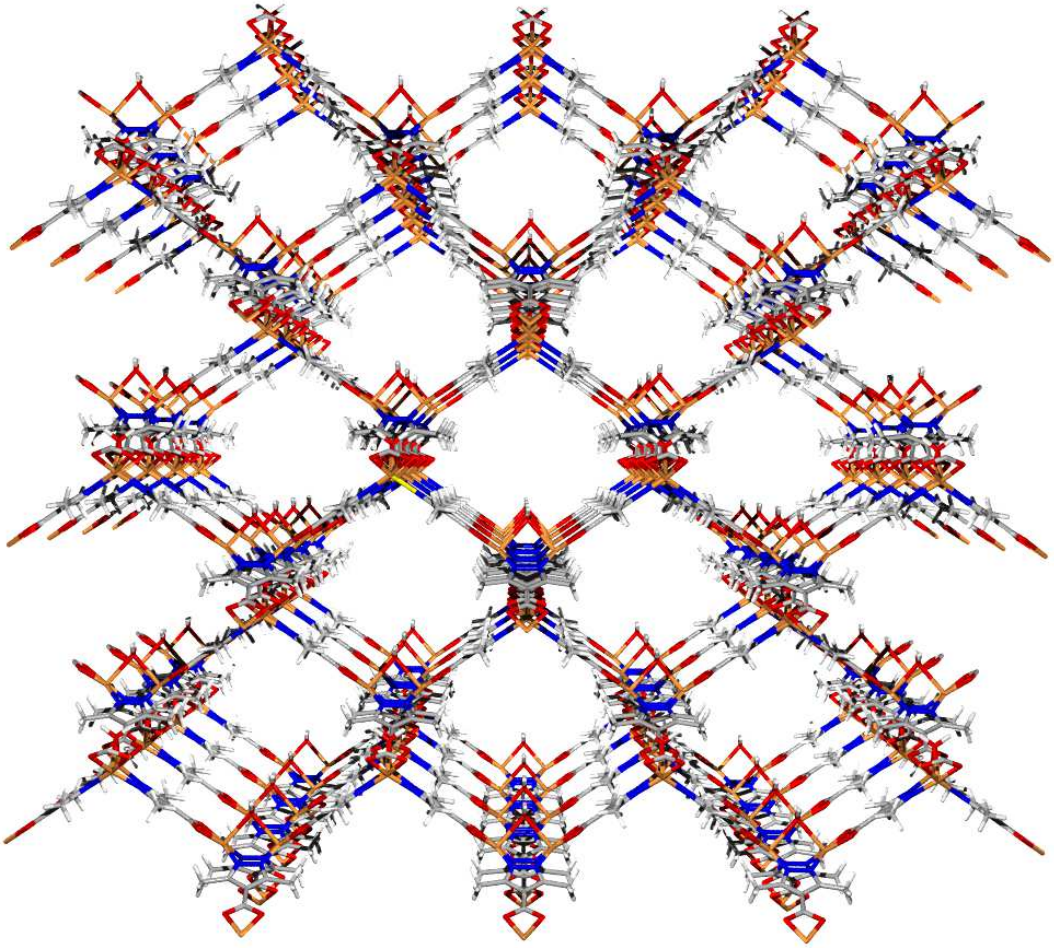

Figure 3.13. 3D view of $[Cu_2(H_2O)(L2)_2]$ porous framework along the *a* axis.

The reaction between CuX_2 (X = Cl, Br, NO_3) salts with 3,5-dimethyl-4-carboxypyrazole (H_2L2) in a DMF/MeOH 1:1 mixture at 60 ºC for 20 h, gives blue single crystals of suitable size for single crystal X-ray diffraction measurement, of formulation $([Cu_2(L2)_2(OH_2)]DMF_{1.5})_n$ (α-$[Cu_2(H_2O)(L2)_2]$, see Figure 3.13). Under similar reaction conditions (80 ºC, 24 h) phase pure α-$[Cu_2(H_2O)(L2)_2]$ bulk solid is easily obtained in good yield (66 %, with $CuCl_2$ as starting material).

α-$[Cu_2(H_2O)(L2)_2]$ material crystallizes in the tetragonal $I4_1md$ space group with $a = b = 16.119(4)$ Å, $c = 16.455(4)$ Å and a resulting cell volume $V = 4275.1(17)$ Å^3.

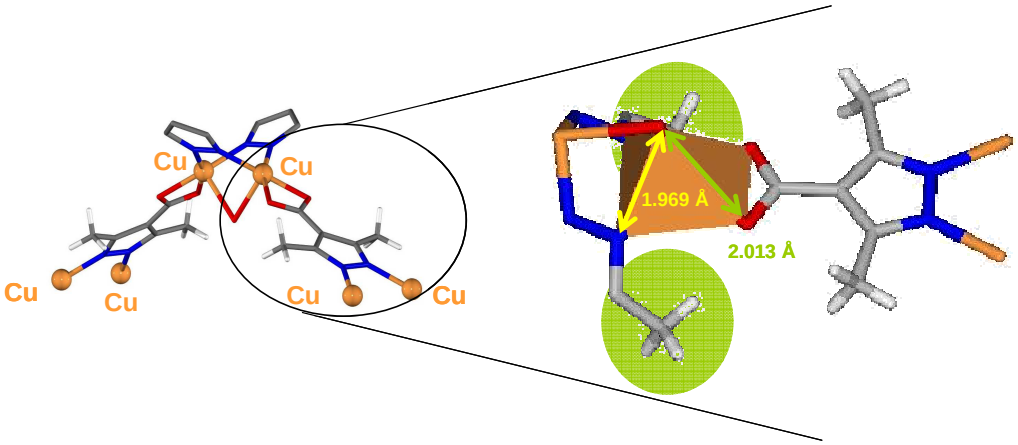

Figure 3.14. View of the basic structural motives found in the single crystal structure of α-$[Cu_2(H_2O)(L2)_2]$ and expansion of the square pyramidal polyhedron of a single Cu^{2+} atom with a special focus on the steric hindrance of CH_3 groups and Cu-O, Cu-N bond distances. **Cu**, **O**, **N**, **C**, **H** (white).

The crystal structure of α-$[Cu_2(H_2O)(L2)_2]$ is based on C_{2v} binuclear copper(II) metal fragments supported by two pyrazolate bridges and an unusual μ_2-OH_2 bridging ligand (Figure 3.14). The CuN_2O_3 coordination polyhedron exhibits a distorted square pyramidal geometry. The basal positions are occupied by two N donor atoms from two different pyrazolate moieties (Cu-N = 1.969(2) Å) and two O donor atoms from the same carboxylate group (Cu-O = 2.013(2) Å) acting in a bidentate coordination mode. The apical position is occupied by a O donor atom from the acua bridging molecule which gives rise to an elongated Cu-O coordination bond of 2.400(2) Å. It should be noted that the octahedral coordination of Cu atoms is prevented by the steric hindrance of methyl groups on $L2^{2-}$ ligands. The Cu-Cu distance within the binuclear unit is 3.270(1) Å.

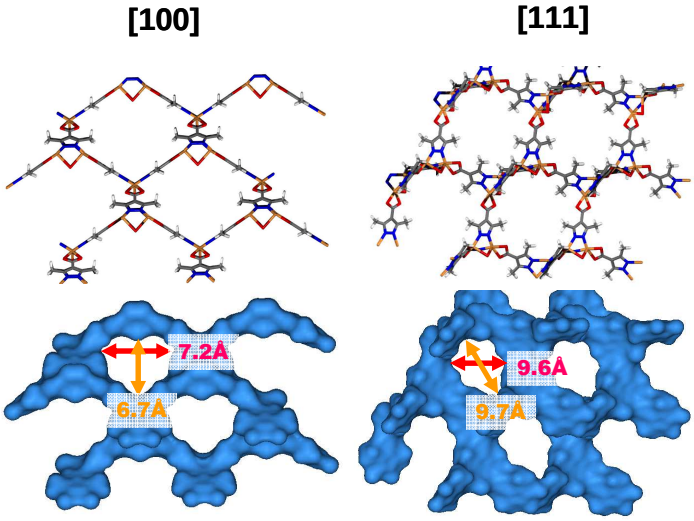

Figure 3.15. Perspective view of α-$[Cu_2(H_2O)(L2)_2]$: (above) crystal structure and (below) solvent accessible surface and size of the pore windows along [100] and [111] crystallographic directions.

The 3D structure is generated by binuclear Cu_2 units acting as 4 connecting nodes through μ_3-L2 bridges which give rise to the formation of a 3D diamond-like open framework with pore window openings of 6.7 x 7.2 $Å^2$ and 9.7 x 9.6 $Å^2$ along [100] and [111] crystallographic directions, respectively (Figure 3.15). The channels are filled with disordered DMF molecules as well as a small amount of free H_2L2, but their exact positions can not be determined on the basis of diffraction data. The exact formulation of the bulk α-$[Cu_2(H_2O)(L2)_2]$ solid is $\{[Cu_2(L2)_2OH_2]\cdot 1.5(DMF)\cdot 0.1(H_2L2)\}_n$, as suggested by IR spectrum (two frequencies in the C=O stretching region in Figure 3.16, corresponding to DMF guest solvent molecules at 1677 cm^{-1} and H_2L2 uncoordinated ligand at 1646 cm^{-1}) and quantitatively determined by ^1H NMR spectrum (Figure 3.17). In this experiment, the bulk α-$[Cu_2(H_2O)(L2)_2]$ material is suspended in DMSO-d_6 and the ratio between the peak integrals of the internal standard $CHCl_3$ (8.29 ppm, 1H), and those of DMF (2.87 ppm, 3H) and unreacted H_2L2 (2.31 ppm, 3H) permits to quantify the content of these molecules into the cannels of bulk α-$[Cu_2(H_2O)(L2)_2]$ material.

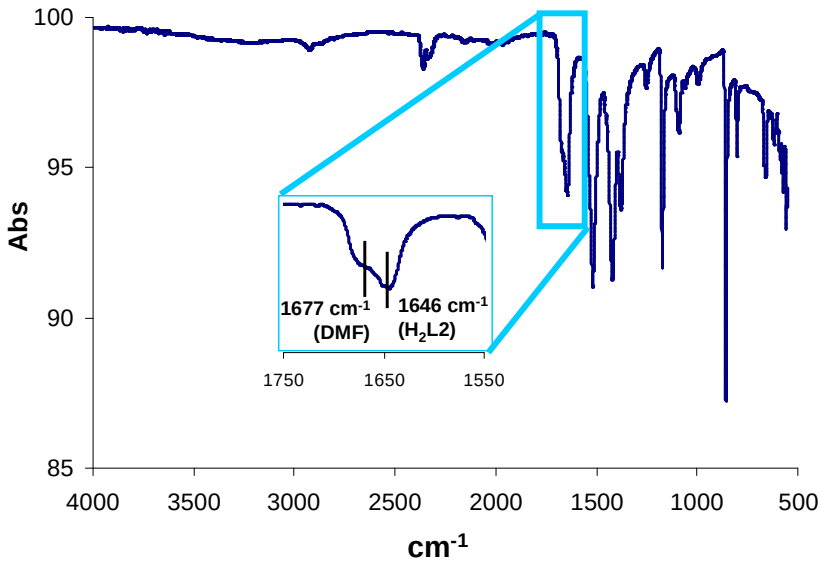

Figure 3.16. IR spectrum of α-$[Cu_2(H_2O)(L2)_2]$ and expansion of the C=O stretching region (1750-1550 cm^{-1}).

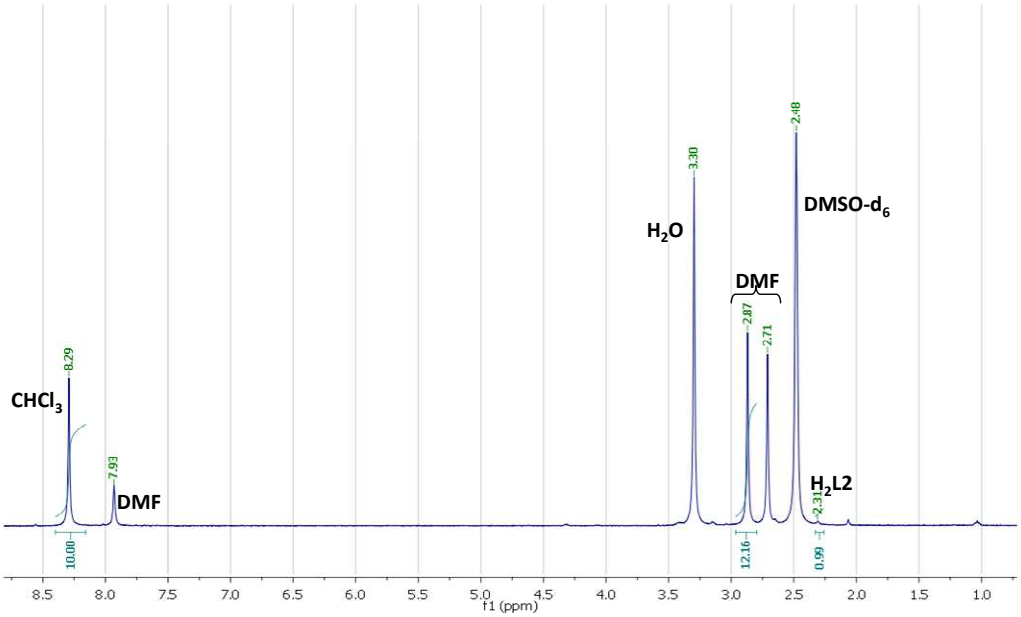

Figure 3.17. ^{1}H NMR of 10 mg of α-[$Cu_2(H_2O)(L2)_2$] in DMSO-d_6 with 10 μL of $CHCl_3$ as internal standard.

Noteworthy, the presence of bridging water molecules is a rather unusual feature among 3D PCPs,[20] with no precedents in copper based materials. Although the quality of single crystal diffraction data does not permit to locate hydrogen atoms, the nature of μ_2-OH_2 bridge can be confirmed taking into account Cu-O bond distances and Cu-O-Cu bond angles which are typical of a weakly bonded μ-OH_2 bridges[21] and discard the presence of either μ-OH^-,[22] or μ-O^{2-}.[23] In fact, the values reported in literature for the uncommon μ_2-OH^- bridge in Cu dimers' crystal structures, are in the range 1.90 – 2.00 Å while the Cu-OH-Cu angles use to measure 106 – 118º. Likewise, for the μ_2-O^{2-} bridge, Cu-O reported bond lengths are in the range 1.87 – 1.97 Å and Cu-O-Cu angles measure always more than 100º, up to 116º. It is evident that Cu-O bond length in α-[$Cu_2(H_2O)(L2)_2$] (2.400 Å) and Cu-O-Cu angle (85.90º) are much more similar to those reported for the very rare μ-OH_2 bridge (2.48 Å and 88º – 89º, respectively).

Table 3.1. Ratios of the elements contained in α-[$Cu_2(H_2O)(L2)_2$] material, determined by XPS analysis.

ELEMENT	C1s	N1s	O1s	Cu2p	Cl2p
RATIOS %	58.05	18.00	16.22	6.91	0.82

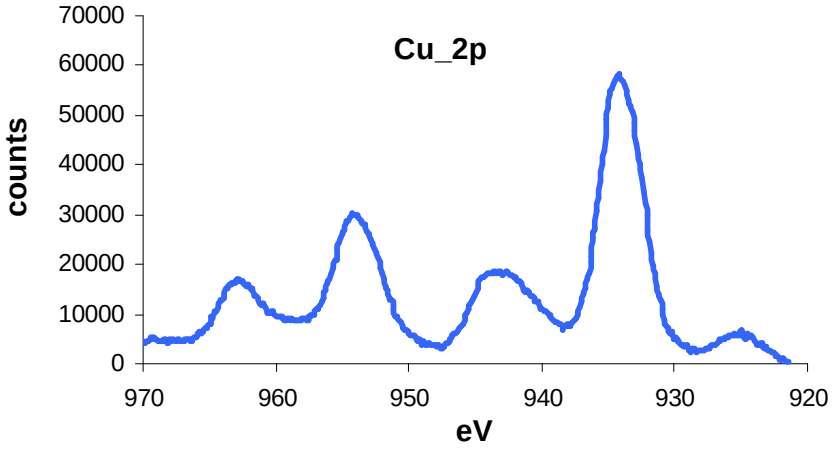

Figure 3.18 XPS spectrum of Cu_2p in α-[$Cu_2(H_2O)(L2)_2$] material.

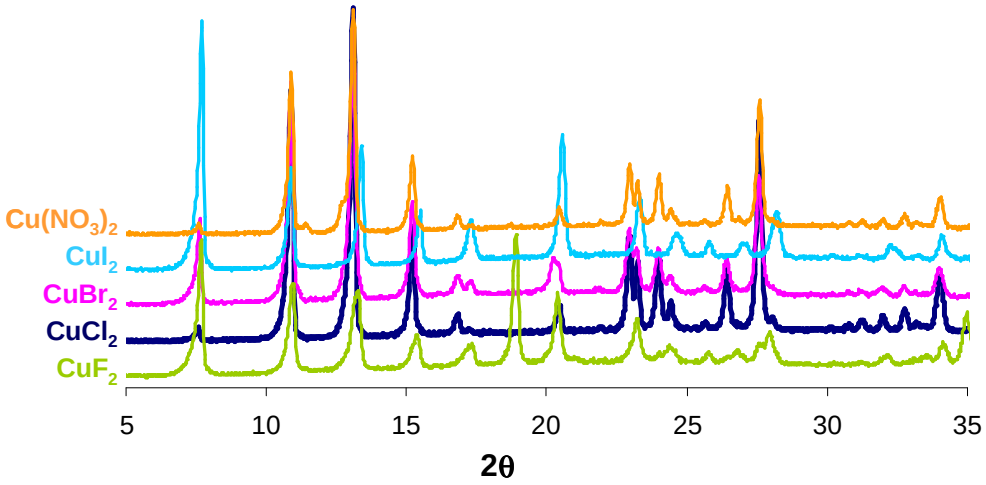

Figure 3.19. XRPD patterns of the α-[$Cu_2(H_2O)(L2)_2$] material prepared by using different CuX_2 (X = F, Br, I, NO_3) metal salts.

Additional XPS analysis of α-[$Cu_2(H_2O)(L2)_2$] (Table 3.1) also discarded the presence of μ_2–Cl^- (Cl = 0.083 mol %) and confirms the divalent charge state of copper centre (Figure 3.18). Moreover, the achievement of the same XRPD pattern if CuX_2 (X = F, Br, I, NO_3) is used instead of $CuCl_2$ as metal source in the synthesis of α-[$Cu_2(H_2O)(L2)_2$] (Figure 3.19), further exclude the presence of μ_2-Cl^- bridging ligands. In particular, for the case of $Cu(NO_3)_2$, no peaks corresponding to NO stretching vibration mode are found in the IR spectrum of α-[$Cu_2(H_2O)(L2)_2$] (Figure 3.20), which also confirms the absence of NO_3^- bridging ligands. Finally, the thermal parameters for the bridging atom in α-[$Cu_2(H_2O)(L2)_2$] further agree with its oxygen nature as this value is lower for oxygen than for any other atom.

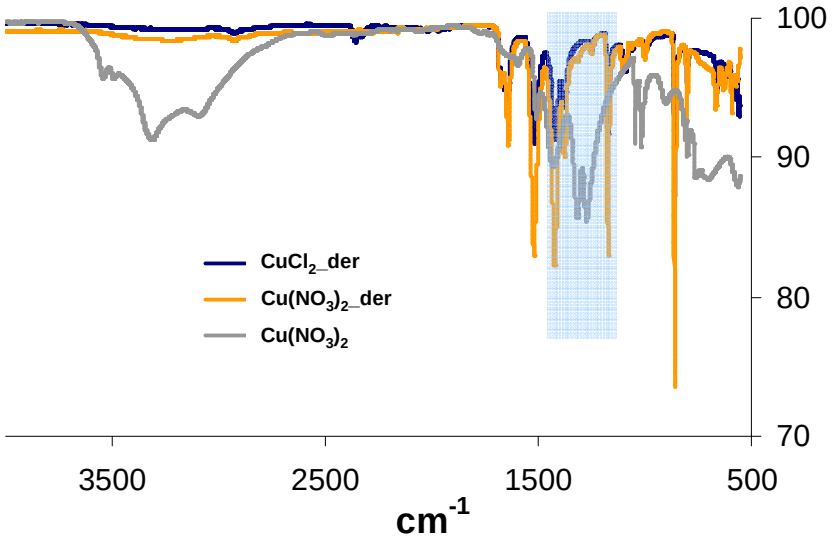

Figure 3.20. IR spectra of the α-[$Cu_2(H_2O)(L2)_2$] material prepared by using different CuX_2 (X = Cl, NO_3) metal salts and that of $Cu(NO_3)_2$.

It should be noted that the evacuation of as-synthesized α-[$Cu_2(H_2O)(L2)_2$] at 120 ºC under vacuum, affords a partially desolvated framework of formulation {[$Cu_2(H_2O)(L2)_2$]·0.9DMF}$_n$ (β-[$Cu_2(H_2O)(L2)_2$], sky blue colour), which maintains the original $I4_1md$ space group but shows some changes in unit cell parameters, which are indicative of [$Cu_2(H_2O)(L2)_2$] framework flexibility. Indeed, there is a small expansion of *a* and *b* axes (Δa = 4.0 %) and a larger contraction of the *c* axis (Δc = –13.6 %) resulting in a small contraction of the cell volume (ΔV = –6.7 %). Interestingly, single crystals of β-[$Cu_2(H_2O)(L2)_2$], suitable for X-ray diffraction, can be obtained by soaking crystals of α-[$Cu_2(H_2O)(L2)_2$] in dry CH_2Cl_2 for three days. The experimental powder diffraction pattern of β-[$Cu_2(H_2O)(L2)_2$] perfectly matches the one simulated from single crystal diffraction data, as shown in Figure 3.21.

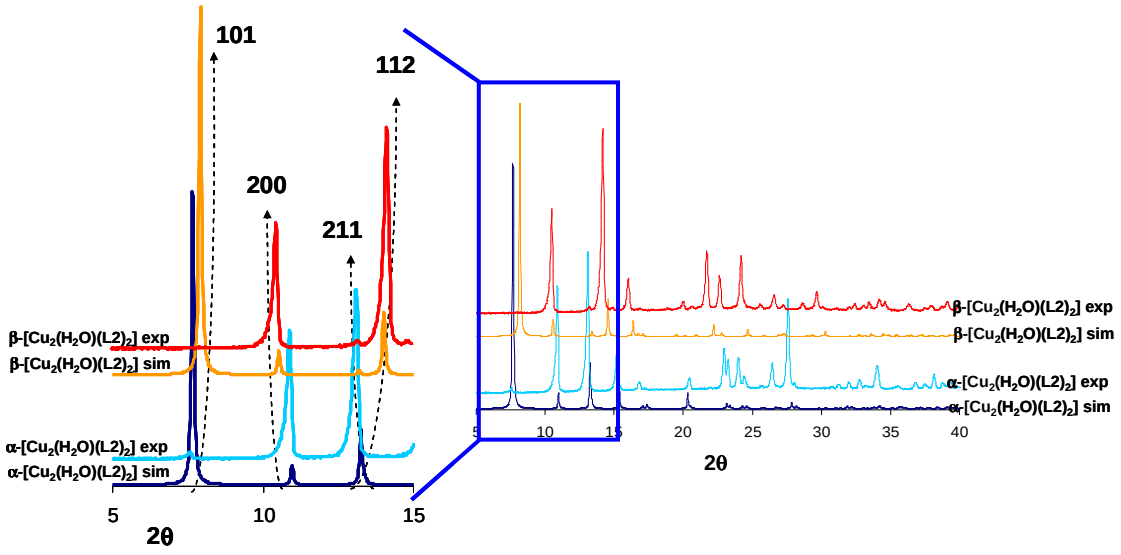

Figure 3.21. (Right) Comparison between simulated (from single crystal data) and experimental XRPD for α-$[Cu_2(H_2O)(L2)_2]$ and β-$[Cu_2(H_2O)(L2)_2]$; (left) expansion of the region 5º < 2θ < 15º and shift of the first peaks in the α-$[Cu_2(H_2O)(L2)_2]$ → β-$[Cu_2(H_2O)(L2)_2]$ transition.

Remarkably, the structure of β-$[Cu_2(H_2O)(L2)_2]$ retains the basic features of α-$[Cu_2(H_2O)(L2)_2]$. The main differences are related to the bending of L2 ligands (N-Cu-N angle changes from 94.69º in α-$[Cu_2(H_2O)(L2)_2]$ to 96.95º in β-$[Cu_2(H_2O)(L2)_2]$) and to the content of DMF guest molecules in the porous structure, whose number is reduced to *ca.* 1 molecule per formula unit in β-$[Cu_2(H_2O)(L2)_2]$ material.

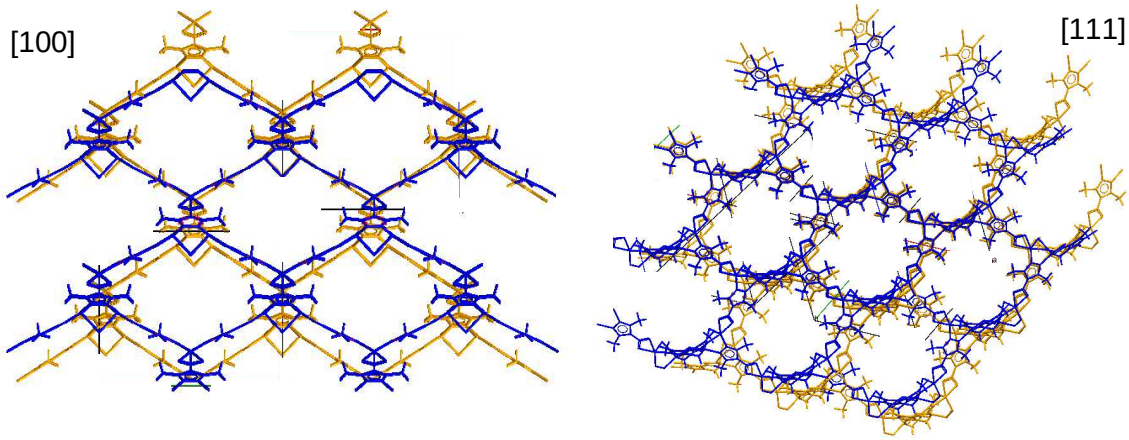

Figure 3.22. Superimposition of the crystal structures of **α-$[Cu_2(H_2O)(L2)_2]$** and **β-$[Cu_2(H_2O)(L2)_2]$** along [100] and [111] crystallographic directions.

The overall effect of these textural changes on the structure of the material can be appreciated in Figure 3.22, where superimposition of the two single crystal structures is shown along the [100] and [111] crystallographic directions.

When β-[$Cu_2(H_2O)(L2)_2$] is suspended in distilled water for 24 h, the complete removal of any DMF and H_2L2 residual molecules can be achieved (as confirmed by IR spectroscopy, Figure 3.23) and water exchanged material $\{[Cu_2(H_2O)(L2)_2]\cdot 4.5(H_2O)\}_n$ (β*-[$Cu_2(H_2O)(L2)_2$]) is obtained. β*-[$Cu_2(H_2O)(L2)_2$] material maintains the same powder diffraction pattern of β-[$Cu_2(H_2O)(L2)_2$], which indicates that the porous framework remains unchanged (Figure 3.24), although slight variations in peaks height confirm the differences in the nature and amount of solvent molecules in the channels. Therefore, we found that the difference between β-[$Cu_2(H_2O)(L2)_2$] and β*-[$Cu_2(H_2O)(L2)_2$] solids is limited to molecules hosted in the channels but, anyhow, the need to achieve a material containing only water molecules in the channels becomes evident when adsorption properties and structural transformations are measured and pretend to be explained.

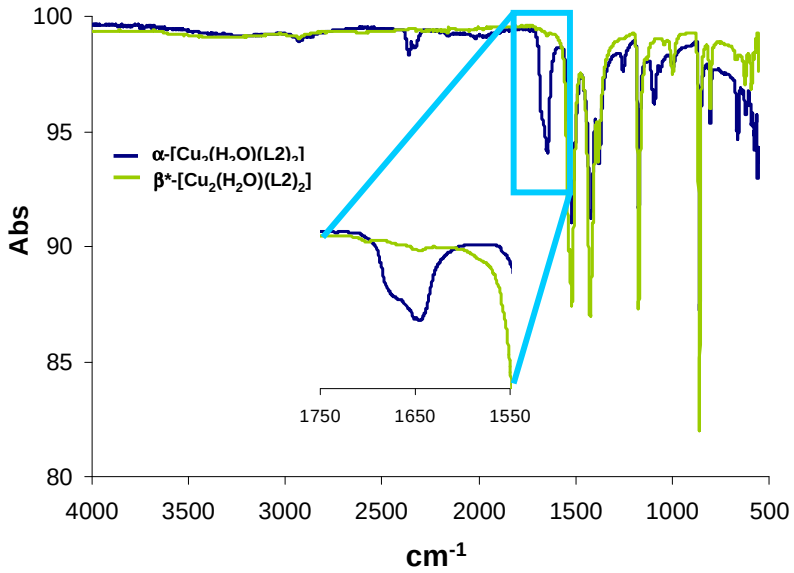

Figure 3.23. IR spectra of α-[$Cu_2(H_2O)(L2)_2$] and β*-[$Cu_2(H_2O)(L2)_2$] with expansion of the C=O stretching region (1750-1550 cm^{-1}). No DMF and H_2L2 C=O stretching peaks can be found in β*-[$Cu_2(H_2O)(L2)_2$] spectrum.

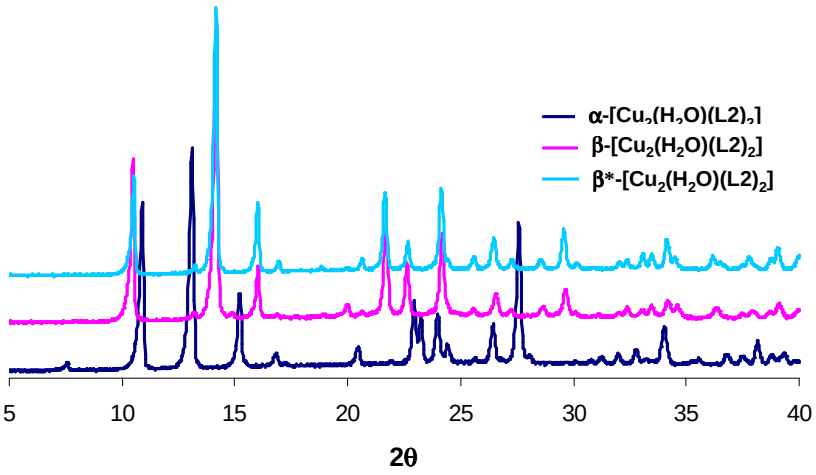

Figure 3.24. XRPD of α-$[Cu_2(H_2O)(L2)_2]$, β-$[Cu_2(H_2O)(L2)_2]$ and β*-$[Cu_2(H_2O)(L2)_2]$ materials.

Thermal stability

The study of thermal stability of α-$[Cu_2(H_2O)(L2)_2]$ and β∗-$[Cu_2(H_2O)(L2)_2]$ materials have been performed using thermogravimetric analysis. The thermogravimetric diagram of α-$[Cu_2(H_2O)(L2)_2]$ (Figure 3.25) shows a large weight loss (-30 %) around 100 ºC that corresponds to the removal of water and MeOH molecules (probably found on the external surface of the sample) and of guest DMF molecules. A second and well defined drop in sample weight starts between 270 ºC and 300 ºC which corresponds to framework decomposition process. The TGA curve of water exchanged β∗-$[Cu_2(H_2O)(L2)_2]$ solid is slightly different as the first step (-15 %) ends at lower temperature (T = 80 ºC) and clearly corresponds to the loss of guest water molecules (4.5 *per* formula unit, calculated -16.1 %). Around 120 ºC, a second small step reveals the loss of 1 H_2O molecule *per* $Cu_2(L2)_2$ unit (experimental -3.8 %, calculated -4.3 %) that is attributed to the removal of the water molecule bridging the two copper central atoms. After this event, there is a flat plateau, up to temperatures above 300 ºC when a steep weight loss takes place indicating framework decomposition.

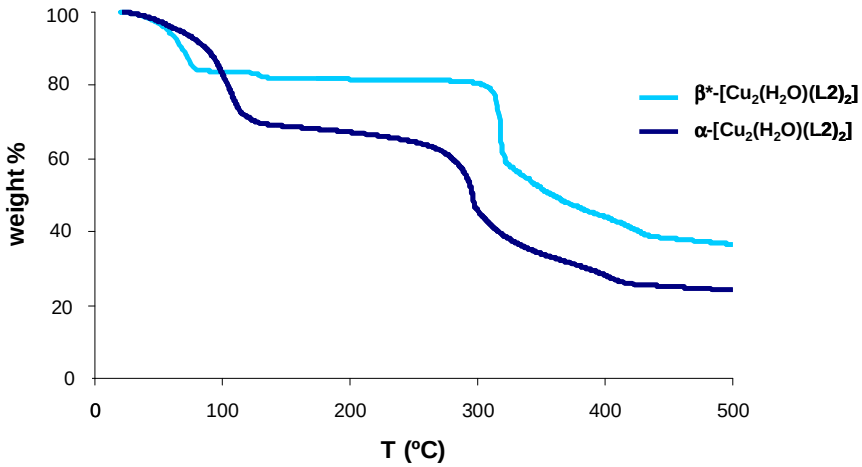

Figure 3.25. TGA traces for α-$[Cu_2(H_2O)(L2)_2]$ and β*-$[Cu_2(H_2O)(L2)_2]$ materials.

It is worth noticing that the overall amount of water molecules in β*-$[Cu_2(H_2O)(L2)_2]$ material determined by TGA (namely 5.5 molecules *per* $Cu_2(L2)_2$ unit) is in perfect agreement with the water vapour adsorbed amount obtained for β*-$[Cu_2(H_2O)(L2)_2]$ solid at 298 K (5.4 molecules per $Cu_2(L2)_2$ unit, see below) as well as with the results obtained from elemental analysis (see Appendix I).

Taking into account the guest exchange properties of α-$[Cu_2(H_2O)(L2)_2]$ and TGA curves, it is clear (as already mentioned before) that pore guest molecules have an impact in the activation conditions and that gas adsorption properties may strongly depend on them. Therefore, it is necessary to obtain a completely evacuated framework (without any solvent molecules and/or free ligand inside the pores) in order to optimize the gas adsorption properties of this material. With this aim, we decided to activate the as- synthesized α-$[Cu_2(H_2O)(L2)_2]$ as follow: i) evacuation at 120 ºC for 7 h under high vacuum, ii) soaking in H_2O for 24 h (to remove any impurity of unreacted H_2L2 ligand, $CuCl_2$ or DMF), iii) evacuation at 150 ºC for 7 h under high vacuum. In this way, a dark blue, fully activated material is obtained (of γ-$[Cu_2(L2)_2]$ formulation) (Figure 3.26). We must underline that this solid does not contain anymore the acua molecules, bridging the two Cu centres in the dimeric unit, as evidenced by TGA (see below) and by elemental analysis (see Appendix I).

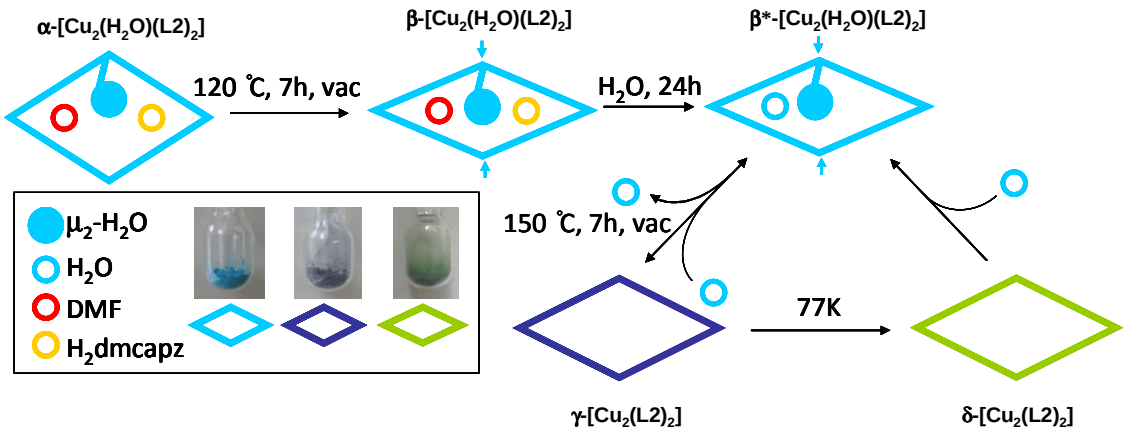

Figure 3.26. Summary of the activation processes of $([Cu_2(H_2O)(L2)_2]_n$ and structural state which responds to external stimuli. Bridging water (blue circle), free water (empty blue circle), free DMF (empty red circle), free H_2L2 (empty orange circle); α-$[Cu_2(H_2O)(L2)_2]$ (blue diamond), β-$[Cu_2(H_2O)(L2)_2]$ and β*-$[Cu_2(H_2O)(L2)_2]$ (squeezed blue diamond), γ-$[Cu_2(L2)_2]$ (dark blue diamond), δ-$[Cu_2(L2)_2]$ (green diamond).

γ-$[Cu_2(L2)_2]$ is extremely sensitive to ambient moisture, which is manifested by a rapid colour change to sky blue (within few minutes) upon exposure to open air. This feature is consistent with the loss of the μ_2-OH_2 bridge between Cu atoms in α-$[Cu_2(H_2O)(L2)_2]$ to yield the fully activated γ-$[Cu_2(L2)_2]$ material. Indeed, the weight loss at 120 ºC in TGA trace and the concomitant marked colour change are indicative of a change in the coordination environment of Cu centres (see above) upon the formation of γ-$[Cu_2(L2)_2]$ phase. This process can be related to the one taking place during the activation of CuBTC material,[24] for which an appreciable colour change (from light blue to deep purple) takes place upon loss of the water molecules coordinated to Cu centres. In both cases, the metal atom reduces its coordination number from 5 (distorted square pyramidal geometry) to 4 (distorted square planar).

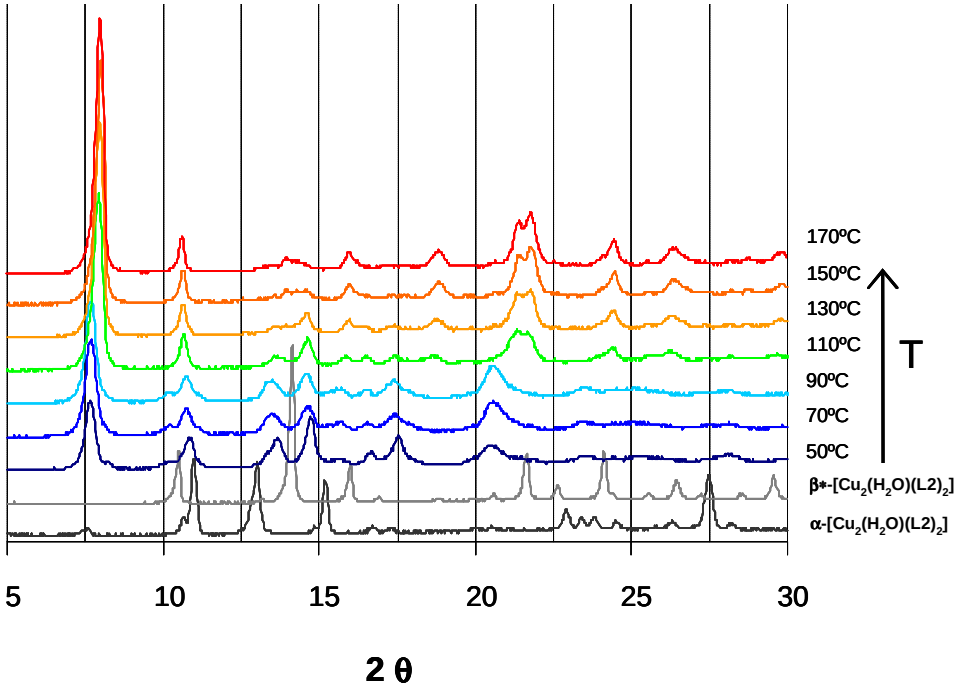

Figure 3.27. Variable temperature XRPD on β*-$[Cu_2(H_2O)(L2)_2]$ showing the formation of γ-$[Cu_2(L2)_2]$ above 100 ºC. Temperature range: 50 ºC - 170 ºC. Temperature program: steps of 20 ºC, temperature kept constant for 1.5 h for each step.

Switchable behaviour

Structural changes taking place during the β*-$[Cu_2(H_2O)(L2)_2]$ → γ-$[Cu_2(L2)_2]$ transformation have been monitored by variable temperature XRPD (Figure 3.27) and are indicative of changes in cell parameters even if the transformation to γ-$[Cu_2(L2)_2]$ phase is not clearly defined. Indeed, at 50 ºC the powder diffraction pattern of the solid does not correspond anymore to that measured for β*-$[Cu_2(H_2O)(L2)_2]$ indicating that a structural transformation takes place in the low temperature range. The most evident change occurs between 90 ºC and 110 ºC when the reflection at 2θ = 20.5º shifts to higher angles and splits into two peaks (2θ = 21.6º and 21.9º). Unfortunately, β-$[Cu_2(H_2O)(L2)_2]$ → γ-$[Cu_2(L2)_2]$ transition is not single-crystal-to-single-crystal, due to the breakage of the β-$[Cu_2(H_2O)(L2)_2]$ crystal as a consequence of profound structural modifications. Therefore, the lack of single crystal diffraction data for γ-$[Cu_2(L2)_2]$ material makes impossible any unequivocal consideration, even if reliable suppositions can be figured out to explain structural changes. Therefore we presume that, in the 90 º-110 ºC temperature range, the H_2O bridging molecule is progressively removed. Anyway, the small difference in the temperature at which the water molecule is lost, in comparison to TGA trace (120 ºC), should be attributed to the different heating rate

used in both experiments: namely, 10 ºC min^{-1} thermogravimetric analysis and temperature kept constant for 1.5 h for each temperature step in variable temperature XRPD experiment.

Interestingly, when γ-$[Cu_2(L2)_2]$ material is frozen at liquid nitrogen temperature (to perform gas adsorption experiment at this temperature) a manifest change of sample's colour from dark blue to forest green occurs. Very importantly, this reveals that a further phase transition γ-$[Cu_2(L2)_2]$ → δ-$[Cu_2(L2)_2]$ that takes place at 77 K under dynamic vacuum (see Figure 3.26). The new green phase (δ-$[Cu_2(L2)_2]$) is very stable in air and, unlike γ-$[Cu_2(L2)_2]$, does not adsorb ambient moisture to turn into β*-$[Cu_2(H_2O)(L2)_2]$ phase, even after 1 month. δ-$[Cu_2(L2)_2]$ only reverts to β*-$[Cu_2(H_2O)(L2)_2]$ phase within few minutes, if soaked in distilled water (Figure 3.26). However, if this material is soaked in dry, weakly polar solvents such as CH_2Cl_2 or $CHCl_3$ the transition to β*-$[Cu_2(H_2O)(L2)_2]$ phase does not occur and the material keeps the forest green colour for few days. These findings indicate that δ-$[Cu_2(L2)_2]$ is an empty material and, indeed, its TGA curve (see Figure 3.28) shows no weight loss until framework decomposition around 280 ºC. Consequently, δ-$[Cu_2(L2)_2]$ can be considered as a new completely evacuated porous phase with a reduced hydrophilicity compared to γ-$[Cu_2(L2)_2]$, as it will be confirmed by H_2O adsorption isotherms presented below.

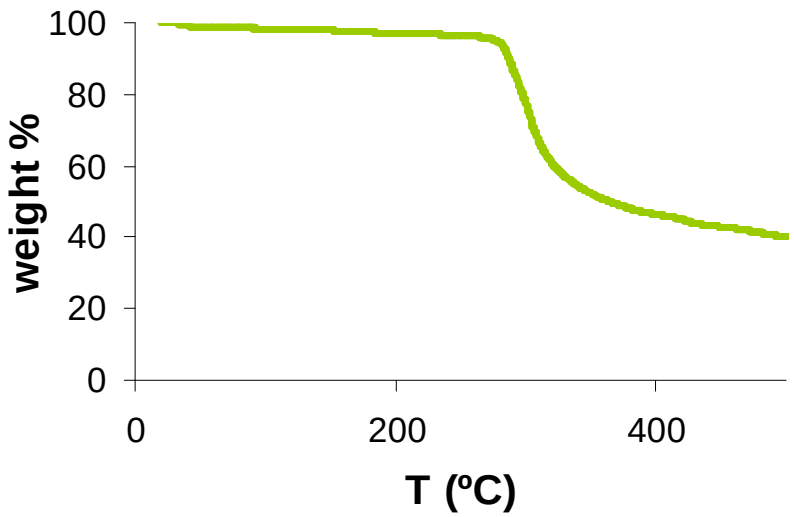

Figure 3.28. TGA trace for δ-$[Cu_2(L2)_2]$ material in N_2 atmosphere.

The change in colour from dark blue in γ-[$Cu_2(L2)_2$] to forest green in δ-[$Cu_2(L2)_2$] evidences a further change in the stereochemistry the metal centres.[25] We presume that this change might be promoted by a small twist of L2 ligands, which may lead to a distortion from the original square planar geometry in γ-[$Cu_2(L2)_2$] to a tetrahedrally distorted square planar environment in δ-[$Cu_2(L2)_2$]. This assumption would agree with the much more hydrophobic nature of δ-[$Cu_2(L2)_2$] material compared to γ-[$Cu_2(L2)_2$] since the access to the framework porosity is expected to be more difficult if L2 ligands are slightly twisted. Unfortunately, it has not been possible to register the electronic spectrum of γ-[$Cu_2(L2)_2$] as a consequence of its moisture sensitivity. However, the supposition of a tetrahedral distortion is also supported by the comparison of UV-vis spectra of β*-[$Cu_2(H_2O)(L2)_2$] and γ-[$Cu_2(L2)_2$] materials (Figure 3.29) and by magnetic measurements (see below).

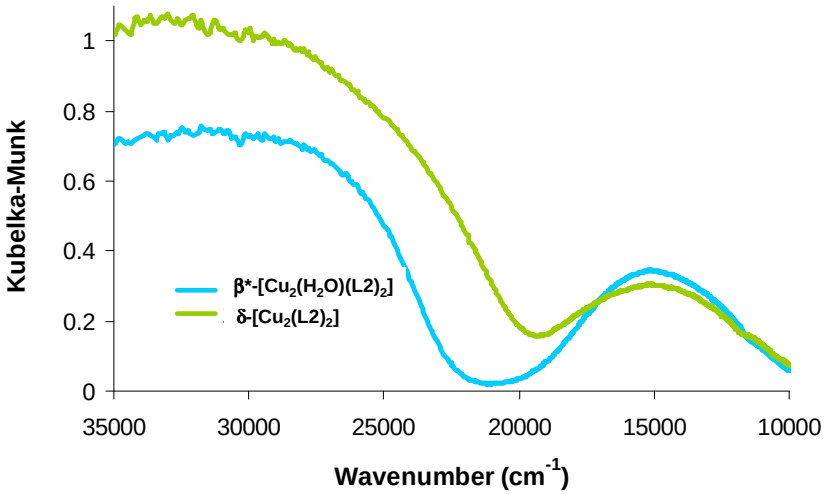

Figure 3.29. UV-visible spectra of β*-[$Cu_2(H_2O)(L2)_2$] and δ-[$Cu_2(L2)_2$] materials.

In both UV-vis spectra, we can see a well defined peak at 15300 cm^{-1} corresponding to the *d-d* transition of Cu(II) species and a broad edge at higher energies (much broader and red shifted for δ-[$Cu_2(L2)_2$] compound than for β*-[$Cu_2(H_2O)(L2)_2$]). The red shift of the latter transition, attributable to a LMCT transition,[26] can be explained considering that the removal of water molecules from the copper dimeric unit increases the electron density on the carboxylate and pyrazolate groups still coordinated to Cu(II) centres. This local structural change leads to an increase of the ionicity of Cu(II) ions and a red shift of the LMCT transition.[27] Moreover, the difference in the intensity ratio between *d-d* and MLCT transitions for the two materials, suggests a different degree of *p-d*

hybridization, that is caused by a change in the geometry around copper ions, namely form square pyramidal (β*-$[Cu_2(H_2O)(L2)_2]$, higher hybridization) to tetrahedrally distorted square planar (δ-$[Cu_2(L2)_2]$, lower hybridization).[28]

Magnetic properties

We deeply investigated the local structural information of Cu(II) centres from the magnetic point of view, since it is expected that the magnetic exchange will mainly take place through pyrazolate bridges from a Cu(II) binuclear system. The thermal behaviour of the magnetic susceptibility for β*-$[Cu_2(H_2O)(L2)_2]$ and δ-$[Cu_2(L2)_2]$ has been measured in the 2-300 K temperature range and is shown in Figure 3.30. β*-$[Cu_2(H_2O)(L2)_2]$ shows the typical χ_M *vs* T plot for a moderately strong antiferromagnet. The $\chi_M T$ values decay continuously to reach zero value at low temperatures and the χ_M values increase gradually up to a maximum of 0.0028 cm^3 mol^{-1} at 150 K, which is typical of a copper(II) binuclear system. Interestingly, magnetic measurements on δ-$[Cu_2(L2)_2]$ show a very similar trend with the maximum of χ_M being shifted down to 125 K. The experimental data have been fitted to the Bleaney-Bowers equation[29] (see Figure 3.30):

$$\chi_M = \frac{2Ng^2\mu^2}{kT(3 + \exp(-2J/kT))}$$

which results from a consideration of the eigenvalues of $H = -2J \cdot S1 \cdot S2$, the Heisenberg exchange Hamiltonian. In this expression, χ_M represents the susceptibility per mole of the binuclear unit corrected for diamagnetism and temperature independent paramagnetism, $2J$ is the singlet-triplet energy gap, g is the g-tensor for the individual metal centres and μ is the magnetic dipole of the binuclear unit.

The best fit results give a value of g = 2.08 and $2J$ = - 163 cm^{-1} for β*-$[Cu_2(H_2O)(L2)_2]$ and g = 1.99 and $2J$ = -149 cm^{-1} for δ-$[Cu_2(L2)_2]$. These values are consistent with the efficiency of pyrazolate bridges to transmit an antiferromagnetic interaction in copper(II) binuclear systems.[30] The slight difference between the two materials found in the magnetic exchange is probably related to the stereochemical modification concomitant to the removal of the bridging water molecule in δ-$[Cu_2(L2)_2]$.

It should be noted, however, that the μ_2-OH_2 bridge is probably not affecting significantly the magnetic properties of the copper binuclear system as a consequence of the weak interaction with the axial positions of copper coordination polyhedra. Therefore, the small differences found in the magnetic behaviour of these systems should be attributed to a possible tetrahedral distortion of the metal centres and/or to deviations of the pyrazole ring from Cu-N-N-Cu plane,[31] as already discussed in the previous section.

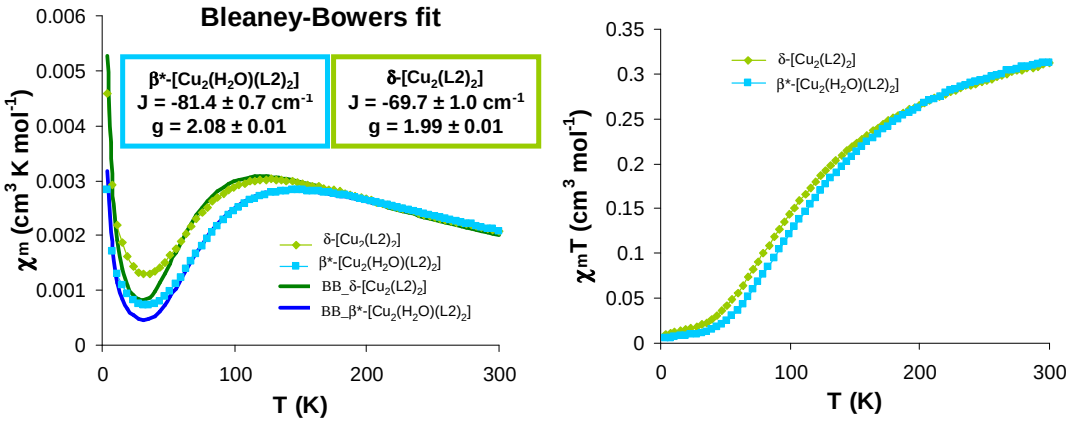

Figure 3.30. (Left) Thermal variation of the molar susceptibility with Bleaney-Bowers fit and (right) $\chi_m T$ *vs* T plot for β*-[$Cu_2(H_2O)(L2)_2$] (blue squares) and δ-[$Cu_2(L2)_2$] (green diamonds).

The above described ionicity change of coordination bond and coordination geometry will also reduce the accessibility of guest molecules to the open metal sites. Moreover, it will lead to a larger exposition of the hydrophobic methyl groups of L2 ligand, preventing the entrance of moisture water molecules into the cavities. Therefore water can only diffuse into the porous structure at relative higher moisture pressures for δ-[$Cu_2(L2)_2$] compared to γ-[$Cu_2(L2)_2$] (see water adsorption isotherms presented below).

Gas and vapour separation experiments

Static solid-gas adsorption

The flexible nature of α-[$Cu_2(H_2O)(L2)_2$] porous framework, as well as the formation of accessible open metal sites, prompted us to investigate the adsorptive properties of this system. With this purpose, we have studied, in detail, solid-gas adsorption features of δ-

$[Cu_2(L2)_2]$ (and/or γ-$[Cu_2(L2)_2]$) towards a wide variety of gas and vapour probe molecules.

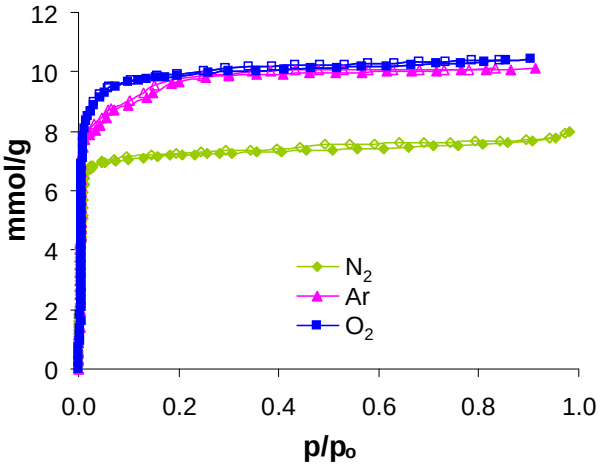

Figure 3.31. N_2 (green diamonds), Ar (pink triangles) and O_2 (blue squares) adsorption isotherms (77 K) for δ-$[Cu_2(L2)_2]$. Empty symbols denote desorption.

δ-$[Cu_2(L2)_2]$ exhibits reversible type I adsorption isotherms towards N_2, (kinetic diameter: 3.64 Å), Ar (3.4 Å) and O_2 (3.46 Å)[32] at 77 K which are typical of crystalline microporous materials (Figure 3.31). The N_2 isotherm reveals the reversible uptake of 7.5 mmol g^{-1} at p/p_o = 0.5 which corresponds to a BET specific surface area of 539 m^2 g^{-1} and a pore volume of 0.227 cm^3 g^{-1} (at p/p_o = 0.981). The adsorption capacities for O_2 and Ar are quite similar, although in the pressure range $0.1 < p/p_o < 0.2$ the Ar adsorption isotherm shows some steps which are characteristics of a flexible framework,[33] in agreement with the above described results. The adsorbed gas amount reaches 10 mmol g^{-1} (at p/p_o = 0.5) for both O_2 and Ar, and the corresponding BET specific surface areas account for 663 and 643 m^2 g^{-1}, respectively. These values are slightly larger than those obtained with N_2, which is in agreement with the decreasing kinetic diameters of essayed probe gases (N_2 > Ar > O_2). As already pointed out before, sample's activation conditions must be carefully determined since the porosity of the material is strongly affected by pre-treatment steps. As an example, we show in Figure 3.32 the O_2 adsorption isotherms (77 K) for the fully activated δ-$[Cu_2(L2)_2]$ phase and for the bulk α-$[Cu_2(H_2O)(L2)_2]$ solid, heated at 120 ºC for 7 h under high vacuum. A marked difference in the oxygen adsorbed amount is detected and it is a direct consequence of the inefficient removal of DMF and H_2L2 guest molecules form α-$[Cu_2(H_2O)(L2)_2]$ framework that, necessarily, shows a lower accessible void volume.

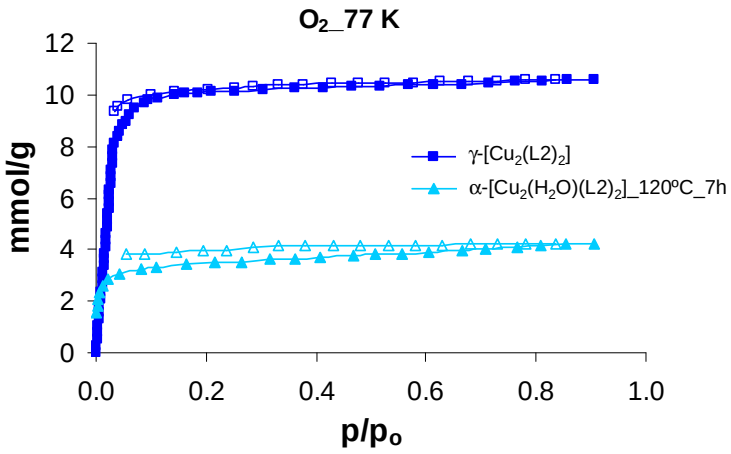

Figure 3.32. O_2 adsorption isotherms (77 K) for α-$[Cu_2(H_2O)(L2)_2]$ (activated at 120 ºC, 7 h under vacuum) and δ-$[Cu_2(L2)_2]$ as an exhaustive example of the effect of activation conditions on the material's porosity.

We have also measured gas adsorption isotherms of γ-$[Cu_2(L2)_2]$ at 195 K for a variety of probe molecules, namely CH_4, C_2H_2, C_2H_4, C_2H_6, CO_2 (Figure 3.33), CO and N_2 (Figure 3.34), inspired by the growing interest in separation of complex mixtures of these molecules.[34] For methane, the adsorption capacity is very low and the adsorption branch of the isotherm can be considered of type II, which is characteristic of a weak interaction of this probe molecule with the framework. However, the desorption branch follows type I isotherm giving rise to the formation of a wide hysteresis loop. This behaviour is in agreement with the flexible nature of γ-$[Cu_2(L2)_2]$ framework and supercritical nature of CH_4 at this temperature. By contrast, acetylene, ethane, ethylene and carbon dioxide are strongly adsorbed by the porous framework.

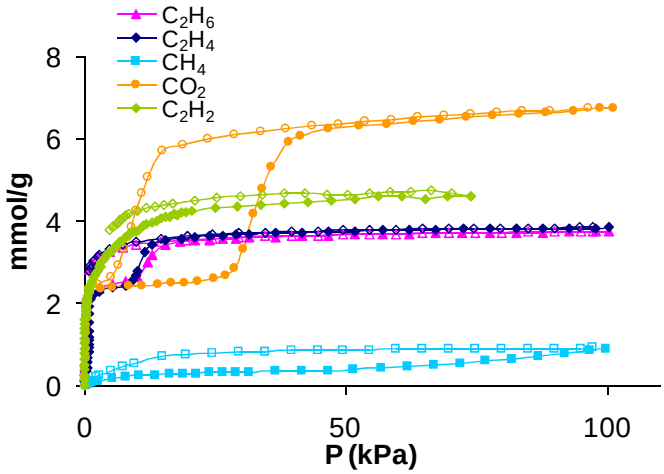

Figure 3.33. C_2H_2 (green diamonds), C_2H_4 (blue diamonds), C_2H_6 (pink triangles), CH_4 (light blue squares) and CO_2 (orange circles) adsorption isotherms (195 K) for γ-$[Cu_2(L2)_2]$. Empty symbols denote desorption.

Interestingly, acetylene exhibits type I adsorption isotherm while the other gases (C_2H_4, C_2H_6, CO_2) exhibit an unusual two step shape. In the case of acetylene, we can take into account its large quadrupole moment [35] that would lead to a better accommodation of the molecules into the channels. Differently, for C_2H_4, C_2H_6 and CO_2, in the very low pressure region, a steep uptake of 2.3 mmol g^{-1} takes place corresponding to the adsorption of 1 molecule of gas *per* each Cu_2 dinuclear unit, suggesting that a strong host-guest interaction with the convergent open metal sites is involved in this first step. Afterwards, at P = 10 kPa, a second step for ethane and ethylene isotherms is observed, giving rise to an uptake of 3.5 mmol of gas *per* g of γ-$[Cu_2(L2)_2]$, indicating a gate opening behaviour with concomitant entrance of further guest molecules which are physisorbed into the pores. Interestingly, the desorption branch of the isotherm does not follow the adsorption branch at pressures below 20 kPa and, as a consequence, a hysteresis loop is formed. This behaviour implies that ethane and ethylene molecules are strongly retained in the porous framework and are released only at very low relative pressures.

Noteworthy, for CO_2 the gate opening effect is more profound permitting the final accommodation of more than 6 mmol of CO_2 *per* g of PCP. It should also be noted that the desorption branch is not recovering the adsorption one and a larger hysteresis loop is observed. However, in contrast to the previous cases, the loop closing takes place at higher pressures, which means that interaction of CO_2 (adsorbed molecules but not physisorbed ones) with the pore surface in the framework is less strong than with light hydrocarbon molecules since CO_2 is no longer retained by the framework at pressures as high as 15 kPa.

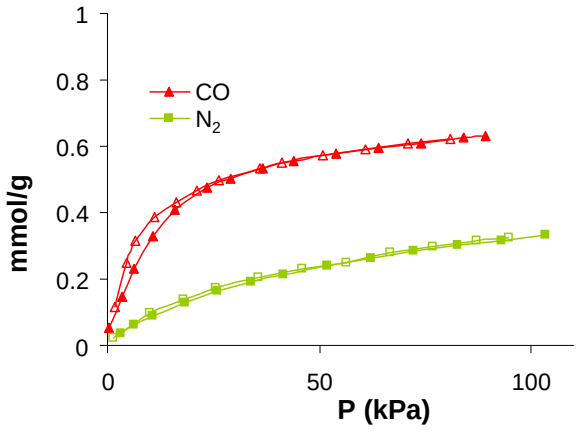

Figure 3.34. N_2 (blue squares) and CO (pink triangles) adsorption isotherms at 195 K for γ-$[Cu_2(L2)_2]$. Empty symbols denote desorption.

On the other hand, N_2 and CO adsorption at 195 K are almost negligible (see Figure 3.34) indicating low interaction of these probe molecules with both the metal active sites and the pore surface of the framework. As a consequence, in the low pressure range, i.e. at P < 10 kPa, the framework shows just partial adsorption selectivity of C_2H_2 *vs* C_2H_4, C_2H_6 and CO_2, while a very high selectivity of all adsorbed probe molecules (C_2H_2, C_2H_4, C_2H_6 and CO_2) towards CO and N_2 gases (see Table 3.2). In the higher pressure region, i.e. P = 50 kPa, the adsorption selectivity of C_2H_2 *vs* C_2H_4 and C_2H_6 diminishes while adsorption of CO_2 overcomes the values of the rest of probe gases. These results (although obtained from single component gas adsorption isotherms) should be of interest for industrial gas separation processes.

Table 3.2. Partition coefficients for γ-$[Cu_2(L2)_2]$ with different probe gas molecules from single component isotherms (195 K) and gas chromatographic method.

Entry	P = 10 kPa	P = 50 kPa	GC method
C_2H_2 / CO_2	1.5	0.7	3.6
C_2H_2 / C_2H_4	1.4	1.2	0.7
C_2H_2 / C_2H_6	1.4	1.2	0.5
C_2H_4 / C_2H_6	1.0	1.0	0.7
C_2H_4 / CO_2	1.1	0.6	5.3
C_2H_6 / CO_2	1.1	0.6	7.2
CO_2 / CO	5.3	10.9	∞
CO_2 / N_2	16.9	26.2	∞

It is also possible to calculate the partition coefficients from the results obtained in pulse gas chromatographic experiments on γ-$[Cu_2(L2)_2]$. In this case, the best performances of the material are found in the separation of C_2H_n gases from CO_2, since the latter component is not strongly retained by the framework at high temperatures. It is worth noticing that results in Table 3.2 show some differences if we compare the two methods. We can justify this taking into account the very low gas partial pressures in pulse-GC experiments and the different temperature range of the experiments.

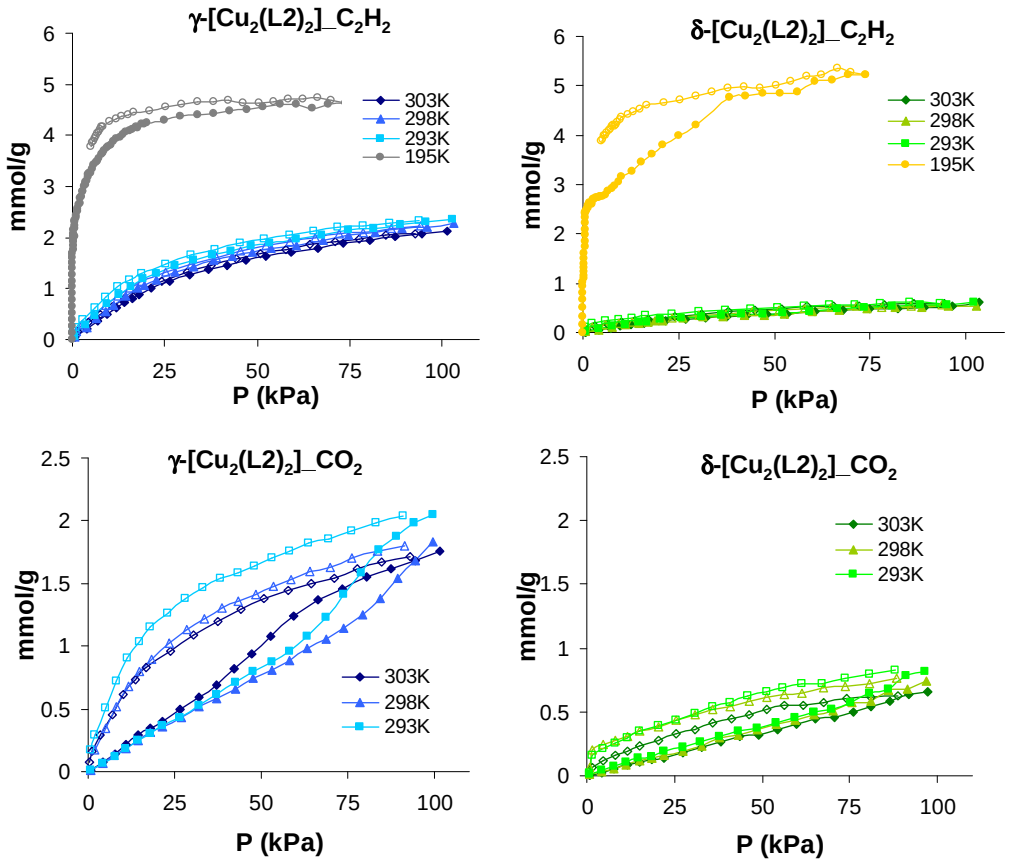

Figure 3.35. (Above) C_2H_2 gas adsorption isotherms at 195, 293, 298 and 303 K for γ-[Cu_2(L2)$_2$] (left) and δ-[Cu_2(L2)$_2$] (right); (below) CO_2 gas adsorption isotherms at 293, 298 and 303 K for γ-[Cu_2(L2)$_2$] (left) and δ-[Cu_2(L2)$_2$] (right).

In addition, we were also interested in investigating the effect of γ-[Cu_2(L2)$_2$] → δ-[Cu_2(L2)$_2$] phase transition as switchable adsorptive properties. To this aim we measured the adsorption isotherms of CO_2 and C_2H_2 probe gases in the 195-303 K temperature range for both γ-[Cu_2(L2)$_2$] and γ-[Cu_2(L2)$_2$] phases (Figure 3.35). Experimental results show that γ-[Cu_2(L2)$_2$] porous structure is able to uptake a larger amount of gasses in the low pressure range than δ-[Cu_2(L2)$_2$], which agrees with a more accessible porous structure for the former material, as widely proved and discussed before. Interestingly, for δ-[Cu_2(L2)$_2$] there is hysteretic behaviour (especially at low temperature) as well as a stronger temperature dependence for the adsorption of acetylene than for γ-[Cu_2(L2)$_2$]. For example, the amount of C_2H_2 adsorbed in γ-[Cu_2(L2)$_2$] at P = 100 kPa and 195 K reaches 4.6 mmol g^{-1} and it diminishes to 2.3 mmol g^{-1} at 293 K. By contrast, in the case of δ-[Cu_2(L2)$_2$] the adsorbed amount at 195 K is 5.2 mmol g^{-1} and it diminishes to 0.6 mmol g^{-1} at 293 K. The observed difference

should be explained considering the better accessibility to the porous structure and open metal sites in γ-[$Cu_2(L2)_2$] than in δ-[$Cu_2(L2)_2$]. In the case of CO_2, at temperatures close to ambient conditions, the maximum amount of adsorbed gas is similar to the C_2H_2 one. However, it should be noted that the shape of the isotherms is highly dependent on the nature of the probe gas, namely of type III with hysteresis loop formation for CO_2 *versus* reversible type I for C_2H_2. These results should be taken as a proof of highly selective porous networks, which are able to distinguish between two very closely related probe guest molecules with the same kinetic diameters (3.3 Å), similar shape and physical properties.

Vapour adsorption studies

In order to shed further light on the adsorptive and structural differences between γ-[$Cu_2(L2)_2$] and δ-[$Cu_2(L2)_2$] solids, we have also studied vapour adsorption of H_2O and MeOH at 298 K (Figure 3.36). In fact, water adsorption isotherm is, in general, a very useful tool for evaluating the hydrophobicity of a porous material and, in this case, would allow one to consolidate the hypothesis made on the slight twist of L2 ligand during the γ-[$Cu_2(L2)_2$] → δ-[$Cu_2(L2)_2$] transformation.

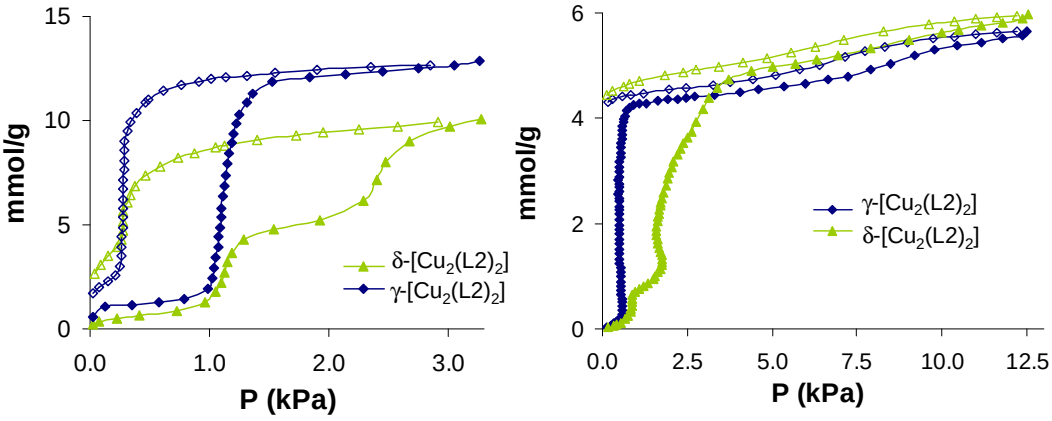

Figure 3.36. (Left) H_2O and (right) MeOH vapour adsorption isotherms at 298 K for γ-[$Cu_2(L2)_2$] (blue diamonds) and δ-[$Cu_2(L2)_2$] (green triangles). Empty symbols denote desorption.

So, in the case of H_2O adsorption, we distinguish for γ-[$Cu_2(L2)_2$] an initial step at very low pressures which should correspond to the incorporation of bridging water molecules to the open metal sites. This step is followed by a pronounced gate opening at P = 1.0 kPa for both γ-[$Cu_2(L2)_2$] and δ-[$Cu_2(L2)_2$], which should be related to the concomitant entrance of probe molecules into the porous structure. Interestingly, while

for γ-$[Cu_2(L2)_2]$ there is a single step in the adsorption branch, in the case of γ-$[Cu_2(L2)_2]$, this step is smaller and is followed by a second step at higher pressures of 2.3 kPa. Probably, the accommodation of the bridging acua molecule (1 molecule *per* Cu_2 unit at P = 1.0 kPa) is not providing the driving force required to twist L2 ligands and restore the square pyramidal geometry around the metal centre. However, this conformational change can take place just when a higher pressure is forcing water vapour molecules to enter the structure.

It should also be noted that, as previously found for CO_2 and C_2H_2, the guest accessibility to the porous structure of δ-$[Cu_2(L2)_2]$ is smaller than for γ-$[Cu_2(L2)_2]$ which is manifested by the higher gate pressure for γ-$[Cu_2(L2)_2]$. As previously found for other essayed probe gases (see above), desorption branches of the vapour adsorption isotherm for both phases do not recover the adsorption ones and consequently large hysteresis loops are found.

In the case of methanol adsorption, γ-$[Cu_2(L2)_2]$ and δ-$[Cu_2(L2)_2]$ phases again show large differences. As just described for water isotherms, the gate pressure for γ-$[Cu_2(L2)_2]$ is lower than for δ-$[Cu_2(L2)_2]$ and below the values found for H_2O.

Noteworthy, a second step in the adsorption branch of the isotherm of δ-$[Cu_2(L2)_2]$ is evident. The total amount of adsorbed methanol reaches 5.8 mmol g^{-1} for both samples. Regarding the desorption branches of the isotherms, we can conclude that the adsorption process is irreversible. Summarizing, once again, all the results point to a less accessible porous structure of δ-$[Cu_2(L2)_2]$ as compared to γ-$[Cu_2(L2)_2]$ and reveal that a higher energy input in δ-$[Cu_2(L2)_2]$ than in γ-$[Cu_2(L2)_2]$ is necessary in order to rearrange the network into the wide open form. The higher framework affinity for this probe molecule compared to water could be explained taking into account the anphiphilic nature of MeOH molecule: the concomitant presence of the polar -OH group and the apolar Me moiety could facilitate the adsorption of this species into a framework containing both Me groups and highly polarized open metal sites.

Dynamic gas adsorption studies

Gas-phase adsorption at zero coverage surface was studied using the pulse chromatographic technique employing a gas chromatograph and a packed column with *ca.* 1 g of 0.5 mm-pellets of both γ-$[Cu_2(L2)_2]$ and δ-$[Cu_2(L2)_2]$ materials. The maintenance of the original crystal structure (mechanical stress test) has been

demonstrated by means of XRPD (Figure 3.37). Since δ-[$Cu_2(L2)_2$] structure seems to be slightly affected by the application of pressure of 2 tons, we decide to directly freeze at liquid nitrogen temperature pellets of γ-[$Cu_2(L2)_2$] material in order to achieve δ-[$Cu_2(L2)_2$] solid suitable for gas chromatographic experiments.

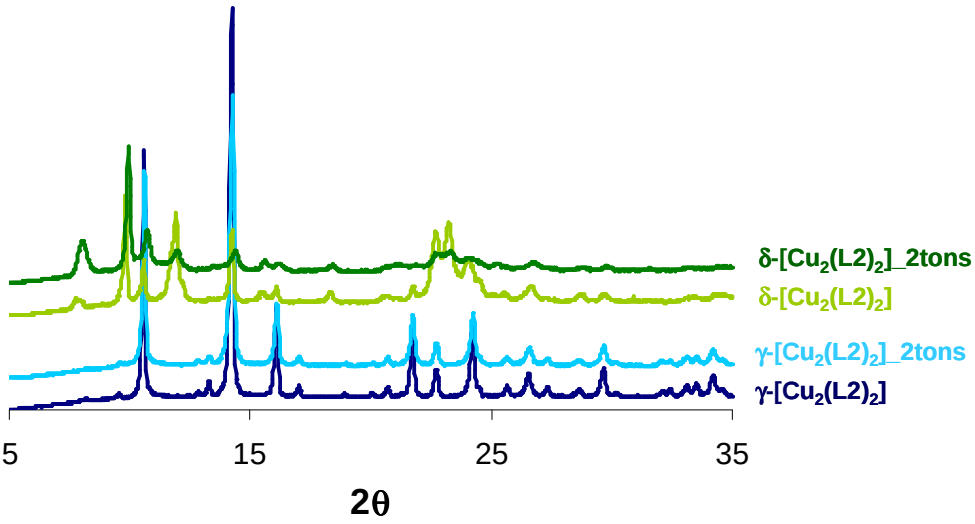

Figure 3.37. XRPD data for γ-[$Cu_2(L2)_2$] and δ-[$Cu_2(L2)_2$] before and after the application of 2 tons pressure.

Variable-temperature pulse gas chromatographic studies[36] have been carried out for NO, CO_2, C_2H_2, C_2H_4, C_2H_6, Ar, Kr and CO gas mixtures to establish the thermodynamic aspects of adsorption, as well as the separation abilities of γ-[$Cu_2(L2)_2$] and δ-[$Cu_2(L2)_2$] (Figure 3.38, as an example).

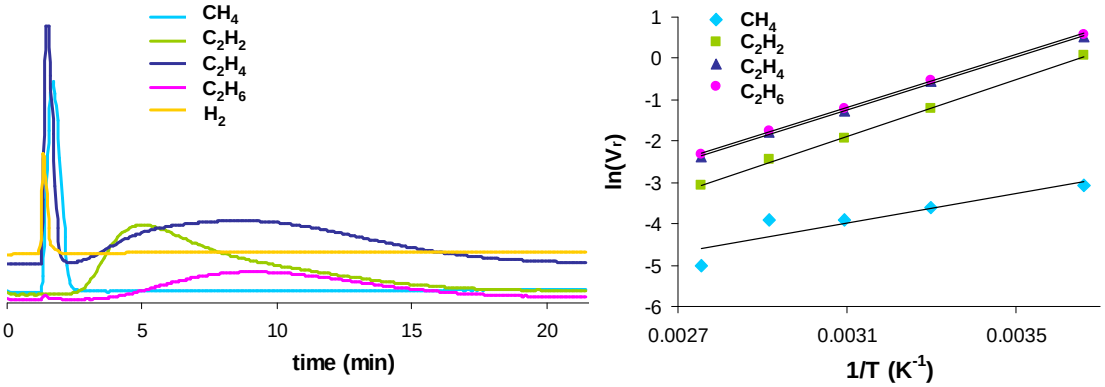

Figure 3.38. (Left) Variable-temperature pulse gas chromatograms for CH_4, C_2H_2, C_2H_4, C_2H_6 and H_2 mixture passed through a chromatographic column packed with γ-[$Cu_2(L2)_2$] using a He flow of 30 mL min^{-1}; (right) variation of the retention volume V_r (in cm^3 g^{-1}) as a function of adsorption temperature (273-363 K).

To quantify the strength of the interaction of these guest molecules, we have calculated the zero-coverage adsorption heats (ΔH_{ads}) from the variation of the retention volumes (V_g) as a function of temperature according to the equation $\Delta H_{ads} = -R[\partial(\ln V_g)/\partial(1/T)]$.[37] The direct relationship between the retention volume (V_g) and the Henry constant (K_H) also allowed us to calculate values of the Henry constant under ambient conditions (298 K). These studies revealed relatively high retention times for ethane, ethylene, acetylene and carbon dioxide, as well as relatively high adsorption heats (Table 3.3) indicative of a strong interaction of these probe gas molecules with γ-$[Cu_2(L2)_2]$ and δ-$[Cu_2(L2)_2]$ porous frameworks. These results agree with single gas adsorption isotherms presented above, and are indicative of the interaction between guest probe molecules and the open metal sites.

By contrast, methane, carbon monoxide, nitrogen monoxide, argon and krypton were characterized by low retention times. Although the strength of the host-guest interaction is generally higher for γ-$[Cu_2(L2)_2]$ framework than for δ-$[Cu_2(L2)_2]$, only slight differences between these two materials were found, which can be explained taking into account their closely related nature.

Table 3.3. Calculated Heats of Adsorption ΔH_{ads} (kJ mol^{-1}) and Henry Constants K_H (cm^3 m^{-2}) for γ-$[Cu_2(L2)_2]$ and δ-$[Cu_2(L2)_2]$materials.

Gas	$-\Delta H_{ads}$ (kJ/mol)		K_H (cm^3/m^2)	
	γ-$[Cu_2(L2)_2]$	**δ-$[Cu_2(L2)_2]$**	**γ-$[Cu_2(L2)_2]$**	**δ-$[Cu_2(L2)_2]$**
NO	17.5	15.8	0.021	0.008
CO	7.6	na	0.011	na
CO_2*	21.4	22.6	0.096	0.095
CH_4	15.0	9.2	0.029	0.013
C_2H_2*	27.7	26.0	0.350	0.173
C_2H_4*	26.4	21.6	0.509	0.156
C_2H_6	26.5	29.0	0.688	0.315
Ar	16.6	15.3	0.006	0.003
Kr	17.5	13.3	0.025	0.012

* Mean of different experiments; na = not available

Finally, breakthrough curve measurements have been performed on γ-$[Cu_2(L2)_2]$ with stream of CO_2/CH_4 1:1. Figure 3.39 shows that carbon dioxide is retained in the final amount of 1 molecule *per* Cu(II) dimer, while methane has no interaction with the

framework, thus confirming once again the consistency of the results obtained for single component adsorption measurements.

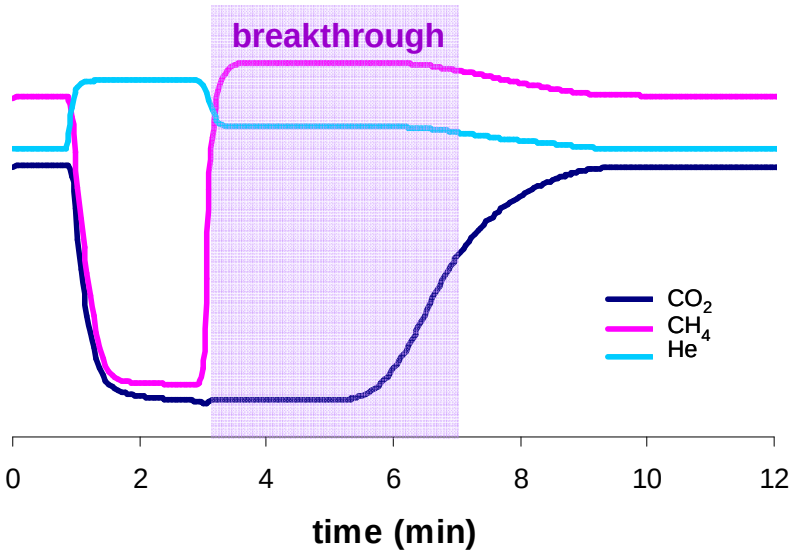

Figure 3.39. Breakthrough curves of the separation, performed by γ-[$Cu_2(L2)_2$], of 10 mL min^{-1} of CO_2 and 10 mL min^{-1} of CH_4 in a 10 mL min^{-1} He flow.

3.2.2. $Cu(HL2)_2$ compound

Crystal structure

The reaction between CuF_2 and H_2L2 in a mixture DMF/H_2O 1:1 for 24 h at 60 ºC affords a purple bulk solid containing purple-blue block crystals, of suitable size for single crystal X-ray diffraction measurement, of formulation $\{[Cu(HL2)_2]\cdot 4H_2O\cdot 2DMF\}_n$ ($Cu(HL2)_2$). Although fluoride ions are not found in the crystal structure, they play a significant role during the crystals growth (coordinative nature/basic nature) since they can not be replaced by chloride or bromide anions.

$\{[Cu(HL2)_2]\cdot 4H_2O\cdot 2DMF\}_n$ material crystallize in the *P2₁* space group with cell parameters a = 8.048(10) Å, b = 15.770(12) Å, c = 16.427(14) Å, β = 104.180(5)º and a corresponding cell volume V = 2021.4 $Å^3$. Cu^{2+} ions show a distorted octahedral configuration and connect four distinct $HL2^-$ ligands (partial deprotonation, see above). Indeed the apical positions are occupied by two N atoms from two organic linkers while the four axial positions are occupied by four O atoms belonging to two carboxylate groups from other two $HL2^-$ ligands. Therefore, the coordination mode of each ligand is O,O'-endobidentate, N-monodentate that result in the linear bridging of two Cu^{2+} ions (Figure 3.40-left). Noteworthy, H_2L2 ligand is not fully deprotonated under the reaction conditions since the hydrogen on N(1) is not removed during the crystallization process.

Moreover, the O,O'-endobidentate coordination of the carboxylate moiety to Cu^{2+} cation is asymmetric as the two Cu-O bonds have a length of 2.652 Å and 1.964 Å. Such a big difference is relied on the partial maintenance of the single and double nature of the C-O bonds in the carboxylate functional group. As a matter of fact, C-O bond lengths of 1.26 Å and 1.28 Å are found in the crystal structure, these values being too short for a typical C-O single bond (1.3 Å) and too long for a typical C=O double bond (1.2 Å) for carboxylate anions (Figure 3.40-right). Actually, in the $\{[Cu_2(H_2O)L2_2]\cdot solv\}_n$ compound presented in the previous section (3.2.1) a delocalization of the C=O double bond of the carboxylate occurs, hence both Cu-O distances measure 1.272 Å.

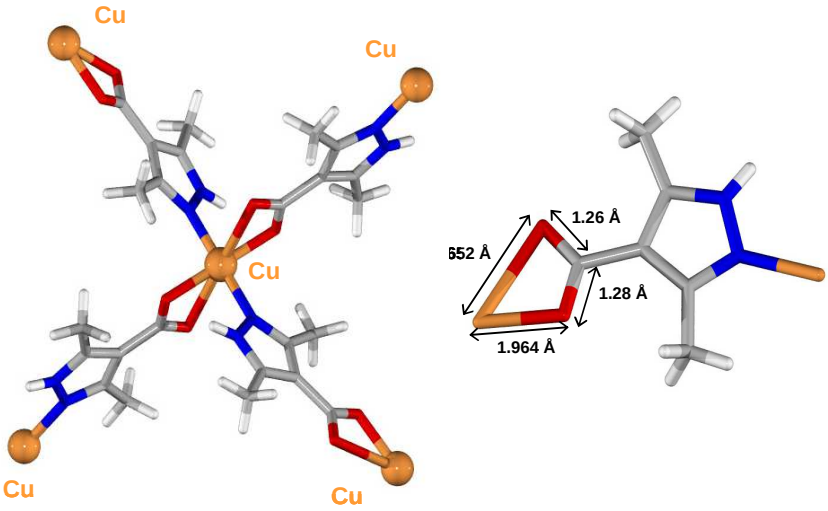

Figure 3.40. View of the basic structural motives found in the single crystal structure of $\{[Cu(HL2)_2]\cdot 4H_2O\cdot 2DMF\}_n$. **Cu**, **O**, **N**, C, **H** (white).

The square planar structural fragments formed by one Cu^{2+} ion and four $HL2^-$ ligands give rise to a layered structure of square grids packed along the *a* crystallographic axis. As can be appreciated in Figure 3.41, the layers horizontally lye along the *b* crystallographic axis while they form a zig-zag arrangement along the *c* axis.

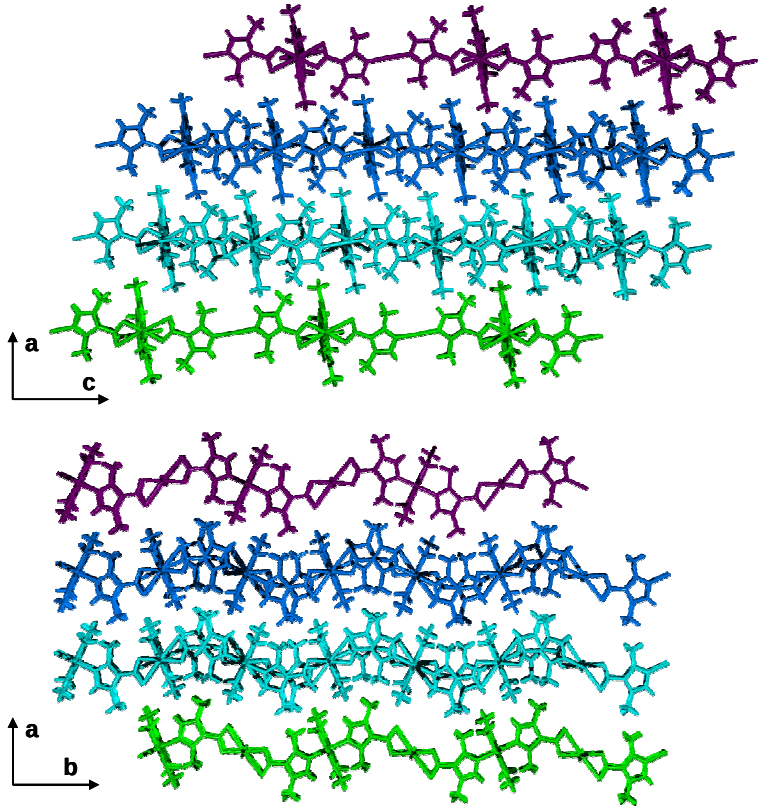

Figure 3.41. View of the layered structure of $Cu(HL2)_2$ material along the *b* (above) and *c* (below) crystallographic axes. Each independent layer is depicted in different colour; solvent molecules have been omitted for clarity.

If we consider a single layer (Figure 3.42.a and 3.42.b), we can see that DMF guest molecules are located at the centre of each square formed by four Cu^{2+} nodes connected by four ligand molecules. On the other hand, (Figure 3.42.c) water guest molecules lye in the space between two adjacent layers and form a grid of complex H-bonds with O- and N-donor atoms of $HL2^-$ ligands. In this way, as far as water molecules reside in the structure, the approaching of neighbour layers is avoided.

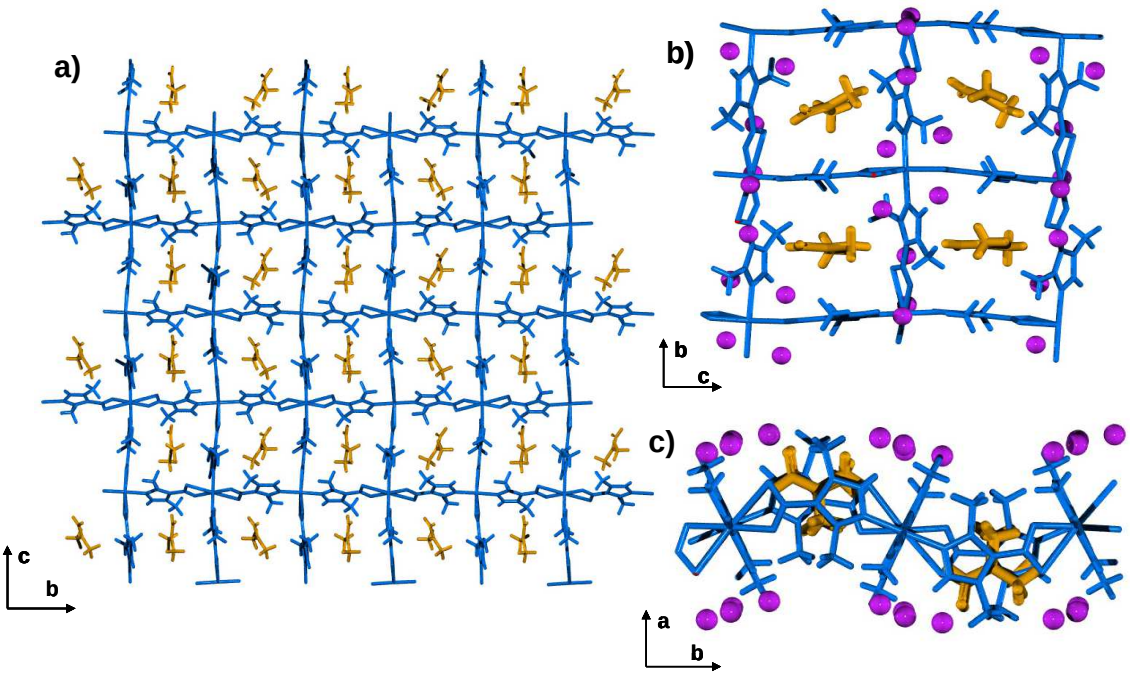

Figure 3.42. View of a single layer in $Cu(HL2)_2$ material along the *a* axis (a) and (b), and along the *c* axis (c). In a), water molecules have been omitted for clarity. **$Cu(HL2)_2$ grid**, **DMF**, **H_2O**.

Unfortunately, as already mentioned, the bulk material obtained as main product in the reaction between CuF_2 and H_2L2 ligand has a different structure, as can be deduced comparing measured XRDP of bulk solid and of $Cu(HL2)_2$ crystals (carefully separated from the purple powder in the reaction mixture), with the one simulated form single crystal X-ray diffraction data (Figure 3.43). Moreover, any attempt of obtaining $Cu(HL2)_2$ as main product resulted fruitless. Noteworthy, the powder diffraction pattern of $Cu(HL2)_2$ crystals indicates that preferential orientation of the sample occurs during its deposition on the sample holder, causing the anisotropic increase of peaks with (*n*00) Miller index as, for example, (100) at $2\theta = 11.33^{o}$ and (200) at $2\theta = 22.78^{o}$.

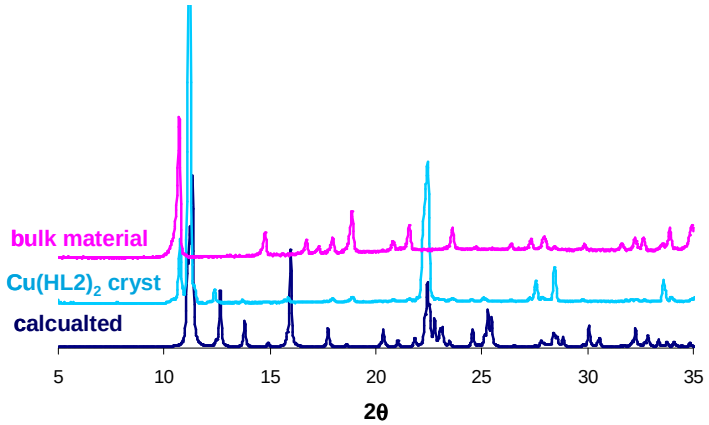

Figure 3.43. XRPD patterns for $Cu(HL2)_2$ material (calculated from single crystal data and experimental) and the one of the bulk material obtained in the same reaction.

Thermal stability

The thermal stability of $Cu(HL2)_2$ crystals has been studied. As shown in Figure 3.44 there is a quite good, although not perfect, agreement between the crystal structure and the results from thermogravimetric analysis. The water content has been calculated to be 2.5 molecules per $Cu(HL2)_2$ unit, instead of 2 as obtained from the single crystal data, on the basis of the elemental analysis results (see Appendix I). Therefore a first drop in the sample weight (exp: -14.1 %) around 70 ºC is attributed to the loss of water molecules (both crystallization and external surface water), while the second (exp: -11.4 %) around 165 ºC should correspond to the loss of crystallization DMF molecules. The complete rotting of the framework, concomitant to the ligand decomposition, takes place at 250 ºC.

Taking into account the framework structure and, in particular, the location of water molecules between $[Cu(HL2)_2]_n$ layers, the first drop of sample weight is likely to cause a significant structural change with the empty space between layers being filled by the approaching of successive layers.

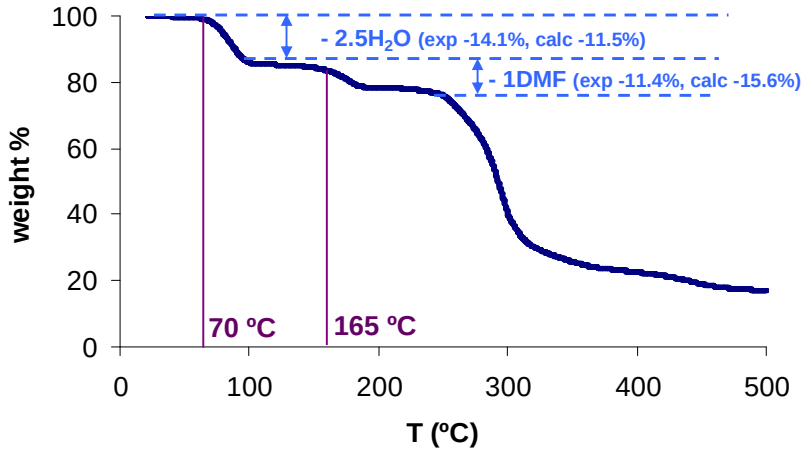

Figure 3.44. TGA trace for $Cu(HL2)_2$ material.

As a consequence of the difficulties encountered to get phase pure $Cu(HL2)_2$ material, no further characterization of this solid (magnetic measurement, adsorption isotherms…) has been performed. Moreover, N_2 adsorption isotherm (77 K) of the bulk material obtained during the synthesis of $Cu(HL2)_2$, show no porosity, confirming the probable dense nature of the activated material and its irrelevance for the purposes of this thesis.

3.3. Conclusions

The mixed O- and N-donor 3,5-dimethyl-4-carboxypyrazole ligand (H_2L2) has been used as a linker in the construction of two coordination polymers both based on Cu^{2+} ions, namely $[Cu(HL2)_2]\cdot solv$ and $[Cu_2(OH)(L2)_2]\cdot solv$.

The former material has been only characterized from the structural point of view, because of the difficulties encountered in order to get a pure phase bulk solid. It is a layered material where each copper ion is connected to four $HL2^-$ molecules in an octahedral geometry thereby generating square grid layers. The empty space within the grid is filled with DMF molecules while crystallization water molecules lye in the interlayer gap. No characterization of its porosity has been performed since no phase pure material has been achieved. Nevertheless, this material is an example of the richness of structures that can be obtained when the combination of metal ions and ligands is explored under different reaction conditions.

As a matter of fact, in the reaction of the same building blocks under similar conditions a 3D open porous framework, of formulation $[Cu_2(H_2O)(L2)_2]\cdot solv$, has been obtained. This material combines a set of unusual features: i) it has an unprecedented H_2O bridge between the two copper atoms in the dimeric building unit; ii) the removal of these water molecules by thermal treatment gives rise to the bi-stable $[Cu_2(L2)_2]$ (γ-$[Cu_2(L2)_2]$, δ-$[Cu_2(L2)_2]$) open network, which combines framework flexibility with unusual coordinatively unsaturated convergent adsorption active sites; iii) γ-$[Cu_2(L2)_2]$ converts into a novel δ-$[Cu_2(L2)_2]$ phase by simple freezing at liquid nitrogen temperature. The latter phase transition is accompanied by a concomitant drastic change in colour, from dark blue to forest green, thereby confirming a change in coordination stereochemistry of the metal centres. The extremely high stability of δ-$[Cu_2(L2)_2]$ in air is also a rare feature for an open framework. The higher hydrophobicity of δ-$[Cu_2(L2)_2]$ material (compared to γ-$[Cu_2(L2)_2]$) is a proof of the structural reorganization taking place during the freezing process.

The selective gas adsorption properties of γ-$[Cu_2(L2)_2]$ and δ-$[Cu_2(L2)_2]$ materials have been studied and compared. The adsorptive properties of both materials are dominated by the presence of highly active adsorption sites on the convergent coordinatively unsaturated metal centres and by framework flexibility which give rise to gated adsorption with many of the essayed probe gases. Noteworthy, γ-$[Cu_2(L2)_2]$ gives rise to large partition coefficients thus suggesting a possible application of this material

in gas separation processes. On the other hand, δ-[$Cu_2(L2)_2$] at temperatures close to room temperature has a reduced adsorption capacity compared to γ-[$Cu_2(L2)_2$]. This is a direct consequence of the reduced accessibility of the porous structure in δ-[$Cu_2(L2)_2$] compared to γ-[$Cu_2(L2)_2$], which is confirmed by lower values of interaction energy between the framework and the gas guest molecules, obtained in dynamic gas adsorption experiments.

Summarizing, the studied [$Cu_2(H_2O)(L2)_2$]·solv system is a very intriguing material which combines the presence of coordinatively unsaturated metal centres with framework plasticity giving rise to unusual gas adsorption properties. The origin of this behaviour is the coordination versatility and plasticity of copper(II) centres.

3.4. Bibliography

[1] S. Horike, S. Shimomura, S. Kitagawa, *Nat. Chem*. **2009**, *1*, 695.

[2] B. Murphy, B. Hathaway, *Coord. Chem. Rev*. **2003**, *243*, 237.

[3] J. A. Real, A. B. Gaspar, M. C. Muñoz, *Dalton Trans*. **2005**, 2062.

[4] C. H. Elscheinhorn, A. Salzer, *Organometallics*, Wiley-VCH, Weinheim, **2003**.

[5] G. Ferey, M. Latroche, C. Serre, F. Millange, T. Loiseau, A. Percheron-Guegan, *Chem. Commun.* **2003**, 2976.

[6] S. Horike, R. Matsuda, D. Tanaka, S. Matsubara, M. Mizuno, K. Endo, S. Kitagawa, *Angew. Chem. Int. Ed*. **2006**, *45*, 7226.

[7] D. Hagrman, R. D. Haushalter, J. Zubieta, *Chem. Mater*. **1998**, *10*, 361.

[8] M. A. Withersby, A. J. Blake, N. R. Champness, P. A. Cooke, P. Hubberstey, A. L. Realf, S. J. Teat, M. Schroder, *J. Chem. Soc., Dalton Trans*. **2000**, 3261.

[9] a) A. J. Blake, S. J. Hill, P. Hubberstey, W.-S. Li, *J. Chem. Soc., Dalton Trans.* **1998**, 909; b) A. J. Blake, N. R. Champness, S. S. M. Chung, W.-S. Li, M. Schröder, *Chem. Commun.* **1997**, 1005; c) S. R. Batten, J. C. Jeffrey, M. D. Ward, *Inorg. Chim. Acta,* **1999**, *292*, 231; d) J. M. Knaust, S. W. Keller, *Inorg. Chim. Acta*, **2001**, *324*, 81.

[10] J. M. Knust, S. W. Keller, *Inorg.Chem*. **2002**, *41*, 5650.

[11] C. Roux, J. Zarembowitch, B. Gallois, T. Granier, R. Claude, *Inorg. Chem*. **1994**, *33*, 2273.

[12] S. Henke, R. Schmid, J.-D. Grunwaldt, R. A. Fischer, *Chem. Eur. J*. **2010**, *16*, 14296.

[13] K. Takaoka, M. Kawano, T. Hozumi, S. Ohkoshi, M. Fujita, *Inorg. Chem*. **2006**, *45*, 3976.

[14] K. S. W. Sing, D. H. Everett, R. A. W. Haul, L. Moscou, R. A. Pierotti, J. Roquerol, T. Siemieniewska, *Pure and Appl. Chem.* **1985**, *57*, 603.

[15] H. Choi, M. Dincă, J. R. Long, *J. Am. Chem. Soc.* **2008**, *130*, 7848.

[16] R. Matsuda, R. Kitaura, S. Kitagawa, Y. Kubota, T. C. Kobayashi, S. Horike, M. Takata, *J. Am. Chem. Soc*. **2004**, *126*, 14063.

[17] T. Uemura, D. Hiramatsu, Y. Kubota, M. Takata, S. Kitagawa, *Angew. Chem. Int. Ed*. **2007**, *46*, 4987.

[18] S. S.-Y. Chui, S. M.-F. Lo, J. P. H. Charmant. A. G. Orpen, I. D. Williams, *Science*, **1999**, *283*, 1148.

[19] J. Seo, R. Matsuda, H. Sakamoto, C. Bonneau, S. Kitagawa, *J. Am. Chem. Soc*. **2009**, *131*, 12792.

[20] G.-S. Yang, Y.-Q. Lan, H.-Y. Zang, K.-Z. Shao, X.-L. Wang, Z.-M. Su, C.-J. Jiang, *Cryst. Eng. Comm*. **2009**, *11*, 274.

[21] a) I. Søtofte, K. Nielsen, *Acta Chem. Scand. A*, **1984**, *38*, 253; b) Y. Gong, X-H. Huang, Z-N. Xia, M-X. Gao, H-L. Zheng, *Acta Cryst*. **2007**, *E63*, m216.

[22] a) E. V. Govor, A. B. Lysenko, E. B. Rusanov, A. N. Chernega, H. Krautscheid, K. V. Domasevitch, *Z. Anorg. Allg. Chem.* **2010**, *636*, 209; b) S. Contaldi, C. Di Nicola, F. Garau, Y. Y. Karabach, L. Martins, M. Monari, L. Pandolfo, C. Pattinatri, A. Pombeiro, *Datlon Trans.* **2009**, 4928; c) M. Casarin, C. Corvaja, C. Di Nicola, D. Falcomer, L. Franco, M. Monari, L. Pandolfo, C. Pettinari, F. Piccinelli, *Inorg. Chem.* **2005**, *44*, 626; d) M. Casarin, C. Corvaja, C. Di Nicola, D. Falcomer, L. Franco, M. Monari, L. Pandolfo, C. Pettinari, F. Piccinelli, P. Tagliatesta, *Inorg. Chem.* **2004**, *43*, 5865.

[23] a) W. R. Tikkanen, C. Krüger, K. D. Bomben, W. L. Jolly, W. C. Kaska, P. C. Ford, *Inorg. Chem.* **1984**, *23*, 3633; b) L. Li, H. Xu, X. Shi, H. Hou, Y. Fan, *Inorg. Chim. Acta*, **2010**, *363*, 3939; c) Z. Shi, L. Li, S. Niu, J. Jin, Y. Chi, L. Zhang, J. Liu, Y. Xing, *Inorg. Chim. Acta*, **2011**, *368*, 101; d) B. F. Straub, F. Rominger, P. Hofmann, *Chem. Comm*. **2000**, *17*, 1611.

[24] S. S. Y. Chui, S. M. F. Lo, J. P. H. Charmant, A. G. Orpen, I. D. Williams, *Science*, **1999**, *283*, 1148.

[25] B. Murphy, B. Hathaway, *Coord. Chem. Rev*. **2003**, *243*, 237.

[26] C. Prestipino, L. Regli, J. G. Vitillo, F. Bonino, A. Damin, C. Lamberti, A. Zecchina, P. L. Solari, K. O. Knogshaug, S. Bordiga, *Chem. Mater*. **2006**, *18*, 1337.

[27] K. Schlichte, T. Kratzke, S. Kaskel, *Microp. Mesop. Mater*. **2004**, *73*, 81.

[28] L. Pauling, in *The Nature of the Chemical Bond,* Cornell University Press, Ithaca, New York, **1960**.

[29] B. Bleaney, K. D. Bowers, *Proc. Roy. Soc. London A*, **1952**, *214*, 451.

[30] L. Penkova, S. Demeshko, M. Haukka, V. A. Pavlenko, F. Meyer, I. O. Fritsky, *Z. Anorg. Allg. Chem.* **2008**, *634*, 2428.

[31] H. Matsushima, H. Hamada, K. Watanabe, M. Koikawa, T. Tokii, *J. Chem. Soc., Dalton Trans*. **1999**, 971.

[32] D. W. Breck, in *Zeolite Molecular Sieves*, Jhon Wiley & Sons, New York, **1973**, p. 636.

[33] F. Salles, G. Maurin, C. Serre, P. L. Llewellyn, C. Knöfel, H. J. Choi, Y. Filinchuk, L. Oliviero, A. Vimont, J. R. Long, G. Férey, *J. Am. Chem. Soc.* **2010**, *132*, 13782.

[34] a) E. D. Bloch, W. L. Queen, R. Krishna, J. M. Zadrozny, C. M. Brown, J. R. Long, *Science*, **2012**, *335*, 1606; b) J.-R. Li, Y. Mab, M. C. McCarthyb, J. Sculleya, J. Yub, H.-K. Jeongb, P. B. Balbuenab, H.-C. Zhou, *Coord. Chem. Rev.* **2011**, *255*, 1791; c) Y. He, S. Xiang, B. Chen, *J. Am. Chem. Soc.* **2011**, *133*, 14570; d) J. Liu, S. Keskin, D. S. Sholl, J. K. Johnson, *J. Phys. Chem. C*, **2011**, *115*, 12560; e) D. Britt, H. Furukawa, B. Wang, T. G. Glover, O. M. Yaghi, *Proc. Natl. Acad. Sci. USA*, **2009**, *106*, 20637; f) Y.-S. Bae, K. L. Mulfort, H. Frost, P. Ryan, S. Punnathanam, L. J. Broadbelt, J. T. Hupp, R. Q. Snurr, *Langmuir*, **2008**, *24*, 8592; g) K. Li, J. Y. Lee, D. H. Olson, T. J. Emge, W. Bi, M. J. Eibling, J. Li, *Chem. Commun.* **2008**, 6123.

[35] a) C. R. Reid, K. M. Thomas, *Langmuir*, **1999**, *15*, 3206; b) Y.-S. Bae, C.-H. Lee, *Carbon*, **2005**, *43*, 95.

[36] G. Guiochon, A. Felinger, A. M. Katti, D. G. Shirazi, in *Fundamentals of Preparative and Nonlinear Chromatography*, Elsevier, Amsterdam, **2006**.

[37] E. Diaz, S. Ordoñez, A. Vega, *J. Colloid Interface Sci*. **2007**, *305*, 7.

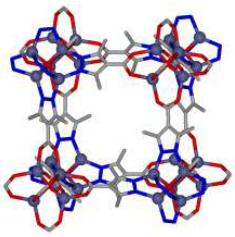

4. MOF-5 ANALOGUES

4.1. Introduction

4.1.1. Structure and stability

In 1999 Yaghi and co-workers published, for the first time, the structure of the Zn-based open metal-organic framework [Zn_4O(benzene-1,4-dicarboxylate)$_3$] which was termed MOF-5.[1] The structure of this material, depicted in Figure 4.1, is based on oxide centred tetranuclear zinc clusters, forming a regular Zn_4O tetrahedron. Each edge of the Zn_4O tetrahedrons is then capped by a -CO_2 group to form a $Zn_4(O)(CO_2)_6$ fragment. These Secondary Building Units (SBUs) are connected by benzene residues to give rise to an extended network with a highly accessible three-dimensional intersecting channel system accounting for the 55-61 % of the crystal volume.

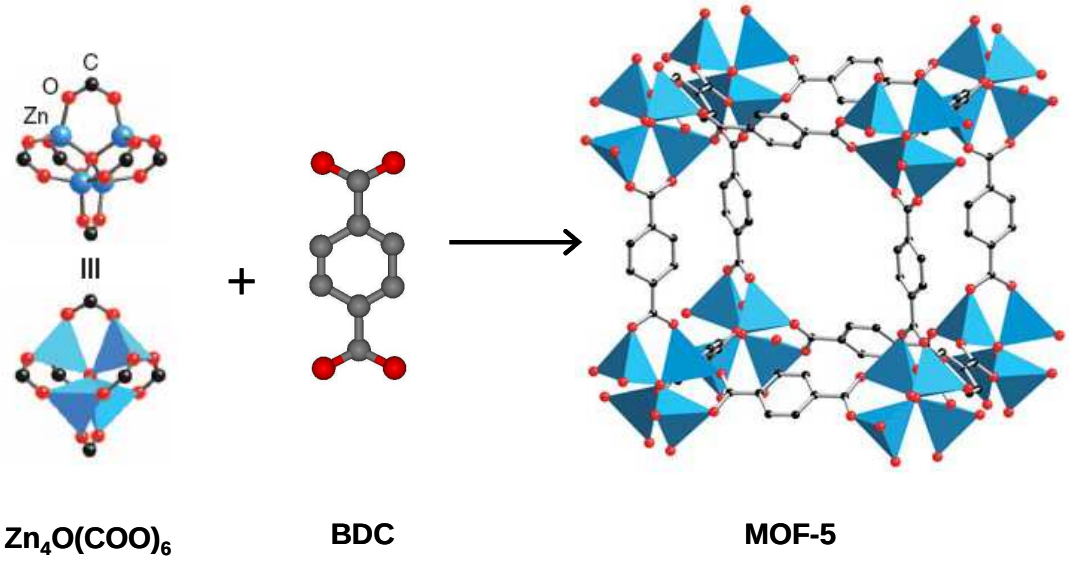

Figure 4.1. Construction of MOF-5 framework. (Left) $Zn_4O(COO)_6$ cluster; (middle) benzene dicarboxylate (BDC) ligand; (right) one of the cavities in MOF-5 framework. **Zn**, **O**, **C**. H atoms have been omitted for clarity.

Very importantly, the title of the above mentioned paper was: “Design and synthesis of an exceptionally stable and highly porous metal-organic framework”. Until that time, very few and typically not very stable porous coordination polymers were known. The exceptional stability mentioned by the authors concerns the fact that MOF-5 material remains crystalline and stable when fully desolvated and when heated up to 300 ºC. Notwithstanding, no detailed description of the experimental conditions employed during the handling of this compound was provided in the paper.

Three years later, in 2002, the same authors published the IRMOF series of isoreticular compounds, based on the same Zn_4O tetrahedral clusters found in MOF-5 structure, now connected by dicarboxylate anions of different lengths and bearing different functionalities.[2] These materials resulted to be very porous toward gas and vapour probe molecules (with particular attention devoted to methane adsorption) but, once again, no explicit mention about their stability in air was made. The text pointed out just that TGA measurements had been carried out under inert atmosphere while in the supporting information details it was said that IRMOF materials were not soluble in water and common organic solvents. Afterwards, in 2003, three materials of the IRMOF series have been further employed in the study of H_2 adsorption at room temperature and, as previously, their stability in air had not been commented.[3] Anyhow, two months earlier (March 2003), Yan and collaborators had reported on the effect of moisture on Zn_4O based MOF-5 structure, with the clear evidence that hydrolysis of one Zn-O bond (oxygen from BDC ligand) takes place upon exposure of MOF-5 framework to air moisture.[4] Actually, they proved experimentally that "exposure of MOCP (metal-organic coordination polymers based on Zn_4O clusters) materials to water resulted in dramatic drop in surface area and porosity" and concluded that "it appears that MOCP materials are not stable in moisture/water and acid, and this may limit their practical applications".

Later on, in 2005, a detailed study on the influence of water molecules (eventually found in the solvent used for the synthesis) on the 3D assembly of MOF-5 material had been carried out by Burrows and co-workers.[5] In fact, authors reported for the first time a detailed study of dialkylammonium cations influence on the products of a metal based assembly, with these cations coming from the small hydrolysis of DMF or DEF solvents in air. Therefore, they proved that the base ($NH_2R_2^+$) is responsible for MOF-5 material degradation upon exposure to moisture.

Although in 2004 and 2005 some papers appeared containing the results of the simulations of the adsorption by MOF-5 framework of small gas molecules (Ar, CH_4, CO_2, N_2, and H_2),[6] only in 2006 a molecular dynamics simulation on the interaction of water with this material was published by Greahouse and Allendorf.[7]

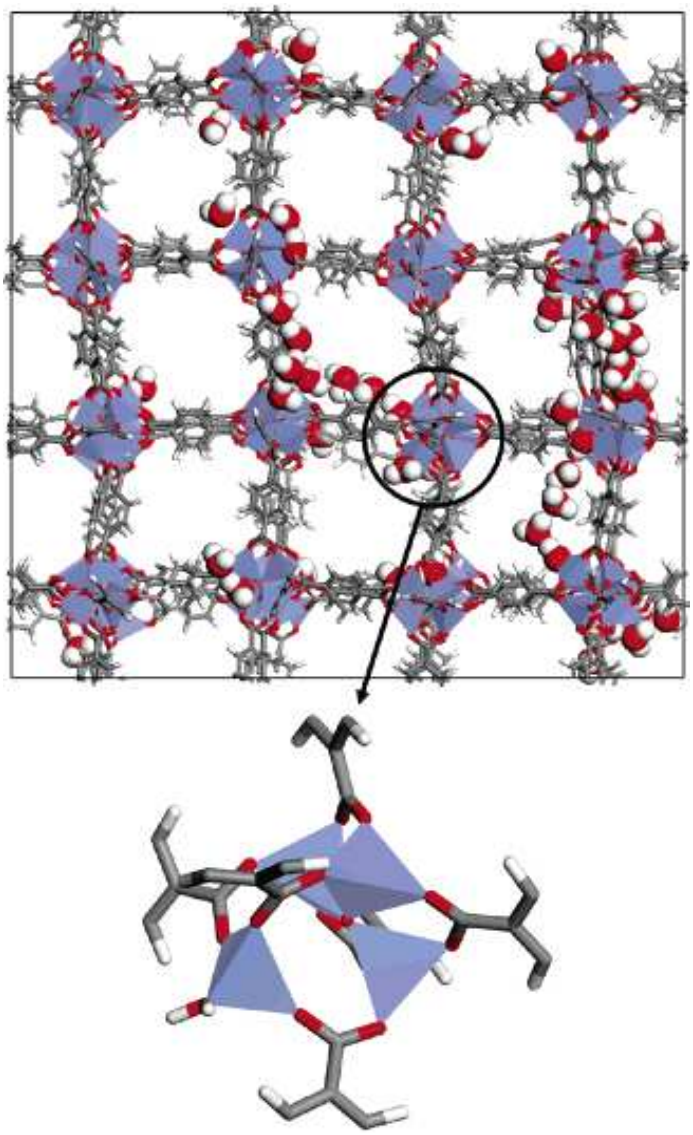

Figure 4.2. (Above) Disruption of MOF-5 structure at 2.3 % water; (below) Zn_4O centre in which an inorganic O atom has been replaced by a water O atom. **Zn**, **O**, **C**, **H** (white), ZnO_4 tetrahedra are represented as polygons.

In this paper the authors monitor the variation of MOF-5 lattice parameters upon addition of water. The results show that at low water content (up to 2.3 %) the structure is maintained with a small decrease in lattice parameters while at higher water contents of 3.9 % and 9.5 % MOF-5 structure collapses to a high density phase (Figure 4.2). The role of water in the disruption of MOF-5 structure becomes evident by monitoring the coordination of Zn ions to neighbouring O atoms. Indeed, Zn ion retains tetrahedral coordination, with water O atoms taking positions in the first shell, thus progressively replacing the central oxide atom and carboxylate groups of BDC. The simulations indicate that water molecules interact with the framework in three ways: i) direct attack on a Zn_4O tetrahedron with a water O atom replacing the central oxide, ii) hydrogen

bonding between a water H atom and BDC O atom, iii) a hydrogen-bonded network of water molecules surrounding one or more ZnO_4 tetrahedra (see Figure 4.2). Unequivocally, the first is the most destructive mode of interaction. In this case, the O atom in the centre of Zn_4O tetrahedra becomes triply coordinated when a water molecule takes the position of a Zn atom. The Zn ion is still coordinated to three BDC ligands, but one of the O atoms of a carboxylate anion is not anchored anymore and BDC ligand is now free to rotate. As the water content increases, water molecules continue to attack ZnO_4 tetrahedra, and the framework eventually collapses.

At the text closure, the authors recognize that the main cause of this occurrence is the relatively weak interaction between Zn ions and O atoms so the structure can be attacked by water molecules. As a concluding remark, they underline the importance of developing new water-resistant frameworks that, unlike MOF-5, could increase the technological application of this class of materials.

4.1.2. Applications

Despite the recognized low stability of MOF-5 material in humid conditions and in particular in open air, in the last years this material has been the object of many research works suggesting a wide range of possible applications. Some, significant examples are given below.

Gas storage

As already mentioned, the high porosity and structural stability of MOF-5 as well as the low cost of reagents and ease of preparation of this material prompted the investigation of its adsorptive properties toward gas and vapour molecules. When MOF-5 structure was first published,[1] its permanent porosity towards Ar, N_2, CH_2Cl_2 $CHCl_3$, C_6H_6, CCl_4 and C_6H_{12} was evaluated. Since the pore volumes calculated for all adsorbates resulted to be almost identical (0.61 – 0.54 cm^3 cm^{-3}), this was taken as a proof of uniform pore structure. Noteworthy, apparent Langmuir surface area was estimated at 2900 m^2 g^{-1} that was the largest (and still is one of the largest) value reported for a porous coordination polymer to date.

Afterwards, CH_4 (298 K)[2] and H_2 adsorption isotherms (78 K)[3] were measured for MOF-5 activated material with hydrogen uptake reaching the value of 17.2 molecules per $Zn_4O(BDC)_3$ formula unit which opened up a strong debate of the possible utility of

this kind of materials for the storage of environmentally friendly energetic gases in mobile applications.

Unfortunately, the adsorption capacity of this material strongly depends on the synthetic method employed, and apparent Langmuir surface areas for N_2 asorption isotherm (77 K) range from 1010[8] to 4400 m^2 g^{-1}.[9] The latter value refers to a sample prepared and handled with a special attention to avoid any exposure of the solid to water molecules since they had been found to be the main cause of surface area diminution. Therefore, to reduce this inconvenient, Dingemans and co-workers synthesized two MOF-5 methyl modified materials, introducing one (or two) methyl group on the H_2BDC ligand used in the construction of MOF-5 framework (see Scheme 4.1).[10]

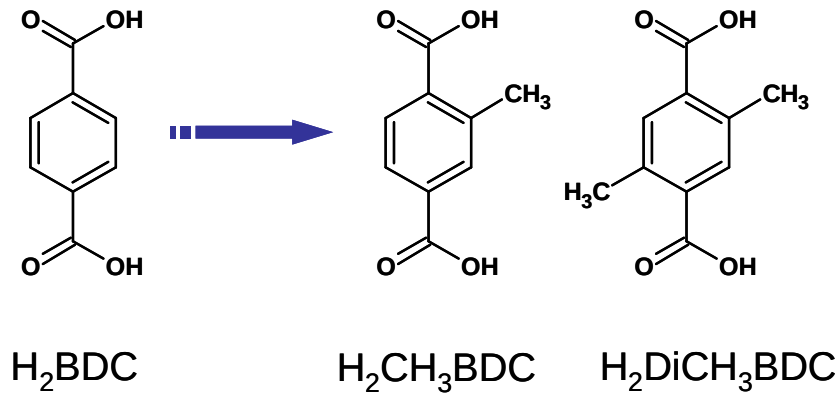

Scheme 4.1. Modification of H_2BDC ligand in the synthesis of MOF-5 analogues reported in reference 10.

The authors found that incorporation of hydrophobic methyl groups effectively improve the water stability of MOF-5, without seriously compromising its hydrogen uptake capability. The exposition of CH_3MOF-5 and DiCH_3MOF-5 to ambient air did not change their crystal structure and reduce their H_2 uptake capability by only 35 %. Therefore, the introduction of hydrophobic functionalities reduces the air sensitivity of MOF-5 material, demonstrating that the adoption of methyl modified MOF-5 materials for gas storage could be effective. Another modified MOF-5 structure, with enhanced stability and permanent porosity towards N_2 and H_2, was published in 2011 by Kim and collaborators.[11] It consists in the interpenetrated form of MOF-5 with a doubly interpenetrated primitive cubic network (Figure 4.3). Although the structure of this material had been previously published,[12] its bulk properties had not been studied, probably because a phase pure material had not been obtained so far.

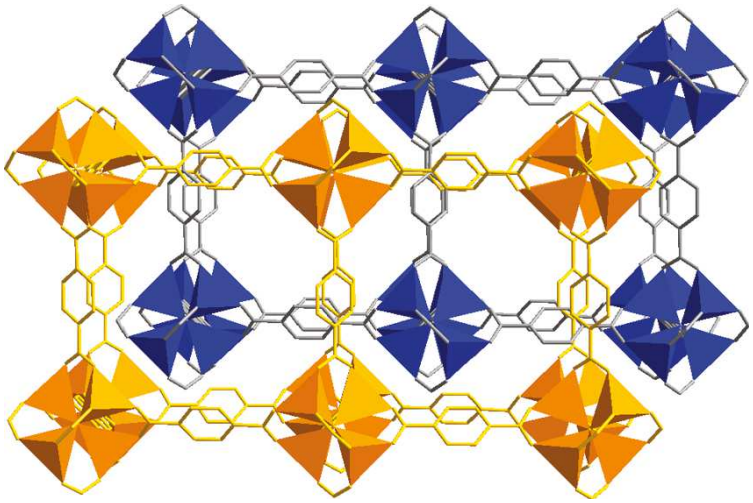

Figure 4.3. X-Ray crystal structure of interpenetrated MOF-5.

Two important characteristics make this material interesting for possible practical application: its improved stability in air, and its hydrogen capacity at 77 K and 1 bar. Indeed, guest-free interpenetrated MOF-5 shows higher stability toward airborne moisture than non-interpenetrated MOF-5, since the crystallinity of the former remains intact for 5 days, while the latter decomposes after 1 day under the same conditions. Moreover, even if its surface area is much smaller than that of MOF-5 due to interpenetration, interpenetrated MOF-5 shows a significantly higher hydrogen capacity (both gravimetric and volumetric) than MOF-5 at 77 K and 1 bar.

These modified materials (CH_3MOF-5, DiCH_3MOF-5 and interpenetrated-MOF-5) came over the stability issues of MOF-5 structure that otherwise would make them unsuitable for any practical application concerning gas adsorption.

Gas separation properties of membranes

The possibility to obtain thin membranes of MOF-5 material with the secondary growth method was reported by Zhao and co-workers in 2011.[13] This growth method consists in the dip-coating of the membrane support (homemade porous α-Al_2O_3 disk) into a MOF-5 suspension, followed by typical solvothermal synthesis of MOF-5 crystals in a glass vial. Therefore, ~14 μm thick MOF-5 membranes (Figure 4.4) have been used in the study of permeation and separation properties of CO_2/H_2 and CO_2/N_2 mixtures.[14]

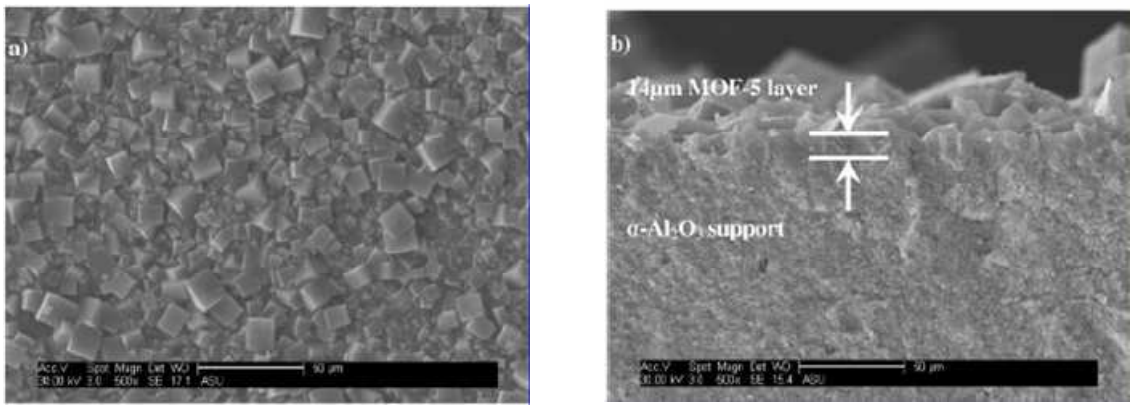

Figure 4.4. SEM images of a) the surface and b) cross-section of MOF-5 membrane synthesized by the secondary growth method.

The results show that MOF-5 membranes are more permeable to CO_2 over H_2 or N_2 and actually they exhibit a separation factor for CO_2/H_2 close to 5 with a feed CO_2 composition of 82 % and a separation factor for CO_2/N_2 greater than 60 with a feed CO_2 composition of 88 % at 445 kPa and 298 K. The key point of this interesting investigation is the similarity of experimental conditions to the ones eventually used in industrial gas separation applications.

Photoelectrical response

Thin films of MOF-5 have also been used in the study of photoelectrical behaviour of this archetypal metal-organic material (Figure 4.5).[15] Indeed, MOF-5 10-100 μm thick films have been grown on conductive fluorine-doped tin oxide substrates and further exposed to white light illumination while immersed in acetonitrile electrolytes. Interestingly, MOF-5 innately exhibits photomodulated conductivity since an increase in anodic (negative) current is clearly detected, evidencing an increase of the hole flux at the MOF/solution interface compared to the one in absence of illumination.

Noteworthy, the same experiment has been carried out after film exposure to an aqueous solution or in electrolytes with cation mismatched to the pore aperture of MOF-5. The evident lowering of the photoresponse of these films is considered by the authors as a proof of framework's integrity during the previous experiments, but, anyhow, it underlines once again the extreme delicacy of MOF-5 net and its unsuitability for most practical purposes.

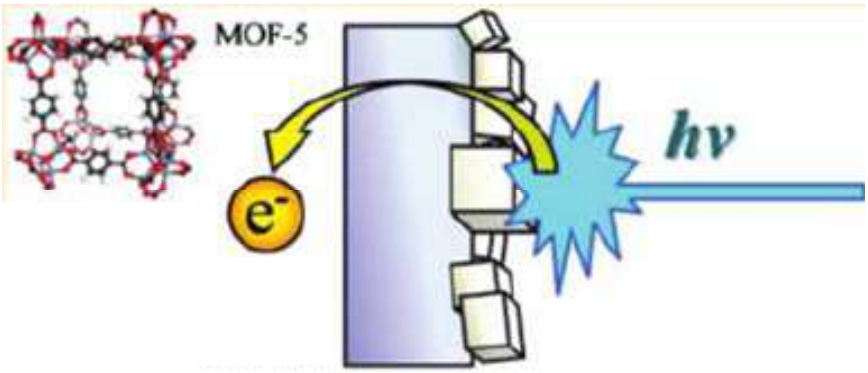

Figure 4.5. Schematic representation of the photoelectrochemical experiment carried out on MOF-5 thin films.

Incorporation of nanoparticles

Among the numerous applications of MOF-5 material investigated in the last years, we should mention the embedding of nanoparticles inside its cavities. In this regard, Fisher and co-workers reported in 2008 on the successful formation of Ru-nanoparticles inside the cubic pores of MOF-5.[16]

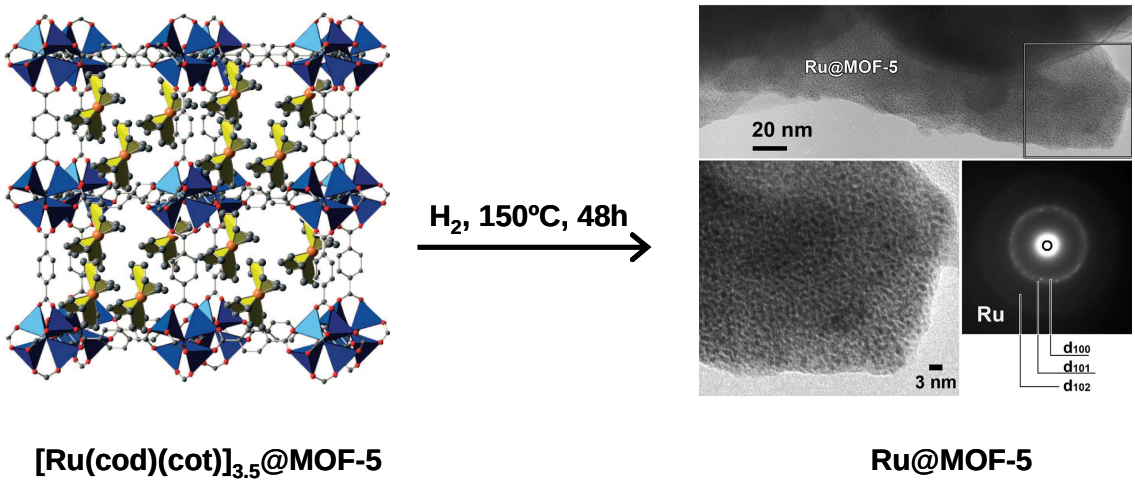

Figure 4.6. (Left) Model of the inclusion compound $[Ru(cod)(cod)]_{3.5}$@MOF-5 and (right) TEM images of Ru@MOF-5.

As schematically represented in Figure 4.6, firstly the authors achieved the loading of MOF-5 with the volatile compound [Ru(cod)(cot)] (cod = 1,5-cyclooctadiene, cot = 1,3,5-cyclooctatriene) and afterwards they proceeded to quantitative hydrogenolysis of the adsorbed ruthenium complex yielding ruthenium nanoparticles in a typical size range of 1.5–1.7 nm, embedded in the intact MOF-5 matrix. Later on, the performance of final Ru@MOF-5 solid as catalyst for alcohol oxidation was investigated, but (as

predictable) results clearly revealed the limitations of the water-sensitive MOF-5 host material for catalytic applications of the modified Ru@MOF-5 system.

4.1.3. Related structures

The $Zn_4O(COO)_6$ tetrahedric cluster found in MOF-5 structure is not very common among metal organic materials. As already mentioned in this chapter (4.1), the central oxide ion is surrounded by four Zn atoms, placed on the vertices of a perfect tetrahedron and, similarly, each zinc atom has a ZnO_4 tetrahedral geometry. Three of the oxygen atoms surrounding Zn metal cations belong to carboxylate anions, while the fourth is an oxide shared among four ZnO_4 tetrahedra (see Figure 4.7). As expected from the different nature of oxygen atoms, Zn-O(carboxylate) distance is slightly longer than Zn-O(oxide) distance.

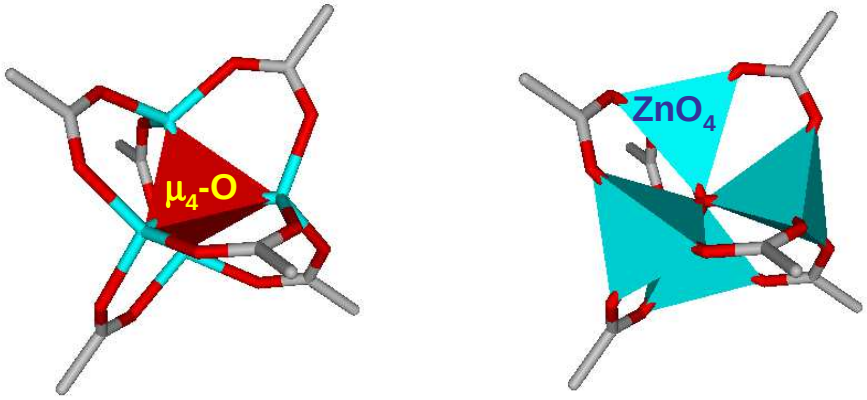

Figure 4.7. View of $Zn_4O(COO)_6$ tetrahedral cluster found in MOF-5 structure with tetrahedra for (left) μ_4-O and (right) ZnO_4 moieties.

A detailed search on the CCDC shows that this tetranuclear metal cluster can be mainly found for Zn-based compounds of both discrete and extended nature. Among the discrete structures based on Zn we can mention the $[Zn_4O(O_2CNEt_2)_6]$ cluster reported in 1991 by Strähle and co-workers,[17] the $[Zn_4(\mu_2\text{-}FcCOO)_6(\mu_4\text{-}O)]$ tetramer published in 2003 by Hhu [18] and collaborators or the tetranuclear (carbamato)zinc cluster of formulation $[Zn_4(\mu_4\text{-}O)(O_2CN\textit{i}Pr_2)_6]$ reported in 2008 by Lamb's group (Figure 4.8).[19]

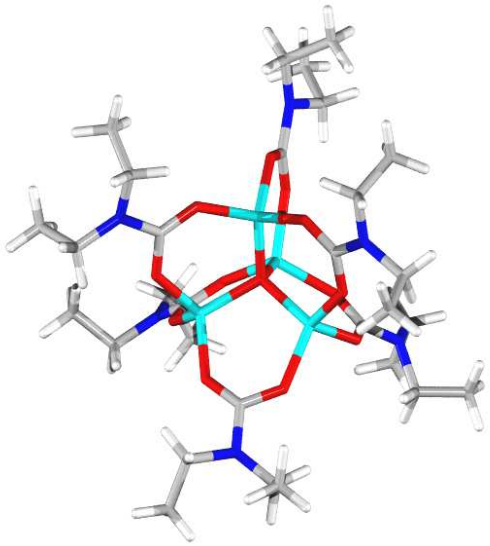

Figure 4.8. Crystal structure of $[Zn_4(\mu_4\text{-}O)(O_2CN\textit{i}Pr_2)_6]$ (carbamato)zinc complex. **Zn**, **O**, **C**, **N**, **H** (white).

Regarding extended polymers, most of their crystal structures are strongly related to MOF-5 and MOF-177 since, often, the main difference is limited to the functionalization of BDC and BTC ligands. Anyway, new different extended polymers based on Zn_4O clusters can be easily constructed with di- tri- or tetra-topic carboxylate ligands as well as a combination thereof. Nice examples are the UMCM-1[20] and UMCM-2[21] MOFs (UMCM = University of Michigan Crystalline Material), published in 2007 and 2009 by Matzger and co-workers (see Figure 4.9).

In UMCM-1 material, six BDC linkers and five BTB (H_3BTB = 1,3,5-benzene tribenzoic acid) linkers connect nine Zn_4O clusters giving rise to micropores (in cage-like structures) that assemble together in an edge-sharing fashion, defining 1D hexagonal channels of mesoporous size. In UMCM-2 material, the BDC ligand is replaced by the slightly longer thieno[3,2-b]thiophene-2,5-dicarboxylate (T^2DC) linker and the structure reveals two different microporous cages and a mesoporous cage.

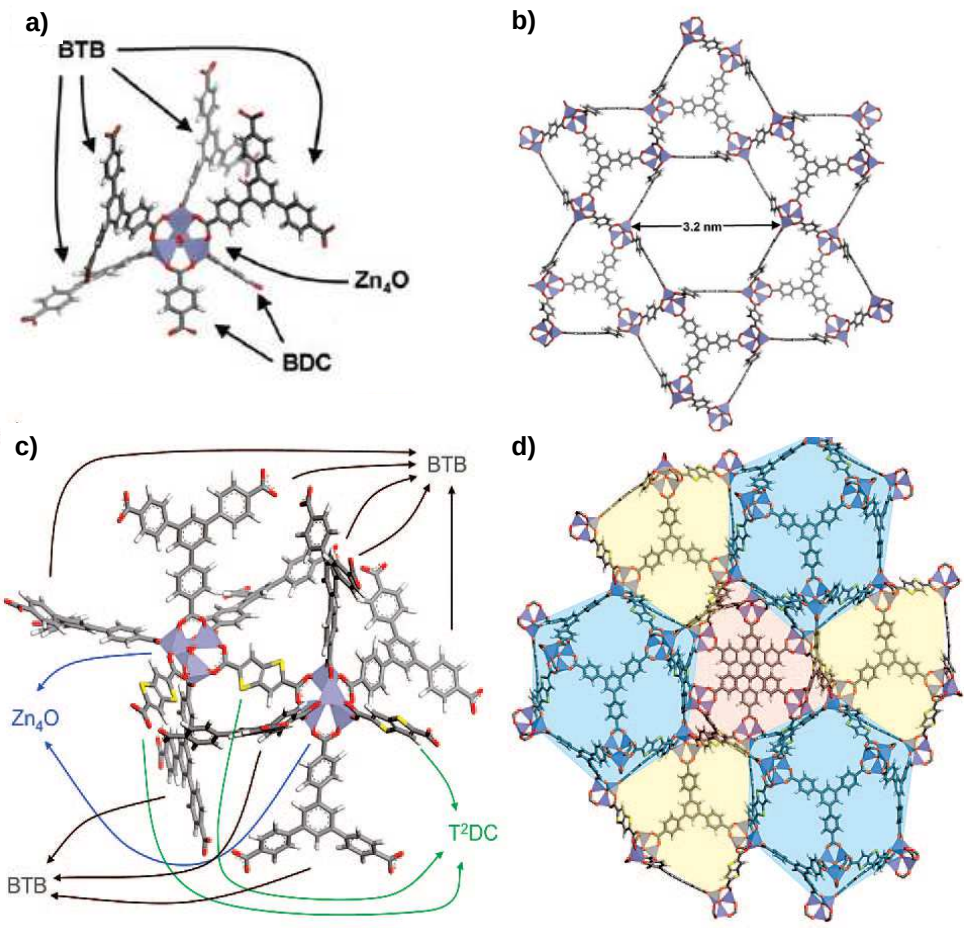

Figure 4.9. a) Zn_4O cluster in UMCM-1 connecting two BDC and four BTB linkers; b) UMCM-1 structure viewed along the *c* axis; c) two Zn_4O clusters in UMCM-2 coordinated to three T^2DC linkers and eight BTB linkers; d) structure of UMCM-2 viewed along the *c* axis. **Zn**, **O**, **C**, **S**, **H** (white).

Other examples are MOF-646 material[22] where BDC linker in MOF-5 is replaced by 1,3-azulenedicarboxylate (Scheme 4.2-left) and $[Zn_4O(D_2\text{-tcppda})_{1.5}]_n$ (D_2-tcppda = N,N,N',N'-tetrakis(4-carboxyphenyl)-1,4-phenylenediamine, Scheme 4.2-right) coordination polymer,[23] the latter based on a four connected tetracarboxylate ligand.

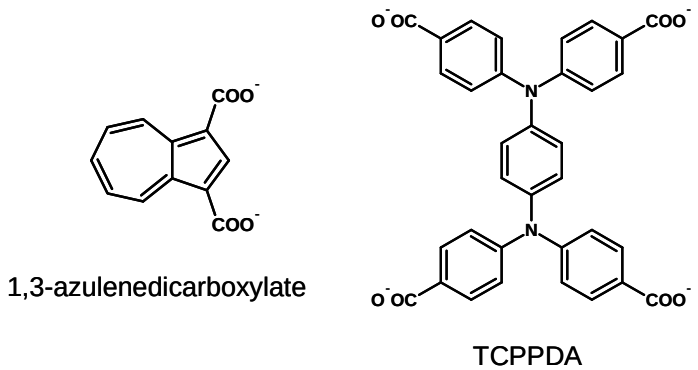

Scheme 4.2. (Left) Azuleneicarboxylate and (right) tetracarboxylate TCPPDA ligands used in the synthesis of porous MOFs based on Zn_4O clusters.

Interestingly, Chen and collaborators reported on the synthesis of a Zn-based PCP where both bis-carboxylate (BDC) and bis-pyrazolate (bpz = 3,3',5,5'-tetramethyl-4,4'-bipyrazolate) ligands are used to built a 3D porous network of the same topology of MOF-5.[24] Indeed, μ_4-oxo-centered tetranuclear Zn_4O clusters are connected by BDC and bpz linkers, so each cluster forms an octahedral $Zn_4O(CO_2)_2(NN)_4$ SBU through edge-bridging coordination of four pyrazolate and two carboxylate groups (Figure 4.10).

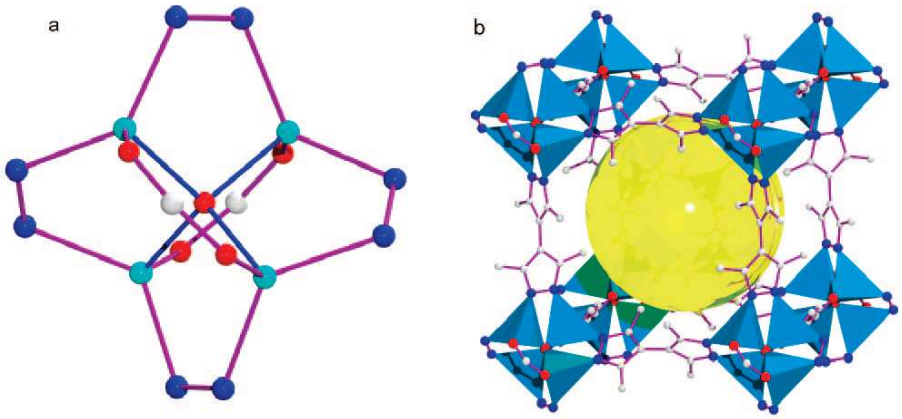

Figure 4.10. (Left) Representation of the $Zn_4O(CO_2)_2(NN)_4$ SBU in $[Zn_4O(BDC)(bpz)_2]\cdot 4DMF\cdot 6H_2O$; (right) cavity within $[Zn_4O(BDC)(bpz)_2]\cdot 4DMF\cdot 6H_2O$ formed by eight tetranuclear clusters. **Zn**, **N**, **O**, **C**, (white). H atoms have been omitted for clarity.

In this material, each Zn_4O cluster connects four bpz ligands, and each bpz binds two clusters into a 4^4 2D layer parallel to the *ab* plane. The layers are further pillared along the *c*-axis by BDC ligands to form a neutral, non-interpenetrated 3D porous network. The resulting porous material has a surface area of ~2000 $m^2\ g^{-1}$, a void volume of ~60 % and pore windows of ~6 x 6 $Å^2$. Its permanent porosity towards N_2 (77 K) suggests the potential accessibility to the framework by a variety of small solvent molecules, such as methanol, benzene, and toluene that indeed, can be efficiently hosted into the solid. Furthermore, this material shows photoluminescent behaviour with an interesting guest-dependent blue shift of the emission maxima, as a consequence of the structural reinforcement upon inclusion of rigid guest molecules.

It should be highlighted that if we move to structures containing $M_4O(COO)_6$ clusters based on metal ions other than Zn, we can not find any 3D-extended structure solved by single crystal X-ray diffraction. Among the discrete compounds, we find the Be_4O core in beryllium acetate salt as well as in (μ_4-Oxo)-hexakis(μ_2-benzoato-O,O')-tetra-beryllium benzene solvate and in (μ_4-Oxo)-hexakis(μ_2-2,4,6-trimethylbenzoato-

O,O')-tetra-beryllium carbon tetrachloride solvate. [25] Moreover, a mixed Co/Zn tetranuclear cluster is reported by Himmel in $[M_4O(O_2CNEt_2)_6]$ complex.[26]

Finally, it has been proved that the complete substitution of all dicarboxylates with bis-pyrazolates in the prototype $[Zn_4O(BDC)_3]$ could be achieved just if Co(II), rather than Zn(II), is used. So, the $[Co_4O(pz)_6]$ building unit is found in the MFU-1 material, a Co-based coordination polymer reported by Volkmer and collaborators in 2009.[27] This 3D-framework is based on Co_4O secondary building units analogues to those found in MOF-5 structure, although their connection is made through 1,4-bis[(3,5-dimethyl)-pyrazol-4-yl]benzene (H_2bdpb) linkers instead of through H_2BDC ligands (see Figure 4.11). The same connectivity is found in $[Co_4O(3,5\text{-}dmpz)_6]$[28] discrete complex, but MFU-1 resulted to be the first MOF containing $[Co_4O(pz)_6]$ building units.

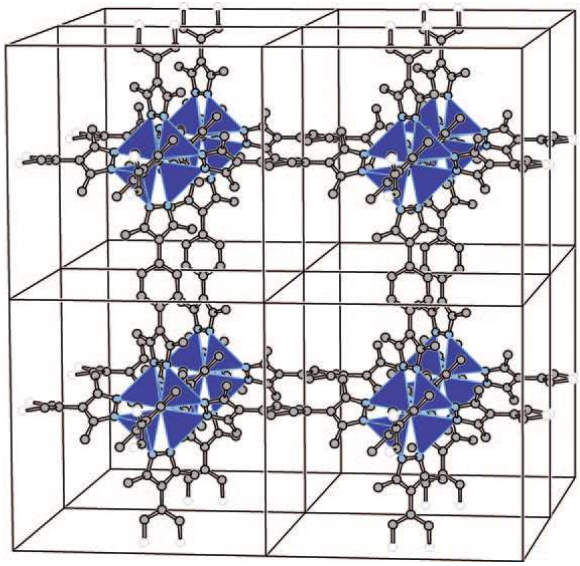

Figure 4.11. Crystal packing of MFU-1. C, N, $\{CoON_3\}$ coordination units are shown as blue polyhedra.

Hence, we can conclude that, to date, M_4O building unit has been found just in Be-, Co- and Zn-based materials and that this connectivity seems not to be suitable for any other metal.

4.2. Results and discussion

We have been able to synthesize three new Co- and Zn-based porous coordination polymers containing the same M_4O secondary building unit found in the materials described above. Interestingly, the organic linkers contain either both carboxylate and pyrazolate functionalities (L2) or just two pyrazolate groups (L6) leading to robust

frameworks with much higher stability than analogues based just on M-O(carboxylate) coordination bonds.

4.2.1. $M_4O(L2)_3$ compounds

Crystal structure

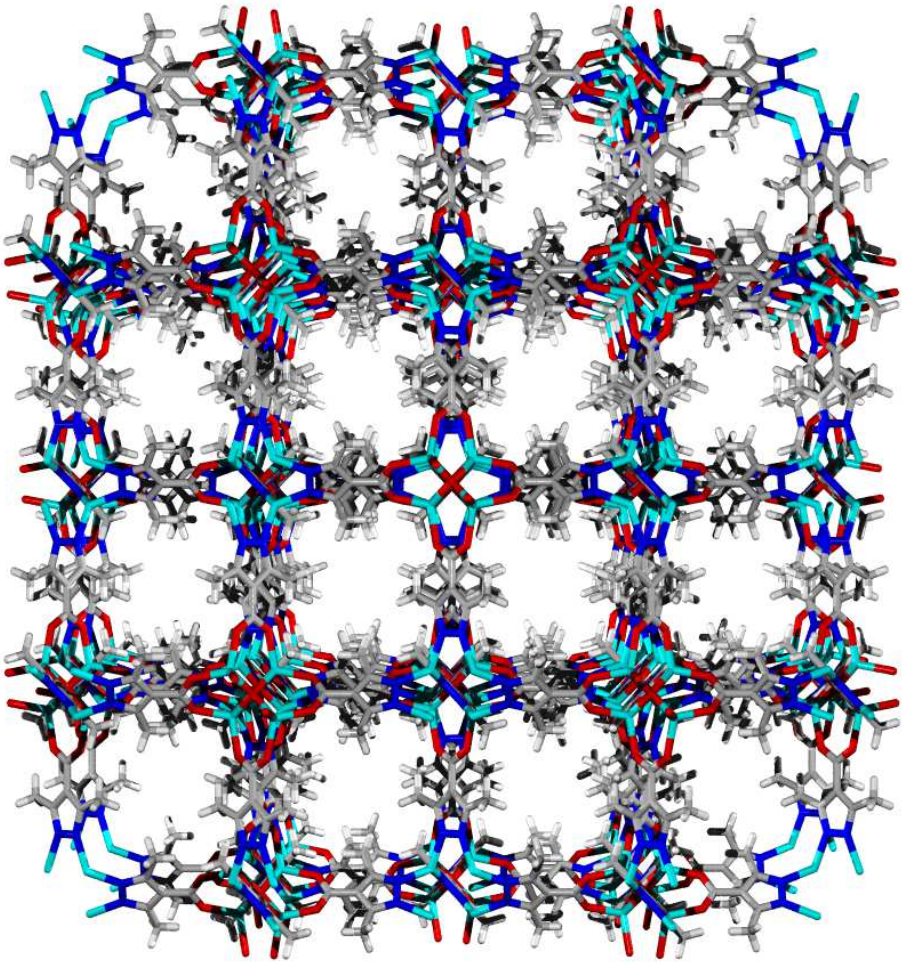

Figure 4.12. Perspective view of $[Zn_4O(L2)_3]$ porous coordination polymer. **Zn**, **O**, **N**, C, **H** (white).

The reaction of $M(NO_3)_2$ (M = Zn, Co) with 3,5-dimethyl-4-carboxypyrazole (H_2L2) in basic ethanol medium under reflux, affords microcrystalline materials of formulation $[M_4O(L2)_3]_n \cdot$solv ($[M_4O(L2)_3]$) in large amounts and high yields (up to 20 g *per* batch) (Figure 4.12). The same products could be achieved by using DMF as solvent. Anyhow, no difference was appreciated for the two synthetic strategies, therefore ethanol has been preferred for obvious environmental reasons.

Despite the great effort devoted to the achievement of single crystals for X-ray diffraction measurements, both samples have been isolated only in the form of microcrystalline powders and their structure has been resolved by powder X-ray

diffraction data. Fortunately, a meticulous visual inspection of acquired diffractograms, reveals that the two compounds are isostructural to MOF-5 (Figure 4.13)[29] so that it has been possible to solve the structure with ease by applying the Rietveld method.

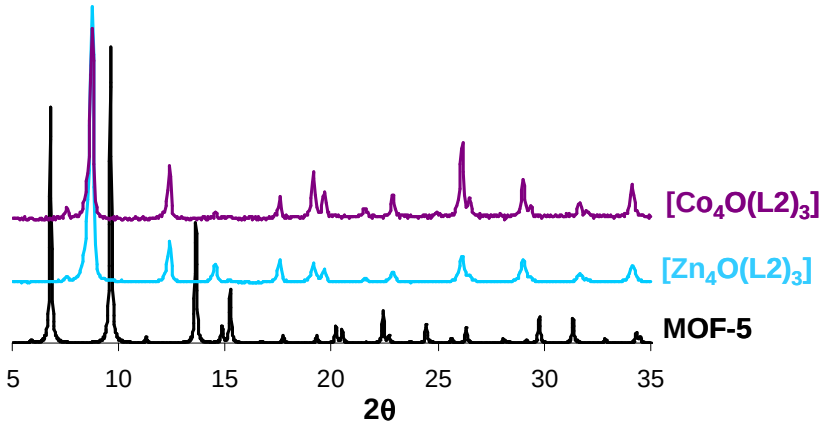

Figure 4.13. XRPD spectra of MOF-5 (simulated from X-ray powder diffraction data), $[Zn_4O(L2)_3]$ and $[Co_4O(L2)_3]$ materials.

Thus, we resorted to MOF-5 structural details to position M_4O nodes, while the orientation of the (crystallographic independent portion) $L2^{2-}$ spacer was determined by simulated annealing technique, as implemented in TOPAS-R, employing a rigid, idealized model.[30] The final refinement was carried out by the Rietveld method, maintaining the rigid body introduced at the structure solution stage.

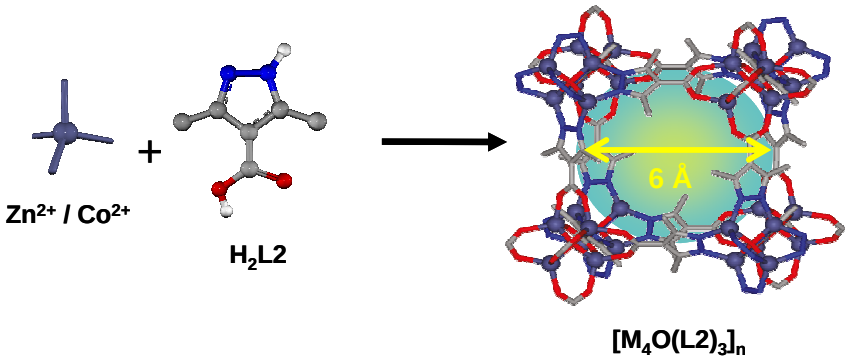

Figure 4.14. Chemical bricks used in the syntheses of $[M_4O(L2)_3]$ frameworks and view of a portion of their crystal structure. The size of the inner cavity as well as segregated $Zn_4O(CO_2)_6$ and $Zn_4O(pz)_6$ SBUs can be visualized. **Zn**/**Co**, **O**, **N**, C. H atoms have been omitted for clarity.

The two $[M_4O(L2)_3]$ materials are isomorphous and crystallize in the cubic *Fm-3m* space group with a = 20.1581(3) Å and V = 8191.2(3) Å^3. Within their three-dimensional porous framework, M_4O tetranuclear nodes are connected to six symmetry-

related ones by (50 % orientationally disordered) N,N',O,O'-exo-tetradentate 3,5-dimethyl-4-carboxypyrazolato ($L2^{2-}$) spacers. Rather narrow windows (less than 4 Å x 4 Å) give access to pores with diameters of ~ 6 Å[31] comprising, after solvent removal, a void volume of ~ 47 % (Figure 4.14).

As can be distinctly appreciated in Figure 4.15, methyl groups on L2 linkers protrude into the pores and are reasonably responsible of the high hydrophobicity featured by $[M_4O(L2)_3]$ materials (see below) and strongly contributes to their chemical inertness, by protecting M-O(carboxylate) bonds from hydrolysis. As a matter of fact, it should be highlighted that the use of H_2L1 instead of H_2L2 gives rise to related $[M_4O(L1)_3]$ materials with much more reduced stability. Reducing the symmetry down to the *F23* space group, *i.e.* eliminating the disorder, the framework possesses a rock salt-type topology, in which $M_4O(CO_2)_6$ and $M_4O(pz)_6$ SBUs are joined by L2 spacers (see Figure 4.14). Accordingly, the structure of $[M_4O(L2)_3]$ is reminiscent to that of MOF-5[32] and the disorder observed in our material is retraceable to the nearly equal coordination features of *N*- and *O*-ends of the L2 ligand.

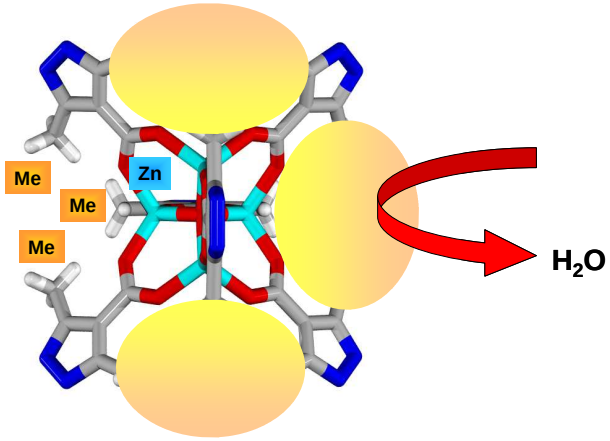

Figure 4.15. Magnified view of the $Zn_4O(CO_2)_6$ secondary building unit. Hydrophobic methyl groups clearly protect Zn-O bonds from hydrolysis.

Stability tests

As extensively pointed out in the introduction of this chapter, the utility of MOF-5 for practical applications is hampered by the easy hydrolysis of the Zn-O coordinative bond, which makes the whole framework extremely sensitive to moisture.[33] However, this drawback can be reduced by substituting carboxylate ligands with structurally related *N*-donor spacers (tetrazolates, triazolates, pyrazolates), as well as by the

incorporation of methyl groups, thus preparing materials with enhanced thermal and chemical stabilities, as a consequence of the higher robustness of M-N bonds.[27, 34, 35] In the case of $[M_4O(L2)_3]$ MOFs, where a hybrid *N*,*O*-ligand has been employed, we have assessed frameworks' robustness by performing a series of thermal essays, as well as chemical and mechanical stability tests.

Zn- and Co-based materials have quite different chemical stabilities. The main cause of this discrepancy is the rather easier hydrolysis of Co-PCP eventually combined with the oxidation of Co(II) to Co(III), while Zn(II) is less sensitive to water and redox inactive under tested conditions.

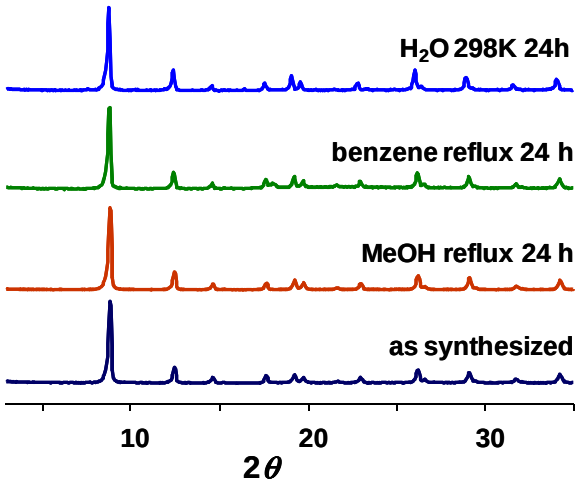

Figure 4.16. Chemical stability tests on $[Zn_4O(L2)_3]$ suspended in water at room temperature and in boiling organic solvents for 24 h.

Significantly, $[Zn_4O(L2)_3]$ resists key treatments such as suspensions in water, at room temperature, or in boiling organic solvents (methanol, benzene, cyclohexane) for a prolonged period of time (see Figure 4.16). Only after a severe heating in water at 80 ºC for 8 h, the formation of (still uncharacterized) dense material of $[Zn_3(OH)_2(L2)_2]$ formulation is observed (Figure 4.17).

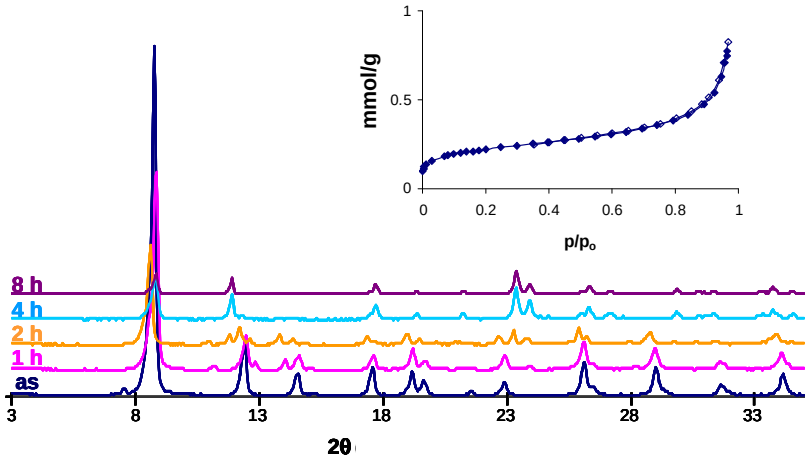

Figure 4.17. Evolution of hydrolysis reaction of a suspension of $[Zn_4O(L2)_3]$ in water at 80 ºC and N_2 adsorption isotherm (77 K) for the resulting $[Zn_3(OH)_2(L2)_2]$ dense material.

Differently, $[Co_4O(L2)_3]$ is not as chemically stable as its Zn analogue, in particular in water. Indeed, when the solid is suspended in water at room temperature, its colour changes to pink-brown within a few hours and its crystallinity is no longer maintained after 4 h. Otherwise, the treatment of $[Co_4O(L2)_3]$ in boiling methanol or benzene is not affecting the local structure of the material, and XRPD patterns remain unchanged (Figure 4.18).

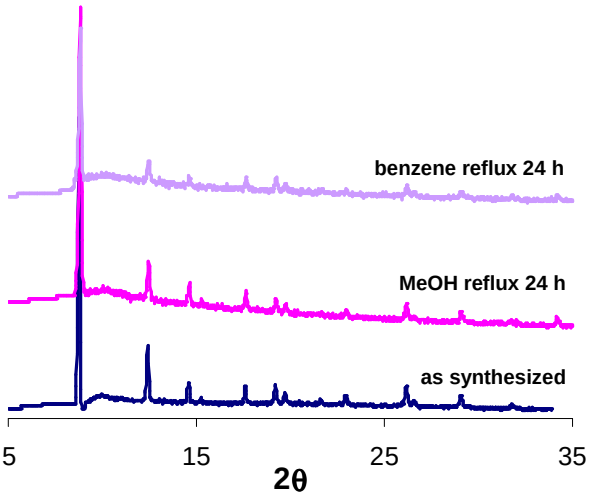

Figure 4.18. Chemical stability tests on $[Co_4O(L2)_3]$ in boiling methanol and benzene for 24 h.

On the other hand, thermogravimetric analyses performed on both $[M_4O(L2)_3]$ materials in a reactive atmosphere of air, demonstrate their outstanding thermal robustness, with decomposition beginning only at 375 ºC for the Co-PCP and at 455 ºC for the Zn analogue as can be appreciated in Figure 4.19.

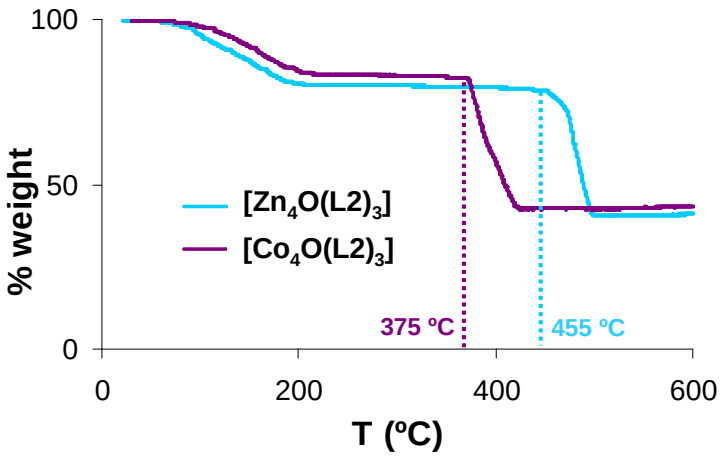

Figure 4.19. TGA traces for $[Zn_4O(L2)_3]$ and $[Co_4O(L2)_3]$ materials.

Thermodiffractometric measurements (TXRPD, Figure 4.20) on the zinc material highlight that $[Zn_4O(L2)_3]$ preserves its structural features and high crystallinity up to pirolysis, but are also indicative of the framework rigidity: upon heating, the unit cell volume undergoing a very small decrease down to -0.5 %.

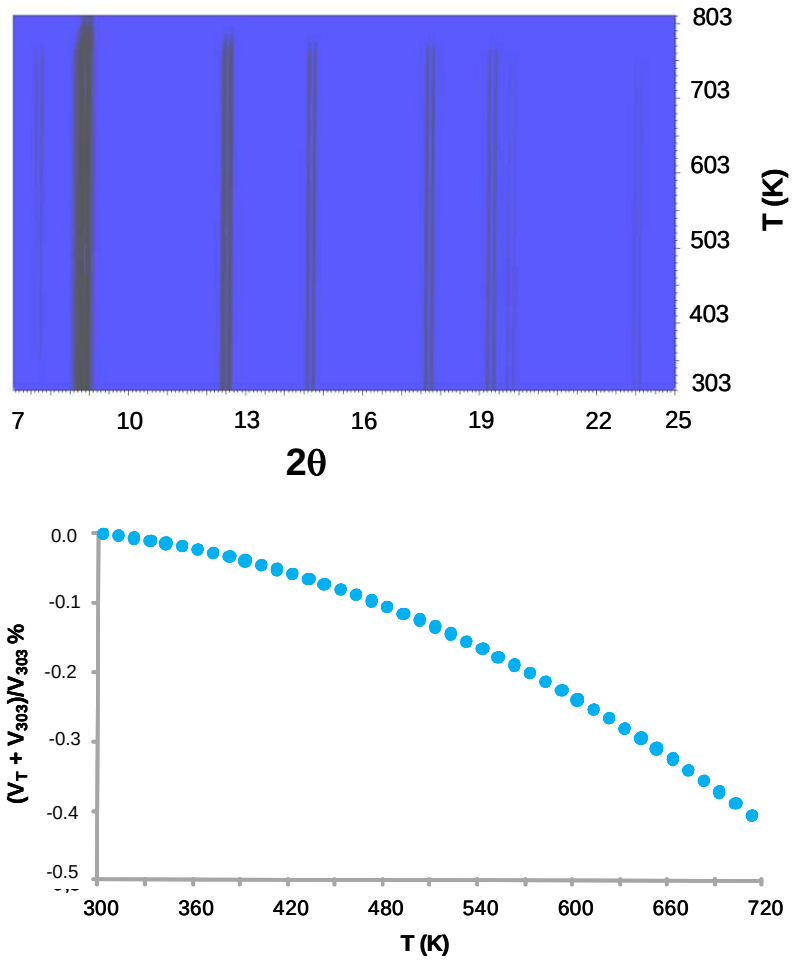

Figure 4.20. (Above) Two-dimensional contour plot of the XRPD data acquired on $[Zn_4O(L2)_3]$ in the 2θ range 7-25º, raising the temperature form 303 K up to 823 K; (below) variation of the unit cell volume of $[Zn_4O(L2)_3]$ (V_T) normalized to the corresponding 303 K value (V303) as a function of temperature.

The mechanical stability of both materials is also remarkably high. Indeed, the two crystal structures are practically unaffected by the application of pressures up to 2 tons (Figure 4.21).

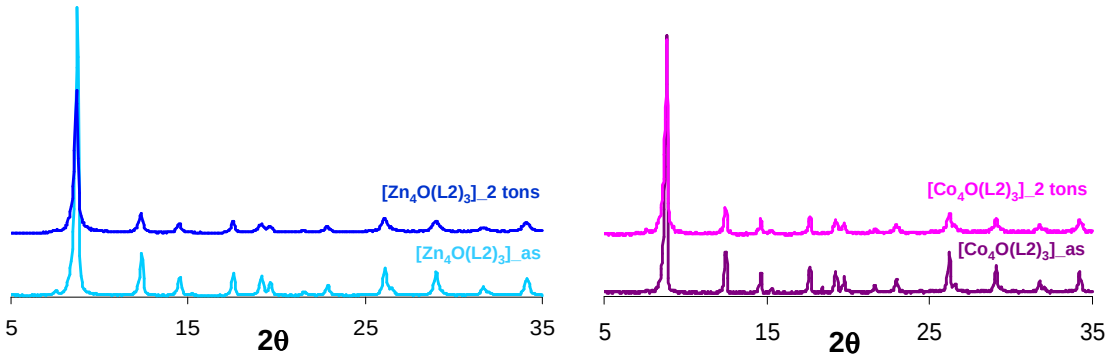

Figure 4.21. XRPD data for (left) $[Zn_4O(L2)_3]$ and (right) $[Co_4O(L2)_3]$ before and after the mechanical stress tests.

In the case of $[Co_4O(L2)_3]$ material, no significant porosity reduction is detected after the pressure treatment, while for $[Zn_4O(L2)_3]$ material, 2 tons pressure induces a *ca.* 20 % decrease of the specific surface area (Figure 4.22).

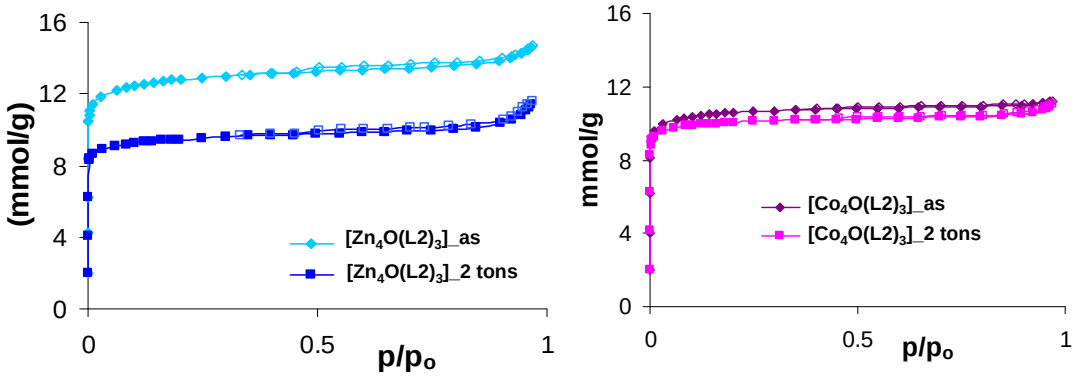

Figure 4.22. N_2 adsorption isotherms for (left) $[Zn_4O(L2)_3]$ and (right) $[Co_4O(L2)_3]$ before and after the mechanical stress tests. Empty symbols denote desorption.

By contrast, under similar conditions, the highly porous $[Cr_3F(H_2O)_2O(1,4\text{-benzenedicarboxylato})_3]$ (MIL-101) [36] and $[Cu_3(1,3,5\text{-benzenetricarboxylate})_2]$

(CuBTC)[37] MOFs undergo a significant amorphisation, with loss of up to 90 % of the original porosity.

Gas and vapour separation experiments

The accessibility of guest molecules into $[M_4O(L2)_3]$ porous networks has been assessed by solid-gas adsorption experiments towards a wide range of probe gases, namely N_2 (77 K), H_2 (77 K), CF_4 (298 K), SF_6 (298 K), and H_2O (298 K). No substantial differences in the adsorptive behaviour of the two solids can be appreciated for any of the tested molecules, as a consequence of their structural similarity.

N_2 adsorption isotherms (Figure 4.23.a) exhibit type I behaviour, which is typical of crystalline microporous materials, with BET specific surface area values of 840 ($[Zn_4O(L2)_3]$) and 805 ($[Co_4O(L2)_3]$) $m^2\ g^{-1}$. The adsorption capacity of micropores is quite high: *ca.* 12 mmol of $N_2\ g^{-1}$, corresponding to a micropore volume of 0.45 cm^3 *per* cm^3 of $[M_4O(L2)_3]$.

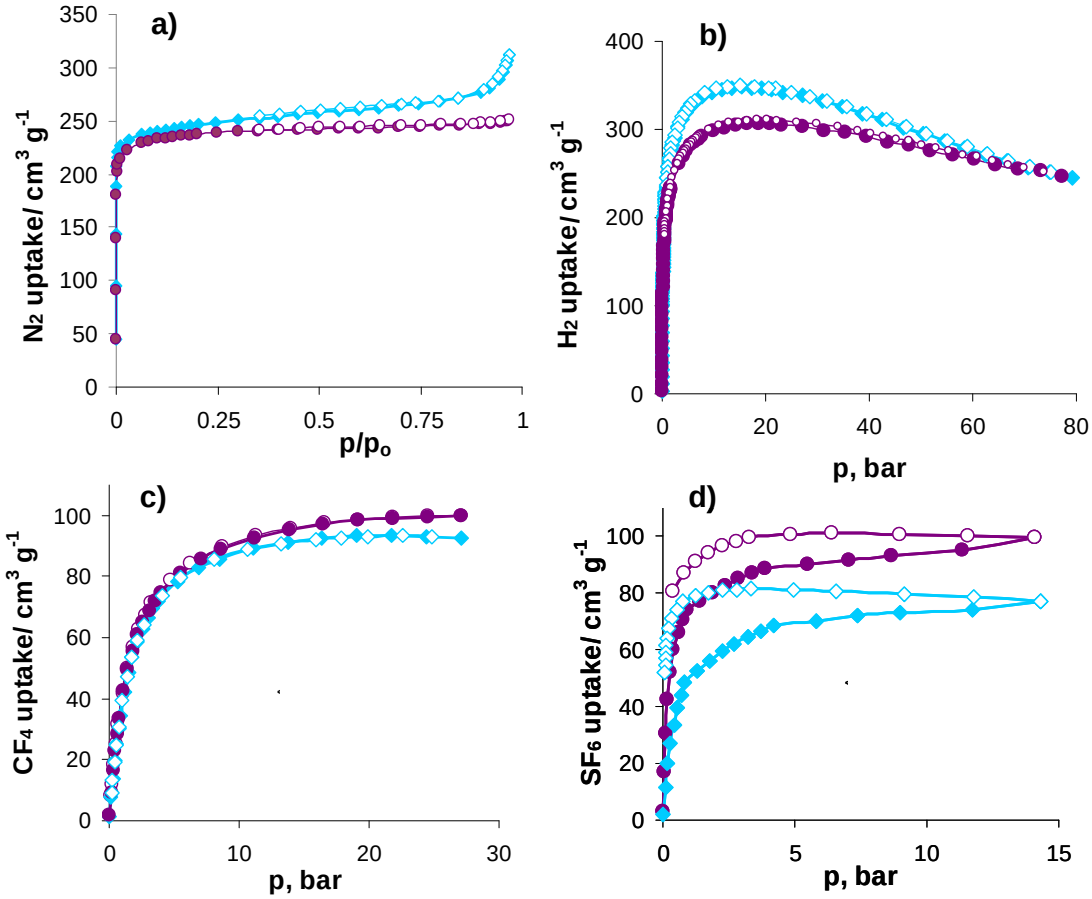

Figure 4.23. a) N_2 (77 K), b) H_2 (77 K), c) CF_4 (298 K) and d) SF_6 (298 K) adsorption isotherms for $[Zn_4O(L2)_3]$ (light blue diamonds) and $[Co_4O(L2)_3]$ (purple circles) materials. Empty symbols denote desorption.

H_2 adsorption isotherms (77 K) in the 0-80 bar range show a maximum uptake around 15 bar, with the adsorbed amount reaching 350 and 300 $cm^3\ g^{-1}$ for the Zn- and Co-based materials, respectively, that corresponds to an uptake of 3.0 and 2.6 % in weight (Figure 4.23.b). These experimental values are slightly lower than those reported for IRMOF-8 material measured under similar conditions, for which the uptake at 15 bar and 77 K is reported to be 3.6 % wt.[38] For pressures higher than 15 bar, the uptake of this probe molecule decreases slowly, because of the diminution of available pore volume as a consequence of the pressure stress exerted on the framework.

Moreover, adsorption properties of these two frameworks towards CF_4 and SF_6 greenhouse gases have also been tested at room temperature and high pressures (Figures 4.23.c and .d respectively). The scientific interest in these high global warming potential gases is related to the increasing need to reduce their concentration in the atmosphere. In this regard, it should be recommendable to find appropriate scaffolds to store tertafluoromethane and sulphur hexafluoride eventually obtained as by-products during chemical reactions, with the aim of preventing contamination of the atmosphere. Hence, $[M_4O(L2)_3]$ materials are robust enough to find a possible application in this extremely important field. Adsorption measurements reveal that $[M_4O(L2)_3]$ solids are porous to both gases at 298 K, with maximum uptakes reaching 100 $cm^3\ g^{-1}$ for both CF_4 and SF_6 gas molecules (at 30 and 15 bar respectively) adsorbed in the Co framework.

The adsorption of these greenhouses gases by the Zn-based material has been investigated in detail[39] because of the higher stability of this MOF compared to its Co analogue (see above).

The SF_6 adsorption isotherm follows the Langmuir Type with the desorption branch not following the adsorption one, so that a pronounced hysteresis is observed. This phenomenon might be best described by the term ‘‘kinetic trapping’’, since the structure is actually rigid and no extensive changes were observed during solvent removal, adsorption of gases, or under thermal or mechanical stress (as previously shown). Pore openings (4.0 x 4.0 Å) in the structure of $[Zn_4O(L2)_3]$ appear to be too small to let pass SF_6 molecules (kinetic diameter 5.5 Å). The adsorption is thus limited by the diffusion processes and the system might not reach equilibrium during the adsorption/desorption process. In order to further assess this behaviour, the adsorption kinetics of SF_6 at 25 and 60 ºC at 5 bar were investigated. As can be seen in Figure 4.24, the temperature

increase causes the increase of the molecules diffusivity and therefore forces the system towards equilibrium.

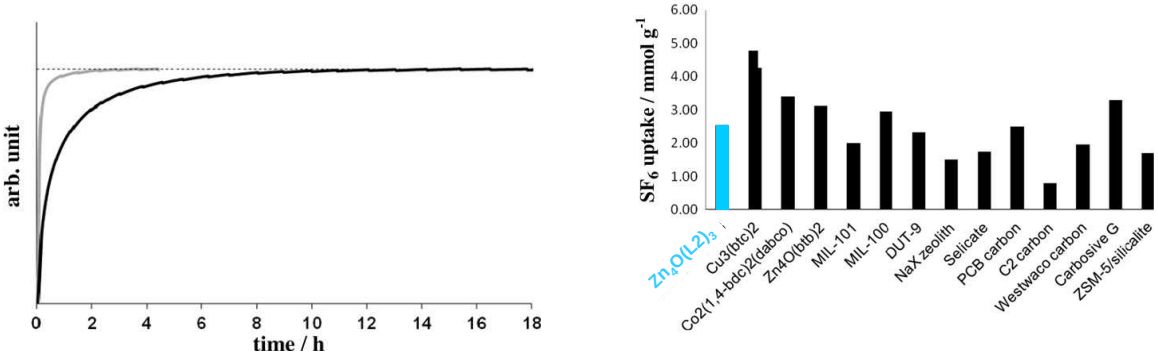

Figure 4.24. (Left) Kinetic adsorption curves for SF_6 on $[Zn_4O(L2)_3]$ measured at 5 bar: 25 ºC (black) and 60 ºC (gray); (right) comparison of different materials regarding SF_6 uptake at 1 bar and 298 K.

Moving further, the CF_4 physisorption isotherm is reversible and of type I. From the more flat isotherm slope (compared to the corresponding SF_6 isotherm), the binding energy of CF_4 to the adsorbent can be estimated being lower than that for SF_6 in the low pressure region (up to 1 bar). In this pressure range, $[Zn_4O(L2)_3]$ outperforms other well known porous MOF materials and, as shown in Figure 4.25, $[Zn_4O(L2)_3]$ shows the best performance: 42 $cm^3\ g^{-1}$; 1.88 mmol g^{-1}. Indeed, the kinetic diameter of CF_4 is just 4.7 Å and no trapping effect can be detected, as a consequence of the smaller kinetic diameter that perfectly adjusts to the pore/windows size.

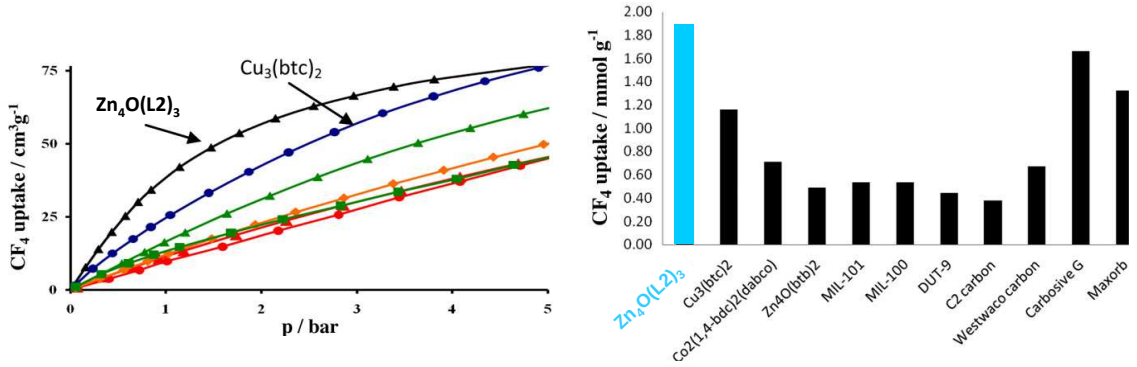

Figure 4.25. (Left) CF_4 (298 K) excess adsorption isotherm of $[Zn_4O(L2)_3]$ (black triangles), CuBTC (blue circles), MIL-100(Fe) (orange diamonds), MIL-101 (green squares), DUT-9 (red circles), Zn_4O(BTB) (red triangles) and Co_2(1,4-BDC)$_2$(dabco) (green triangles); (right) comparison of different materials regarding CF_4 uptake at 1 bar and 298 K.

Of particular interest is the water adsorption isotherm (298 K) measured for both materials. This measurement gives a clear idea of the hydrophobicity[40] of the studied system as well as of the robustness of the network toward hydrolysis. As already

pointed out in the introduction of this chapter, the most important limitation of MOF-5 material (and analogues thereof) is its sensitivity to moisture since hydrolysis of the M-O bond causes the damage and further breakage of the 3D structure. In the case of $[M_4O(L2)_3]$ materials, H_2O adsorption takes place only at very high relative pressures, which is indicative of highly hydrophobic structures (Figure 4.26). The total pore volume calculated from water adsorption isotherms amounts to 0.40 cm^3 *per* cm^3 of $[M_4O(L2)_3]$. Worthy of note, $[Zn_4O(L2)_3]$ shows very high reproducibility of H_2O adsorption isotherms on multiple cycles (that further supports its high stability towards hydrolysis). However, $[Co_4O(L2)_3]$ structure is affected by water adsorption as indicated by the shape change of the isotherm within three cycles. This result is in agreement with the low stability of this Co-based MOF when soaked in water.

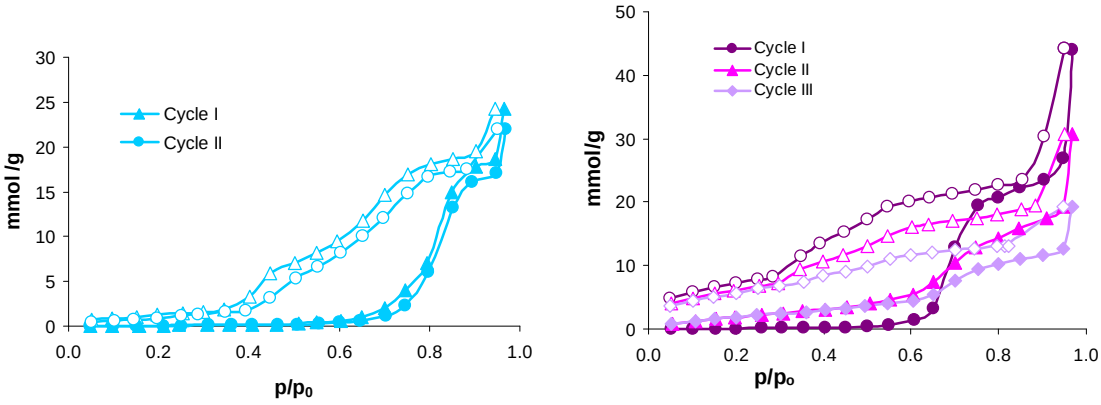

Figure 4.26. H_2O physisorption isotherm at 298 K for (left) $[Zn_4O(L2)_3]$ and (right) $[Co_4O(L2)_3]$. Empty symbols denote desorption.

The hydrophobic nature of $[Zn_4O(L2)_3]$ prompted us to investigate its utility for the capture of harmful volatile organic compounds (VOCs). These studies have been carried out by means of pulse gas chromatography [41] and measurement of breakthrough curves.[42] In order to assess the significance of the results, we have also studied the performances of cornerstone porous materials toward the capture of the essayed VOCs. To this purpose, we have selected a MOF with coordinatively unsaturated metal centers, $[Cu_3$(benzene-1,3,5-tricarboxylate$)_2]$ (CuBTC),[37] and a molecular sieve activated carbon material, namely Carboxen™ Adsorbent, from Sigma-Aldrich Co. The rationale behind this selection is the following: CuBTC is recognized as an outperforming material for the capture of the *S*-containing VOC tetrahydrothiophene in dry conditions, as a consequence of sulphur coordination to the unsaturated Cu centres.[43] On the other hand, activated carbon molecular sieve Carboxen™ possesses pore sizes in the 4-8 Å range

and a specific surface area of 485 $m^2 g^{-1}$ which are quite similar to $[Zn_4O(L2)_3]$ making of interest to compare the performances of these two materials to those of our material.

Therefore, columns packed with *ca.* 1 g of 0.5 mm-pellets of the studied materials have been prepared. As the particles of $[Zn_4O(L2)_3]$ were too small, and in order to avoid column pressure drops, the particles were aggregated by emulsifying them in a water suspension of starch. The solvent was removed under reduced pressure and the resulting solid was grounded down to 0.5 mm and characterized by XRPD and N_2 adsorption, showing that there is no loss of crystallinity and porosity. CuBTC was treated in a similar way to $[Zn_4O(L2)_3]$ while Carboxen™ was used as received. Prior to measurements, samples were outgassed and the columns were conditioned in He flow. Later on, 2 μL of each VOC were injected at 1 bar and the separation performance of each chromatographic column was examined at different temperatures (313 K-513 K) using the FID detector. Among the possible VOCs to be tested, we focused on the chemical warfare agents isopropylmethylfluorophosphate (IMFP, Sarin nerve gas), and bis(2-chloroethyl)sulphide (BCES, Mustard vesicant gas), although in our experiments we used their model compounds, namely disisopropylfluorophosphate (DIFP) and diethylsulphide (DES) depicted in Figure 4.27.

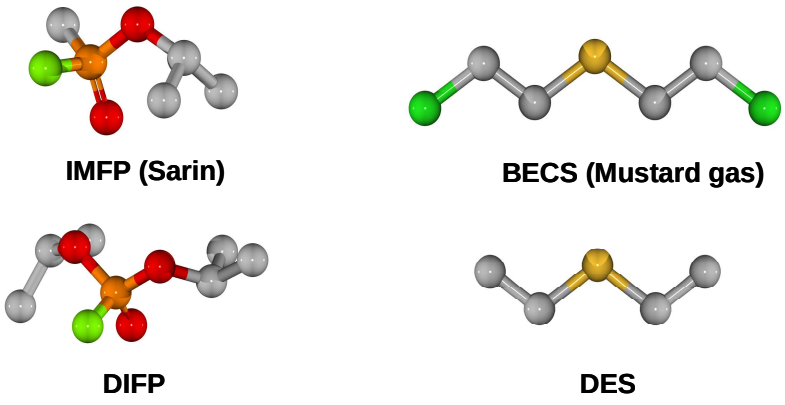

Figure 4.27. Chemical warfare agents isopropylmethylfluorophosphate (IMFP, Sarin nerve gas), and bis(2-chloroethyl)sulphide (BCES, Mustard vesicant gas), as well as their model compounds used in our studies (DIFP, disisopropylfluorophosphate; DES, diethylsulphide). **P**, **F**, **O**, **S**, **Cl**, **C**. H atoms have been omitted for clarity.

Moreover, we also investigated the possible utility of this material for the separation of benzene/cyclohexane mixtures by size selective adsorption since these two molecules cannot be separated by distillation due to the similarity in their boiling points (see Chapter 2).

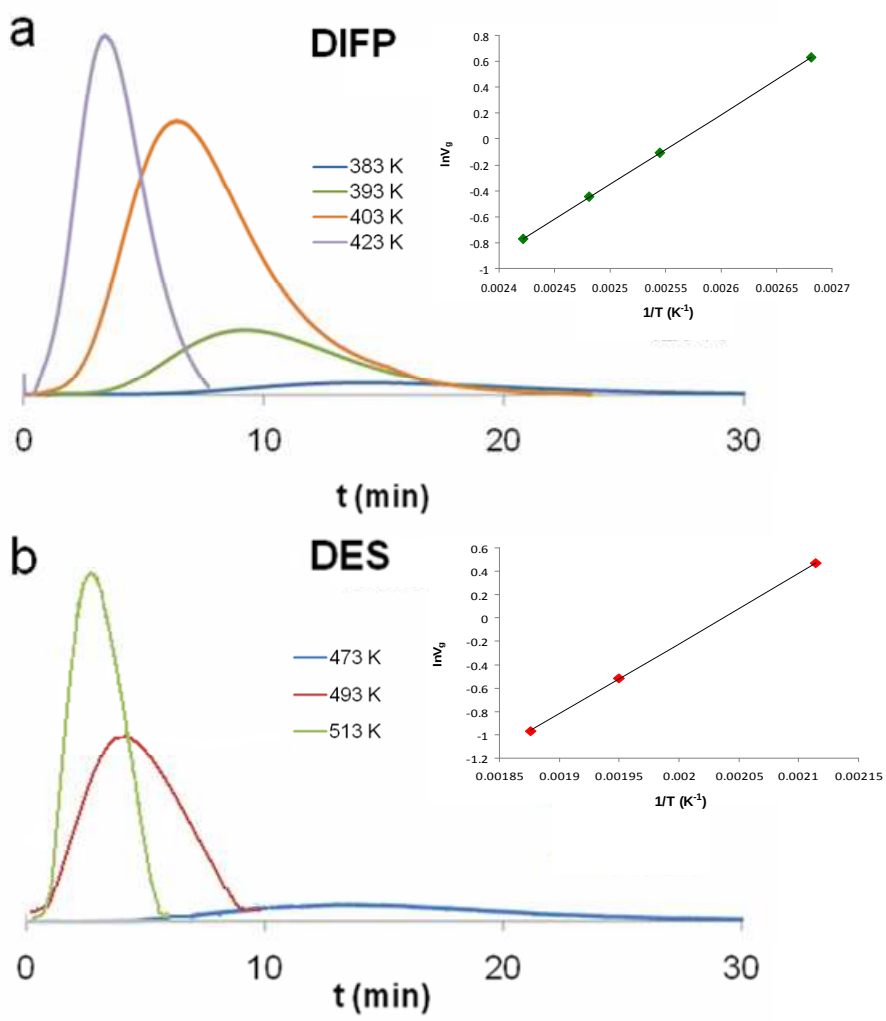

Figure 4.28. Variable-temperature pulse gas chromatograms for a) disopropylfluorophosphate (DIFP) and b) diethylsulphide (DES) passed through a chromatographic column packed with $[Zn_4O(L2)_3]$ using a He flow of 30 mL min^{-1}. The insets represent the variation of retention volume V_g (cm^3 g^{-1}) as a function of adsorption temperature (383-513 K).

The variable-temperature pulse gas chromatographic studies reveal high retention times for benzene and for chemical warfare models DIFP and DES (see Figure 4.28 and Table 4.1), indicative of a strong interaction of this type of adsorbates with the porous framework of $[Zn_4O(L2)_3]$. By contrast, cyclohexane and water vapour are characterized by very low retention times. The small interaction of cyclohexane with $[Zn_4O(L2)_3]$ is probably related to its average molecular diameter (higher than 6 Å), larger than the small pore window opening of 4.4 Å for $[Zn_4O(L2)_3]$, while the weak interaction of H_2O agrees, once again, with the hydrophobic nature of this MOF (see above).

Table 4.1. Calculated heats of adsorption (ΔH_{ads}), Henry constants (K_H) and partition coefficients (K_r) for VOCs.

VOC*	$-\Delta H_{ads}$ (kJ mol^{-1})	K_H (cm^3 m^{-2})	K_r
DES	50.1	2850	9950
DIFP	44.8	71.2	275
BZ	48.2	1090	4170
CH	9.4	0.07	0.24
H_2O	17.9	0.26	-

* DIFP = disisopropylfluorophosphate, DES = diethylsulphide, BZ = benzene, CH = cyclohexane.

In order to quantify the strength of the interaction of these guest molecules with $[Zn_4O(L2)_3]$, we have calculated their zero-coverage adsorption heats (ΔH_{ads}) from the variation of retention volumes (V_g) as a function of temperature, according to $\Delta H_{ads} = -R\delta(\ln V_g)/\delta(1/T)$.[44] Henry constant values at ambient conditions (298 K) have then been obtained in the direct relation between retention volume (V_g) and Henry constants (K_H). The results are summarized in Table 4.1. The high values of ΔH_{ads} and K_H in the case of benzene and of essayed chemical warfare models further indicate the strength of their interaction with $[Zn_4O(L2)_3]$. On the other hand, the low affinity of this material to water gives rise to very high VOC/H_2O partition coefficients (K_r), suggesting that ambient moisture should not hamper VOCs incorporation into $[Zn_4O(L2)_3]$. In order to perform an experiment that would mimic the constant exposure (over time) to a humid stream containing benzene, we decide to measure breakthrough curves at room temperature (293 K) on $[Zn_4O(L2)_3]$. Hence, 10 mL min^{-1} He flux containing 130 ppm of benzene has been flowed through the activated sample packed into a column initially purged with helium. A similar experiment was followed containing 50 % humidity. The relative amounts of the gases passing through the column were monitored on a mass spectrometer gas analysis system.

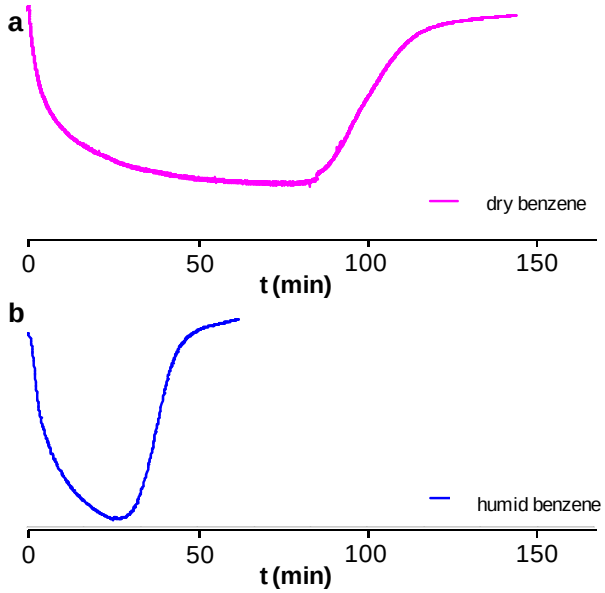

Figure 4.29. Breakthrough curves performed by $[Zn_4O(L2)_3]$ with 10 mL min^{-1} He flow containing 130 ppm of benzene in a) dry and b) humid conditions.

Breakthrough curves measurements performed on $[Zn_4O(L2)_3]$ with streams of dry and humid benzene support the effectiveness of this material in VOCs capture at room temperature (293 K) also in the presence of moisture (see Figure 4.29). Indeed, in dry conditions, $[Zn_4O(L2)_3]$ adsorbs 130 mg of benzene *per* gram, while, if previously exposed to open air for 48 h, and in humid conditions (50 % moisture) it still adsorbs 60 mg g^{-1} of this VOC, confirming that ambient moisture is not a strong competitor.

Table 4.2. Calculated heats of adsorption (ΔH_{ads}), Henry constants (K_H) and partition coefficients (K_r) for VOCs

Adsorbent	**VOC***	**$-\Delta H_{ads}$ (kJ mol^{-1})**	**K_H (cm^3 m^{-2})**	**K_r**
CuBTC	DES	78.1	6570	116
CuBTC	DIFP	48.4	67.9	1.2
CuBTC	H_2O	43.9	56.3	-
Carboxen™	DES	49.0	1170	58000
Carboxen™	DIFP	38.3	76.9	3800
Carboxen™	H_2O	2.7	0.02	-

* DIFP = disisopropylfluorophosphate, DES = diethylsulphide.

Variable temperature zero-coverage adsorption measurements of CuBTC and Carboxen™ are summarized in Table 4.2. Zero-coverage adsorption heats and Henry constants values for Carboxen™ are very similar to those obtained with $[Zn_4O(L2)_3]$,

thus suggesting similar adsorption processes, mainly dominated by the small size and apolar nature of pores in both materials. At variance, ΔH_{ads} and K_H values for CuBTC when probed by DES and H_2O are remarkably higher than those obtained with the two former porous materials, as a consequence of the interaction of these probe molecules with the coordinatively unsaturated metal centres through their *S*- and *O*-donor sites, respectively. Anyway, the high affinity of water for Cu(II) in CuBTC, induces very low VOC/H_2O partition coefficients: this unfortunate effect (unequivocally manifested by a color change from deep purple to light blue) that takes place when CuBTC pellets are exposed to ambient moisture, definitely hampers the usefulness of this material in ambient conditions. Accordingly, if CuBTC is previously exposed to air and than placed in the chromatographic column, neither DES nor DIFP are retained. It should be noted that, since DES retention by CuBTC should be favoured by its high DES/H_2O K_r, we can conclude that under the essayed dynamic conditions the thermodynamic equilibrium is not reached.[45] By contrast, as expected on the basis of their hydrophobic nature, both Carboxen^{TM} and $[Zn_4O(L2)_3]$ should retain DES under humid conditions.

Of particular interest are the results obtained for the interaction of the porous materials under investigation with the highly toxic DIFP Sarin analogue. In this regard, it should be noted that human exposition to 50-100 ppb concentration levels of Sarin for 1 min by inhalation or to 100-500 mg through skin are lethal.[46] Considering an atmosphere containing 50 % humidity at 298 K, the H_2O/Sarin ratio should be maintained above the 100-200 range. Hence, only hydrophobic adsorbents like Carboxen^{TM} or $[Zn_4O(L2)_3]$ with K_r(DIFP/H_2O) > 200 would be effective in maintaining the DIFP concentration below the lethal levels. By contrast, $[Cu_3(BTC)_2]$, with K_r(DIFP/H_2O) = 1.2, would be not useful for Sarin removal under ambient conditions.

4.2.2. $Co_4O(L6)_3$ compound

Crystal structure

The reaction of $Co(AcO)_2$ with 4,4'-buta-1,3-diyne-1,4-diylbis(1-Boc-3,5-dimethyl-pyrazole) (Boc_2L6) in DMF medium at 125 ºC in a Teflon liner, affords a bright blue microcrystalline material of formulation $[Co_4O(L6)_3]_n \cdot$solv ($[Co_4O(L6)_3]$). This Co-PCP crystallizes in the cubic space group *Im-3m* with a = 16.6573(4) Å and V = 4620.65(2) Å^3, although the space group *I-43m* can be used as well to describe the topology. No discrimination between the two space groups can be done since they possess the same

systematic extinctions. The L6 ligands and $\{Co_4O\}$ units are linked into an interpenetrated network (Figure 4.30).

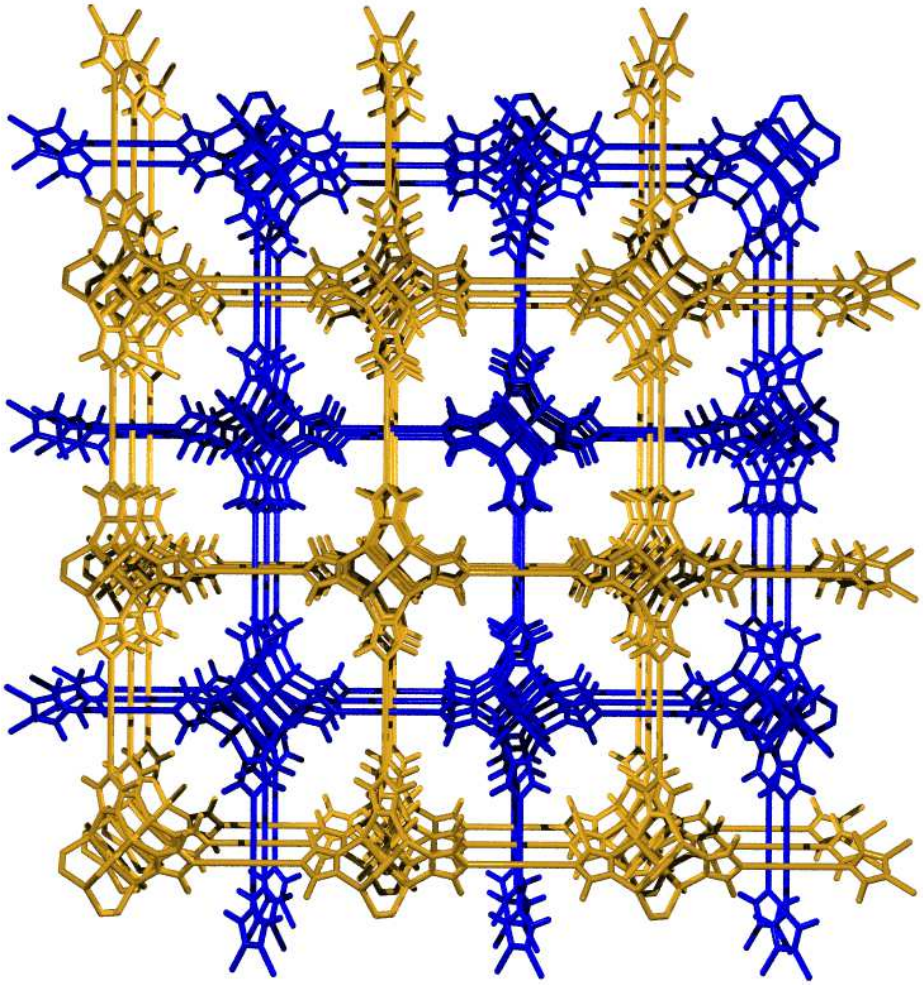

Figure 4.30. Perspective view of interpenetrated $[Co_4O(L6)_3]$ porous coordination polymer. The two independent frameworks are depicted in blue and orange.

The structure of $[Co_4O(L6)_3]$ is similar to that of interpenetrated MOF-5 (see above), which has a interdigitated CaB_6-type framework topology. The $[Co_4O(L6)_3]$ network encloses octahedral $\{Co_4O(dmpz)_6\}$ nodes that are reminiscent of the $\{Zn_4O(CO_2)_6\}$ secondary building units of MOF-5 (Figure 4.31).

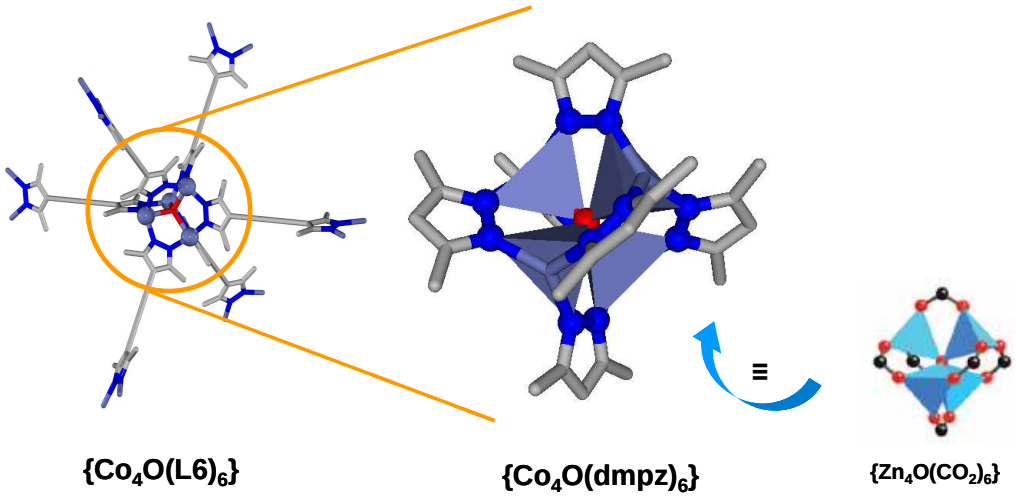

Figure 4.31. View of the $\{Co_4O(L6)_6\}$ cluster with magnification of its $\{Co_4O(dmpz)_6\}$ core, reminescent to the $\{Zn_4O(CO_2)_6\}$ cluster found in MOF-5 material.

The occurrence of interpenetration dramatically reduces the void volume as well as the pore size and pore window. Indeed, pore's windows along *a*, *b* and *c* axes would be more than 10 Å wide for the non-interpenetrated structure while, for the interpenetrated one, these openings are partially filled by the second interwoven net. Thereby, the largest pore's windows can be found along the [100] crystallographic direction and correspond to an opening of approx 8.3 Å, as indicated in Figure 4.32. The void volume has been calculated to be 46 % of the cell volume, a very high value if we consider that the system is interpenetrated.

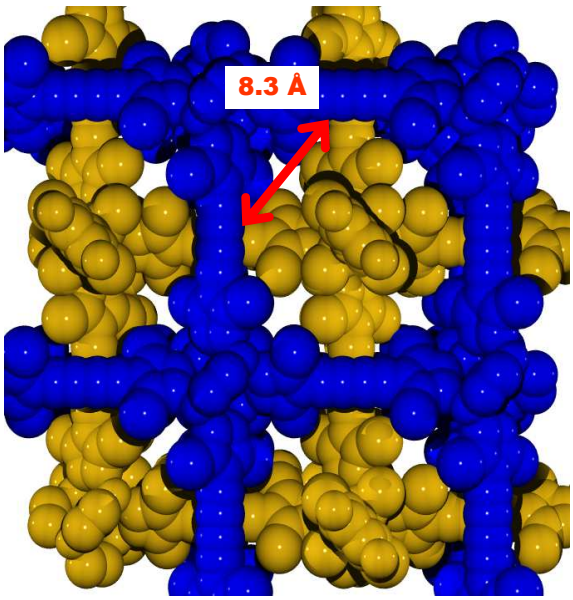

Figure 4.32. Space filling view of the interpenetrated $[Co_4O(L6)_3]$ structure along the [100] crystallographic direction. The size of the pore's window is highlighted. The two independent frameworks are depicted in blue and orange.

We are aware of the scientific interest for the comparison of structural and textural properties of interpenetrated and non-interpenetrated nets (likely for MOF-5 material, see above), but unfortunately our attempts to achieve the non-interpenetrated $[Co_4O(L6)_3]$ framework failed. The use of templates (of various chemical nature and different concentrations) as well as the modification of reaction conditions (i.e. concentration and ratio of reagents, temperature, time of reaction, solvents, anion for the Co^{2+}) unavoidably lead to $[Co_4O(L6)_3]$ interpenetrated structure or else to amorphous solids.

Thermal stability

Thermogravimetric analyses performed on $[Co_4O(L6)_3]$ in both air and nitrogen atmosphere have revealed a considerably high thermal robustness, with decomposition beginning only at 360 ºC, as can be appreciated in Figure 4.33. The two traces perfectly overlap, so the material proves to be neither oxidized by atmospheric oxygen nor damaged by ambient moisture, even if solvent guest molecules already left the framework.

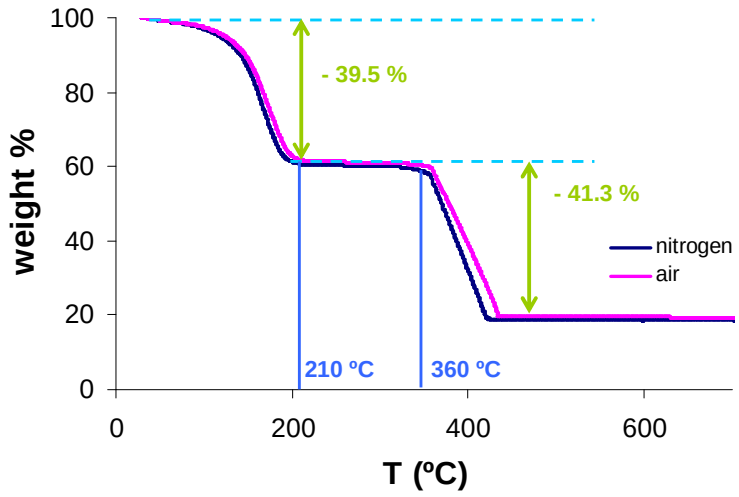

Figure 4.33. TGA traces for $[Co_4O(L6)_3]$ material in air and N_2 atmosphere.

The material progressively loses solvent guest molecules in the temperature range 25-200 ºC, with a relative weight loss of 39.5 %. This experimental evidence is in agreement with the total solvent amount calculated by means of AE data (41.2 %, see Appendix I) as well as with the nature of included solvent molecules. Indeed, it has been calculated that the framework contains 5 H_2O molecules and 8 DMF molecules per

molecular formula unit that would progressively leave the structure under thermal treatment. The fact that DMF molecules still leave the net at temperatures higher than their boiling point is indicative of the occurrence of a trapping phenomenon since the size of the pore windows is quite small and evaporation of the included solvent molecules would require extra energy input.

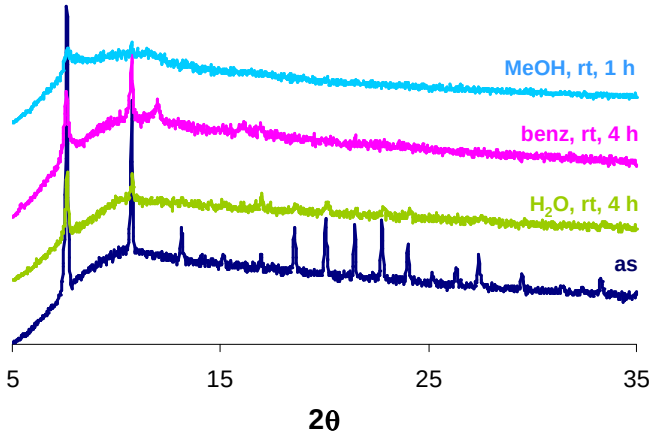

Figure 4.34. Chemical stability tests on $[Co_4O(L6)_3]$ suspended in methanol (1 h), benzene (4 h) and water (4 h) at room temperature.

Chemical stability tests performed on $[Co_4O(L6)_3]$ (Figure 4.34) show that the material suspended in water, benzene and methanol at room temperature significantly loses crystallinity. Indeed, when the solid is suspended in water at room temperature, the intensities of main peaks noticeably lowers within 4 h, although the diffraction pattern remains unchanged. Differently, when the solid is stirred in dry benzene, a phase transformation starts after 4 h, as confirmed by the appearance of a new peak at $2\theta = 12.1^{o}$. Finally, $[Co_4O(L6)_3]$ seems not to be very stable in MeOH at room temperature since its XRPD becomes nearly flat just after 1 h treatment. Chemical stability tests confirm the hydrophobic nature of the framework since water does not damage the material as rapidly as benzene and methanol do.

Anyway, the bulging shape of XRPDs presented in Figure 4.34 is indicative of the presence of a significant amount of amorphous material as well as of low electronic density in the crystal (high porosity). Therefore, it is likely that a highly porous and poorly crystalline framework could be severely damaged by the exchange of guest solvent molecules.

Gas adsorption properties

A preliminary study of the gas adsorption properties of $[Co_4O(L6)_3]$ material has been conducted in order to evaluate its permanent porosity towards N_2 (77 K) and CO_2 (273 K) gas probe molecules (Figure 4.35). Prior to measurements, the solid has been activated under high vacuum at 200 ºC, as suggested by thermogravimetric analysis curve.

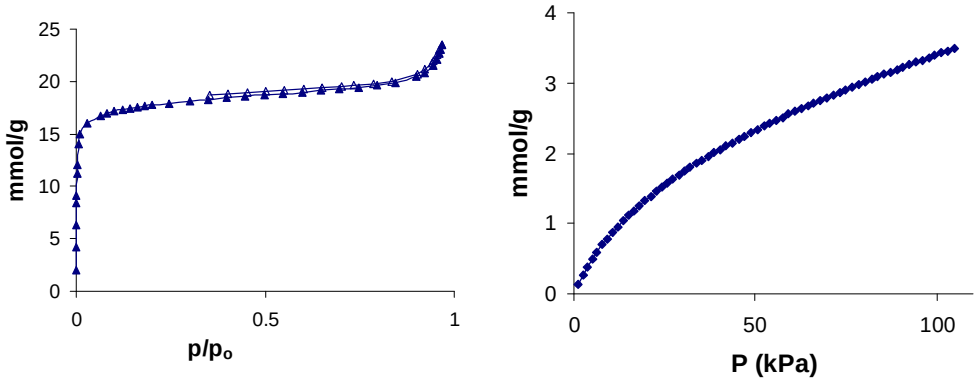

Figure 4.35. (Left) N_2 (77 K) (right) CO_2 (273 K) adsorption isotherms for $[Co_4O(L6)_3]$ material. Empty symbols denote desorption.

Nitrogen adsorption isotherm (77 K) is of type I, as expected for a microporous solid, and the desorption branch perfectly follow the adsorption one. The maximum N_2 uptake approaches 20 mmol g^{-1} at $p/p_o = 0.9$ and the BET specific surface area is 1355 $m^2\ g^{-1}$. It should be highlighted that these values are considerably high and consequently are indicative of the highly accessible nature of its porous network in spite of the interpenetrated nature of the framework. CO_2 physisorption isotherm (273 K) is again of type I. The flat isotherm slope indicates that the binding energy of CO_2 to the adsorbent is very small and the adsorbed gas amount progressively increases as the gas pressure increases.

As previously said, it would be very interesting to compare the shape of gas adsorption isotherms as well as the maximum adsorbed gas amounts for the non-interpenetrated and interpenetrated structure but, at the moment, only one of these two materials has been obtained.

4.3. Conclusions

The unusually high thermal, mechanical and chemical stabilities of the novel $[Zn_4O(L2)_3]$ MOF material clearly outperforms the stability of the archetypical MOF-5

material particularly towards moisture, as a consequence of the strength of M-N(pyrazole) coordination bonds and the protection exerted by the methyl groups on the Zn_4O moieties. Moreover, the outperforming behavior of $[Zn_4O(L2)_3]$ MOF for the selective capture of harmful VOCs (chemical warfare models) suggests a possible practical application of this material. Indeed, this type of materials could be incorporated into air filters or protective textiles that could be used to capture harmful gases, ensuring decontamination of the air stream passing through the protective equipment (see Figure 4.37). In this regard, the high stability of this MOF in ambient air and its extraordinary selectivity for VOCs vs. moisture will be the key features to guarantee their possible use under real operative conditions.

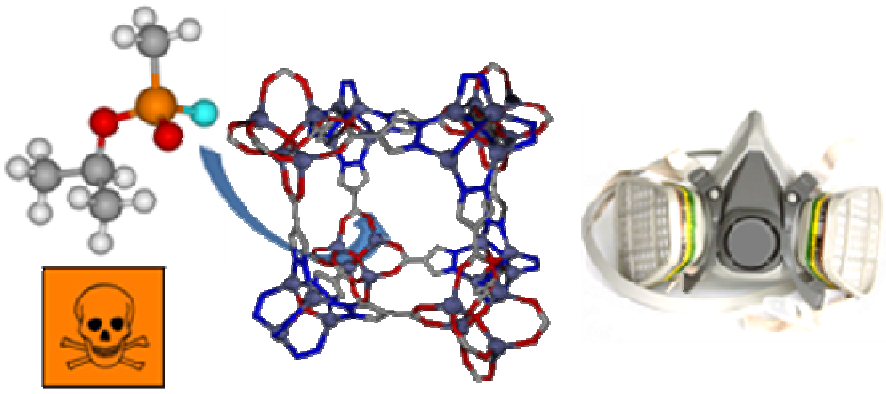

Figure 4.37. Pictorial summary of the possible application of $[Zn_4O(L2)_3]$ material.

On the other hand, the Zn_4O moiety, characteristic of both $[Zn_4O(L2)_3]$ and MOF-5 materials, is also found in two novel Co-based porous materials: $[Co_4O(L2)_3]$ and $[Co_4O(L6)_3]$. The former PCP is isostructural to $[Zn_4O(L2)_3]$ and shows similar gas adsorption properties although lower stability in the presence of water. The latter, as a consequence of the low steric demand and increased length of L6 ligand compared to L2, consists of two interpenetrated independent nets with the same cubic topology of MOF-5. Despite the occurrence of interpenetration, this material is still highly porous although poorly chemically stable when the solvent guest molecules are exchanged.

4.4. Bibliography

[1] H. Li, M. Eddaoudi, M. O'Keeffe, O. M. Yaghi, *Nature*, **1999**, *402*, 276.

[2] M. Eddaoudi, J. Kim, N. Rosi, D. Vodak, J. Wachter, M. O'Keeffe, O. M. Yaghi, *Science*, **2002**, *295*, 469.

[3] N. L. Rosi, J. Eckert, M. Eddaoudi, D. T. Vodak, J. Kim, M. O'Keeffe, O. M. Yaghi, *Science*, **2003**, *300*, 1127.

[4] L. Huang, H. Wang, J. Chen, Z. Wang , J. Sun, D. Zhao, Y. Yan, *Microp. and Mesop. Mat*. **2003**, *58*, 105.

[5] A. D. Burrows, K. Cassar, R. M. W. Friend, M. F. Mahon, S. P. Rigbyb, J. E. Warren, *Cryst. Eng. Comm*. **2005**, *7*, 548.

[6] a) A. I. Skoulidas, D. S. Sholl, *J. Phys. Chem. B,* **2005**, *109*, 15760; b) G. Garberoglio, A. I. Skoulidas, J. K. Johnson, *J. Phys. Chem. B,* **2005**, *109*, 13094; c) T. Duren, R. Q. Snurr, *J. Phys. Chem. B,* **2004**, *108*, 15703; d) T. Sagara, J. Klassen, E. Ganz, *J. Chem. Phys.* **2004**, *121*, 12543.

[7] J. A. Greathouse, M. D. Allendorf, *J. Am. Chem. Soc*. **2006**, *128*, 10678.

[8] B. Panella, M. Hirscher, *Adv. Mater.* **2005**, *17*, 538.

[9] S. S. Kaye, A. Dailly, O. M. Yaghi, J. R. Long, *J. Am. Chem. Soc.* **2007**, *129*, 14176.

[10] J. Yang, A. Grzech, F. M. Mulderb, T. J. Dingemans, *Chem. Commun.* **2011**, *47*, 5244.

[11] H. Kim, S. Das, M. G. Kim, D. N. Dybtsev, Y. Kim, K. Kim, *Inorg. Chem*. **2011**, *50*, 3691.

[12] J. Hafizovic, M. Bjørgen, U. Olsbye, P. D. C. Dietzel, S. Bordiga, C. Prestipino, C. Lamberti, K. P. J. Lillerud, *J. Am. Chem. Soc*. **2007**, *129*, 3612.

[13] Z. Zhao, X. L. Ma, Z. Li, Y. S. Lin, *J. Membr. Sci*. **2011**, *382*, 82.

[14] Z. Zhao, X. Ma, A. Kasik, Z. Li, Y. S. Lin, *Ind. Eng. Chem. Res*. in press, DOI: dx.doi.org/10.1021/ie202777q.

[15] J. I. Feldblyum, E. A. Keenan, A. J. Matzger, S. Maldonado, *J. Phys. Chem. C*, **2012**, *116*, 3112.

[16] F. Schröder, D. Esken, M. Cokoja, M. W. E. van den Berg, O. I. Lebedev, G. Van Tendeloo, B. Walaszek, G. Buntkowsky, H.-H. Limbach, B. Chaudret, R. A. Fischer, *J. Am. Chem. Soc*. **2008**, *130*, 6119.

[17] A. Bellfoorte, F. Calderazzo, U. Englert, J. Strähle, *Inorg. Chem.* **1991**, *30*, 3778.

[18] H. Hou, L. Li, G. Li, Y. Fan, Y. Zhu, *Inorg. Chem*. **2003**, *42*, 3501.

[19] P. F. Haywood, M. R. Hill, N. K. Roberts, D. C. Craig, J. J. Russell, R. N. Lamb, *Eur. J. Inorg. Chem.* **2008**, 2024.

[20] K. Koh, A. G. Wong-Foy, A. J. Matzger, *Angew. Chem. Int. Ed*. **2008**, *47*, 677.

[21] K. Koh, A. G. Wong-Foy, A. J. Matzger, *J. Am. Chem. Soc*. **2009**, *131*, 4184.

[22] S. Barman, H. Furukawa, O. Blacque, K. Venkatesan, O. M. Yaghi, H. Berke, *Chem. Commun.* **2010**, *46*, 7981.

[23] D. Sun, D. J. Collins, Y. Ke, J.-L. Zuo, H.-C. Zhou, *Chem. Eur. J*. **2006**, *12*, 3768.

[24] L. Hou, Y.-Y. Lin, X.-M. Chen, *Inorg. Chem.* **2008**, *47*, 1346.

[25] R. J. F. Berger, M. A. Schmidt, J. Juselius, D. Sundholm, P. Sirsch, H. Schmidbaur, *Naturforsch. B:Chem.Sci*. **2001**, *56*, 979.

[26] D. Domide, O. Walter, S. Behrens, E. Kaifer, H.-J. Himmel, *Eur. J. Inorg. Chem.* **2011**, 860.

[27] M. Tonigold, Y. Lu, B. Bredenkötter, B. Rieger, S. Bahnmüller, J. Hitzbleck, G. Langstein, D. Volkmer, *Angew. Chem. Int. Ed*. **2009**, *48*, 7546.

[28] N. Masciocchi, G. A. Ardizzoia, S. Brenna, G. LaMonica, A. Maspero, S. Galli, A. Sironi, *Inorg. Chem.* **2002**, *41*, 6080.

[29] H. Li, M. Eddaoudi, M. O'Keeffe, O. M. Yaghi, *Nature*, **1999**, *402*, 276.

[30] To build the rigid model describing the ligand, bond distances and angles have been adopted according to the results of a query throughout the Cambridge Structural Database on similar moieties. In detail, for the pyrazole ring: C-C, C-N, N-N = 1.36 Å; C-H = 0.95 Å; internal ring angles = 108°; C-C-H = 126°; $C_{pyrazole}$ - $C_{carboxylate}$ = 1.49 Å; $C_{carboxylate}$ - $O_{carboxylate}$ = 1.25 Å.

[31] D. Eufri, A. Sironi, *J. Mol. Graphics*, **1989**, *7*, 165.

[32] H. Deng, C. J. Doonan, H. Furukawa, R. B. Ferreira, J. Towne, C. B. Knobler, B. Wang, O. M. Yaghi, *Science*, **2010**, *327*, 846.

[33] S. Proch, J. Herrmannsdorfer, R. Kempe, C. Kern, A. Jess, L. Seyfarth, J. Senker, *Chem. Eur. J*. **2008**, *14*, 8204.

[34] D. Britt, D. J. Tranchemontagne, O. M. Yaghi, *Proc. Natl. Acad. Sci. USA*, **2008**, *105*, 11623.

[35] H. J. Choi, M. Dincă, A. Dailly, J. R. Long, *Energy Environ. Sci*. **2010**, *3*, 117.

[36] G. Ferey, C. Mellot-Draznieks, C. Serre, F. Millange, J. Dutour, S. Surble, I. Margiolaki, *Science*, **2005**, *309*, 2040.

[37] S. S. Y. Chui, S. M. F. Lo, J. P. H. Charmant, A. G. Orpen, I. D. Williams, *Science*, **1999**, *283*, 1148.

[38] A. Dailly, J. J. Vajo, C. C. Ahn, *J. Phys. Chem. B*, **2006**, *110*, 1099.

[39] I. Senkovska, E. Barea, J. A. R. Navarro, S. Kaskel, *Micro. and Meso. Mater*. **2012**, *156*, 115.

[40] C. Serre, *Angew. Chem. Int. Ed*. **2012**, *51*, 6048.

[41] G. Guiochon, A. Felinger, A. M. Katti, D. G. Shirazi, in *Fundamentals of Preparative and Nonlinear Chromatography*, Elsevier: Amsterdam, **2006**.

[42] E. Quartapelle Procopio, F. Linares, C. Montoro, V. Colombo, A. Maspero, E. Barea, J. A. R. Navarro, *Angew. Chem. Int. Ed*. **2010**, *49*, 7308.

[43] a) G. Ferey, *Chem. Soc. Rev.* **2008**, *37*, 191; b) D. Farrusseng, S. Aguado, C. Pinel, *Angew. Chem. Int. Ed*. **2009**, *48*, 7502; c) A. Corma, H. García, F. X. Llabrés Xamena, *Chem. Rev*. **2010**, *110*, 4606.

[44] E. Diaz, S. Ordoñez, A. Vega, *J. Colloid Interf. Sci*. **2007**, *305*, 7.

[45] D. Britt, D. J. Tranchemontagne, O. M. Yaghi, *Proc. Natl. Acad. Sci. USA*, **2008**, *105*, 11623.

[46] Gulf War and Health. Vol 1. Division of Health Promotion and Disease Prevention, Institute of Medicine, Washington, **2000**.

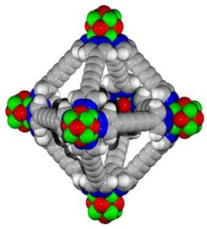

5. Ni_8L_6 SERIES OF ISOMORPHOUS PCPs

5.1. Introduction

Nowadays, many research groups are trying to synthesize new Porous Coordination Polymers with very large surface areas and pore volumes,[1] in order to obtain highly porous compounds suitable for the adsorption of a huge amount of gas, vapours or small/middle size molecules. In general, the employment of longer linkers, should give rise to PCPs with larger cell parameters[2] although inconveniences such as low stability and interpenetration can limit the scalability of their properties. As a matter of fact, the infinite number of organic ligands that could be used as building blocks for the construction of PCPs could inspire the design of a series of porous structures in which pore dimension can be tuned systematically. In particular, the longer the linker the larger will become the pore size. Thus, for a group of organic molecules with the same functional groups but different length, it might be possible to obtain a library of isoreticular compounds covering the range between microporous to mesoporous materials by keeping constant the reaction conditions and only changing the linker.

As already discussed in Chapter 1, interpenetration is an important aspect to be considered when the size of the organic ligand is getting considerably large. Indeed, two or more frameworks can grow in a 3D interweaved structure that can be disentangled only by breaking internal connections. In some cases, interpenetration is an advantage since the resulting structure could be much more stable than its non-interwoven counterpart thanks to a mutual stabilization of the two (or more) intertwined nets. Anyhow, in all cases interpenetration occurs, the pore volume is reduced with respect to that corresponding to the single network. So, if the new structure is envisaged for small size molecule adsorption/release, the dimension of the pores should be carefully checked taking into account the *n*-weaved nature of the net. Thereby, depending on the chances of interpenetration for a certain framework, the reaction conditions must be carefully controlled and the use of template molecules should be contemplated in order to achieve the desired non-interwoven three-dimensional architecture.

An example of a library of isoreticular compounds is the well known IRMOF (IsoReticular Metal Organic Framework) series published in 2002 by Yaghi and co-workers.[3] They reported the systematic design and construction of a series of crystalline MOFs that have the same cubic structure of MOF-5 (Figure 5.1), wherein the size and the functionality of the pores have been changed in a systematic rational way.

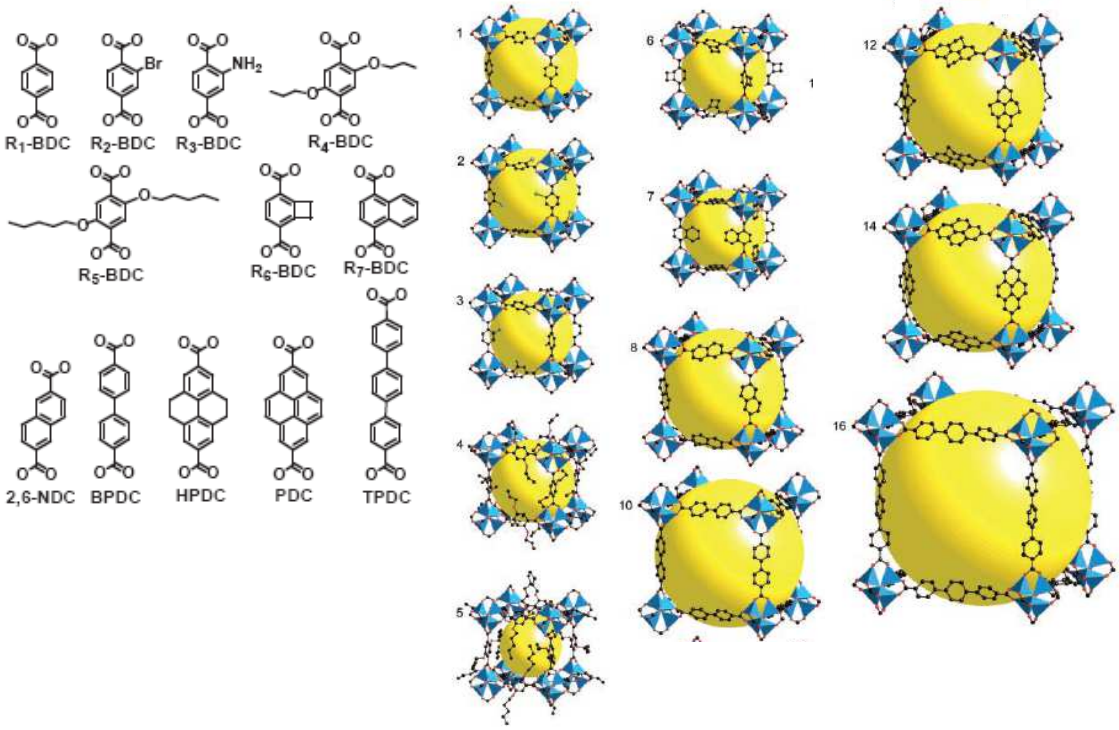

Figure 5.1. Scheme of the ligands used in the IRMOF series (left) and single crystal X-ray structures of IRMOF-n (right). **Zn** (polyhedra), **O** (spheres), **C** (spheres), **Br** (spheres in 2), **amino-groups** (spheres in 3). The yellow spheres represent the largest van der Waals spheres that should fit in the cavities.

The authors studied the dependence of some physical and chemical properties of these compounds (i.e. crystal densities, % free volume) with the size of the employed linker and found a kind of periodicity in the studied properties, due to the increase in pore size and to the different functionalization of the employed ligands. Anyway, the low stability of IRMOF-1 (also known as MOF-5) in the presence of humidity is well known and this feature is the biggest limitation for this class of compounds (see Chapter 4).

More recently, another series of three isomorphic MOFs, based on $Zr_6O_4(OH)_4(CO_2)_{12}$ bricks, has been published by Lillerud and co-workers.[4] These materials belong to the so called UiO (University of Oslo) class of MOFs and they are called UiO-66 (with 1,4-benzene-dicarboxylate linkers), UiO-67 (with 4,4'biphenyl-dicarboxylate linkers) and UiO-68 (with 4,4''terphenyl-dicarboxylate linkers) (Figure 5.2).

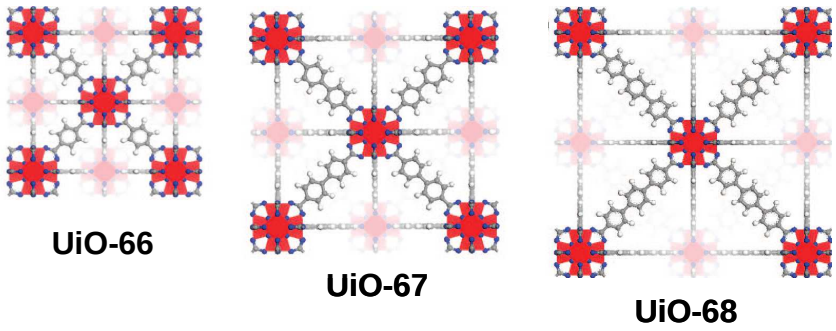

Figure 5.2. Zr-MOFs: UiO-66 with 1,4-benzene-dicarboxylate (BDC), UiO-67 with 4,4'biphenyl-dicarboxylate (BPDC) and UiO-68 with terphenyl dicarboxylate (TPDC) as linkers. **Zr**, **O**, C, **H** (white).

The most interesting property of these compounds is their high stability. In particular, they show very high thermal stability (T_{dec} = 540 ºC for both UiO-66 and UiO-67) since the weakest point in the structure is not the Zr_6-cluster but the bond between the benzene rings and the terminal carboxylate groups. Therefore, a change in the ligand length is proved not to alter the thermal stability of the net. Moreover, these solids have an excellent structural resistance toward solvents and mechanical pressure.

Furthermore, on the pursuit of MOFs with ultrahigh porosity, Yaghi and collaborators tested the likelihood of reaching higher porosities by expanding the links in MOF-177.[5] To this aim, they prepared the expanded forms of MOF-177 from 4,4′,4″-[benzene-1,3,5-triyl-tris(ethyne-2,1-diyl)]tribenzoate (BTE) and 4,4′,4″-[benzene-1,3,5-triyl-tris(benzene-4,1-diyl)] tribenzoate (BBC) to give MOF-180 and MOF-200, respectively (Figure 5.3).

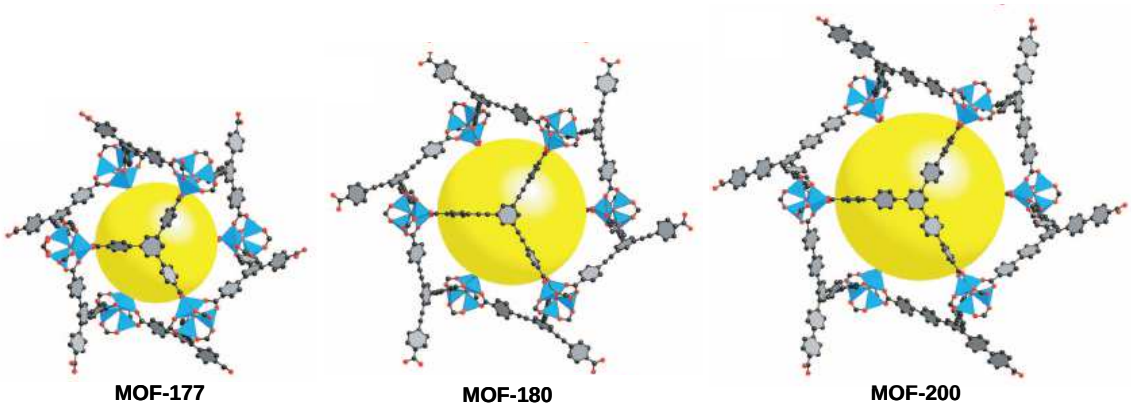

Figure 5.3. Crystal structures of MOF-177, MOF-180 and MOF-200. The yellow ball is placed in the structure for clarity and to indicate the space in the cage. **Zn**, **O**, C. H atoms have been omitted for clarity.

The unit cell volumes of MOF-180 and -200 are 1.9 and 2.6 times greater than that of MOF-177, respectively, with void volumes of 89 and 90 % of the crystal volume.

Hence, as a consequence of the increasing void volume, the Langmuir surface area of MOF-177 doubles in MOF-200 material, reaching the value of 10400 m^2 g^{-1} for the latter compound. This ultrahigh surface area is near the ultimate limit for solid materials and the properties of methane, carbon dioxide and hydrogen adsorption give rise to very high storage values on a gravimetric basis.

Just a few months ago, another very interesting series of isoreticular compounds (IRMOF-74-I to XI, Figure 5.4) based on Mg and Zn divalent cations have been published, by the same group.[6]

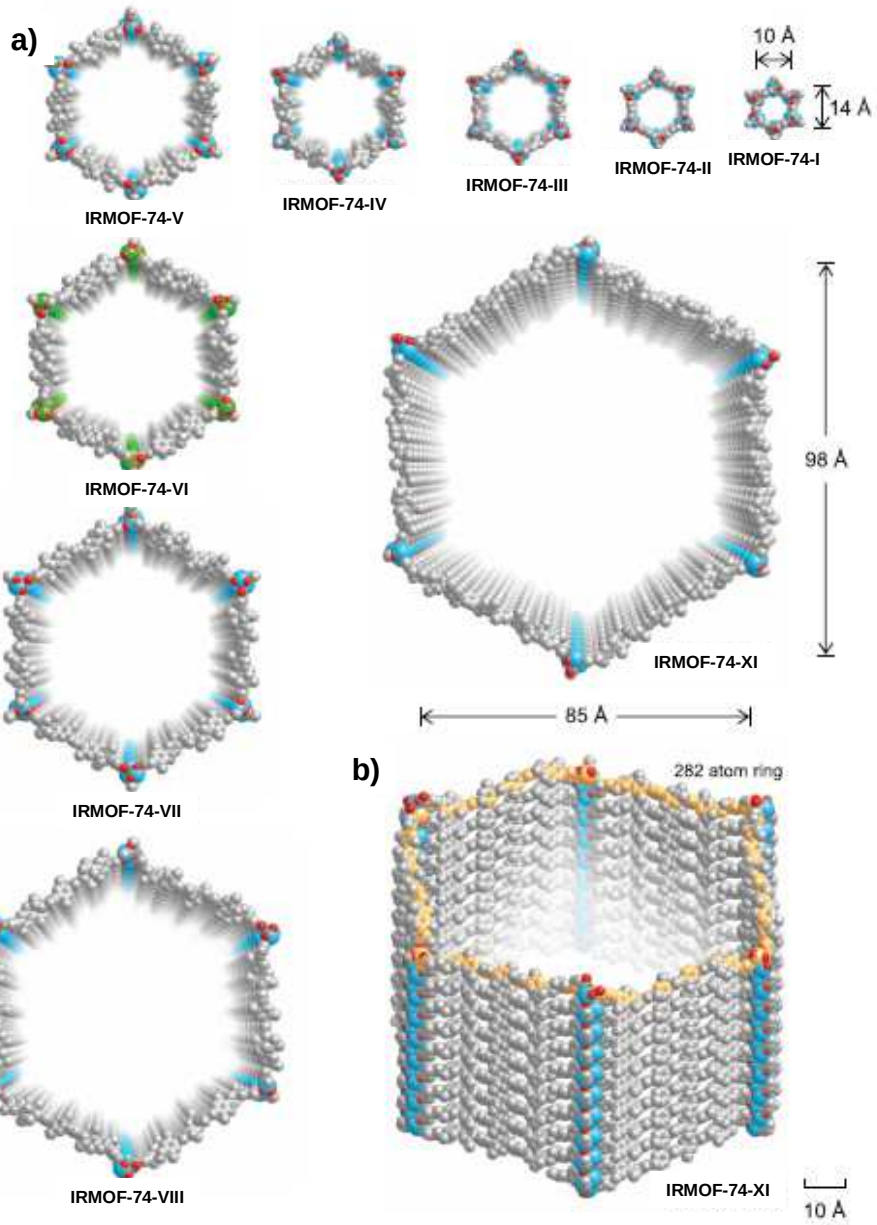

Figure 5.4. Crystal structures of IRMOF-74 series. a) Perspective views of a single one-dimensional channel shown for each member of IRMOF series. **Mg**, **Zn**, **O**, **C**. Hexyl chains and H atoms have been omitted for clarity. b) Perspective side view of the hexagonal channel, showing the ring of 282 atoms (gold) that define the pore aperture of the largest member of the series, IRMOF-74-XI.

The authors report on the expansion of MOF-74 structure (M_2(2,5-DOT), M = Zn^{2+}, Mg^{2+} and DOT = diolateterephthalate), from the original DOT link of one phenylene ring (I) to two (II), three (III), four (IV), five (V), six (VI), seven (VII), nine (IX), and eleven (XI) to give the isoreticular series of MOF, termed IRMOF-74-I to -XI. The dimension of the pore apertures ranges from 14 to 98 Å. All members of this series have non-interpenetrating structures and exhibit robust architectures, as evidenced by their permanent porosity and high thermal stability (up to 300 °C). Ar adsorption isotherms were measured on the activated samples of IRMOF-74-II to -XI each of which displays a type IV isotherm, typical of mesoporous materials. The magnitude of the relative pressure of the second step in the isotherm is attributed to the decrease in the effective energy of adsorption (pore-filling or condensation), in which higher pressures (p/p_o) are required for progressively larger pore sizes.

Given the remarkable stability, ultrahigh porosity, and extremely large pore aperture characteristic of the IRMOF-74 series, it is possible to access a new size regime for the inclusion of large organic, inorganic, and biological molecules (i.e. vitamin B_{12}, myoglobin and GPF) inside the pores of these crystals, feature that might be of interest for advanced drug delivery purposes.

Noteworthy, these examples show the possibility to modulate the pore size of metal organic frameworks with different topologies, as far as the stability of the net is not affected by the use of larger and larger ligands.

In this context, we considered the possibility of obtaining a series of isoreticular porous compounds using pyrazolate based linear ligands of progressively increasing length. As previously mentioned, an increment in cell parameters in the MOF crystalline structure is generally accompanied by an increment in the void volume that might lead to the framework collapse upon removal of guest molecules included in the voids. In order to overcome this inconvenience, a series of key factors have to be taken into account in order to succeed in producing a stable isoreticular series: i) robust M-L coordinative bonds that ensure the chemical and mechanical stability of the resulting framework; ii) highly directional and robust SBUs which ensure the formation of the desired structure type; iii) stiff linkers that avoid the collapse of the porous structure upon removal of the guest molecules.

With this aim, we have employed a series of pyrazolate based stiff ligands which is depicted in Scheme 5.1, in combination with highly directional octanuclear Ni clusters which lead to an isoreticular Ni-MOFs series. The chosen ligands are either based only on the pyrazolate functional group (L4, L5 and L7) or based on heteroligands bearing both pyrazolate and carboxylate functionalities (L1 and L3). In this chapter, we show how the reaction of these organic linkers with nickel(II) metal ions gives rise to five isoreticular and highly porous metal organic frameworks of general formulation $[Ni_8(OH)_4(OH_2)(L)_6]_n$ (shortened: $Ni_8(L)_6$) in which the octanuclear secondary building units are structurally similar to the one previously reported in a 3D porous framework by Masciocchi and co-workers.[7] Noteworthy, no interpenetration has been identified for any of the isolated solids, although the longest ligands (i.e. L5 and L7) could, in principle, give rise to two-interwoven interconnected networks.

In the following, the synthesis and the structural and textural characterization of these isomorphous novel Ni-PCPs are presented, together with some of the possible biological application of one of them for metallodrug delivery.

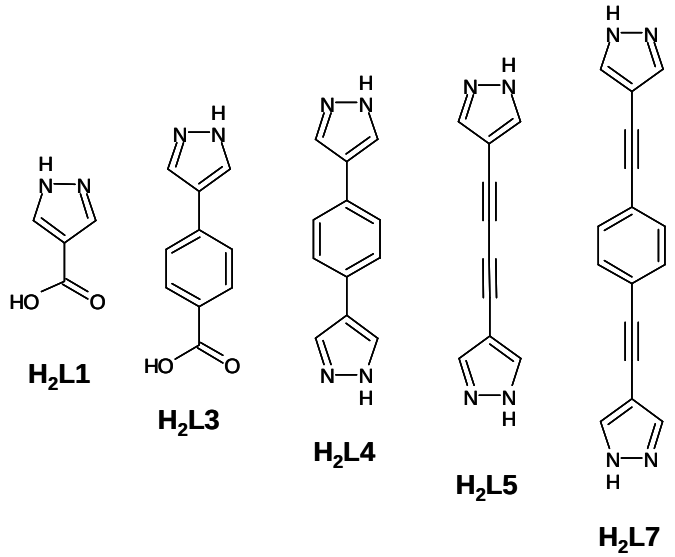

Scheme 5.1. Depiction of the pyrazolate based ligands used in the synthesis of Ni-MOFs series. Abbreviations: H_2L1 = 1*H*-pyrazole-4-carboxylic acid; H_2L3 = 4-(1*H*-pyrazol-4-yl)benzoic acid, H_2L4 = 4,4'-benzene-1,4-diylbis(1*H*-pyrazole); H_2L5 = 4,4'-buta-1,3-diyne-1,4-diylbis(1*H*-pyrazole) and H_2L7 = 4,4'-(benzene-1,4-diyldiethyne-2,1-diyl)bis(1*H*-pyrazole).

5.2. Results and discussion

5.2.1. Synthesis and structure

It should be noted that two of the organic ligands (L5 and L7) used in the MOFs synthesis bear the tert-butyloxycarbonyl (Boc) protecting group on the nitrogen atoms of both pyrazole rings. We decided not to cleave the -Boc groups from the organic linker prior to its use in MOF synthesis, since it seems to favour the slow release of the active ligand in the reaction medium. Such a slow release facilitates the formation of an ordered structure, therefore improving the crystallinity of the isolated materials.

Taking into account the experimental conditions reported in reference 7, each ligand was reacted with $Ni(OAc)_2 \cdot 4H_2O$ in some solvent mixtures (pure DMF, DMF/H_2O, DMF/DEF), with different Ni:L ratios (1:1, 1:2, 4:3) and at different temperatures in the 100-160 ºC range. The best reaction conditions have been found to be: DMF/H_2O 4:1 as a solvent, Ni:L ratio of 4:3 and heating at 130 ºC for 7 hours. These conditions are suitable for all employed ligands and phase pure materials have been isolated in good yields as green solids (with minor colour differences depending on the ligand). Unfortunately, the notable strength of the Ni-N bond did not permit to obtain single crystals of any of the isolated PCPs. Indeed, unlike the more labile M-O bond, once the M-N bond is formed its breaking results more difficult under typical reaction conditions and the solid suddenly precipitates in the form of highly insoluble powder. Because of this, none of the isolated PCPs presented in this chapter have been characterized by single crystal X-ray diffraction but, anyhow, X-ray powder diffraction analysis permitted us to structurally characterize them and to relate the measured properties to the local structure of each MOF.

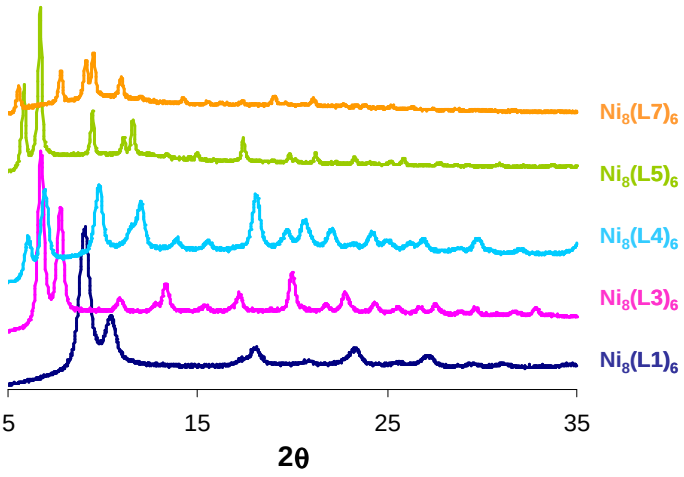

Figure 5.5. Plot of the low-angle portion (5º < 2θ < 30º) of the XRPD patterns for $[Ni_8(OH)_4(H_2O)_2(L)_6]$ MOF material series.

Figure 5.5 contains the low-angle portion of the collected diffraction data in the 5-35º 2θ range. Although peaks have different broadness for the different compounds of the series (depending on the size of the nanoparticles), it is evident that the same pattern is repeated along the series with the peaks shifting to lower angles as far as the ligand is increasing its length.

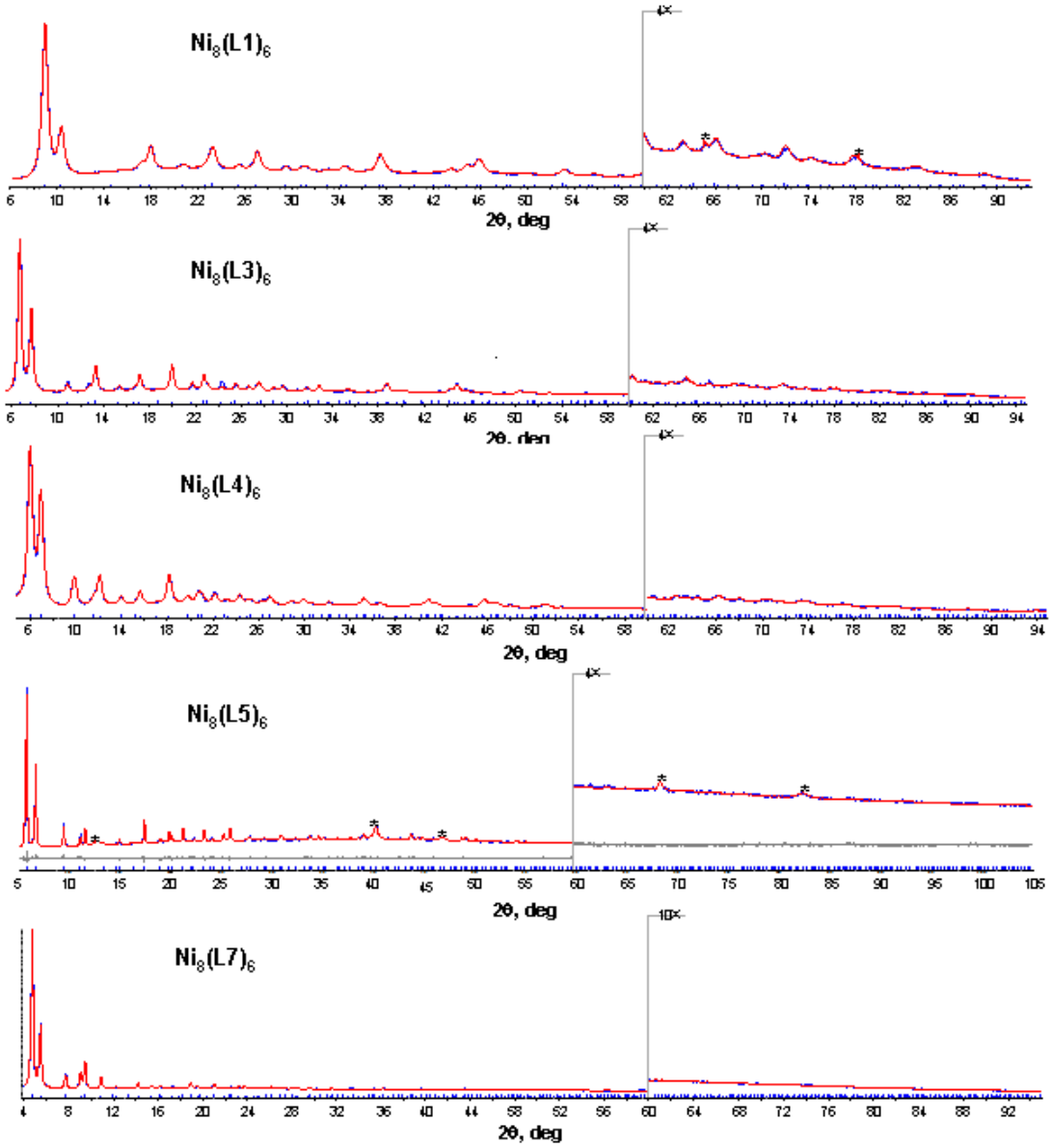

Figure 5.6. Rietveld refinement plots for $[Ni_8(OH)_4(H_2O)_2(L)_6]$ MOF material series. The inserts show the high-angle regions at a magnified scale.

Moreover, overnight scans in the 4-100º 2θ range followed by indexing with TOPAS[8] and treatment by the Le Bail refinement permits to assign cell parameters and

space group. Afterwards, structure solution was performed by the simulated annealing technique and the final refinement was carried out by the Rietveld method. Final Rietveld refinement plots are shown in Figure 5.6.

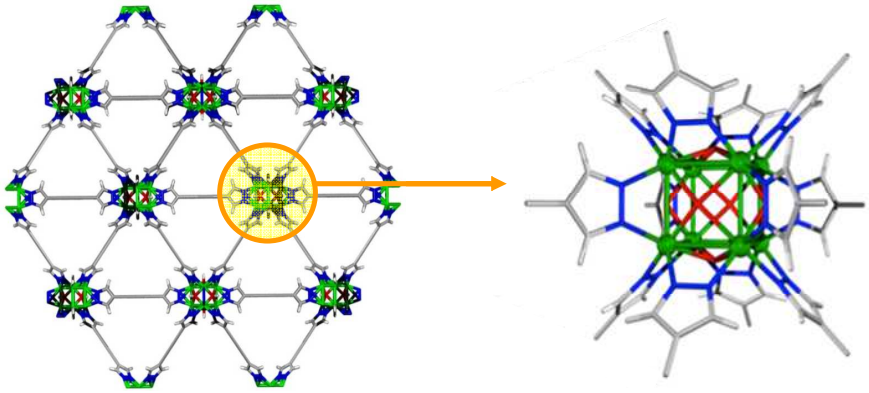

Figure 5.7. View of the crystal structure of $[Ni_8(\mu_4\text{-}OH)_4(\mu_4\text{-}OH_2)_2(\mu_4\text{-}L5)_6]_n$ along the [111] direction and magnified view of the 12-connecting $Ni_8(\mu_4\text{-}OH)_4(\mu_4\text{-}OH_2)_2$ nodes. **Ni**, **N**, **C**, **O**, **H** (white).

All the Ni-PCPs presented in this chapter crystallize in the cubic, *Fm-3m* space group and are constituted by octanuclear Ni(II) hydroxo clusters linked by tetradentate μ_4-L ligands (regardless their bis-pyrazolate or carboxypyrazolate nature) in a complex $Ni_8(\mu_4\text{-}X)_6(\mu_4\text{-}L)_6$ polyhedron of cubic symmetry (X = OH^- or H_2O). Figure 5.7 shows the local stereochemistry of the octametallic nodes in which each Ni(II) ion is hexacoordinated in a *fac*-NiN_3O_3 fashion and shows intermetallic non-bonding distances close to 3.0 Å. Each $Ni_8(OH)_4(OH_2)_2$ cubic cluster is connected to 12 adjacent ones by linear exo-tetradentate *N,N,N',N'* or *N,N,O',O'* linkers. Noteworthy, this topology is reminiscent to the cubic close packing (*fcc*) structure found in many elemental solids, among them elemental nickel (Figure 5.8). This coordination geometry results in highly porous 3D frameworks featuring octahedral and tetrahedral voids as gathered in Figure 5.9 for three of the $[Ni_8(OH)_4(H_2O)_2(L)_6]_n$ structures.

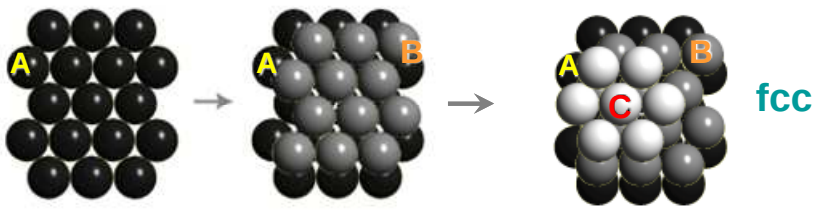

Figure 5.8. Cubic close packing (*fcc*) topology found in $[Ni_8(\mu_4\text{-}OH)_4(\mu_4\text{-}OH_2)_2(\mu_4\text{-}L)_6]_n$ materials.

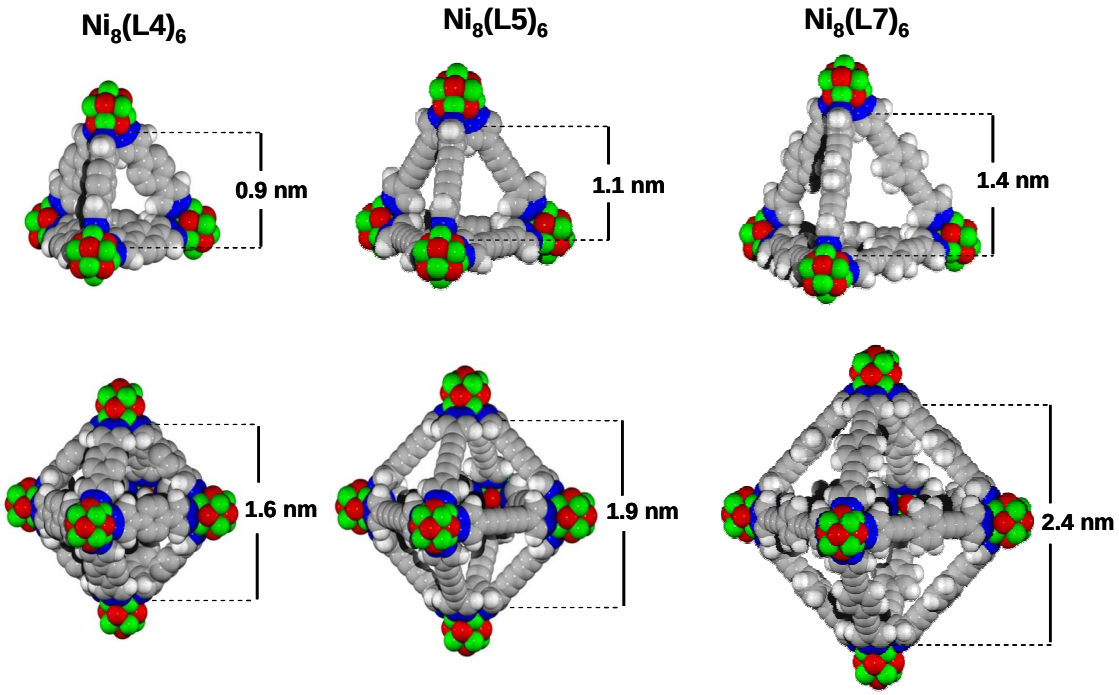

Figure 5.9. View of the octahedral and tetrahedral voids found in the crystal structure of $[Ni_8(OH)_4(H_2O)_2(L4)_6]_n$ (left), $[Ni_8(OH)_4(H_2O)_2(L5)_6]_n$ (middle) and $[Ni_8(OH)_4(H_2O)_2(L7)_6]_n$ (right), and the corresponding inner sizes. **Ni**, **O**, **N**, **C**, **H** (white).

It is worth pointing out that there is a relevant structural disorder in the structures above described, since solvent molecules (trapped in the framework either in the nucleation phase, in the washing process or coming from aerial moisture) occupy the large voids of the structure. This makes almost impossible to assess the real nature of the X ligands which has been modelled as a 2:1 ratio of OH^- and H_2O moieties, basically based on the charge balance and inspired by the similar $[Ni_8(OH)_4(H_2O)_2(C_5H_9O_2)_{12}]$ cluster reported by Ovcharenko and co-workers.[9]

Table 5.1. Values of the cell dimensions, cell volumes, surface area and calculated pore volume for the isoreticular $[Ni_8(OH)_4(H_2O)_2(L)_6]_n$ MOF material series.

	***a* (Å)**	**V (Å^3)**	**S_{BET} (m^2 g^{-1})**	**Pore vol (cm^3 g^{-1})**
$Ni_8(L1)_6$	17.17	5059	299	0.19
$Ni_8(L3)_6$	23.21	12507	803	0.40
$Ni_8(L4)_6$	25.40	16383	1770	0.92
$Ni_8(L5)_6$	26.49	18589	1918	0.95
$Ni_8(L7)_6$	32.53	34413	2164	1.04

As expected from the increasing length of the organic linkers, cell parameters for the isolated compounds become progressively larger, ranging from a = 17.17 Å for $[Ni_8(OH)_4(H_2O)_2(L1)_6]_n$ to a = 32.53 Å for $[Ni_8(OH)_4(H_2O)_2(L7)_6]_n$. In Table 5.1 the values of the cell dimension and cell volume for each compound are reported, as well as calculated BET surfaces and pore volume. It can be clearly seen that the three PCPs formed with L3, L4 and L5 have close cell dimensions and similar cell volumes due to the slightly difference in the linker's length.

Before any further measurement, the bulk solids obtained in the synthesis have been suspended in CH_2Cl_2 for 4 h to exchange the high boiling point DMF solvent trapped into the pores during the synthesis, with the much more volatile dichloromethane solvent.

5.2.2. Thermal stability

In Figure 5.10 the TG traces of the studied compounds are reported. The thermal stability of the five studied compounds has been investigated by TGA under air atmosphere. The CH_2Cl_2 exchanged samples have been previously evacuated 7 h at 130 ºC, under high vacuum, and further exposed to air for more than 3 days. In this way, no residual DMF molecules can remain into the structure and it will not be skewed by the presence of formic acid that can eventually be formed during heating dimethylformamide in acidic medium. In this way the temperature of decomposition of the framework can be assessed with accuracy and reliability.

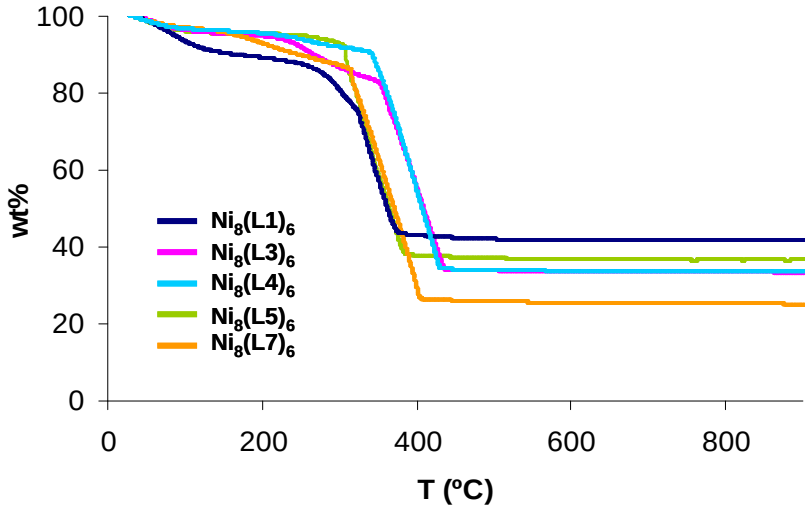

Figure 5.10. TGA traces for the isoreticular $[Ni_8(OH)_4(H_2O)_2(L)_6]_n$ MOF material series.

In all cases we can see a steep drop in the samples weight that starts between 300 and 350 ºC and ends around 400 ºC, clearly indicating the decomposition of the structure. As expected, the weight of the remaining residue is higher for the PCPs with the shortest linkers, simply due to the lower content (in weight %) of the organic material. Noteworthy, compounds with medium size ligands bearing the benzene spacer, namely $Ni_8(L3)_6$ and $Ni_8(L4)_6$, are the ones that exhibit the higher thermal stability with decomposition starting around 350 ºC, which may be a consequence of the larger steric hindrance of benzene moiety thereby protecting the degradation of the framework.

5.2.3. Mechanical and chemical stability for $Ni_8(L5)_6$ material

Mechanical and chemical stability tests have been carried out on $Ni_8(L5)_6$ material in order to establish the possible use of this type of systems under operative industrial conditions. The results show that both crystallinity and porosity remain almost unaffected when the material is pressed up to 2 Mg cm^{-2} which is indicative of a high mechanical stability (see Figure 5.11).

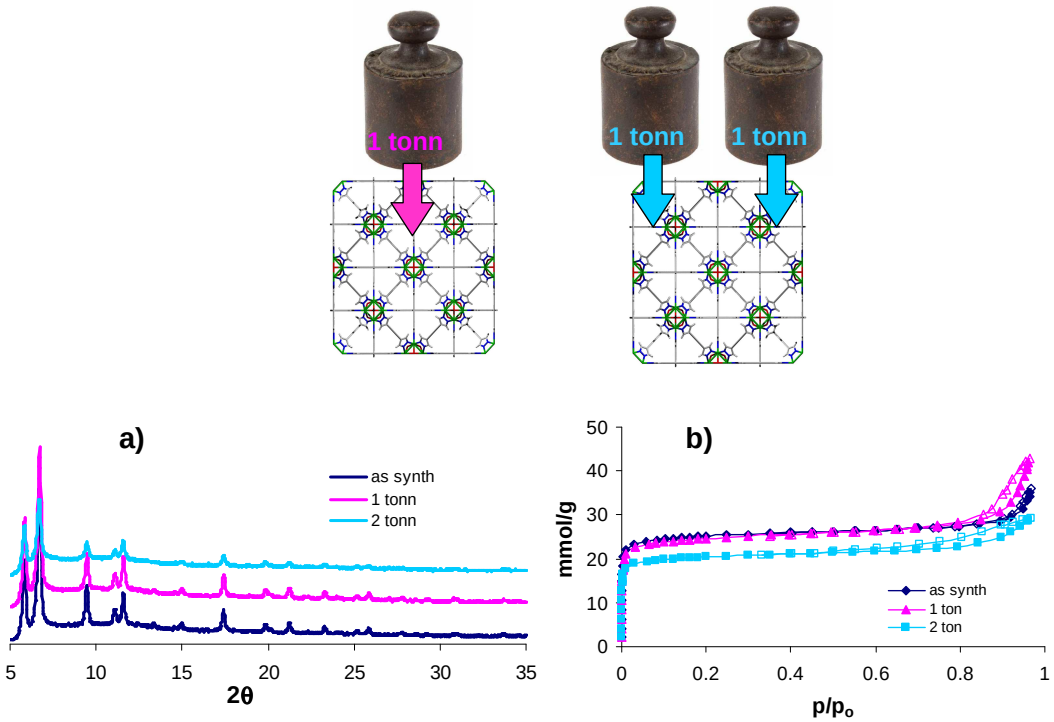

Figure 5.11. a) XRPD data and b) N_2 adsorption isotherms (77 K) for $Ni_8(L5)_6$ material before and after mechanical tests. Empty symbols denote desorption.

On top of that, this material has an extraordinary chemical stability, exemplified by the fact that its XRPD pattern remains unaltered up to 24 h in boiling water and in common organic solvents (methanol, benzene and cyclohexane) as well as in basic

(NaOH 0.05 M, pH 12.80) and acidic (HCl 0.01 M, pH 2.30) aqueous solutions (see Figure 5.12).

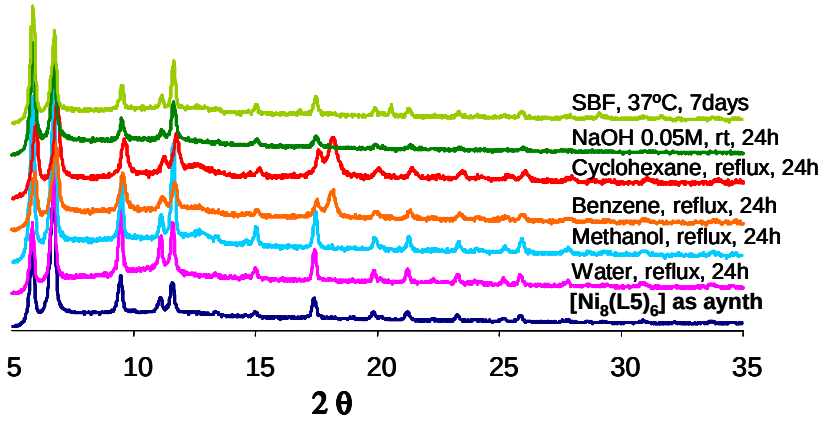

Figure 5.12. XRPD patterns acquired on species $Ni_8(L5)_6$ as synthesized and after different chemical stability tests.

Such a combination of extremely high thermal and chemical stability is a rare feature for PCPs. To the best of our knowledge, this is a class of 3-D frameworks that presents a very extensive range of thermal and chemical stability, only outperformed by $[Ni_3(BTP)_2]$ (H_3BTP= 1,3,5-tris(1H-pyrazol-4-yl)benzene) recently reported by Long and co-workers.[10]

5.2.4. Gas adsorption properties

The permanent porosity of these materials has been evaluated by collecting N_2 adsorption isotherms at 77 K. All the CH_2Cl_2 exchanged samples have been activated at 130 ºC under dynamic vacuum (10^{-6} mbar) for 7 h. In Figure 5.13 the measured isotherms are reported. We can see that the longer the ligand, the higher the adsorbed nitrogen amount. Moreover, $Ni_8(L4)_6$ and $Ni_8(L5)_6$, that have almost the same cell dimension, have nearly the same uptake of nitrogen, especially in the low pressure region. It should also be noted that all the PCPs of the series except $Ni_8(L7)_6$ show a type I isotherm, characteristic of microporous solids. In the case of the latter material, the larger size of the organic linker gives rise to pores in the mesoporous region (2.4 nm wide) and therefore the uptake of N_2 in the low pressure region is not as steep as for the others compounds.

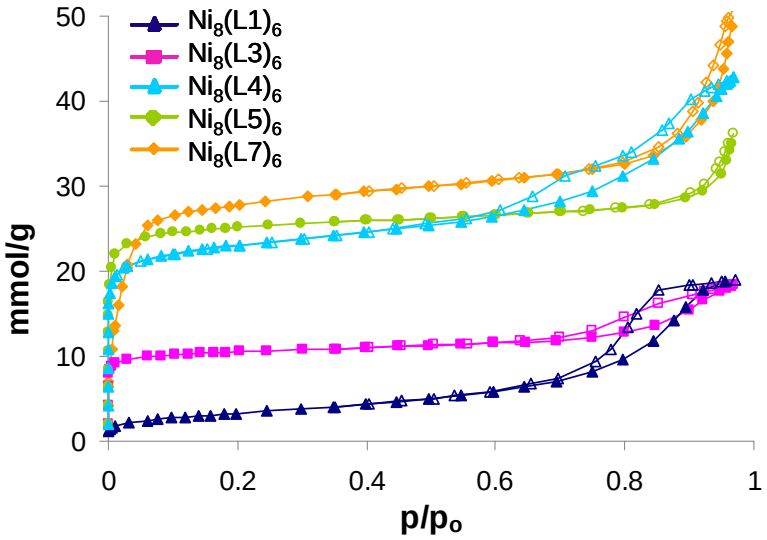

Figure 5.13. N_2 adsorption isotherms (77 K) for the isoreticular $[Ni_8(OH)_4(H_2O)_2(L)_6]_n$ MOF material series.

As expected, we found a correlation between the cell volume and the BET specific surface area calculated from the adsorption isotherms. Indeed, the larger the cell, the higher the surface area, reaching the very high value of 2164 m^2 g^{-1} for the MOF with the longest organic linker, namely $Ni_8(L7)_6$ (see Table 5.1). The same trend is followed by the pore volume calculated from the adsorption isotherms. Its value varies form 0.19 cm^3 g^{-1} for $Ni_8(L1)_6$ to the extremely high value of 1.04 cm^3 g^{-1} for $Ni_8(L7)_6$.

5.2.5. Water vapour adsorption properties

Water adsorption isotherms at 298 K have been measured on the Ni_8L_6 series cycling the adsorption-desorption isotherm three times for each compound in order to evaluate the hydrophobicity of the materials and their stability under humid conditions.

The results, shown in Figure 5.14, evidence a different behaviour for materials containing mixed carboxylate and pyrazolate ligands (L1, L3), with regard to bis-pyrazolate ligands (L4, L5 and L7). Thus, water adsorption isotherms for the materials containing the bis-pyrazolate ligands L4, L5 and L7 are indicative of very low water affinity and high stability to environmental moisture. Indeed, at low relative pressures of water, no loading is achieved. Moreover, water vapour partial pressures increase upon lengthening of the spacer, namely $p/p_o > 0.3$ for $Ni_8(L4)_6$, $p/p_o > 0.5$ for $Ni_8(L5)_6$ and $p/p_o > 0.6$ for $Ni_8(L7)_6$ which are indicative of the increasing hydrophobicity of the frameworks.

It is also important to highlight that the maximum amount of adsorbed water is in line with the pore volume size, therefore it increases progressively with the cell dimension. The hydrophobic nature of the pores should also be related to the low polarity of the organic spacers between the pyrazolate residues. Moreover, the high reproducibility of H_2O adsorption isotherms in multiple cycles and the maintenance of sample crystallinity after water adsorption (Figure 5.15) further support the extreme stability of the samples toward hydrolysis. By contrast, $Ni_8(L1)_6$ and $Ni_8(L3)_6$ materials based on carboxylate/pyrazolate heteroligands were proven to be sensitive to moisture. Thus, for $Ni_8(L3)_6$ the adsorption-desorption cycling gives rise to significant changes in the shape of the isotherm as well as an important loss of crystallinity.

Noteworthy, the $Ni_8(L1)_6$ system appears to be more robust towards water moisture with no effect being observed on sample crystallinity (Figure 5.15). The enhanced stability of the latter material can be related to its higher density nature which is also manifested in its higher hydrophilicity with water vapour condensing at low values of relative pressure, namely at $p/p_o = 0.1$. Consequently, the key point of the high stability for the highly porous bispyrazolate based materials towards moisture should be related to the insensitivity of Ni-N coordinative bonds to hydrolysis.

Finally, in order to highlight the possible relevance of the behaviour of these materials under operative humid conditions, their water adsorption behaviour has been compared to those of highly hydrophobic activated carbons provided by Blücher GmbH company.[11] The results show that $Ni_8(L7)_6$ framework is as hydrophobic as Blücher-101408 since H_2O enters the structures only at $p/p_o > 0.6$ for the two solids (Figure 5.14).

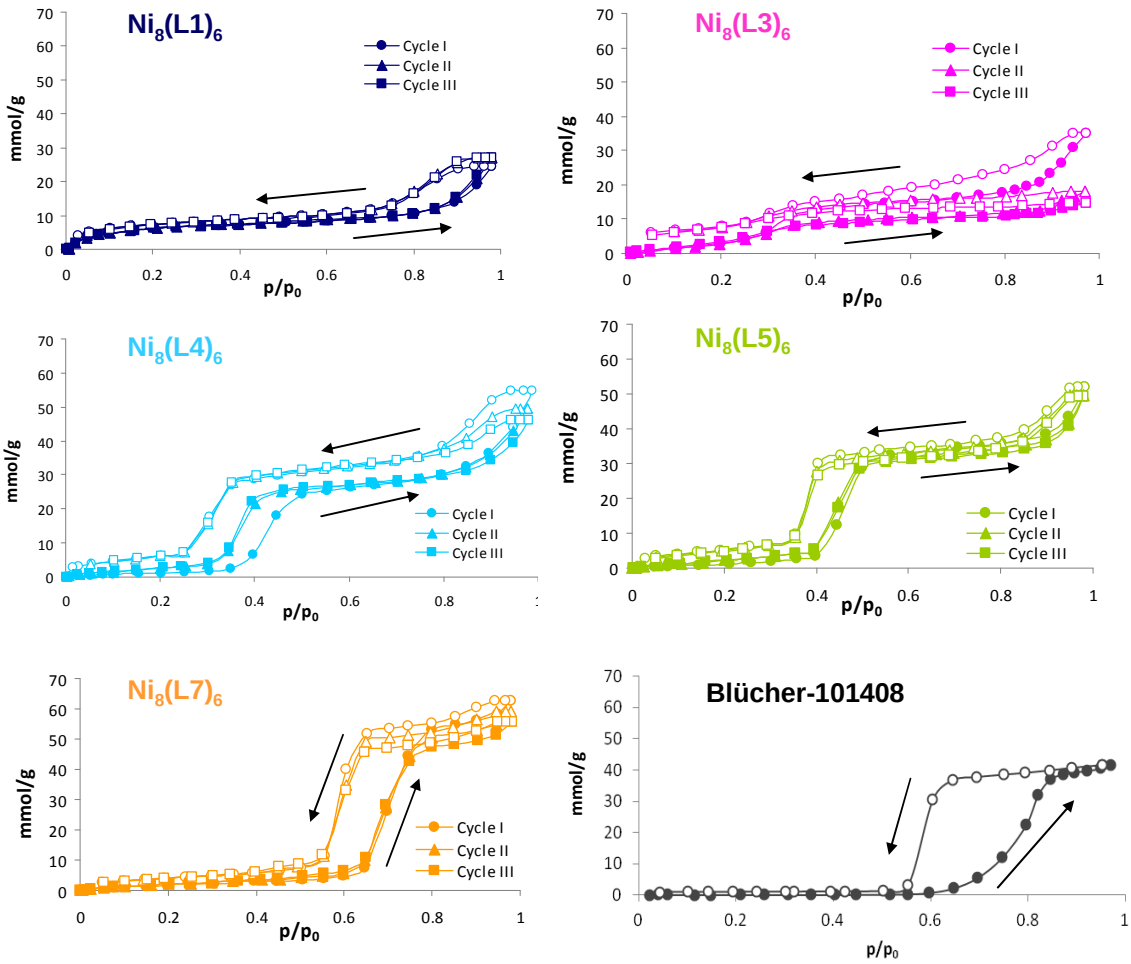

Figure 5.14. Water vapours adsorption isotherms (298 K) for the isoreticular $[Ni_8(OH)_4(H_2O)_2(L)_6]_n$ MOF material series and commercial molecular sieve activated carbon Blücher-101408 material.

5.2.6. Volatile organic vapour adsorption properties

The high hydrophobic nature of the $[Ni_8(OH)_4(OH_2)_2(L)_6]_n$ systems with the longest linkers, namely L5 and L7 (see Figure 5.14), is a very interesting feature for air purification applications in which moisture is unavoidably present and will be a strong competitor to the adsorbates of interest.

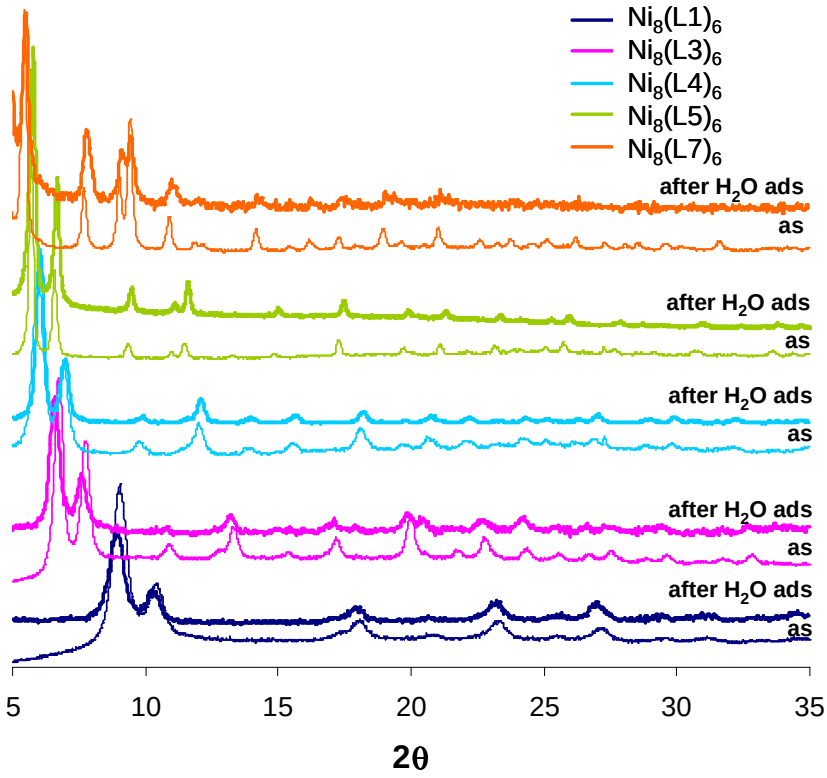

Figure 5.15. XRPD traces for the isoreticular $[Ni_8(OH)_4(H_2O)_2(L)_6]_n$ MOF material series before (thin line) and after (thick line) the water adsorption isotherms (298 K).

Therefore, we have investigated the ability of these systems to capture harmful VOCs under dynamic conditions. With this purpose we have essayed the performance of these materials for the capture of diethylsulfide (DES, a model of mustard gas, see Chapter 4) from dry and humid Ar/N_2 streams. The experiments have been carried out by checking the dynamic increase in weight of activated $Ni_8(L)_6$ MOF (*ca* 40 mg of material) at room temperature. In order to control de composition of DES in the gas stream, a constant flux of Ar (15 mL min^{-1}) was bubbled in a flask containing DES at room temperature so that the outcoming stream will be saturated of this gas. The Ar flow is then mixed with a N_2 flow (5 mL min^{-1}) before reaching the balance chamber where the adsorbent material is located, as can be seen in Figure 5.16. In the experiments under dry conditions, N_2 flows at a rate of 5 mL min^{-1}, while in those under humid conditions it is forced to pass through a flask containing distilled water (likewise for DES) at a flow rate of 15 mL min^{-1}, so that the overall flux contains 50 % humidity.

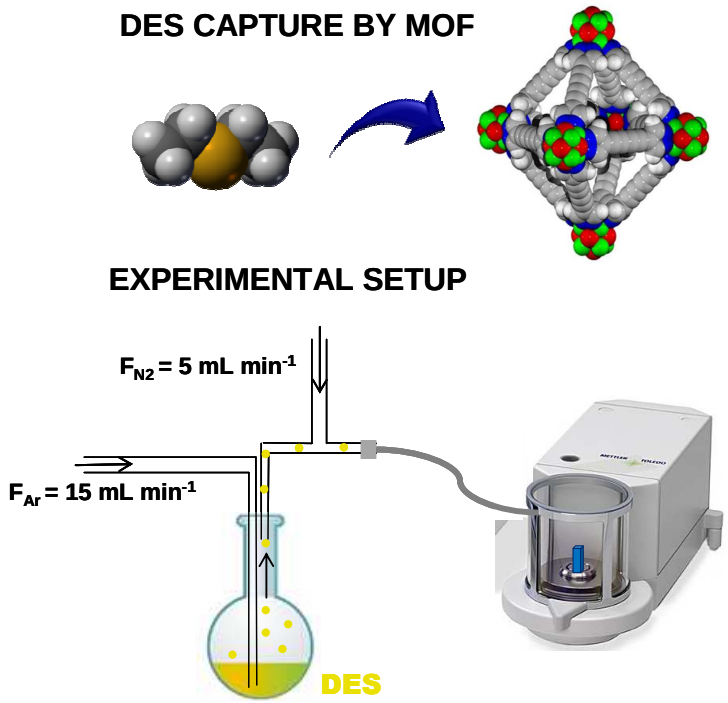

Figure 5.16. Schematic representation of the experimental setup used to evaluate DES capture by $Ni_8(L)_6$ MOFs.

The experimental results are represented in Figure 5.17 and summarized in Table 5.2. The results are indicative of a rapid incorporation of DES as well as a high adsorption capacity for all the tested materials. Both capacity and kinetics are comparable to best performing materials in the market, namely B-101408 and B-100950, two highly porous and hydrophobic activated carbons provided by Blücher company.

In the case of dry DES streams, we can see that the kinetics of the incorporation process is basically not dependent on the tested material, suggesting that the adsorption process depends only on the DES flow which determines the rate at which the saturation is reached. $Ni_8(L7)_6$ material adsorbs a lower amount of DES than its analogous $Ni_8(L5)_6$, although the higher void volume of the former compound would suggest the opposite trend. This behaviour can be explained considering the mesoporous nature of the latter and that DES is mainly adsorbed on the pore walls of the MOF material. Therefore, the adsorbed gas amount does not linearly increase with the pore volume.

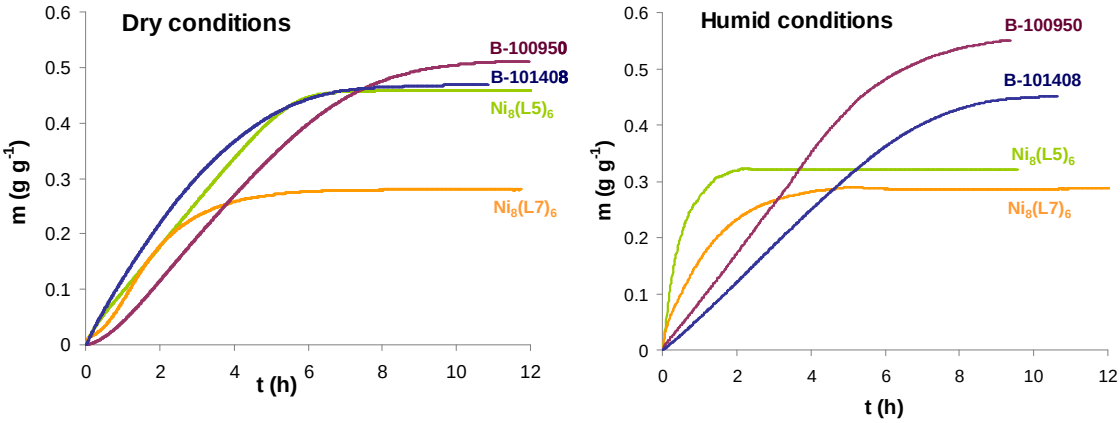

Figure 5.17. Dynamic adsorption profiles of DES streams for $Ni_8(L5)_6$ and $Ni_8(L7)_6$ MOF materials as well as for B-101408 and B-100950 activated carbons, under dry (left) and humid (right) conditions at 293 K.

Table 5.2. Summary of adsorption data of DES stream for $Ni_8(L5)_6$ and $Ni_8(L7)_6$ MOF materials as well as for B-101408 and B-100950 activated carbons under dry and humid conditions.

	Dry conditions		**Humid conditions**	
	Wt increase (%)	*$t_{1/2}$ (h)*	*Wt increase (%)*	*$t_{1/2}$ (h)*
$Ni_8(L5)_6$	45.8	2.82	32.0	0.37
$Ni_8(L7)_6$	27.9	0.97	28.9	0.78
B-101408	51.1	3.98	54.9	3.21
B-100950	46.8	1.83	45.1	3.50

Moving to the experimental data for DES stream under humid conditions, we can find a strong dependence of the material hydrophobic nature and VOC capture capacity and kinetics. Indeed, the adsorption kinetics profiles under dry and humid conditions for $Ni_8(L7)_6$ are almost identical (i.e. 27.9 % and 28.9 % of weight increase, and 0.97 h and 0.78 h for $t_{1/2}$, respectively). These results confirms the highly hydrophobic nature of the $Ni_8(L7)_6$ framework as well as its inertness to moisture. On the other hand, for the less hydrophobic $Ni_8(L5)_6$ compound (see Figure 5.14), the presence of water in the feeding stream accelerate the kinetics of the adsorption ($t_{1/2}$ drops from 2.82 h to 0.37 h), as a consequence of the concomitant coadsorption of H_2O and DES. Indeed, under these conditions, the increase in sample weight (32.0 %) results to be lower than in the case of dry DES stream (45.8 %) possibly due to a lower packing density of the adsorbed molecules or to a partial damage of the framework during the adsorption process.

Experimental results for activated carbons under humid DES stream confirm that these materials hardly interact with water, since no significant difference in the increase of sample weight can be found between the isotherms with dry and humid DES streams

for both materials. Only the kinetics of adsorption for B-100950 material seems to be affected by the presence of water as $t_{1/2}$ value doubles (from 1.83 h to 3.50 h) when the feeding stream contains humidity. This marked difference can be a consequence of the competition between H_2O and DES molecules for the adsorption sites that would reduce the DES adsorption rate.

As a matter of fact, the dynamic check of weight increase results to be an appropriate method for the evaluation of volatile organic vapour adsorption properties, also permitting the visual comparison of the adsorption kinetics profiles for the measured samples.

5.3. Biological application of $[Ni_8(OH)_4(OH_2)_2(L5)_6]_n$ material

The high chemical stability of these Ni-based materials, even in aqueous media, prompted us to investigate the possibility to use them for biological applications, particularly, as drug delivery systems. Actually, we selected $Ni_8(L5)_6$ material and we studied the incorporation/release of a Ru-complex that is under current investigation for applications in cancer therapy, namely RAPTA-C (see Figure 5.l8). So, first of all, it is necessary to explain briefly the role of coordination chemistry in biology and in cancer therapy, as well as the state of the art for the applications of MOFs in drug delivery.

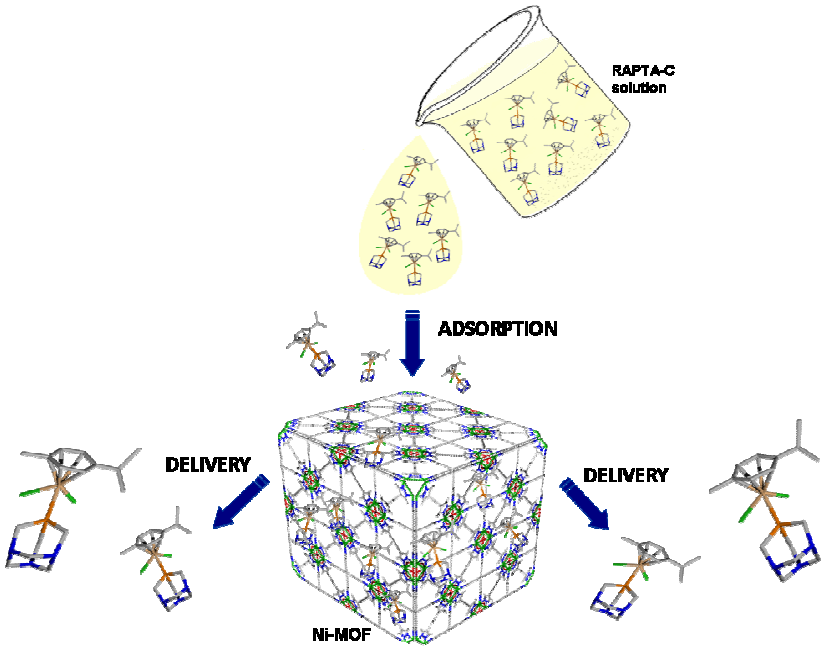

Figure 5.18. Pictorial summary of the biological application of $Ni_8(L5)_6$ material as a scaffold for the delivery of RAPTA-C metallodrug.

5.3.1. MOFs for metallodrugs delivery

Ru-based metallodrugs in cancer therapy

Since more than 30 years, coordination chemistry contributed to great an extent to the development of chemotherapeutic treatments against cancer. It is well known that the use of Pt(II)-based cytotoxic metallodrugs is one of the most widespread treatments against cancer.[12] Indeed, cisplatin is still the most used organometallic drug in the treatment of solid tumours and it is proved to have more than 90 % efficiency against testicular tumours.[13] However, the adverse side effects and the development of resistance are related to the unspecific interactions of Pt(II) metallodrugs with biomolecules, in particular with the desired biological target, DNA. The low selectivity of the treatment use to bear secondary effects such as nausea, vomit, nefrotoxicity, alopecia, lowering of white corpuscle levels, etc. and consequently, there is much interest in finding new metallodrugs with a different mechanism of action.

A number of half-sandwich type organometallic compounds of Ru, Rh, Ir and Os have emerged as alternative anti-tumour and anti-metastasic metallodrugs, exhibiting a different mechanism of action that may lead to fewer adverse side effects. Indeed, it seems that the primary activity of these species does not involve DNA but the inhibition of the exacerbated metabolism of many cancer cell types (i.e. inhibition of over-expressed enzymes like cathepsines),[14] or the interference with physiological redox processes.[15]

In this regard, interesting examples of Ru(III) complexes are (ImH)*trans*-$[RuCl_4(Im)_2(DMSO)]$ (Im = imidazol) (NAMI-A) and (IndH)*trans*-$[RuCl_4(Ind)_2]$ (IndH = indazol) (KP1019) that currently are in the phase I of clinical trials.[16] Another notable example is the nonconventional metallodrug [Ru(*p*-cymene)Cl_2(pta)] (pta = 1,3,5-triaza-7-phospha-adamantane), termed ‘‘RAPTA-C’’(Figure 5.19), which is proved to inhibit lung metastases in mice.[17]

Accordingly, it would be highly beneficial for patients to find methods for the controlled delivery of these novel metallodrugs. Therefore we present here the study of the incorporation and release of RAPTA-C by $Ni_8(L5)_6$ framework.

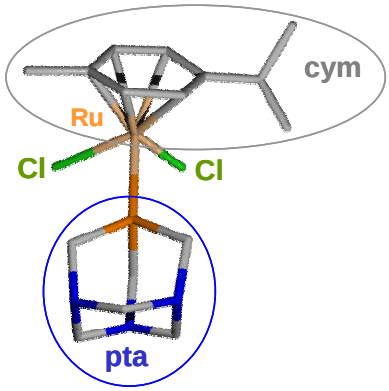

Figure 5.19. The anti-tumour metallodrug [Ru(*p*-cymene)Cl_2(pta)] (pta = 1,3,5-triaza-7-phospha-adamantane), RAPTA-C, used in the drug delivery process. Ru, Cl, P, N, C. H atoms have been omitted for clarity.

Mesoporous materials for drug delivery

The idea of using porous materials as scaffold for controlled drug delivery appeared for the first time in 2001 when Vallet-Regí and co-workers proposed the silica-based material MCM-41 as a system for the delivery of the anti-inflammatory ibuprofen drug.[18] Afterwards other zeolite-like materials such as SBA-15[19] or MCM-48,[20] and some metal–organic frameworks have been investigated as drug carriers and controlled release systems. Among the studied MOFs, an interesting work has been published in 2006 by Horcajada and co-workers.[21] In this paper the highly porous MIL-100 and MIL-101 materials were employed again for the delivery of ibuprofen molecule. The research in this field has then been extended to a wider range of Fe-MOFs and drugs to be delivered, in an important paper published in 2010.[22] In this work, specific non-toxic porous iron(III)-based metal–organic frameworks with engineered cores and surfaces function are considered as superior nanocarriers for efficient controlled delivery of challenging antitumoural and retroviral drugs (i.e. busulfan, azidothymidine triphosphate, doxorubicin or cidofovir) against cancer and AIDS.

Despite the interesting results presented in the above mentioned papers, the possibility to deliver organometallic drugs (and not purely organic ones) by a micro- or mesoporous system had not been envisaged before.

5.3.2. Results and discussion

The choice of the $Ni_8(L5)_6$ material, among the ones presented in this Chapter, is related to both the suitable size of its pore windows and its enhanced thermal, mechanical and chemical stability. Indeed, the non-conventional RAPTA-C metallodrug has an

estimated diameter of 0.9 nm[23] that perfectly matches with the pore windows (0.9 nm) of both tetrahedral and octahedral cavities in the MOF. On the other hand, $Ni_8(L5)_6$ material is highly stable in simulated body fluid (SBF) at 37 ºC (pH 8.05) for 7 days (Figure 5.12). The robustness of this material in SBF is proved by means of atomic absorption (AA) measurements, indicating very low Ni leaching. As a matter of fact, suspensions of $Ni_8(L5)_6$ in SBF at 37 ºC (20 mg of $Ni_8(L5)_6$ in 40 mL of SBF) give rise to 0.7 ppm of Ni concentration levels, which indicate that only 0.43 % of the MOF material has been degraded. This value corresponds to the liberation of 70 mg of Ni per 100 mL of SBF with suspended MOF. It should be noted that this amount is neatly below the daily average uptake of 170 mg of Ni in food.[24] This is an important point when considering the possible employment of this material for biological applications since every source of toxic compounds must be carefully avoided to prevent human body poisoning.

Therefore, as already pointed out, the stability of $Ni_8(L5)_6$ under simulated biological conditions, the pore size and the non-charged nature of its framework prompted us to explore the possible incorporation and posterior release of the non-conventional RAPTA-C metallodrug. Indeed, impregnation of $Ni_8(L5)_6$ with an aqueous solution of RAPTA-C (0.025 M) leads to the rapid incorporation of this metallodrug, the equilibrium being reached after 4 h. As we can see in Figure 5.20.a, the N_2 uptake capacity after RAPTA-C loading dramatic decreases from 21.2 mmol g^{-1}, for the as synthesized material, to 4.4 mmol g^{-1} after RAPTA-C loading. It can be taken as a proof of the occupancy of the cavities by the drug since we have the experimental evidence (XRPD, see Figure 5.20.b) that the structural integrity of the framework is maintained after the loading.

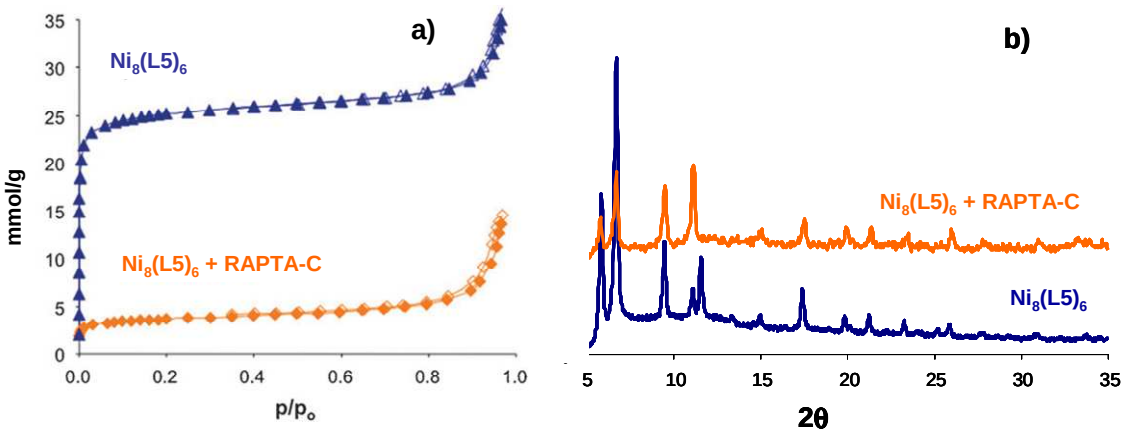

Figure 5.20 a) N_2 adsorption isotherms (77 K) for activated $Ni_8(L5)_6$ (blue triangles) and the RAPTA-C loaded $Ni_8(L5)_6 \cdot 4$RAPTA-C product (orange diamonds). Empty symbols denote desorption. b) XRPD patterns acquired on species $Ni_8(L5)_6$ as synthesized and after incorporation of RAPTA-C ($Ni_8(L5)_6 \cdot 4$RAPTA-C).

After this initial proof of RAPTA-C incorporation, confirming the metallodrug loading into the framework, we have studied more in detail the solid–liquid adsorption process at 298 K. The results show a type I adsorption isotherm (Figure 5.21), whose data-points have been satisfactorily fitted to the linear form of the Langmuir model (Equation 5.1):

$$C/n = C/n_m + 1/(Kn_m) \qquad (5.1)$$

where C is the concentration of RAPTA-C in the aqueous solution (M) at the equilibrium, n is the amount of RAPTA-C incorporated in $Ni_8(L5)_6$ (mmol g^{-1}), K is the Langmuir equilibrium constant and n_m corresponds to the predicted saturation loading of RAPTA-C in $Ni_8(L5)_6$ (mmol g^{-1}).

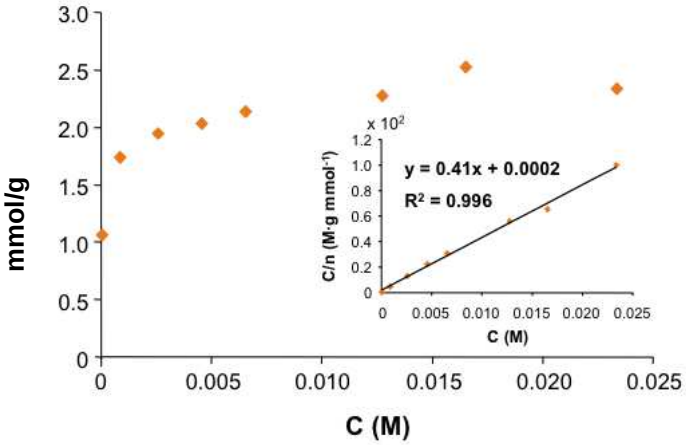

Figure 5.21. Solid–liquid adsorption isotherm of an aqueous solution of RAPTA-C by $Ni_8(L5)_6$ at 298 K. The inset shows the linear fitting of the experimental data to the Langmuir model.

The results show a maximum loading n_m value of 2.4 mmol (1.1 g) of RAPTA-C per gram of $Ni_8(L5)_6$, reached at RAPTA-C concentration of 0.012 M. Noteworthy, this high loading value corresponds to four RAPTA-C molecules per MOF formula unit. Therefore, taking into account the inner size of the octahedral and tetrahedral voids in $Ni_8(L5)_6$ (*ca.* 1.6 and 1.0 nm, respectively), as well as the size of RAPTA-C molecule (0.9 nm), we can tentatively conclude that the octahedral and tetrahedral cavities, present in a 1 : 2 ratio, host two and one RAPTA-C molecules each, respectively, to

give rise to $Ni_8(L5)_6 \cdot 4$RAPTA-C (Figure 5.22). We must point out that in this way the maximum loading of the framework with RAPTA-C drug, is achieved. Anyway there is still residual porosity, since we proved that N_2 can still be adsorbed in solid $Ni_8(L5)_6 \cdot 4$RAPTA-C (see Figure 5.20a), but it cannot be filled with further RAPTA-C molecules due to its bulky size.

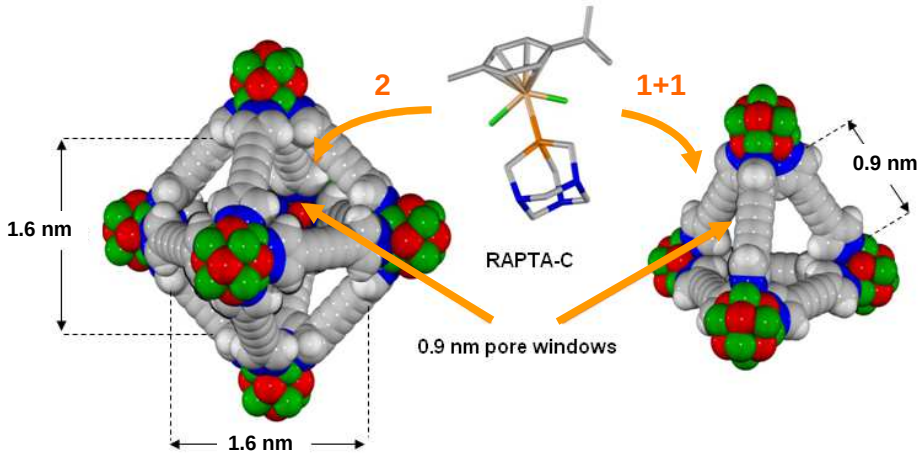

Figure 5.22. Pictorial representation of the incorporation of RAPTA-C (4 molecules per MOF formula unit) into $Ni_8(L5)_6$ material.

Once we proved that RAPTA-C can enter the MOF structure without any degradation of both the framework and the metallodrug, we decided to study its release under experimental conditions that mimic the biological ones, therefore in a Simulated Body Fluid (SBF) at 37 ºC. This would permit us to use this system as a model for drug delivery purposes. Thereby, 10 mg of $Ni_8(L5)_6 \cdot 4$RAPTA-C were suspended in 20 mL of SBF and the resulting suspension incubated at 37 ºC with stirring. Aliquots of the supernatant solution were studied by means of UV-vis at different periods of time in order to determine the amount of released RAPTA-C. We can see in Figure 5.23 that the equilibrium of RAPTA-C release from $Ni_8(L5)_6 \cdot 4$RAPTA-C is reached after 5 h. In the first two hours a fast and continuous release takes place, while in the following three hours the rate of desorption decreases rapidly, until reaching the final equilibrium.

Desorption data can be satisfactorily fitted with a first order kinetic model according to the following equation:

$$q_E - q_t = q_E \, e^{-kt} \qquad (5.2)$$

where q_E and q_t are the amounts of RAPTA-C released per gram of MOF (mmol g^{-1}) at the equilibrium and at the time *t* (h), respectively, and *k* is the first order kinetic constant (h^{-1}). The fitting of the data gives rise to a *k* value of 1.63 h^{-1} which corresponds to a $t_{1/2}$ for the release of the metallodrug, of 25 min (Figure 5.23). This is indicative of the physisorption of the metallodrug in $Ni_8(L5)_6$, ruling out its chemical binding, through ligand exchange reactions, to the extended π-system of diynes provided by the MOF itself. The reversibility of the adsorption process can be further stated by quantifying the amount of released drug after the equilibrium is reached (desorption branch of solid–liquid isotherm at 37 ºC). The results show that, when 10 mg of $Ni_8(L5)_6 \cdot 4$RAPTA-C are suspended in 20 mL of SBF, 20 % of the hosted metallodrug is released leading to a 0.1 mM RAPTA-C solution.

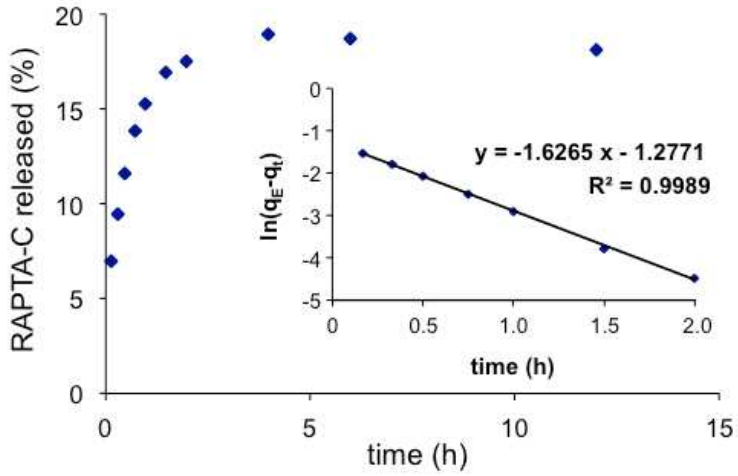

Figure 5.23. Desorption process of RAPTA-C from $Ni_8(L5)_6 \cdot 4$RAPTA-C (10 mg) into a simulated body fluid (20 mL) at 37 ºC. The inset shows the fitting of the data to a first order kinetic model.

We were also interested in determining the maximum amount of metallodrug that can be released by the loaded MOF in highly diluted solutions. Therefore, we suspended $Ni_8(L5)_6 \cdot 4$RAPTA-C in progressively higher volumes of SBF and we sonicated the suspension for 1.5 h at 37 ºC. We found that the released amount at the equilibrium increases to 70 % when the SBF volume is enlarged to 200 mL, which corresponds to a 0.004 mM RAPTA-C solution.

We are aware that an ideal system for drug delivery should release the same amount of drug over a quite long period of time (from some hours up to few days), so that the concentration of the pharmaceutical can be kept constant in the human body.[25] Moreover, we are also aware that the ideal system for drug delivery should be made with healthy friendly materials such as zinc, calcium, iron etc. Anyhow, the system we

have presented here is so stable in Simulated Body Fluid that almost no leaching of nickel is detected (see above) so that it can be considered as a good proof of concept of the utility of MOFs for the delivery of non-conventional metallodrugs.

5.4. Conclusions

In this chapter we have presented a series of isoreticular PCPs built up with Ni(II) metal ions and both bis-pyrazolate and carboxy-pyrazolate linear ligands. These materials, of general formulation $[Ni_8(OH)_4(OH_2)_2(L)_6]_n$ ($Ni_8(L)_6$), crystallize in the cubic *Fm-3m* space group with a cubic close packing (*fcc*) topology, and present a permanent porosity with *n* octahedral and 2*n* tetrahedral cavities. The permanent porosity has been evaluated by means of N_2 adsorption isotherms (77 K) and the values of BET specific surface areas have been found to increase as the length of the ligand increases, up to the extraordinary value of 2164 $m^2\ g^{-1}$ for the MOF with the longest organic linker, namely $Ni_8(L7)_6$.

The materials containing bis-pyrazolate ligands have been proved to be extremely hydrophobic since water can enter the structure at quite high values of relative pressures. Once again, $Ni_8(L7)_6$ material is the most hydrophobic. Nevertheless, all the compounds of the series maintain their crystallinity after water vapour adsorption measurements indicating the exceptional stability of this class of materials in humid conditions. The capture of DES (diethylsulfide, chemical warfare analogue) has been evaluated in dry and humid conditions. The results are indicative of a rapid adsorption kinetic as well as a high capacity of these materials towards the incorporation of the model VOC studied. Moreover the performance of these materials is in the same range to those of carbon materials exhibiting the highest capacity and highest hydrophobicity in the market.

The compound with 4,4'-buta-1,3-diyne-1,4-diylbis(pyrazolate) ligand, ($Ni_8(L5)_6$) has been used as a scaffold for the incorporation of the unconventional metallodrug [Ru(*p*-cymene)Cl_2(pta)] (RAPTA-C). The extraordinary stability of $Ni_8(L5)_6$ framework in water and in Simulated Body Fluid are fundamental prerequisites for this purpose. The activated material has been proved to load a significant quantity of RAPTA-C, namely 1.1 g of drug per gram of MOF, corresponding to 4 molecules per MOF formula unit that are hosted both in octahedral (2 molecules) and tetrahedral (1 molecule) cavities. Noteworthy, the adsorption process is reversible as a consequence of physisorption and RAPTA-C can be easily released into simulated body fluid.

All these features concur in making $Ni_8(L)_6$ series an outstanding proof of concept for the suitability of MOFs as materials for protecting applications as well as systems for releasing non-conventional metallodrugs.

5.5. Bibliography

[1] a) H. Furukawa, N. Ko, Y. Go, N. Aratani, S. Choi, E. Choi, A. Yazaydin, R. Snurr, M. O'Keeffe, J. Kim, O. Yaghi, *Science*, **2010**, *329*, 424; b) G. Férey, C. Mellot-Draznieks, C. Serre, F. Millange, J. Dutour, S. Surblé, I. Margiolaki, *Science*, **2005**, *309*, 2040.

[2] H. K. Chae, D. Y. Siberio-Perez, J. Kim, Y. B. Go, M. Eddaoudi, A. J. Matzger,M. O'Keeffe, O. M. Yaghi, *Nature*, **2004**, *427*, 523.

[3] M. Eddaoudi, J. Kim, N. Rosi, D. Vodak, J. Wachter, M. O'Keeffe, O.M. Yaghi, *Science*, **2002**, *295*, 469.

[4] J. H. Cavka, S. Jakobsen, U. Olsbye, N. Guillou, C. Lamberti, S. Bordiga, K. P. Lillerud, *J. Am. Chem. Soc*. **2008**, *130*, 13850.

[5] H. Furukawa, N. Ko, Y. B. Go, N. Aratani, S. B. Choi, E. Choi, A. Ö. Yazaydin, R. Q. Snurr, M. O'Keeffe, J. Kim, O. M. Yaghi, *Science*, **2010**, *329*, 424.

[6] H. Deng, S. Grunder, K. E. Cordova, C. Valente, H. Furukawa, M. Hmadeh, F. Gándara, A. C. Whalley, Z. Liu, S. Asahina, H. Kazumori, M. O'Keeffe, O. Terasaki, J. F. Stoddart, O. M. Yaghi, *Science*, **2012**, *336*, 1018.

[7] N. Masciocchi, S. Galli, V. Colombo, A. Maspero, G. Palmisano, B. Seyyedi, C. Lamberti, S. Bordiga, *J. Am. Chem. Soc*. **2010**, *132*, 7902.

[8] Version 3.0, Buker AXS 2005, Karlsruhe, Geramny.

[9] V. Ovcharenko, E. Fursova, G. Romanenko, I. Eremenko, E. Tretyakov, V. Ikorskii, *Inorg. Chem.* **2006**, 45, 5338.

[10] V. Colombo, S. Galli H. J. Choi, G. D. Han, A. Maspero, G. Palmisano, N. Masciocchi, J. R. Long, *Chem. Sci*. **2011**, *2*, 1311.

[11] http://www.bluecher.com/en/

[12] B. Rosenberg in *Cisplatin, Chemistry and Biochemistry of a Leading Anti-Cancer Drug*, (Ed. B. Lippert), Wiley-VCH, Weinheim, **1999**.

[13] R. A. Alderden, M. D. Hall, T. W. Hambley, *J. Chem. Ed.* **2006**, *83*, 728.

[14] a) A. Casini, F. Edafe, M. Erlandsson, L. Gonsalvi, A. Ciancetta, N. Re, A. Ienco, L. Messori, M. Peruzzini, P. J. Dyson, *Dalton Trans*. **2010**, *39*, 5556; b) H. Amouri, J. Moussa, A. K. Renfrew, P. J. Dyson, M. N. Rager and L.-M. Chamoreau, *Angew. Chem., Int. Ed.* **2010**, *49*, 7530.

[15] Y. K. Yan, M. Melchart, A. Habtemarian, A. F. A. Peacock, P. J. Sadler, *J. Biol. Inorg. Chem*. **2006**, *11*, 483.

[16] G. Süss-Fink, *Dalton Trans.* **2010**, *39*, 1673.

[17] C. Scolaro, A. Bergamo, L. Brescacin, R. Delfino, M. Cocchietto, G. Laurenczy, T. J. Geldbach, G. Sava, P. J. Dyson, *J. Med. Chem*. **2005**, *48*, 4161.

[18] M. Vallet-Regí, A. Rámila, R. P. del Real, J. Pérez-Pariente, *Chem. Mater*. **2001**, *13*, 308.

[19] F. Qu, G. Zhu, S. Huang, S. Li, J. Sun, D. Zhang, S. Qiu, *Microporous Mesoporous Mater*. **2006**, *92*, 1.

[20] I. Izquierdo-Barba, A. Martínez, A. L. Doadrio, J. Pérez- Pariente, M. Vallet-Regí, *Eur. J. Pharm. Sci.* **2005**, *26*, 365.

[21] P. Horcajada, C. Serre, M. Vallet-Regí, M. Sebban, F. Taulelle, G. Férey, *Angew. Chem. Int. Ed.* **2006**, *45*, 5974.

[22] P. Horcajada, T. Chalati, C. Serre, B. Gillet, C. Sebrie, T. Baati, J. F. Eubank, D. Heurtaux, P. Clayette, C. Kreuz, J.-S. Chang, Y. K. Hwang, V. Marsaud, P.-N. Bories, L. Cynober, S. Gil, G. Férey, P. Couvreur, R. Gref, *Nature Mat.* **2010**, *9*, 172.

[23] The size of RAPTA-C has been estimated as the diameter of the equivalent sphere occupying the same volume occupied by a CCDC-derived model of the metallodrug, as calculated by SMILE (D. Eufri, A. Sironi, *J. Mol. Graphics*, **1989**, *7*, 165).

[24] Toxicological Profile for Nickel, August 1995, Draft Update, Agency for Toxic Substances and Disease Registry, United States Public Health Service.

[25] Y. W. Chien, S. Lin in *Encyclopedia of Pharmaceutical Technology*, (Ed. James Swarbrick).Third Edition. **2006**, pp. 1082-1103.

CONCLUSIONES

Para el desarrollo de esta investigación, se han seleccionado cuidadosamente (y sintetizado en colaboración con el Departamento de Química Orgánica de la Universidad de Granada) una serie de moléculas lineales funcionalizadas con uno (o dos) anillos pirazol adecuadas para ser empleadas como bloques de construcción de redes de coordinación porosas robustas. Las estructuras resultantes poseen una estabilidad excepcional como consecuencia de la naturaleza más robusta de los enlaces de coordinación M-N(pirazolato) en comparación con los enlaces de coordinación M-O(carboxilato) que se encuentran típicamente en la mayoría de las estructuras de PCPs publicados. Con esta estrategia, se ha logrado sintetizar una serie de polímeros de coordinación porosos obtenidos en la reacción entre ligandos mixtos carboxilato-pirazolato o bis-pirazolato y los últimos metales de la primera serie de transición (Co^{2+}, Ni^{2+}, Cu^{2+} y Zn^{2+}).

Los resultados experimentales presentados en esta tesis doctoral se han detallado en cuatro capítulos en los que se han clasificado los compuestos de interés en función de su estructura y/o propiedades funcionales.

Así, el Capítulo 2 se centra en los materiales zeomiméticos. La nueva red aniónica de formulación $NH_4[Cu_3(\mu_3\text{-}OH)(\mu_3\text{-}L1)_3]_n \cdot solv$ ($NH_4@Cu_3(OH)L1_3$, donde H_2L1 = 4-carboxipirazol) da lugar a reacciones de intercambio de los cationes libres, de manera similar a las zeolitas. Como resultado de los procesos de intercambio, ha sido posible la modulación de la porosidad de la red. En particular, se ha investigado el efecto del intercambio de los cationes sobre la selectividad de adsorción frente a diferentes procesos de separación de gases y vapores de interés industrial y ambiental. De hecho, los resultados muestran que los sistemas $A@Cu_3(OH)L1_3$ (A = catión intercambiable) pueden resolver, de manera eficiente, mezclas de gases con propiedades físicas similares (por ejemplo: acetileno/dióxido de carbono). Es interesante resaltar que dichos procesos de separación presentan una dependencia con la temperatura sin precedentes, que puede ser ajustada al modelo de Clausius-Clapeyron. Además, estos materiales resultan útiles en la separación de mezclas benceno/ciclohexano como consecuencia de los procesos de adsorción selectivos por exclusión de tamaño. También hemos

encontrado que el sistema $NH_4@Cu_3(OH)L1_3$ se comporta de manera eficiente como catalizador heterogéneo en la oxidación de cicloalcanos. Esta propiedad está relacionada con la naturaleza redox activa de los centros de coordinación insaturados de Cu.

El Capítulo 3 está dedicado a aquellos materiales que presentan un comportamiento flexible como consecuencia de estímulos externos, también llamados PCPs-plásticos. El nuevo PCP flexible de formulación $([Cu_2(L2)_2(OH_2)]DMF_{1.5})_n$ (α-$[Cu_2(H_2O)(L2)_2]$, donde H_2L2 = 3,5-dimetil-4-carboxipirazol) sufre modificaciones estructurales directamente relacionadas con la estructura peculiar de sus unidades de construcción secundarias. En efecto, este material tiene un puente acua entre los dos átomos de cobre de la unidad dimérica que, hasta ahora, no había sido encontrado nunca en Cu-PCPs. Además, la eliminación de este puente acua da lugar a una fase evacuada metaestable γ-$[Cu_2(L2)_2]$ que posee centros metálicos insaturados convergentes. Estos dan lugar a propiedades de adsorción de gases inusuales: las isotermas de adsorción presentan peculiares formas escalonadas que confirman la flexibilidad estructural en la red. Además de eso, la congelación a 77 K de la fase γ-$[Cu_2(L2)_2]$ da lugar a una nueva fase abierta (δ-$[Cu_2(L2)_2]$), extremadamente estable al aire. Cabe destacar que estas modificaciones estructurales vienen acompañadas de cambios de color, indicativos de variaciones en la disposición espacial de los ligandos alrededor de los centros metálicos Cu^{2+}. Estas modificaciones estructurales dan lugar a cambios significativos en las propiedades de adsorción de moléculas de gas/vapor (es decir, N_2, CO_2, CO, CH_4, C_2H_2, C_2H_4, C_2H_6, H_2O...). También, tal como resulta de los experimentos de adsorción monocomponente, γ-$[Cu_2(L2)_2]$ presenta una interacción más fuerte que δ-$[Cu_2(L2)_2]$ frente a todos los adsorbatos probados. Mediante cromatografía de gases de pulso se han obtenido resultados análogos, confirmando así la reducida accesibilidad de la estructura porosa de este último material.

El capítulo 4 está dedicado a compuestos análogos al material conocido como MOF-5. De hecho, estos PCPs contienen el mismo grupo M_4O (M = Zn, Co) característico de la estructura del MOF-5. Sin embargo, en los compuestos presentados, los tetraedros M_4O están conectados por ligandos mixtos pirazolato-carboxilato (3,5-dimetil-4-carboxipirazol, H_2L2) o bis-pirazolato (4,4'-buta-1,3-diino-1,4-diilbis(1-*H*-3,5-dimetil-

pirazol, H_2L6) en lugar de ligandos bis-carboxilato, lo que da lugar a estructuras extremadamente robustas y estables como consecuencia de la fortaleza de los enlaces de coordinación M-N(pirazolato). Además, la protección de los clusters M_4O ejercida por los grupos metilo, da lugar a materiales altamente hidrofóbicos, útiles para la captura selectiva de compuestos orgánicos volátiles nocivos, tal como se demuestra con medidas de cromatografía de gases sobre compuestos modelo de agentes de guerra química.

Por último, el capítulo 5 está dedicado a una serie de PCPs isoreticulares de formulación general $[Ni_8(OH)_4(OH_2)_2(L)_6]_n$ ($Ni_8(L)_6$). El empaquetamiento cúbico compacto de los clusters octanucleares de Ni, conduce a la formación de *n* huecos octaédricos y *2n* huecos tetraédricos, cuyo tamaño, hidrofobicidad y capacidad de adsorción dependen directamente del tamaño del espaciador orgánico. Asimismo, la naturaleza hidrofóbica de estos materiales ha resultado fundamental para la captura de DES (dietil sulfuro, modelo de gas de guerra química) tal como se deduce de las medidas de adsorción en condiciones secas y húmedas. Los resultados, relativos a la incorporación del vapor orgánico estudiado, son indicativos de una alta capacidad de adsorción, así como de una cinética rápida. El comportamiento de adsorción es comparable a los de los carbones activos más hidrofóbicos en el mercado. Finalmente, inspirados por la excepcional estabilidad química y la alta porosidad del PCP $Ni_8(L5)_6$, hemos demostrado su idoneidad como vehículo para la liberación controlada del métalo-fármaco no convencional de Ru [Ru(*p*-cimeno)Cl_2(pta)] (RAPTA-C).

En resumen, en esta tesis doctoral, hemos estado explorando la química de los ligandos orgánicos pirazolato para la formación de materiales porosos permanentes que presentan alta estabilidad mecánica, térmica y química que superan las que se encuentran normalmente en la gran mayoría de los PCPs descritos. Además, hemos demostrado que algunos de ellos son adecuados para aplicaciones prácticas ya que la humedad del aire, básicamente no altera sus propiedades de adsorción. Asimismo, uno de estos materiales se ha tomado como una demostración del posible empleo de los MOFs para la liberación controlada de metalofármacos.

Los resultados descritos en este trabajo muestran cómo los PCPs podrían encontrar aplicaciones prácticas en una amplia gama de áreas de interés industrial, medioambiental y biológico, de alto impacto social.

CONCLUSIONS

For the development of this research, series of linear molecules containing one (or two) pyrazole rings have been carefully selected (and synthesized in collaboration with the Department of Organic Chemistry of the University of Granada) as suitable building blocks for the construction of robust coordination networks. Indeed, the extraordinary stability for the resulting frameworks is a consequence of the more robust nature of the M-N(pyrazolate) coordination bonds compared to the M-O(carboxylate) coordination bonds typically found in most of the PCP structures reported so far. With this strategy, we have successfully synthesized a series of porous coordination polymers obtained in the reaction of either mixed carboxylate-pyrazolate or bis-pyrazolate ligands and late first row transition metals (Co^{2+}, Ni^{2+}, Cu^{2+} and Zn^{2+}).

The experimental results presented in this doctoral thesis have been detailed in four Chapters in which the compounds of interest have been categorized according to their structural and/or functional properties.

So, Chapter 2 focuses on zeomimetic materials. The novel anionic network of formulation $NH_4[Cu_3(\mu_3\text{-}OH)(\mu_3\text{-}L1)_3]_n \cdot solv$ ($NH_4@Cu_3(OH)L1_3$, where H_2L1 = 4-carboxypyrazole) has been proven to give rise to exchange of the extraframework cations, similarly to zeolitic materials. As a result of the exchange processes, the modulation of the porosity of the network can be achieved. In particular, we have been investigating the effect of the cation exchange on the adsorption selectivity for different separation processes of gases and vapours of industrial and environmental interest. Indeed, the results show that $A@Cu_3(OH)L1_3$ systems (A = extraframework cation) can efficiently resolve mixtures of gases with similar physical properties (i.e. acetylene/carbon dioxide). Surprisingly, these systems show an unprecedented temperature dependence which can be rationalized on the basis of Clausius-Clapeyron plots. Moreover, these materials are also useful for the separation of benzene/cyclohexane mixtures as a consequence of size selective adsorption processes. Furthermore, we have also found that the $NH_4@Cu_3(OH)L1_3$ system behaves as an efficient heterogeneous oxidation catalyst of cycloalcanes which might be related to the redox active behaviour of Cu centres and their coordination unsaturated nature.

CONCLUSIONS

Chapter 3 is devoted to those materials exhibiting a flexible behaviour responsive to external stimuli, also called Soft-PCPs. The flexible PCP of formulation $([Cu_2(L2)_2(OH_2)]DMF_{1.5})_n$ (α-$[Cu_2(H_2O)(L2)_2]$, where H_2L2 = 3,5-dimethyl-4-carboxypyrazole) shows intriguing structural modifications strictly related to the peculiar structure of its Secondary Building Units. Indeed, this material has an unprecedented acua bridging between the two copper atoms of the dimeric unit, never found so far in Cu-PCPs. Moreover, the removal of this acua bridge gives rise to a metastable evacuated phase γ-$[Cu_2(L2)_2]$ that possess convergent open metal sites resulting in uncommon gas adsorptive properties with multi step shapes that confirm the occurrence of gate opening phenomena. On top of that, freezing γ-$[Cu_2(L2)_2]$ phase, down to 77 K, gives rise to a novel open phase (δ-$[Cu_2(L2)_2]$) that is extremely stable in air. Noteworthy, these structural modifications are accompanied by colour changes which are indicative of the modification of ligands' spatial arrangement around Cu^{2+} metal centres. The occurrence of structural modifications gives rise to significant changes in the adsorptive properties towards probe gas/vapour molecules (i.e. N_2, CO_2, CO, CH_4, C_2H_2, C_2H_4, C_2H_6, H_2O…). It should be noted that γ-$[Cu_2(L2)_2]$ exhibits a stronger interaction with all the tested adsorbates than δ-$[Cu_2(L2)_2]$, as probed by single component adsorption experiments as well as by pulse gas chromatography, thereby confirming the reduced accessibility of the porous structure for the latter material.

Chapter 4 is devoted to robust analogues of MOF-5 material. Indeed, these PCPs contain the same M_4O (M = Zn, Co) building block characteristic of MOF-5 structure. However, in for the materials described in this Chapter, M_4O tetrahedra are connected by mixed pyrazolate-carboxylate (3,5-dimethyl-4-carboxypyrazole, H_2L2) or bis-pyrazolate (4,4'-buta-1,3-diyne-1,4-diylbis(1-*H*-3,5-dimethyl-pyrazole, H_2L6) ligands instead of bis-carboxylate linker, resulting in extremely robust and stable structures as a consequence of the strength of the M-N(pyrazolate) coordinative bonds. Furthermore, the protection exerted by methyl groups on the M_4O moieties gives rise to highly hydrophobic materials useful for the selective capture of harmful VOCs as proven by gas-chromatographic measurements on model compounds of chemical warfare agents.

Finally, Chapter 5 is devoted to the isoreticular series of PCPs of general formulation $[Ni_8(OH)_4(OH_2)_2(L)_6]_n$ ($Ni_8(L)_6$). The cubic close packing of the

octanuclear Ni clusters, leads to the formation of *n* octahedral and *2n* tetrahedral cages, whose size, hydrophobicity and adsorption capacity directly depend on the length of the linker. The hydrophobic nature of the materials has been foundamental in the capture of DES (diethylsulfide, chemical warfare analogue) as deduced by the adsorption experiments using both dry and humid feed streams. The results are indicative of high capacity as well as rapid adsorption kinetic for the incorporation of the model VOC studied. The adsorptive performances are comparable to those of the most hydrophobic active carbons in the market. Finally, inspired by the exceptional chemical stability and high porosity of $Ni_8(L5)_6$ PCP, we proved its suitability as a carrier for the non-conventional Ru-based metallodrug [Ru(*p*-cymene)Cl_2(pta)] (RAPTA-C).

Summarizing, in this doctoral thesis, we have been exploring the chemistry of pyrazolate based organic ligands in the formation of permanent porous materials that have structural, thermal and chemical stabilities outperforming those typically found for the vast majority of reported PCPs. Moreover, we proved that some of them would be suitable for practical applications since air moisture is basically not altering their adsorptive properties. Furthermore, one of these materials has been taken as a proof of concept for the delivery of metallodrugs by a MOF material.

The results detailed in this work reveal how PCPs could find practical applications in a wide range of areas of industrial, environmental and biological interest, with high social impact.

APPENDIX I – Experimental details

APPENDIX I – Experimental Details

CHAPTER 1

Materials and methods

All materials were obtained from commercial suppliers and used without further purification. IR absorption bands were measured by a Midac FT-IR on KBr pellets. ^{1}H-NMR and ^{13}C-NMR spectra were recorded with a BRUKER ARX 400 (400 MHz).

Synthesis of organic ligands

1*H*-pyrazole-4-carboxylic acid (H_2L1). It was obtained according to the literature method.[1] In a typical synthesis, 2 mL (1.99 g, 24.2 mmol) of 4-methylpyrazole were dissolved in 50 mL of distilled water and 1.5 g of NaOH were added at 60 ºC. Then 11.5 g of $KMnO_4$ dissolved in 250 mL of distilled water, were added dropwise over a period of 4 hours at 80 ºC. The reaction mixture was further heated at 90 ºC for 1 hour and filtered while hot. The solvent was evaporated to 100 mL and the pure product precipitated as a white solid upon acidification to pH < 2 (1.23 g, yield 45 %). IR (KBr) 3450(s), 3269(s), 1687(m), 1657(m), 1562(m), 1502(m), 1385(m), 1315(s), 1254(m), 1184(w), 1153(w), 991(m), 945(m), 779(s), 598(m), 538(m) cm^{-1}. ^{1}H NMR (MeOD) δ: 8.03 (s, 2H). Anal. calc. for $C_4H_4N_2O_2$ (112.09) C, 42.86; H, 3.60, N, 24.99; found C, 42.64; H 4.07, N 24.82.

3,5-dimethyl-4-carboxypyrazole (H_2L2). To a solution of 5 mL of ethyl diacetoacetate (26 mmol) in methanol (50 mL) under stirring at room temperature, 2 mL of hydrazine (50-60 % hydrated) and 3 mL of HCl (37 %) were added. The solution was refluxed for 30 minutes and then concentrated in vacuum. Subsequently, 50 mL of water were added to the solution together with solid NaOH, until the pH reached the range 7-9. The white microcrystalline solid was filtered and refluxed in 50 mL aqueous NaOH (0.2 M) overnight. After addition of HCl (37 %) 2.1 g of pure H_2L2 were obtained as a white solid (global yield 58 %). IR (KBr) 2900(br), 1674(vs), 1598(w), 1516(s), 1429(m), 1383(w), 1329(s), 1283(s), 1134(vs), 1067(w), 1011(w), 937(m), 790(s), 764(vs) cm^{-1}. ^{1}H NMR (DMSO-d_6) δ: 2.28 (s, 6H), 12.26 (s). Anal. calc. for $C_6N_2O_2H_8$ (140.14) C, 51.42; H, 5.75; N, 19.99; found C, 50.02; H, 6.35; N, 19.31.

4-(1*H*-pyrazol-4-yl)benzoic acid (H_2L3). The first intermediate 4-I-1*H*-pyrazole was obtained as follow: 1*H*-pyrazole (4 g, 59 mmol) was suspended in water (30 mL), solid NaOAc (10.6 g, 118 mmol) was added and the mixture was heated at 60 ºC until it got limpid. I_2 (9.4 g. 37 mmol) and KI (18.4 g, 111 mmol) aqueous solution was added dropwise to the former mixture over a period of 30 min. After the addition of H_2O_2 (0.7 mL, 31 mmol, 35 %), the mixture was refluxed 6 h. Afterwards it was cooled to room temperature and the addition of solid NaOH afforded the precipitation of abundant white solid that was carefully washed with water. The solid product was dried under reduce pressure yielding 8.52 g (74 %) of 4-I-1*H*-pyrazole as white-rose solid. ^{1}H NMR (DMSO-d_6) δ: 7.54 (s, 1H), 7.92 (s, 1H), 13.14 (br s, 1H). ^{13}C NMR (DMSO-d_6) δ: 57.0, 133.4, 143.9.

The second intermediate 1-(1-ethoxyethyl)-4-iodo-1*H*-pyrazole was obtained as follow: 4-I-1*H*-pyrazole (3.2 g, 16 mmol) was dissolved in toluene (20 mL), ethilvinylether (3.98 mL, 42 mmol) and HCl 12N were added and the mixture was vigorously stirred and heated at 30 – 40 ºC for 1 h. The progress of the reaction was followed by TLC (*n*-hexane/ethyl acetate 8:2, R_f = 0.45). The mixture was cooled down and

saturated $NaHCO_3$ solution (5 mL) was added. The organic phase was anidrified over anidrus K_2CO_3, filtered on neutral Al_2O_3 and concentered to yield 3.84 g (90 %) of yellowish oil. ^{1}H-NMR ($CDCl_3$) δ: 1.14 (t, 3H), 1.63 (d, 3H), 3.32, 3.44 (d-q, 2H), 5.49 (q, 1H), 7.50 (s, 1H), 7.63 (s, 1H).

1-(1-ethoxyethyl)-4-iodo-1*H*-pyrazole (2.3 g, 8.72 mmol) and 4-carboxyphenilboronic acid (1.45 g, 8.72 mmol) were suspended in EtOH (50 mL), then solid K_2CO_3 (3.61 g, 26.16 mmol) and Pd/C 10% (145 mg) were added. The mixture was refluxed 16 h and followed with TLC (EtOAc, R_f = 0.44). The mixture was allowed to cool to room temperature, filtered on Celite and evaporated to dryness under reduced pressure. The residue was dissolved in the minimum amount of water and stirred few minutes. A precipitate was obtained and fresh water was replaced three times. After removal of most residual water, HCl 3M solution was added under stirring. The solid was filtered and recrystallized in hot EtOH, affording 2.66 g (73 %) of H_2L3 as a white-rose solid. IR (KBr) 3232(vs), 2509(br), 1685(vs), 1610(s), 1493(w), 1329(m), 1269(s), 1188(w), 1151(m), 1043(w), 951(s), 856(m), 798(m), 773(s), 700(w), 639(w) cm^{-1}. ^{1}H NMR (DMSO-d_6) δ: 7.58 (d, 2H), 7.78 (d, 2H), 8.00 (s, 2H). ^{13}C NMR (DMSO-d_6) δ: 120.7, 125.3, 128.3, 130.4, 131.5, 138, 167.6. Anal. calc. for $C_{10}H_8N_2O_2$ (188.18) C, 63.82; H, 4.28; N, 14.89; found C, 63.01; H, 3.88; N, 14.29.

4,4'-benzene-1,4-diylbis(1*H*-pyrazole) (H_2L4). The first intermediate, 1,4-bis(1-dimethylamino-3-dimethylimonio-prop-1-en-2-yl)benzene bis(perchlorate), was prepared as previously reported by Arnold et al.[2] M.p. 300 °C. IR (KBr) 2936(w), 1582(vs), 1489(w), 1452(w), 1393(m), 1287(m), 1211(m), 1078(vs), 975(m), 761(w), 622(m), 586(w) cm^{-1}. ^{1}H NMR ($CDCl_3$) δ: 2.45 (s, 3H), 3.36 (s, 3H), 7.39 (s, 2H), 7.73 (s, 2H). ^{13}C NMR ($CDCl_3$) δ: 40.4 (Me), 49.5 (Me), 105.1 (C), 133.1 (C), 134.3 (C), 163.9 (CH). Anal. calc. for $C_{20}H_{32}Cl_2N_4O_8$ (527.40) C, 45.55; H, 6.12; N, 10.62; found C, 44.95; H, 6.10; N, 10.48.

The bis(perchlorate) intermediate (470 mg, 0.89 mmol) in EtOH (60 mL) was placed in a 100-mL round-bottomed flask under vigorous stirring, while 98% hydrazine monohydrate (95 μL, 1.96 mmol) was added dropwise over 2 min. After being refluxed for 2 h, the pale-yellow solid was filtered off, washed with methanol (2 x 10 mL) and dried in vacuum at room temperature to afford pure H_2L4 in the form of polycrystalline powders (172 mg, yield 92 %). IR (KBr) 3144(br), 1583(w), 1527(w), 1263(w), 1236(w), 1159(s), 1037(w), 965(w), 951(s), 866(s), 824(s), 719(w), 657(w), 627(w) cm^{-1}. ^{1}H NMR ($CDCl_3$) δ: 7.58 (s, 2H), 8.05 (s, 2H), 12.5 (br s, 1H). ^{13}C NMR ($CDCl_3$) δ: 121.9 (C), 126.3 (HC-Ph), 131.3 (C), 137.0 (HC-pz). Anal. calc. for $C_{12}H_{10}N_4$ (210.24): C, 68.56; H, 4.79; N, 26.65; found C, 67.98; H, 4.83; N, 26.26.

4,4'-buta-1,3-diyne-1,4-diylbis(1-Boc-pyrazole) (H_2L5). The first intermediate, 1-Boc-4-iodopyrazole, was obtained in the reaction of the comercial 4-yodo-1*H*-pyrazole (6 g, 30.93 mmol) with $(Boc)_2O$ (10.13 g, 46.30 mmol) in 80 mL of CH_2Cl_2 and 15 mL of Et_3N. After the addition of DMAP (0.30 g, 3.09 mmol), the mixture was stirred at room temperature for 30 min while its colour changes from brown to yellow. The solvent was evaporated under reduced pressure, the solid was extracted with ethylacetate (15 mL), purified by column chromatography (silica gel, hexane/ethylacetate 8:2), and recovered as yellow needle crystals (9.81 g, yield 98 %). ^{1}H NMR ($CDCl_3$) δ: 1.61 (s, 9H), 7.70 (s, 1H), 8.12 (s, 1H). ^{13}C NMR ($CDCl_3$) (DEPT) δ: 27.9 (CH_3), 61.5 (C), 86.5 (C), 134.5 (CH), 146.0 (CH), 146.6 (C).

1-Boc-4-iodopyrazole (2.0 g, 6.86 mmol), dichlorobis(triphenylphosphine)palladium(II) (0.39 g, 0.58 mmol) and copper(I) iodide (0.13 g, 0.68 mmol) were stirred in a deoxygenated mixture of Et_3N (40 mL) and dry THF (80 mL) under an Ar atmosphere for 15 min at 0 °C. Subsequently, tetra-*n*-butylammonium fluoride trihydrate (1.03 g, 3.92 mmol) was added to the stirred solution. 1,4-bis(trimethylsilyl)butadiynetrimethyl[4-(trimethylsilyl)-1,3-butadiynyl]silane (2.57 g, 8.16 mmol) was slowly added and the mixture was stirred for 6 h. The solvent was removed, the residue was dissolved in ethylacetate (25 mL) and washed with a saturated solution of ammonium chloride (15 mL × 3). The organic phase was dried over anhydrous Na_2SO4 and the solvent was removed. The residue was purified by column chromatography (silica gel, hexane/ethylacetate 8:2) to afford pure H_2L5 in the form of polycrystalline powders (891 mg, yield 68 %). IR (KBr) 3240(br), 2148(m), 1684(s), 1595(w), 1506(m), 1437(s), 1219(s), 1144(s), 1047(m), 1007(m), 725(w), 544(w) cm^{-1}. ^1H NMR ($CDCl_3$) δ: 1.65 (s, 18H), 7.79 (s, 2H), 8.25 (s, 2H). ^{13}C NMR ($CDCl_3$) (DEPT) δ: 27.9 (CH_3), 71.5 (C), 76.1 (C), 86.5 (C), 105.2 (C), 134.5 (CH), 146.0 (CH), 146.6 (C). HRMS (ESI) calc. for $C_{20}H_{22}N_4O_4Na$: 405.1539; found 405.1532.

4,4'-buta-1,3-diyne-1,4-diylbis(1-Boc-3,5-dimethyl-pyrazole) (H_2L6). The first intermediate, 1-Boc-3,5-dimethyl-4-iodopyrazole, was obtained as reported in Ref. 3 and recovered quantitatively as yellow needle crystals. 1-Boc-3,5-dimethyl-4-iodopyrazole (1.52 g, 6.86 mmol), dichlorobis(triphenylphosphine)palladium(II) (0.39 g, 0.58 mmol) and copper(I) iodide (0.13 g, 0.68 mmol) were stirred in a deoxygenated mixture of Et_3N (40 mL) and dry THF (80 mL) under an Ar atmosphere for 15 min at 0 °C. Subsequently, tetra-*n*-butylammonium fluoride trihydrate (1.03 g, 3.92 mmol) was added to the stirred solution. 1,4-bis(trimethylsilyl)butadiynetrimethyl[4-(trimethylsilyl)-1,3-butadiynyl]silane (2.57 g, 8.16 mmol) was slowly added and the mixture was stirred for 6 h. The solvent was removed and the residue was dissolved in ethylacetate (25 mL) and washed with a saturated solution of ammonium chloride (15 mL × 3). The organic phase was dried over anhydrous Na_2SO_4 and the solvent was removed. The residue was purified by column chromatography (silica gel, hexane/ethylacetate 8:2) to afford pure H_2L6 in the form of polycrystalline powders (934 mg, yield 64 %). IR (KBr) 2987(m), 2937(m), 2154(m), 1739(vs), 1572(s), 1496(m), 1414(s), 1381(s), 1356(vs), 1311(vs), 1259(m), 1227(w), 1163(vs), 1086(vs), 850(m), 771(m), 660(w), 619(w), 546(w) cm^{-1}. ^1H NMR (CDCl3) δ: 1.62 (s, 18H), 2.32 (s, $2CH_3$), 2.57 (s, $2CH_3$). ^{13}C NMR (CDCl3) (DEPT) δ: 12.9 (CH3), 14.0 (CH3), 27.8(CH3), 72.7 (C), 78.72 (C), 86.6 (C), 105.9 (C), 147.9 (C), 148.6 (C), 153.7 (C).

4,4'-(benzene-1,4-diyldiethyne-2,1-diyl)bis(1-Boc-pyrazole) (H_2L7). The intermediate 1-Boc-4-iodopyrazole (1 g, 3.40 mmol), dichloro-bis(triphenylphosphine) palladium(II) (0.10 g, 0.17 mmol) and copper(I) iodide (0.03 g, 0.20 mmol) were stirred under Ar atmosphere for 5 minutes at room temperature in a mixture of deoxygenated Et_3N (8 mL) and dry THF (10 mL). After this time, 1,4-diethynylbenzene (0.21 g, 1.70 mmol) was added dropwise and the reaction mixture was stirred at room temperature for 3 h. Subsequently, the solvent was removed and the residue was dissolved in ethylacetate (20 mL). The resulting solution was washed with a saturated aqueous solution of ammonium chloride (5 mL × 3). Afterwards, the organic phase was dried over anhydrous Na_2SO_4 and the solvent was removed. The resulting residue was purified by column chromatography (silica gel, hexane/ethylacetate 8:2) to give H_2L7 as white needles (0.55 g, yield 70 %). IR (KBr) 3440(br), 2218(s), 1658(vs), 1995(m), 1390(m), 1261(w), 1186(w), 1107(w), 1063(w), 1018(w), 845(w), 646(w) cm^{-1}. ^1H NMR ($CDCl_3$) δ: 1.66 (s, 18H),

7.45 (s, 4H), 7.81 (s, 2H), 8.24 (s, 2H). ^{13}C NMR ($CDCl_3$) (DEPT) δ: 27.9(CH_3), 80.9 (C), 86.2 (C), 91.5 (C), 106.3 (C), 123.0 (C), 131.4 (CH), 133.1 (CH), 145.5 (CH), 147.2 (C). HRMS (NALDI) calc. for $C_{26}H_{26}N_4O_4Na$: 487.1852; found 487.1863.

CHAPTER 2

Materials and methods

General methods. 4-carboxypyrazole (H_2L1) was obtained as described above (Appendix I, Chapter 1). Other materials were obtained from commercial suppliers and used without further purification. IR absorption bands were measured by a Midac FT-IR on KBr pellets. Thermogravimetric and differential calorimetric analyses were performed, under air atmosphere, on Shimadzu-TGA-50H/DSC equipments, at heating rate of 20 ºC min^{-1}. XRPD were obtained on a Philips PW100 diffractometer using Cu K_α radiation (1.5418 Å). The compounds were manually grounded in an agate mortar, then deposited in the hollow of an aluminium sample holder.

Thermodiffractometric measurements. A custom-made sample heater was mounted on the Philips PW100 diffractometer with CuK_α (1.5418 Å) radiation. The compounds were manually grounded in an agate mortar, then deposited in the hollow of an aluminium sample holder. The thermodiffractometric experiments were planned on the basis of the TGA/DSC result. A sequence of scans, in a significant, low-angle 2θ range (4-15º), was performed at 10 ºC per step, heating in situ from room temperature up to 200 ºC and subsequently down to room temperature.

Gas adsorption measurements. N_2 adsorption isotherms were measured at 77 K on a Micromeritics Tristar 3000 volumetric instrument. Prior to measurement, powder samples were heated at 110 ºC for 7 h and outgassed to 10^{-6} mbar. In the case of $NH_4@Cu_3(OH)L1_3$, prior to activation, the as-synthesized single crystals were grounded for a few minutes in an agate mortar and subsequently suspended in a NH_3:$H_2$0 3:1000 solution and stirred for 8 h.

Ion exchange. The typical procedure makes use of 100 mg of the $NH_4@Cu_3(OH)L1_3$ material which is suspended in 12 mL of a 0.1 M aqueous solution of the corresponding inorganic salt: $LiNO_3$, KNO_3, $Ca(NO_3)_2$, $La(NO_3)_3$. The $Me_3NH@Cu_3(OH)L1_3$ and $Et_3NH@Cu_3(OH)L1_3$ exchanged materials were obtained by suspending 100 mg of $NH_4@Cu_3(OH)L1_3$ in a 0.5 M methanolic solution of the corresponding organic amine base. All the exchanged solids were subsequently filtered, washed with EtOH and Et_2O and later on suspended during 4 h in distilled water in order to remove the eventual adsorbed ion pairs. Afterwards, the materials were filtered again and washed with EtOH. The effect of ion exchange on the materials was examined by means of EA, Thermal analysis, IR, Atomic Absorption, N_2 adsorption and XRPD experiments.

Effect of ion exchange on the adsorption selectivity of $A@Cu_3(OH)L1_3$materials towards benzene:cyclohexane vapour mixtures. The $A@Cu_3(OH)L1_3$ materials (50 mg) were activated at 110 ºC at high vacuum for 7 h. The activated sample was exposed to a saturated atmosphere of a 1:1 benzene/cyclohexane mixture in a Schlenk tube during 24 h at 298 K. Afterwards, the increase of the weight of the materials was measured and the composition of the adsorbed phase was checked by ^1H NMR (DMSO-d_6, 0.5 mL)

Variable temperature pulse chromatography. Gas-phase adsorption at low degrees of pore filling was studied using the pulse chromatographic technique employing a 10-cm column packed with ca. 0.75 g of the material in microcrystalline form. Prior to measurement, powder samples were heated at 110 ºC for 7 h and outgassed to 10^{-6} mbar. Subsequently, the sample was conditioned in He flow (10 mL min^{-1}). Later on, 1 mL of an equimolecular gas mixture (C_2H_2, N_2, CH_4, CO_2) was injected at 1 bar and the separation

performance of the chromatographic column was examined at different temperatures (273 K-363 K) by means of a mass spectrometer gas analysis system (Pfeiffer vacoon) detecting ion peaks at m/z 44 (CO_2), 28 (N_2), 26 (C_2H_2) and 16 (CH_4).

Breakthrough curves. The gas-separation properties of $NH_4@Cu_3(OH)L1_3$ and $Et_4NH@Cu_3(OH)L1_3$ were also examined by breakthrough experiments using CO_2:CH_4 gas mixtures (about 0.5:0.5 w/w; 0.27:0.73 v/v) flowed through an activated sample of $A@Cu_3(OH)L1_3$ (~0.75 g) packed into a glass column (0.3 cm inner diameter ×10 cm length). Helium gas was initially purged into the sample column. The column was cooled to 273 K using an ice bath. The gas mixture (100 kPa) was dosed into the column at a flow rate of 10 mL min^{-1}. The relative amounts of the gases passing through the column were monitored on a mass spectrometer gas analysis system (Pfeiffer vacoon) detecting ion peaks at m/z 44 (CO_2) and 16 (CH_4).

Catalytic behaviour. Tert-butyl hydroperoxide (70 % H_2O solution) was dried over anhydrous $MgSO_4$ and conserved over 4 Å molecular sieves. Cyclohexane and cyclohexene were dried over 4 Å molecular sieves for 24 h. Catalysis reactions were conduced in dried vessels under a N_2 atmosphere. Cyclohexene/cyclohexane oxidation: Activated $NH_4@Cu_3(OH)L1_3$ (81 mg, 0.15 mmol) was suspended in a solution of cyclohexene/cyclohexane (1.66 mL, 16 mmol) and *t*-BuOOH (800 μL, 8 mmol) at room temperature. The suspension was stirred at 70 ºC and subsequently 10 μL aliquots were taken after fixed time steps and the advance of the reaction was examined by ^1H NMR ($CDCl_3$, 0.5 mL). For investigation of catalyst activity in a second cycle, the catalyst was separated from reaction mixture by filtration and washed with EtOH and Et_2O. The filtered $NH_4@Cu_3(OH)L1_3$ catalyst is proved to remain unaltered as stated by XRPD measurement. All yields and conversions are based on cyclohexene/cyclohexane.

Synthesis of PCPs

$[NH_4@Cu_3(OH)L1_3]_n\cdot$solv ($NH_4@Cu_3(OH)L1_3$). An aqueous ammonia solution (NH_3:H_2O 1:15, 30 mL) containing 4-carboxypyrazole (220 mg, 2 mmol) and $Cu(NO_3)_2\cdot 3H_2O$ (480 mg, 2 mmol) leads to a blue solution which afforded in three days dark blue single crystals of $[NH_4@Cu_3(OH)L1_3]_n\cdot$solv formulation, suitable for X-ray diffraction. Those crystals are filtered and washed with EtOH and Et_2O to give 392 mg of dry product (yield 72 %). Anal. calc. for $NH_4[Cu_3(OH)(C_4H_2N_2O_2)_3]\cdot(H_2O)_{15}$ (826.13) C, 17.45; H, 5.00; N, 11.87; found C, 17.06; H, 4.51; N, 12.13.

($[Cd(H_2O)_2L1]H_2O)_n$ (CdL1). In a typical synthesis $Cd(NO_3)_2$ (0.5 mmol, 186 mg) and H_2L1 (0.5 mmol, 55 mg) were stirred in 10 mL of distilled water for few minutes. Upon the addition of 2 mL of NH_3 (32 %), the mixture got transparent and colourless. After four days at room temperature, colourless block crystals were recovered from the solution, filtered and dried in air. Yield: 98 mg (69 %). Anal. calc. for $[Cd(H_2O)_2(C_4H_2N_2O_2)]\cdot(H_2O)_{1.35}$ (282.83) C, 16.99; H, 3.10; N, 9.90; found C, 17.08; H, 3.57; N, 9.81.

CHAPTER 3

Materials and methods

3,5-dimethyl-4-carboxypyrazole (H_2L2) was prepared as described above (Appendix I, Chapter 1). $CuF_2 \cdot 2H_2O$ was obtained from Sigma-Aldrich; $CuCl_2 \cdot 2H_2O$ was obtained from Wako. All solvents have been used as received and without any further purification.

XPS measurements were performed on a ULVAC-PHI Model 5500 spectrometer with 15 kV, 400 W MgK_α emission as the X-ray source. UV-visible spectra of solid samples were recorded on a HITACHI U-3500/U-4000 spectrophotometer over the range 250-900 nm at room temperature. Elemental analyses were carried out on a Flash EA 1112 series, Thermo Finnigan instrument. IR spectra were recorded on a NICOLET iS5, Thermo Scientific. X-ray powder diffraction (XRPD) data were collected on a Rigaku RINT-200 HF (Ultima) diffractometer with CuK_α radiation. Thermal gravimetric analyses (TGA) were carried out on a Thermo plus TG8120, Rigaku instrument in a nitrogen atmosphere with a heating rate of 10 K min^{-1}. The adsorption isotherms of gases were carried out on Belsorp-max and Belsorp-18. The adsorption isotherms of gaseous H_2O and MeOH were measured by using a Belsorp-aqua. The gas-separation properties and breakthrough experiments were performed using 10 mL min^{-1} He flux as gas carrier flowed through the activated samples packed into a 15-cm length, 0.4-cm inner diameter glass column. Helium gas was initially purged into the packed column. The relative amounts of the gases passing through the column were monitored on a mass spectrometer gas analysis system (Pfeiffer Vacoon) detecting ion peak at the appropriate *m/z* value.

Single-crystal X-ray measurements. Data were recorded on a Rigaku/MSC Saturn CCD diffractometer with confocal monochromated MoK_α radiation (λ = 0.7107 Å) and processed by using the CrystalClear Program (Rigaku). The structures of $Cu(HL2)_2$, α-$[Cu_2(H_2O)(L2)_2]$ and β-$[Cu_2(H_2O)(L2)_2]$ were solved by a direct method (Sir 97) and refined by full-matrix least squares refinement using the SHELXL-97 computer program. The positions of non-hydrogen atoms were refined with anisotropic displacement factors. The hydrogen atoms were refined geometrically by using a riding model. The void volume of each framework was estimated by the PLATON program.[4]

Synthesis of PCPs

$\{[Cu(HL2)_2]\cdot 4H_2O\cdot 2DMF\}_n$ ($Cu(HL2)_2$). In a typical synthesis a solution of $CuF_2 \cdot 2H_2O$ (0.05 mmol, 6.9 mg) in 0.5 mL of H_2O and a solution of H_2L2 (0.05 mmol, 7.0 mg) in 0.5 mL of DMF are mixed together at room temperature. After few minutes under stirring, the turbid mixture is sealed in a glass vial with Teflon cap and heated at 60 ºC for 24 h. The reaction mixture is allowed to cool down to room temperature and block violet crystals of $\{[Cu(HL2)_2]\cdot 4H_2O\cdot 2DMF\}_n$ formulation can be isolated from the bulk violet powder. Reaction yield can not be calculated since the crystals are not the main product of the reaction.

$\{[Cu_2(L2)_2OH_2]\cdot 1.5(DMF)\cdot 0.1(H_2L2)\}_n$ (α-$[Cu_2(H_2O)(L2)_2]$). A solution of H_2L2 (110 mg, 1.0 mmol) in DMF (10 mL) was added to a solution of $CuCl_2 \cdot 2H_2O$ (170 mg, 1.0 mmol) in MeOH (10 mL). The mixture was stirred at 90 ºC for 24 h and a sky blue solid is collected by filtration. The solid is quickly washed with DMF and dried in air. (Yield 66%). Anal. calc. for α-$[Cu_2(H_2O)(C_6H_6N_2O_2)_2]$ (544.81) C, 37.68; H, 4.69; N, 14.65; found C, 37.48; H, 4.51; N, 14.73. Single crystals of α-$[Cu_2(H_2O)(L2)_2]$,

suitable for X-ray diffraction data collection, have been obtained heating the reaction mixture at 60 ºC for 20 h in a Teflon capped vial.

{[$Cu_2(L2)_2OH_2$]·0.9DMF}$_n$ (β-[$Cu_2(H_2O)(L2)_2$]). The partially evacuated β-[$Cu_2(H_2O)(L2)_2$] sample (sky blue colour) has been obtained by degassing α-[$Cu_2(H_2O)(L2)_2$] at 120 ºC for 7 h under high vacuum. Single crystals of β-[$Cu_2(H_2O)(L2)_2$] have been obtained suspending single crystals of α-[$Cu_2(H_2O)(L2)_2$] in dry CH_2Cl_2 for three days, changing the fresh solvent daily. Anal. calc. for β-[$Cu_2(H_2O)(C_6H_6N_2O_2)_2$] (487.14) C, 36.24; H, 4.20; N, 14.09; found C, 35.81; H, 4.09; N, 13.97.

{[$Cu_2(L2)_2OH_2$]·4.5H_2O}$_n$ (β∗-[$Cu_2(H_2O)(L2)_2$]). β-[$Cu_2(H_2O)(L2)_2$] solid have been suspended in water for 24 h, filtered and dried on air to yield the water exchanged, sky blue β∗-[$Cu_2(H_2O)(L2)_2$] material. Anal. calc. for β∗-[$Cu_2(H_2O)(C_6H_6N_2O_2)_2$] (502.42) C, 28.69; H, 4.61; N, 11.15; found C, 28.77; H, 4.25; N, 11.07.

[$Cu_2(L2)_2$]$_n$ (γ-[$Cu_2(H_2O)(L2)_2$]). The completely evacuated γ-[$Cu_2(H_2O)(L2)_2$] material (dark blue colour) is obtained heating β∗-[$Cu_2(H_2O)(L2)_2$] at 150 ºC for 7 h under high vacuum. It is not stable in air as it rapidly converts into β∗-[$Cu_2(H_2O)(L2)_2$] after accommodation of water in the channels.

[$Cu_2(L2)_2$]$_n$ (δ-[$Cu_2(H_2O)(L2)_2$]). The treatment of γ-[$Cu_2(H_2O)(L2)_2$] solid at 77 K under He atmosphere for 5 min affords the empty and air stable δ-[$Cu_2(H_2O)(L2)_2$] material (forest green colour). Anal. calc. for δ-[$Cu_2(H_2O)(C_6H_6N_2O_2)_2$] (403.34) C, 34.21; H, 3.35; N, 13.29; found C, 34.48; H, 3.32; N, 13.70.

CHAPTER 4

Materials and methods

3,5-dimethyl-4-carboxypyrazole (H_2L2) and 4,4'-buta-1,3-diyne-1,4-diylbis(1-Boc-3,5-dimethyl-pyrazole) (H_2L6) were prepared as described above (Appendix I, Chapter 1). All the general reagents and solvents were commercially available and used as received. Carboxen™ 569, diethylsulphide and diisopropylfluorophosphate (CAUTION: highly toxic) were purchased from Sigma Aldrich. Cu(BTC)[5] and MIL-101(Cr)[6] were prepared according to published procedures. Thermogravimetric analyses (TGA) were performed, using a reactive air atmosphere, on a Shimadzu-TGA-50H equipment, at a heating rate of 20 K min^{-1}. XRPD data were obtained on a D2 PHASER Bruker diffractometer using CuK_α radiation (λ = 1.5418 Å). The compounds were manually grounded in an agate mortar, then deposited in the hollow of a zero-background silicon sample holder. N_2 and CO_2 adsorption isotherms were measured, at 77 K and 195 K, respectively, on a Micromeritics Tristar 3000 volumetric instrument. Water adsorption isotherms were measured at 298 K using a Quantachrome Hydrosorb 1000 apparatus with an equilibration time of 60 s. Prior to measurement, powder samples were heated 7 h (at 453 K for Cu(BTC) and at 393 K for Carboxen™, $[Zn_4O(L2)_3]$, $[Co_4O(L2)_3]$ and $[Co_4O(L6)_3]$) and outgassed to 10^{-1} Pa.

Thermodiffractometry. The diffractograms were recorded in a reactive air-atmosphere mounting a custom-made sample heater, assembled by Officina Elettrotecnica di Tenno (Ponte Arche, Italy), on the Bruker AXS D8 automated diffractometer. Prior to measurement, a powdered microcrystalline batch of $[Zn_4O(L2)_3]$ was pulverized using an agate mortar and pestle and was deposited in the hollow of an aluminium sample holder. The diffractograms were recorded in a significant low-angle 2θ range, heating *in situ* by increments of 20 K, starting from 303 K, until complete loss of crystallinity was observed. By using the whole-profile Le Bail refinement method, a parametric treatment of those data acquired before the beginning of crystallinity loss was carried out.

High-pressure adsorption experiments. The high pressure SF_6 and CF_4 adsorption/desorption measurements at 298 K were performed on a volumetric BELSORP-HP apparatus (BEL, Japan). Mass of the activated sample used was between 0.6 and 0.8 g. The dead volume of the empty sample cell and of the sample cell with sample was determined using helium at 298 K. Non-ideal corrections were made by applying virial coefficients of real gas equations at the measurement temperature obtained from NIST.[7]

Variable temperature pulse chromatography. Gas-phase adsorption at zero coverage surface was studied using the pulse chromatographic technique employing a Gas Chromatograph and a 15-cm column (0.4-cm internal diameter) packed with *ca.* 1 g of 0.5-mm pellets of the studied materials. Particles of $[Zn_4O(L2)_3]$ were aggregated by emulsifying them in a water suspension (1 mL) of starch (0.1 g) at 343 K for 2 min. The solvent was removed under reduced pressure. The resulting solid was grounded trough a 0.5 mm sieve and characterized by XRPD and N_2 adsorption, showing that there is no loss of crystallinity and porosity. CuBTC was treated in a similar way to $[Zn_4O(L2)_3]$. Carboxen™ was used as received. Prior to measurement, samples were outgassed to 10^{-1} Pa and heated 7 h at 453 K for CuBTC and at 393 K for $[Zn_4O(L2)_3]$ and Carboxen™. The columns were conditioned in He flow (25 mL min^{-1}). Later on, 2 μL of each gas was injected at 1 bar and the separation performance of the chromatographic column was examined at different temperatures (313 K-513 K).

Breakthrough curves. The gas-separation properties of $[Zn_4O(L2)_3]$ were also examined by breakthrough experiments using 10 mL min^{-1} He flux containing 130 ppm of benzene flowed through the activated samples packed into a 15-cm length, 0.4-cm inner diameter glass column. Helium gas was initially purged into the packed column. A similar experiment was followed containing 50 % humidity. The relative amounts of the gases passing through the column were monitored on a mass spectrometer gas analysis system (Pfeiffer Vacoon) detecting ion peak at m/z 78 (C_6H_6).

Synthesis of PCPs

$\{[Zn_4O(L2)_3]\cdot(EtOH)_3\}_n$ ($[Zn_4O(L2)_3]$). A 200 mL ethanol solution (96 % in water) containing H_2L2 (4.2 g, 30 mmol) and triethylamine (8.3 mL, 60 mmol) was mixed with another ethanol solution (200 mL) containing $Zn(NO_3)_2\cdot 4H_2O$ (7.83 g, 30 mmol). The resulting white suspension was refluxed for 4 h. Upon cooling, 6.0 g of white microcrystaline material was filtrated and was washed with ethanol and diethylether (yield 92 %). Anal. calc. for **[**$Zn_4O(C_6H_6N_2O_2)_3]\cdot(CH_3CH_2OH)_3$ (830.14) C, 34.72; H, 4.37; N, 10.12; found C, 34.91; H, 6.26; N, 11.63.

$\{[Co_4O(L2)_3]\cdot(EtOH)_{3.2}\}_n$ ($[Co_4O(L2)_3]$). A 200 mL ethanol solution (96 % in water) containing H_2L2 (4.2 g, 30 mmol) and triethylamine (8.3 mL, 60 mmol) was mixed with another ethanol solution (200 mL) containing $Co(NO_3)_2\cdot 6H_2O$ (8.73 g, 30 mmol). The resulting white suspension was refluxed for 4 h. Upon cooling, 5.8 g of purple-blue microcrystaline material was filtrated and was washed with ethanol and diethylether (yield 95 %). Anal. calc. for **[**$Co_4O(C_6H_6N_2O_2)_3]\cdot(CH_3CH_2OH)_{3.2}$ (813.52) C, 36.02; H, 4.61; N, 10.33; found C, 35.41; H, 5.26; N, 10.63.

$\{[Co_4O(L6)_3]\cdot solv\}_n$ ($[Co_4O(L6)_3]$). In a typical synthesis, $Co(AcO)_2\cdot 4H_2O$ (50 mg, 0.20 mmol) and $(Boc)_2$-L6 ligand (60 mg, 0.15 mmol) were dissolved in 50 mL DMF until the solution became limpid and pink. The mixture was heated in a Teflon liner at 125 ºC for 70 h. The bright blue microcrystalline solid deposited on the walls of the liner was filtered, washed with fresh DMF and dried in air. The dry solid was 41 mg (yield 67 %). Anal. calc. for $[Co_4O(C_{14}N_4H_{12})_3](C_3H_7NO)_8(H_2O)_5$ (1635.37) C, 48.47; H, 2.29; N, 17.13; found C, 48.92; H, 7.09; N, 16.82.

CHAPTER 5

Materials and methods

All the general reagents and solvents were commercially available and used as received.

[Ru(*p*-cymene)Cl_2(pta)] (pta = 1,3,5-triaza-7-phospaadamantane) (RAPTA-C) was synthesized according to the literature method.[8] IR absorption bands were measured by a Midac FT-IR on KBr pellets. ^{1}H NMR and ^{13}C NMR were acquired on a 500 MHz Varian Equipment using CDCl3 as solvent. Thermogravimetric and differential calorimetric analyses were performed, under air atmosphere, on a Shimadzu-TGA-50H/DSC equipment, at a heating rate of 20 ºC min^{-1}.

Except for the structural analysis, XRPD data were collected on a Bruker D2-PHASER diffractometer using CuK_α radiation (λ = 1.5418 Å). The compounds were manually grounded in an agate mortar, then deposited in the hollow of a silicon sample holder. N_2 adsorption isotherms were measured at 77 K on a Micromeritics Tristar 3000 volumetric instrument. Prior to measurement, powdered samples were heated at 130 ºC for 7 h and outgassed to 10^{-6} mbar. RAPTA-C solid-liquid adsorption isotherms were measured at 298 K by suspending 10 mg of activated $Ni_8(L5)_6$ in RAPTA-C aqueous solutions (Milli-Q distilled water), stirring afterwards for 8 h in order to assure that equilibrium was reached. The amount of RAPTA-C incorporated into $Ni_8(L5)_6$ was indirectly calculated monitoring, by means of UV-vis, the decrease of RAPTA-C concentration from the supernatant solution. The metallodrug delivery process was studied by suspending 10 mg of activated $Ni_8(L5)_6 \cdot 4$RAPTA-C in a simulated body fluid (SBF)[14] incubated at 37 ºC and stirring afterwards. Aliquots of the supernatant solution were studied by means of UV-vis at different periods of time in order to determine the amount of released RAPTA-C and the kinetics of the process.

X-ray powder diffraction structural analysis on $Ni_8(L)_6$ materials. Microcrystalline batches of $Ni_8(L)_6$ were gently ground in an agate mortar, then deposited in the hollow of an aluminum sample holder equipped with a zero-background plate. Diffraction data were collected by means of an overnight scan in the 2θ range of 5-105°, with 0.02° steps, on a Bruker AXS D8 Advance diffractometer, equipped with Ni-filtered CuK_α radiation (λ = 1.5418 Å) and with a Lynxeye linear position-sensitive detector, and mounting the following optics: primary beam Soller slits (2.3°), fixed divergence slit (0.5°), receiving slit (8 mm). The generator was set at 40 kV and 40 mA.

A visual inspection of the acquired diffractograms allowed to purport isomorphism between $Ni_8(L)_6$ and [Ni8(μ4-OH)4(μ4-OH2)2(μ4-L)6]·solv systems,[9] as confirmed by independent indexing. Standard peak search, followed by indexing through the Single Value Decomposition approach[10] implemented in TOPAS-R,[11] allowed the detection of the approximate unit cell parameters of $Ni_8(L)_6$. The lattice F-centring was assigned on the basis of the systematic absences, and the space group chosen taking into consideration the purported isomorphism. Unit cell and space group were checked by Le Bail refinements and later confirmed by structure solution and refinement. The structure solution was performed by the simulated annealing technique, as implemented in TOPAS, employing a rigid, idealized model for the crystallographic independent portion of the ligand.[12] The difference Fourier map calculated with the Fcs of the framework alone revealed that the solvent is highly disordered. Its electronic density was modeled by locating, within the cavities, the number of oxygen atoms whose refined site occupation factors, combined with the site multiplicity, represent the total electron density of the solvent, as estimated from

the elemental and TG analyses. The presence of dynamic disorder was taken into account by assigning to these atoms a high isotropic thermal parameter, corresponding to a mean square displacement of 0.9 Å. The final refinement was carried out by the Rietveld method, maintaining the rigid body introduced at the solution stage. The background was modeled by a polynomial function. One, refinable, isotropic thermal parameter was attributed to the metal atoms (B_M), lighter atoms (with the notable exception cited above) being given a $B_{iso} = B_M + 2.0$ Å^2 value. Peak shapes were described by the Fundamental Parameters Approach.[13]

Mechanical stability tests on $[Ni_8(OH)_4(OH_2)_2(L5)_6]_n$. A typical test consisted in the characterization, by XRPD and N_2 adsorption at 77 K, of pellets fabricated with 100 mg of the original sample, by the application of specific values of pressure (1 Mg cm^{-2} and to 2 Mg cm^{-2}) for 60 seconds. The pellets are then gently ground in an agate mortar.

Thermodiffractometry. The diffractograms were recorded in a reactive air-atmosphere mounting a custom-made sample heater, assembled by Officina Elettrotecnica di Tenno (Ponte Arche, Italy), on the Bruker AXS D8 automated diffractometer. Prior to measurement, powdered microcrystalline batches of $Ni_8(L)_6$ wers pulverized using an agate mortar and pestle and was deposited in the hollow of an aluminium sample holder. The diffractograms were recorded in a significant low-angle 2θ range, heating *in situ* by increments of 20 K, starting from 303 K, until complete loss of crystallinity was observed. By using the whole-profile Le Bail refinement method, a parametric treatment of those data acquired before the beginning of crystallinity loss was carried out. For cyclic theromodiffraction experiments, the temperature has been changed in the 30-210 ºC the range five times.

DES adsorption experiments. For the evaluation of the dynamic adsorption of DES vapours, the increase in weight of *ca.* 40 mg of activated solid have been measured by means of a Sartorius M2P microbalance equipped with Sarto-Collect software. The sample weight was recorded every 60 s. Constant flux of Ar (15 mL min^{-1}) was bubbled in a flask containing DES at room temperature. The Ar flow was then mixed with a N_2 flow before reaching the balance chamber where the adsorbent material is located. For experiments in dry conditions, the N_2 flow was of 5 mL min^{-1}, while for experiments in humid conditions, a flow of 15 mL min^{-1} was forced to pass throw a flask containing distilled water at room temperature.

Preparation of Simulated Body Fluid (SBF). For the delivery process a simulated body fluid (SBF)[14] has been used. Due to the possible precipitation of some weakly soluble inorganic salts, we prepare two solutions, A and B (Table I.1), that must be mixed just before each experiment.

	Sol. A (g/L)	Sol. B (g/L)
NaCl	6.213	6.213
$NaHCO_3$	5.948	
KCl	0.450	
$Na_2HPO_4{\cdot}2H_2O$		0,498
$K_2HPO_4{\cdot}3H_2O$	0.462	
$MgCl_2{\cdot}6H_2O$	0.622	
$CaCl_2$		0.584
Na_2SO_4	0.144	

Table I.1. Composition of the A and B solutions for simulated body fluid preparation.

Adsorption and release of RAPTA-C from activated $[Ni_8(OH)_4(OH_2)_2(L5)_6]_n$. Prior to performing the adsorption isotherm of RAPTA-C the as synthesized solid $Ni_8(OH)_4(OH_2)_2(L5)_6]n\ H_2O{\cdot}$DMF (200 mg)

has been suspended 4 hours, in 100 mL CH_2Cl_2 to ensure complete interchange of the guest solvent molecules (H_2O and DMF) with the more volatile CH_2Cl_2 molecules. Powdered samples of $Ni_8(OH)_4(OH_2)_2(L5)_6]n\cdot CH_2Cl_2$ were heated at 130 ºC for 7 h and outgassed to 10^{-6} mbar to achieve the complete removal of the guest molecules.

We prepared RAPTA-C solutions with increasing concentrations by dissolving 5, 10, 20, 30, 35, 40, 50, 65, 80 mg of RAPTA-C in 5 ml of water (Milli-Q distilled water) stirring overnight at room temperature ($[RAPTA\text{-}C]_0$ = 0.0022, 0.0043, 0.0086, 0.0129, 0.0151, 0.0173, 0.0216, 0.0281, 0.0345 M). RAPTA-C solid-liquid adsorption isotherms were measured at 298 K by suspending 10 mg of activated $Ni_8(L5)_6$ in the RAPTA-C aqueous solutions, stirring afterwards for 4 h in order to assure that equilibrium was reached. Therefore, each sample was centrifuged, by means of a Sigma 3-30K centrifuge, using centrifuge tubes with a 30 kDa PES filter, at 8000 rpm for 10 minutes to achieve the separation of the $Ni_8(L5)_6\cdot$RAPTA-C matrix from the solution. The amount of RAPTA-C incorporated into $Ni_8(L5)_6$ was indirectly calculated monitoring, by means of UV-vis, the decrease of RAPTA-C concentration from the filtered solution. Using the Lambert-Beer law, the concentration of RAPTA-C in solution was calculated from the absorbance at 323 nm. Taking into account the initial amount of RAPTA-C in the solution, it is possible to calculate the amount of RAPTA-C adsorbed by $Ni_8(L5)_6$.

For the metallodrug delivery process we suspended 10 mg of activated $Ni_8(L5)_6\cdot$RAPTA-C in SBF, incubated at 37 ºC and stirr afterwards. Aliquots (2 mL) of the supernatant solution were studied by means of UV-vis (λ = 323 nm) at different periods of time (10, 20, 30, 45, 60 min, 2, 4, 6, 8, 12, 24 h) to determine the amount of released RAPTA-C and the kinetics of the process. The solutions were filtered using centrifuge tubes with a 30 kDa PES filter, at 8000 rpm for 2 minutes, than both the solution and the solid were joined to the mother solution to keep the volume constant.

Furthermore we studied the reversibility of the desorption process quantifying the maximum of RAPTA-C delivered after reaching the equilibrium. A suspension of 10 mg of $Ni_8(L5)_6\cdot$RAPTA-C en 10 mL of SBF is treated in an ultrasound bath for 90 minutes. The volume is increased up to 200 mL with fixed steps (V_{tot} = 20, 30, 50, 75, 100, 150 200 mL) and the same treatment is performed after each addition. Aliquots (2 mL) of the supernatant solution were studied by means of UV-vis (λ = 323 nm).

Synthesis of PCPs

$[Ni_8(OH)_4(OH_2)_2(L1)_6]_n\cdot$solv ($Ni_8(L1)_6$). In a typical synthesis, 33.3 mg (0.3 mmol) of 1*H*-pyrazole-4-carboxylic acid (H_2L1) were dissolved in 16 mL of DMF and 99.2 mg (0.4 mmol) of $Ni(AcO)_2\cdot 4H_2O$ were dissolved in 4 mL of H_2O. The two limpid solutions were mixed together and refluxed for 6 h under stirring. The light green solid obtained was filtered and washed with EtOH and Et_2O, yielding 75 mg of $[Ni_8(OH)_4(OH_2)_2(L1)_6]\cdot(H_2O)_{10}\cdot(DMF)_{4.5}$ (86 %). IR (KBr) 3425(br), 1657(vs), 1543(s), 1450(m), 1298(s), 1103(w), 1053(w), 1009(w), 877(w), 793(m), 667(w), 627(w) cm^{-1}. Anal. calc. for $Ni_8(OH)_4(OH_2)_2(C_4N_2O_2H_2)_6(H2O)_{10}(C_3H_7NO)_{4.5}$ (1743.11) C, 25.84; H, 4.13; N, 13.26; found C, 26.03; H, 4.29; N, 13.29.

$[Ni_8(OH)_4(OH_2)_2(L3)_6]_n\cdot$solv ($Ni_8(L3)_6$). In a typical synthesis, 56.5 mg (0.3 mmol) of 4-(1*H*-pyrazol-4-yl)benzoic acid (H_2L3)were dissolved in 16 mL of DMF and 99.2 mg (0.4 mmol) of $Ni(AcO)_2\cdot 4H_2O$ were dissolved in 4 mL of H_2O. The two limpid solutions were mixed together and refluxed for 6 h under stirring. The light green solid obtained was filtered and washed with EtOH and Et_2O, yielding 73 mg of

$[Ni_8(OH)_4(OH_2)_2(L3)_6]\cdot(H_2O)_{11}\cdot(DMF)_{13}$ (73 %). IR (KBr) 3390(br), 1655(vs), 1608(s), 1545(m), 1394(s), 1248(m), 1186(w), 1105(w), 1051(w), 957(w), 854(w), 789(m), 714(w), 669(w) cm^{-1}. Anal. calc. for $Ni_8(OH)_4(OH_2)_2(C_{10}N_2O_2H_6)_6(H_2O)_{13}(C_3H_7NO)$ (1997.90) C, 37.87; H, 3.88; N, 9.11; found C, 37.88; H, 4.24; N, 9.23.

$[Ni_8(OH)_4(OH_2)_2(L4)_6]_n\cdot$solv (**$Ni_8(L4)_6$**). In a typical synthesis, 63.1 mg (0.3 mmol) of 4,4'-benzene-1,4-diylbis(1*H*-pyrazole) (H_2L4)were dissolved in 16 mL of DMF and 99.2 mg (0.4 mmol) of $Ni(AcO)_2\cdot4H_2O$ were dissolved in 4 mL of H_2O. The two limpid solutions were mixed together and refluxed for 6 h under stirring. The light green solid obtained was filtered and washed with EtOH and Et_2O, yielding 89 mg of $[Ni_8(OH)_4(OH_2)_2(L4)_6]\cdot(H_2O)_4\cdot(DMF)_{11}$ (66 %). IR (KBr) 3433(br), 1655(vs), 1574(s), 1390(m), 1358(m), 1250(s), 1182(w), 1124(w), 1057(s), 958(s), 845(m), 658(w), 540(w), 505(w) cm^{-1}. Anal. calc. for $Ni_8(OH)_4(OH_2)_2(C_{12}N_4H_8)_6(H_2O)_4(C_3H_7NO)_{11}$ (2699.01) C, 46.72; H, 5.26; N, 18.16; found C, 46.65; H, 5.10; N, 18.20.

$[Ni_8(OH)_4(OH_2)_2(L5)_6]_n\cdot$solv (**$Ni_8(L5)_6$**). In a typical synthesis, 105.6 mg (0.3 mmol) of Boc-1,4-bispyrazolatobut-1,3-diyne (Boc_2L5) were dissolved in 16 mL of DMF and 99.2 mg (0.4 mmol) of $Ni(AcO)_2\cdot4H_2O$ were dissolved in 4 mL of H_2O. The two limpid solutions were mixed together and refluxed for 6 h under stirring. The light green solid obtained was filtered and washed with EtOH and Et_2O, yielding 95 mg of $[Ni_8(OH)_4(OH_2)_2(L5)_6]\cdot(H_2O)_{11}\cdot(DMF)_{13}$ (80 %). IR (KBr) 3446(br), 2933(m), 2150(m), 1670(vs), 1523(m), 1390(m), 1338(w), 1257(w), 1221(m), 1173(w), 1099(m), 1065(m), 1014(w), 866(w), 787(m), 646(w), 606(w) cm^{-1}. Anal. calc. for $Ni_8(OH)_4(OH_2)_2(C_{10}N_4H_4)_6(H_2O)_{11}(C_3H_7NO)_{13}$ (2802.99) C, 42.65; H, 4.36; N, 18,84; found. C, 42.68; H, 5.21; N, 17.98.

$[Ni_8(OH)_4(OH_2)_2(L6)_6]_n\cdot$solv (**$Ni_8(L7)_6$**). In a typical synthesis, 123.6 mg (0.3 mmol) of 4,4'-(benzene-1,4-diyldiethyne-2,1-diyl)bis(1-Boc-pyrazole) (Boc_2L7) were dissolved in 16 mL of DMF and 99.2 mg (0.4 mmol) of $Ni(AcO)_2\cdot4H_2O$ were dissolved in 4 mL of H_2O. The two limpid solutions were mixed together and refluxed for 6 h under stirring. The light green solid obtained was filtered and washed with EtOH and Et_2O, yielding 111 mg of $[Ni_8(OH)_4(OH_2)_2(L7)_6]\cdot(H_2O)_{45}\cdot(DMF)_5$ (67 %). IR (KBr) 3435(br), 2933(m), 1657(vs), 1491(m), 1388(m), 1255(w), 1167(w), 1103(w), 1061(w), 1018(w), 841(m), 775(w), 665(w), 646(w) cm^{-1}. Anal. calc. for $Ni_8(OH)_4(OH_2)_4(C_{16}N_4H_8)_6(H_2O)_{45}(C_3H_7NO)_5$ (3323.36) C, 40.12; H, 5.61; N, 12.22; found C, 40.06; H, 6.73; N, 12.38.

Bibliography

[1] C. Foces-Foces, A. Echevarría, N. Jagerovic, I. Alkorta, J. Elguero, U. Langer, O. Klein, M. Minguet Bonvehí, H.-H. Limbach, *J. Am. Chem. Soc*. **2001**, *123*, 7898.

[2] Z. Arnold, *Coll. Czech. Chem. Commun*. **1985**, *30*, 2783.

[3] M. I. Rodríguez-Franco, I. Dorronsoro, A. I. Hernández-Higueras, G. Antequera, *Tetrahedron Letters*, **2001**, *42*, 863.

[4] A. L. Spek, *J. Appl. Crystallogr*. **2003**, *36*, 7.

[5] K. Schlichte, T. Kratzke, S. Kaskel, *Micro. and Meso. Mat*, **2004**, *73*, 81.

[6] G. Férey, C. Mellot-Draznieks, C. Serre, F. Millange, J. Dutour, S. Surblé, I. Margiolaki, *Science*, **2005**, *309*, 2040.

[7] V. I. Isaeva, L. M. Kustov *Pet. Chem.* **2010**, *50*, 167.

[8] C. S. Allardyce, P. J. Dyson, D. J. Ellis, S. L. Heath. *Chem. Commun*. **2001**, 1396

[9] N. Masciocchi, S. Galli, V. Colombo, A. Maspero, G. Palmisano, B. Seyyedi, C. Lamberti, S. Bordiga, S. *J. Am. Chem. Soc*. **2010**, *132*, 7902.

[10] A. Coelho, *J. Appl. Cryst.* **2003**, *36*, 86.

[11] TOPAS Version 3.0, Bruker AXS **2005**, Karlsruhe, Germany.

[12] To describe the crystallographically independent portion of the ligand, a rigid model was adopted imposing idealized bond distances and angles as follows: C-C, C-N, N-N of the heterocyclic ring 1.36 Å; single C-C 1.40 Å; triple C-C 1.25 Å; C-H 0.95 Å; heterocyclic ring internal bond angles 108°.

[13] R. W. Cheary, A. Coelho, *J. Appl. Cryst.* **1998**, *31*, 85.

[14] T. Kokubo, H. Kushitani, C. Ohtsuki, S. Sakka, T. Yamamuro, *J. Mater. Sci.: Mater. Med.* **1992**, *3*, 79.

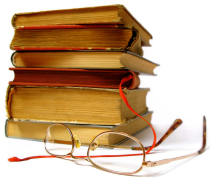

APPENDIX II – List of Publications

APPENDIX II – List of Publications

"*A soft copper(II) porous coordination polymer with unprecedented aqua bridge and selective adsorption properties*" E. Quartapelle Procopio, T. Fukushima, E. Barea, J. A. R. Navarro, S. Horike, S. Kitagawa, *Chem. Europ. J.* **2012**, *18*, 13117-13125. Article selected for the Front Cover Picture.

"*A Robust MOF for the delivery of the non conventional half-sandwich ruthenium(II) metallodrug RAPTA-C*" E. Quartapelle Procopio, S. Rojas, N. M. Padial, S. Galli, N. Masciocchi, F. Linares, D. Miguel, J. E. Oltra, J. A. R. Navarro, E. Barea, *Chem. Commun.*, **2011**, *47*, 11751-11753.

"*Capture of Nerve Agents and Mustard Gas Analogues by Hydropho-bic Robust MOF-5 Type Metal-Organic Frameworks*" C. Montoro, F. Linares, E. Quartapelle Procopio, I. Senkovska, S. Kaskel, S. Galli, N. Masciocchi, E. Barea, J. A. R. Navarro, *J. Am. Chem. Soc.*, **2011**, *133*, 11888–11891.

"*Cation exchange porosity tuning in anionic metal-organic frameworks for selective separation of gases and vapours and catalysis*" E. Quartapelle Procopio, F. Linares, C. Montoro, V. Colombo, A. Maspero, E. Barea, J. A. R. Navarro, *Angew. Chem. Int. Ed.*, **2010**, *49*, 7308-7311.


CHEMISTRY
A EUROPEAN JOURNAL
18/41
2012
PLASTIC OPEN COPPER SITES = SELECTIVE SOFT PCP!
CO_2 per dicopper
Gate pressure
p/p_0
A Journal of
ChemPubSoc Europe
Concept
DNA Metalating–Intercalating Hybrid Agents for the Treatment of Chemoresistant Cancers
U. Bierbach and J. Suryadi
WILEY-VCH
Supported by ACES
CEUJED 18 (41) 12905–13228 (2012) · ISSN 0947-6539 · Vol. 18 · No. 41 · 2012
www.chemeurj.org